CONSTRUCTION SIMULATION OF CURVED STEEL I-GIRDER BRIDGES

A Dissertation
Presented to
The Academic Faculty

By

Ching-Jen Chang

In Partial Fulfillment
Of the Requirements for the Degree
Doctor of Philosophy in Civil Engineering

Georgia Institute of Technology

August 2006

CONSTRUCTION SIMULATION OF CURVED STEEL I-GIRDER BRIDGES

Approved by:

Dr. Donald W. White, Advisor
School of Civil and Environmental Engineering
Georgia Institute of Technology

Dr. Rami M, Haj-Ali
School of Civil and Environmental Engineering
Georgia Institute of Technology

Dr. Roberto T. Leon
School of Civil and Environmental Engineering
Georgia Institute of Technology

Dr. Olivier Bauchau
School of Aerospace Engineering
Georgia Institute of Technology

Dr. Kenneth M, Will
School of Civil and Environmental Engineering
Georgia Institute of Technology

Date Approved: July 10, 2006

ACKNOWLEDGEMENTS

The author would like to express his appreciation to his thesis advisor, Dr. Donald W. White, for his direction, patience and encouragement.

The sponsorship of this research by Professional Services Industries, Inc. (PSI) and the Federal Highway Administration (FHWA), as well as the extensive collaboration with the FHWA and PSI staff, are gratefully acknowledged. Mr. John Yadlosky is thanked for his providing detail engineering drawings of the Ford City Bridge. Mr. Fred Beckmann is thanked for his extensive feedback on fabrication and erection. The findings expressed in this paper are the authors' and do not necessarily reflect the views of the above organizations or individuals.

Special thanks to author's colleague, Se-Kwon Jung, for his assistance with the ABAQUS FEA solutions and the inspiration of the research work.

Great thanks to the author's wife, Sheng-Ting (Christine) Huang, who showed considerable patience during the study, and the author's parents-in-law, who provided the best support for taking care the author's new-born baby, Emily. The greatest appreciation goes to the author's parents, who provided the author the strongest mental support throughout the study.

TABLE OF CONTENTS

LIST OF TABLES

LIST OF FIGURES

SUMMARY

This study addresses the development of a prototype software system for analysis of horizontally curved steel I-girder bridges using open-section thin-walled beam theory. Recommendations are provided for the use of three-dimensional (3D) grid idealizations in analyzing curved I-girder bridge structural systems. The 3D grid idealizations account for the general displacements and rotations common within complex curved I-girder bridge structures, i.e., none of the displacement and rotational degrees-of-freedom are arbitrarily assumed to be equal to zero. Also, these idealizations account for the warping (or cross-bending) deformations of the I-girder flanges that dominate typical girder torsional responses. An approximate approach is investigated for capturing the influence of girder web distortion on composite I-girder responses.

A key focus of this research is the development of prototype methods for simulating the construction of curved steel I-girder bridges, including erection of the steel and staged casting of the slab. The resulting capabilities allow engineers to evaluate the deflections, reactions and/or stresses at different stages of the steel erection or concrete slab construction, determine required crane capacities, tie-down, jacking or come-along forces, and calculate incremental displacements due to removal of temporary supports. Also, the capabilities can be used to determine the influence of different steel detailing methods on the bridge geometry, such as the web plumbness under the steel or total dead load. Key requirements necessary to ensure accuracy of the analysis results are addressed.

CHAPTER 1

INTRODUCTION

Horizontally curved steel I-girder bridges can experience significant three-dimensional deflections and rotations. These deflections and rotations can affect various important attributes of the final constructed geometry such as the lateral position of the slab, the relative displacements at slab expansion joints, the rotations at the bearings, and the plumbness of the girder webs. In addition, differential deflections and rotations between the girders during erection can influence significantly the fit-up of the steel and the erection requirements (e.g., the number of temporary supports, crane capacities, and tie-down, come-along and jacking forces). If the magnitude of the lateral displacements and rotations due to the torsional deformations is large enough, then typically the steel is detailed to partially or fully compensate for them. The most popular (and economical) of these detailing methods induce locked-in stresses in the structure and tend to increase the lack-of-fit between the deformed structural components during erection. In these methods, the cross-frames are detailed such that they force a twist into the girders opposite to the torsional rotations under a certain dead load. AASHTO (2004) Article 6.7.2 indicates:

> **"…out-of-plumbness should be considered in the detailing of the deck and the bearings… the Engineer may need to consider the potential for any problematic locked-in stresses in the girder flanges or the cross-frames or diaphragms… The decision as to when these stresses should be evaluated is currently a matter of engineering judgment."**

As the US becomes more and more urbanized, increasingly strict and complex site constraints are resulting in bridge projects with longer spans, more severe curvature and more complex geometries. These attributes exacerbate the magnitude of the above

deflections and rotations. Inaccurate estimates of these larger deflections and rotations, combined with larger weights and stiffnesses of the bridge components, can lead to erection difficulties, delays, and claims. Furthermore, the larger girders used in longer span bridges tend to be more slender (e.g., smaller flange width to web depth ratios). These characteristics make the girders more susceptible to significant second-order effects and potential instabilities during construction. AASHTO (2004) Section 6.10.3 requires that calculated girder second-order stresses must be maintained below a first-yield level, as well as below design strength limits that in some cases may be less than the first-yield level, under all construction conditions. Conservative equations are provided for second-order amplification of girder flange lateral bending stresses in AASHTO (2004) Section 6.10.1.6. In cases where the second-order amplification during construction is significant, Section C6.10.1.6 recommends that a geometric nonlinear analysis should be considered.

Larger bridges also generally necessitate the placement of the slab in multiple stages. For cast-in-place slabs, the prior stages typically achieve early stiffness gains that cause them to act compositely with the steel girders during subsequent stages. If pre-cast slab panels are used, the many panels are made composite with the structural steel over some period of time. Typically, only a fraction of the panels are in place on the bridge prior to making other panels composite. Prior stages of the slab construction must be checked for tension induced by successive stages. Also, the staged construction of the slab can influence the overall dead load deflections and rotations. This attribute of the construction, as well as the locked-in stresses due to the detailing of the structural steel, can have an important influence on the required vertical camber of the girders.

Potentially all of the above considerations can be addressed effectively and reliably by modern three-dimensional structural analysis methods. However, all 3D analysis methods are of course not the same. There are many different 3D methods,

there are many modeling decisions that must be addressed, and there are many subtle factors that can have an important influence on the predicted responses. Also, to the knowledge of the author, presently (2006) there is no structural engineering software that facilitates the complex 3D problem definition, analysis calculation, and response visualization in curved I-girder bridges associated with:

1) the checking of deflections, rotations and/or stresses at different stages of the steel erection and slab construction,
2) the assembly of additional components into the partially erected structure, accounting for the spatial deformations, displacements and rotations in the additional components as well as in the partially erected structure,
3) the determination of required temporary supports, crane capacities, and tie-down, jacking or come-along forces,
4) the placement of different stages of the slab on the deflected three-dimensional geometry, and
5) the influence of different steel detailing methods and staged slab construction operations on the final constructed geometry and the final dead load stresses in the slab and in the structural steel.

Furthermore, numerous 2D and 1D analysis procedures often are utilized in current curved I-girder bridge design practice. Many of these procedures are sufficient and appropriate for simpler and smaller structures. However, for larger and more complex structures, there are many assumptions embedded in the 2D and 1D methods that can influence the accuracy of their results.

Three-dimensional finite element methods are now used extensively in many cases for bridge engineering analysis. In the context of I-girder bridges, these approaches typically involve the use of shell or solid finite elements for the concrete slab, shell finite elements for the girder webs, beam elements for girder flanges,

stiffeners and connection plates, truss and/or beam elements for the individual cross-frame members, and appropriate constraint relationships to tie the different parts of the model together (BSDI 2006; Jung 2006). Nevertheless, grillage (or grid) analysis methods are still very popular. This popularity comes from the fact that the more general 3D analysis software packages often require significantly greater problem definition and result interpretation effort. Typically, they do not allow the analysis model to be defined directly in terms of girders and other components of the bridge, and they do not synthesize the results specifically into responses such as girder forces and moments, although there is conceptually no technical reason why these packages should not be able to do so.

The main distinguishing characteristic of grid methods is that they are based on a beam-theory idealization of the girders as well as an idealization of the slab by a grid of beam elements. The beam-theory idealization is closer to the way that Engineers typically think about bridge structures in design. Nevertheless, most of the current grid analysis approaches appear to involve the use of a reduced degree-of-freedom (dof) set at the nodes of the analysis model. The selection of this reduced dof set is based on the assumption that certain deflections and/or rotations are negligible (Huang 1996; Descus I and II 2004, MDX 2004). Unfortunately, the inherent 3D behavior of curved I-girder bridges can lead to significant movements along all the dofs at any given node in the structural model. Also, I-girders are open-section thin-walled members. The warping (or cross-bending) of the girder flanges is a predominant feature of their torsional response. This generally requires a seventh warping degree of freedom at the girder nodes.

This research focuses on the development of a prototype software system aimed at practical comprehensive simulation of the construction of curved I-girder bridges. The prototype system uses a complete 3D grid analysis. That is, it involves a comprehensive 3D idealization of the bridge responses, including the warping of the I-girder flanges,

using open-section thin-walled beam theory finite elements for the girders. A 3D grid idealization with 6 dofs per node is used for modeling the slab. The proposed prototype capabilities for construction simulation as well as the derived beam element are implemented in the GT-SABRE software system (acronym for Georgia Tech – Structural Analysis and BRidge Evalution) (Chang 2006). Emphasis is placed on numerous considerations associated with the problem definition, 3D analysis modeling, and result interpretation to achieve a useful application of these types of 3D analysis tools for the construction engineering of curved I-girder bridges.

1.1 Fundamental Behavior of Curved I-Girder Bridge Systems

Horizontal deflections and reactions can be more significant in curved than in straight bridges without skew. Also, the interaction among the girders in curved bridges tends to be larger than among girders in straight bridges without skew. This behavior can be understood by the representative single span curved I-girder bridge shown in Figure 1.1. Since the resultant of the support reactions at the ends of the bridge and the resultant of the self-weight plus the applied load are not collinear, torsional reactions are necessary at the end bearing lines to satisfy global equilibrium. As a result, the vertical reactions must be larger on the outside girder and potential uplift at the inside girder may be a consideration.

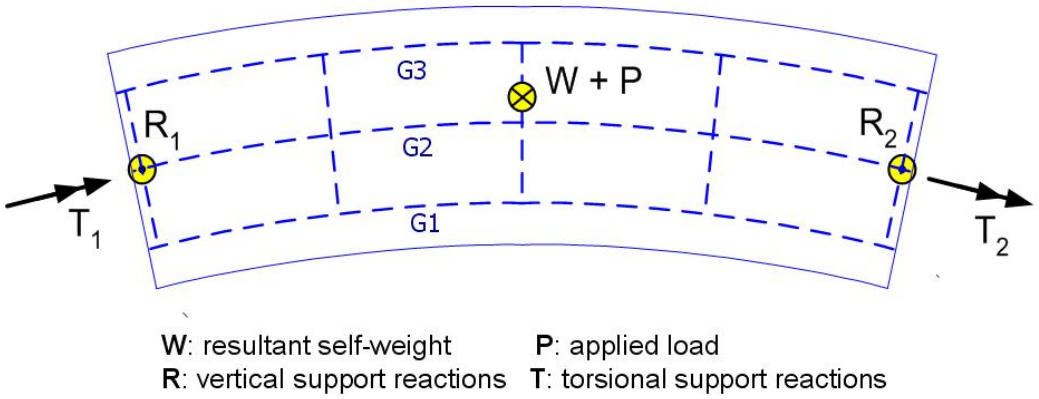

Figure 1.1 A single span curved I-girder bridge utilizing three girders

Also, the cross-frames are essential components of the structural system in curved I-girder bridges, since they are necessary to maintain equilibrium of the girders. The slab, which AASHTO (2003 & 2004) requires to be composite, participates in various significant ways in the final constructed system: (1) along with the cross-frames, it distributes live loads to the girders, (2) it acts as a large top flange with respect to major-axis bending of each of the girders, (3) it provides lateral and twisting restraint to the girder top flanges between the cross-frame locations, and (4) it acts as a large top flange with respect to overall torsion of the bridge, causing the idealized shear center of the bridge cross-section to be located above the slab as shown in Figure 1.2.

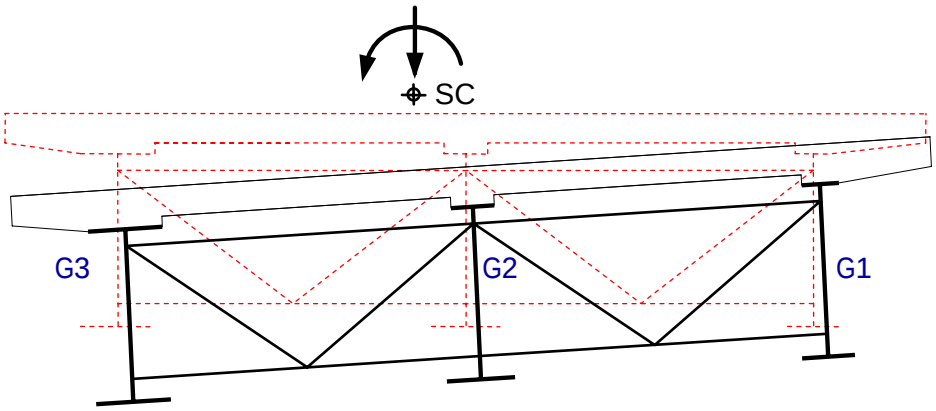

Figure 1.2 Bridge torsional deformations and typical shear center (SC) location

Figure 1.3 shows typical internal forces in the slab, the outside girder and the cross-frame members using the example bridge of Figure 1.1. Figure 1.4 shows the equivalent flange lateral distributed loads associated with positive major-axis bending moments acting through the horizontal curvature. These loads are directed away from the center of curvature at the top flange and toward the center of curvature at the bottom (tension) flange. These equivalent lateral distributed loads represent the torsion induced in the I-section members due to the horizontal curvature. They are resisted predominantly by flange warping (or lateral bending) between the cross-frames as well as by "reactions" at the cross-frames, transferring the torsion of the individual girders into a torsion on the overall bridge system.

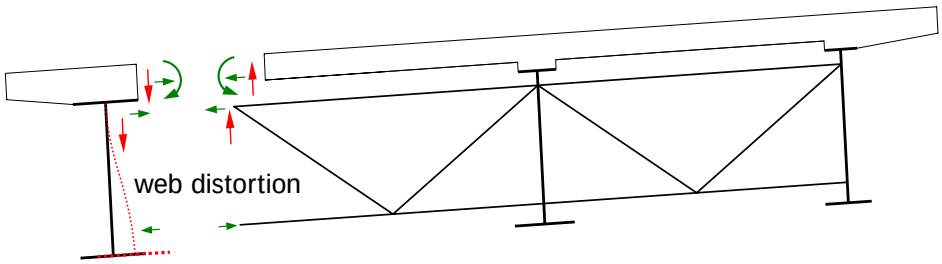

Figure 1.3 Internal forces in slab, outside girder and cross-frame members

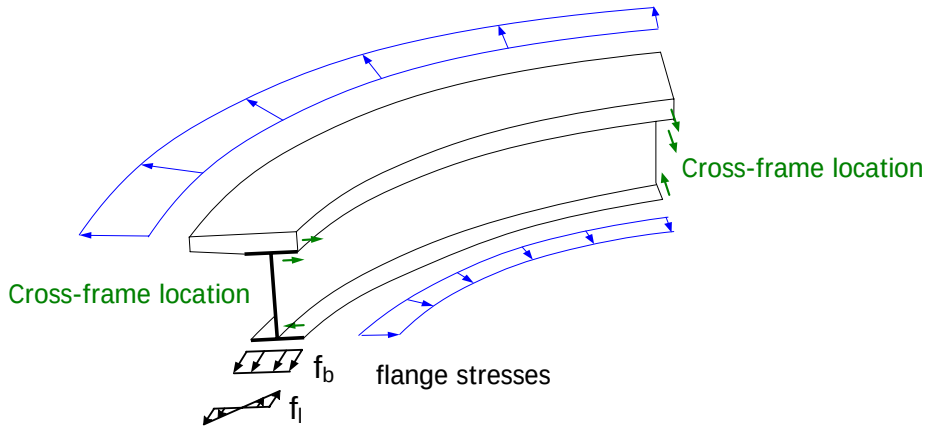

Figure 1.4 Equivalent flange lateral distributed loads associated with positive major-axis bending moments acting through horizontal curvature

I-girders with singly-symmetric cross-sections are common in curved steel I-girder bridges. AASHTO (2004) requires that curved bridge I-girders must be composite with the slab, and thus it is more economical to use a smaller top flange. Also, I-girders with variable web depth are used in longer span bridges for reasons of efficiency and economy. In addition, the girder cross-sections are changed typically at the field splice locations, and in certain cases, at other locations along the length of the bridge. The different cross-section dimensions result in different shear center elevations of the individual girders. As a result, when using open-section thin-walled beam elements for modeling the bridge girders, the warping displacements are discontinuous at the splice locations if cross-sections with different shear centers are spliced together. A transition length is necessary such that the section dimensions can be tapered from one size to the other at girder splice locations.

Moreover, the slab provides restraint to the twisting of the top flange of the I-girders after it is made composite. However, the I-girder webs typically are not stiff enough to transfer this restraint to the bottom flange, resulting in web distortion (see Figure 1.3). Web distortion can significantly influence the warping (or lateral bending) of the girder bottom flanges. This behavior is addressed in this research by using a rotational release between the open-section thin-walled beam model of the steel I-girders and a grid representation of the concrete slab. Other approximations of the general behavior of composite I-girders using open-section thin-walled beam theory also are addressed.

1.2 Requirements for Construction Simulation

The displacement of, internal stresses in and stability of curved I-girder bridges during construction are important considerations. Bridges are usually erected piecewise.

A wide variety of steel erection schemes may be employed depending on the size and specific geometry of the bridge. Because of the differential deflections of curved girders during erection, a major consideration in construction engineering analysis is the fit-up of the steel pieces in the deformed geometry of the partially erected structure. In many cases, girders or girder subassemblies are connected together with cross-frames after they are seated on temporary and/or permanent supports, or are connected at splice locations. However, differential deflections and rotations may make the connections difficult in certain situations. In certain cases, measures may be necessary to limit the magnitude of incompatibilities in the rotations and/or displacements at connection points or girder splice locations.

Another important consideration is the prediction and control of the structure's final geometry. Different steel detailing practices, erection procedures and slab casting sequences can have a significant influence on the final constructed position. Bearings must accommodate the rotations due to dead and live loads or must be installed in a manner to ensure that their rotation limits are not exceeded, girder vertical elevations should be within tolerances accommodated by haunch depths, and tolerances on the horizontal roadway alignment should be met. Also, AASHTO (2004) indicates that in addition to considering the effects of deviations from the ideal final bridge geometry, the Engineer may need to consider the influence of locked-in construction stresses on the structural performance in some bridges.

In many cases, all of the above considerations may be of minor significance. However, in bridges with longer spans, tight radii, sharp skews, and/or highly stiff or flexible flanges in the lateral direction, detailed engineering of the erection process may be required. Therefore, AASHTO (2004) requires Engineers to provide at least one feasible steel erection sequence for the bridge design.

The following notes briefly summarize the essential concepts and features needed for comprehensive construction simulation of curved I-girder bridges:

- ***Cross-frame detailing methods and their relationship to fit-up of steel components, locked-in stresses and girder web plumbness***

Understanding of steel detailing practices is key to addressing construction simulation for steel I-girder bridges. In general, steel I-girders are fabricated with a vertical camber to compensate for their vertical dead load deflections. Due to the horizontal curvature, the vertical deflections are different in each girder. As a result, the required vertical cambers are also different. Furthermore, the cross-frames may be detailed to connect to the girders in any of the following ways:

1. No-Load Fit (NLF): The cross-frames are detailed to connect to the girders in their cambered, plumb, no-load geometry without inducing any locked-in stresses due to fit-up.
2. Total Dead Load Fit (TDLF): The cross-frames are detailed to connect to the girders with their webs plumb in the idealized total dead load geometry, i.e., the vertical position after the total dead load vertical displacements are subtracted from the initial cambered positions.
3. Steel Dead Load Fit (SDLF): The cross-frames are detailed to connect to the girders in their idealized steel dead load geometry (webs plumb but with the steel dead load vertical displacements subtracted from the initial cambered position).
4. Twist Camber Fit (TCF): The girder top and bottom flanges are fabricated with different radii, in addition to the vertical camber. The cross-frames are detailed to fit to the twist cambered geometry in the no-load condition without inducing any locked-in stresses due to fit-up.

The latter three detailing methods are intended to compensate either partially or completely for the girder torsional rotations during the construction. With TDLF detailing, the girder webs are targeted to be plumb at the end of the construction of the slab, whereas with SDLF detailing, the girder webs are targeted to be plumb at the end of the steel erection. TCF may target either of these web plumb conditions. Of these methods, NLF is typically the simplest and most economical assuming that the resulting girder out-of-plumbness and the other movements relative to the no-load geometry are tolerable. TCF is generally viewed as being the most expensive option and is rarely used for I-girder bridge construction.

Detailing for NLF, SDLF, TDLF or TCF generally should be specified by the designer. This is because this decision can have an important influence on construction requirements, the definition of and achievement of a targeted geometry for the completed structure, as well as the performance of the bridge. The differential deflections between the girders in the partially completed structure, and the corresponding forces required for assembly of the components, tend to be somewhat larger for SDLF and TDLF. Also, SDLF or TDLF detailing influences the girder vertical deflections because of the corresponding locked-in stresses. Although the differences between the vertical deflections for TDLF, SDLF or NLF may often be accommodated within the haunch depths at the top of the girders, the Engineer may prefer to avoid using up the vertical tolerances provided by the haunch depths to accommodate these differences.

Chavel and Earls (2001, 2006a) studied the erection procedures for a specific long-span curved steel I-girder bridge and showed that girder displacements and stresses as well as support reactions are significantly affected by the detailing of the girders and the cross-frames. They created a series of finite element models for each of the construction stages and analyzed these models separately. They found that

significant induced displacements, internal stresses and support reactions may be caused by what they refer to as “inconsistent” detailing, i.e., the use of SDLF or TDLF detailing. Also, they pointed out that erection difficulties may occur because of the additional lack of fit caused by these detailing methods. In addition, they recommended that in general the Engineer must check the out-of-plumbness of the web in the final constructed condition, and if specified tolerances are not met, other “consistent” detailing options should be used. This recommendation implies that TCF must be employed. Nevertheless, in cases where the out-of-plumbness of the girder webs under dead load is larger than desired by the Engineer or Owner, the commentary of (AASHTO 2004) recommends either SDLF or TDLF detailing should be used, since TCF detailing is more costly.

- ***Modeling of the I-girders as open-section thin-walled members***

The greatest accuracy and the best efficiency are generally not achieved by the same methods. Approximate one-dimensional and two-dimensional methods are simple and easier to understand but are unable to evaluate stability and deformation effects in more complex structures. Also they usually involve simplifying assumptions that can affect the accuracy of the analysis results. Three-dimensional refined shell models are able to capture the full dimensionality of the structural system and are generally accepted as providing the most reliable predictions. However, they require more effort and time and are more complicated. Three-dimensional beam elements based on open-section thin-walled beam theory have the potential to satisfy a good balance of both accuracy and efficiency. A beam element can be defined to have two nodes. Each node includes seven degrees of freedom: three translations, three rotations and a warping degree of freedom. With appropriate modeling approaches, the open-section thin-walled

beam kinematics can address most of the complex 3D behavioral characteristics of curved I-girders and curved I-girder bridges.

- ***Precise definition of no-load geometry***

To obtain accurate predictions of the response quantities for construction simulation, it is necessary in general to define the physical no-load geometry precisely, i.e., the girder vertical curve due to the grade and superelevation, the girder camber, and positions of the cross-frames through the depth. This information is typically not shown in detail on the engineering drawings (Gaylord et al, 1997). However, the fabricator needs to calculate the detailed influence of the grade, superelevation and camber on the geometry of the structural steel. This information is also essential for modeling of the fit-up of the structural steel during erection.

Because the bridge bearings are offset from the neutral axis of the girders, and because of the load-height effects particularly from the slab weight during casting operations, significant lateral forces can be induced at the bearing locations. These forces cause additional torsion and bending in the girders. Therefore, it is essential to model the elevation of the bearings as well as the position of the loads (i.e., the load height) explicitly within the analysis of curved I-girder bridges.

- ***Handling of potentially significant geometric nonlinearities***

In horizontally curved I-girder bridges, the geometric nonlinearity is potentially important during construction because of the flexibility of the I-girders in torsion and lateral bending. Bradford and Pi (2001) note that nonlinear analysis is needed in general to predict the behavior of curved I-girders under construction loads. In modeling of steel erection operations, compatibility must be achieved between points on the deformed

structural components. This necessitates the consideration of equilibrium on the deformed geometry, i.e., a geometric nonlinear analysis.

- ***Modeling of unconstrained and partially-constrained components***

A single girder may be lifted by a crane and moved to the desired support or splice locations. Once it is placed on its supports or the splice connection is started, typically an individual girder must be held by the crane until it is connected to other components of the bridge with cross-frames. The deformed girder may be only partially constrained against rigid body motion and will not generally fit up with the connection points on the deformed structure. The single girder may or may not be tied down on its supports. The best scheme for lifting a single curved girder (resulting in the smallest induced stresses) is to lift by cables at two locations separated by a spreader beam, and to attach the cables at the intersection of a line through the member center of gravity (Davidson 1996). Several girders may be connected together with cross-frames and then lifted into position as a unit to reduce the deflections and induced stresses during the lifting operations. The stress state in the lifted girder or girders may or may not be of interest. However, the deformations under lifting may have an important influence on the splice or cross-frame installation. The analysis software must be able to calculate the deformations of components during lifting and implement the rigid body motion of these components to position them for assembly with other parts of the structure.

- ***Connecting of deformed components***

The assembly process can be accomplished in the physical structure by seating a lifted girder or subassembly on the bearings, and by bolting or welding to the erected structure. Field welding is acceptable for girder splicing, but it is seldom used due to the economic advantages of bolting (AISC 1994). A typical assembly process is described

by AISC (1994) as follows. The girders are set by a “raising gang” with a sufficient number of pieces to maintain stability after the lifting devices are disconnected. Drift pins are driven into the bolt holes to align the connection points and some bolts are installed. At least two bolts or pins are required at each connection during this stage. This is followed by the installation of the remaining cross-frames, diaphragms or bracing and the completion of all the connections by a “bolt gang.”

The analysis software must be able to calculate the required forces (e.g., jacking or come-along forces) necessary in general to achieve compatibility at all the degrees of freedom at which two deformed components are brought together and connected. Also, the analysis software must be able to model local fine adjustments that are necessary for assembly of the steel components. That is, the components are typically located within close proximity to one another at their connection points by application of overall forces and displacements to the structure and the component(s) being assembled using cranes, jacks, come-alongs, etc.. Once the close proximity of the connection point(s) is achieved, final compatibility of the parts at the connection is achieved by application of forces at the connection. In addition, the software must be able to model the potential uplift at the supports if girders are not tied down on their supports during steel assembly.

- ***Modeling of staged slab construction***

In the finite element model, the slab elements need to be instantiated on the deformed geometry to represent successive slab construction stages. The weight of the instantiated slab must be resisted by the portions of the structure from the prior stages that are already composite, as well as the structural steel that is not yet composite in the structural model. The rapid stiffness gain of the concrete at an early age may be represented by assuming a specified modulus of elasticity for the concrete from prior

stages at each successive stage of the slab construction (Topkaya and Williamson 2004).

- ***Tracking of three-dimensional response***

Warping and torsional effects generally are significant in curved I-girders. A number of different FEA software systems account for warping effects using open-section thin-walled beam elements. However, often they display the beam elements as line segments within their graphical interfaces, and therefore, the detailed torsional response is not easy to discern. It is important for the software to display the actual three-dimensional deformed geometry of the members for the three-dimensionality of the response to be easily discerned.

- ***Taking advantage of uniqueness***

The term uniqueness implies that the analysis results are independent of the order of the component assembly or load application. By taking advantage of this concept, then if the engineer are not interested in the structural responses before a certain steel erection stage, and if none of the erection processes before this stage lead to a non-uniqueness, a model of the bridge can be created containing all the components at this stage and the structure self-weight can be applied to the model all at once to determine the corresponding responses. Typically, the analysis of staged slab construction can begin with this type of instantaneously instantiated model for the complete bridge, representing the effects of the steel self-weight. The results for staged slab casting are generally nonunique, since the bridge response depends on the specifics of the casting sequence. However the results for the bridge response at the end of the steel erection are typically unique, within the limits of a number of key

assumptions. Also, the principal of uniqueness can be applied to simplify the handling of intermediate stages during an overall construction simulation.

1.3 Current methods and available tools for construction simulation

At the present time, analyses of the erection of curved steel I-girder bridges typically are conducted by creating structural models for each of the construction stages and analyzing these models individually (Linzell 1999 and Chavel and Earls 2001, 2006a and 2006b). That is, for each construction stage, a model of the partially erected structure is created in its no-load geometry. Then the self-weight is applied to the model. Therefore, all the erection stages are analyzed independently from one another. The calculation of construction requirements, e.g., the forces required for assembly of the steel components and the influence of these forces on the partially completed structure is difficult using this approach. Also, the calculation of the effects of staged slab construction, including the instantiation of the slab on the deflected geometry of the structure, is not easily accomplished with this type of procedure.

Regarding current software systems for analysis of curved bridge construction, most appear to handle construction analysis by creating structural models for each of the construction stages and analyzing these models individually as mentioned above. Some systems are able to progressively add new non-stressed structural components to the deformed structure at intermediate stages of construction. Several of them are able to handle concrete creep, shrinkage and time-dependent effects for the staged concrete casting analysis. However, the author is not aware of any software that applies these specific capabilities to curved steel I-girder bridges. In addition, the author is not aware of any commercial or research software system that provides the capabilities for modeling the assembly of the structural steel and calculating the corresponding required

forces discussed in the previous section. These types of capabilties can be very useful for assessing constructability.

1.4 Objectives and Scope

The purpose of this research is to investigate and develop methods for simulation of complete construction processes to predict construction requirements and intermediate and final states (displacements, stresses, forces and reactions) in curved I-girder bridges. This research also evaluates the ability of various approximate methods to predict curved I-girder bridge responses. A three-dimensional beam-grillage model is selected and developed in detail for the modeling of curved I-girder bridge structures. The bridge girders are modeled with open-section thin-walled beam elements (7 dofs per node) and the slab is modeled with a grid system using beam elements with 6 dofs per node. Theory, formulation, modeling issues, implementation and application are addressed. The following tasks are targeted to achieve the above goals:

1. Develop a geometric nonlinear open-section thin-walled beam finite element that is able to handle horizontal curvature effects, section monosymmetry, and tapered geometry. Provide targeted benchmark problems for testing the accuracy of the element in capturing the above effects.
2. Quantify the requirements for accurate/sufficient 3D analysis of curved I-girder bridges using open-section thin-walled beam theory.
3. Characterize the fundamental behavior of curved I-girder bridge systems, review simplified models for calculation of elastic stresses, and suggest improvements to these basic methods.
4. Provide guidelines to ensure the creation of models that best represent the physical system behavior and indicate potential modeling pitfalls.

5. Study steel fabrication/detailing and bridge steel erection and staged concrete-slab construction in current practice. Develop finite element methodologies for the analysis and simulation of bridge construction operations.
6. Develop a prototype software system for analysis of curved I-girder bridge construction, including tools for visualization of the analysis results. The beam element in task 1 and finite element methodologies in tasks 3 and 4 are implemented in this software system, referred to in this work as GT-SABRE.
7. Validate and demonstrate the capabilities of the developed prototype software system by performing detailed analyses of a full-scale composite I-girder bridge tested at the Federal Highway Administration (FHWA) Turner-Fairbank Highway Research Center (TFHRC) and a long-span curved I-girder bridge previously studied by Chavel and Earls (2001, 2006a and 2006b).
8. Identify further requirements necessary to achieve the broadest advances in software to support the construction engineering of curved I-girder bridges.

1.5 Organization

Chapter 2 derives the finite element formulations developed in the current study. Several targeted benchmark problems are provided to verify the correctness of these or other alternative finite element procedures.

The modeling and analysis of composite bridge systems is discussed in Chapter 3. The qualities and limitations of several modeling strategies for design analysis of curved I-girder bridge structural systems are investigated and recommendations are provided. Results from a full-scale composite I-girder bridge tested at the FHWA TFHRC are used as a basis for comparison of different analysis methods.

Chapter 4 discusses the detailed fundamental requirements for simulation of steel I-girder bridge construction. Bridge construction procedures and corresponding finite element methodologies are addressed including the handling of girder cambers, cross-frame detailing and steel erection sequences as well as staged concrete casting.

In Chapter 5, the above mentioned FHWA test bridge is utilized as an example for the validation and demonstration of the proposed finite element methodologies for bridge construction simulation provided in Chapter 4. Different steel detailing methods are investigated by modeling them on the test bridge. In addition, the proposed finite element modeling strategies for composite bridges are further validated in this Chapter.

In Chapter 6, the long-span curved I-girder bridge previously studied by Chavel and Earls (2001, 2006a and 2006b) is utilized as a further demonstration of the finite element methodologies for bridge construction simulation. The focus of this chapter is on analyses of steel erection and concrete slab staged casting.

Chapter 7 provides a summary of the developments and findings and the general conclusions from this study. This chapter also recommends potential future work.

Appendices I and II provide detailed derivations pertaining to the finite elements introduced in Chapter 2. Appendix III includes detailed analysis results for the erection simulation discussed in Chapter 6.

CHAPTER 2

FINITE ELEMENT FORMULATION

2.1 Introduction

In this study, the bridge I-girders are modeled using open-section thin-walled beam finite elements based on Vlasov kinematics. Vlasov kinematics invokes the assumption that the shear deformations due to beam shear and due to nonuniform (warping) torsion are negligible. Plane sections are assumed to remain plane with the exception of warping deformations due to nonuniform torsion. In addition, the cross-section profile is assumed to retain its original shape, i.e., there is no distortion of the cross-section geometry.

A displacement-based beam formulation is developed and applied in the current study. The element independent variables are its displacement degrees of freedom, which are interpolated using cubic Hermitian shape functions for the transverse displacements, exponential equations (based on solution of the governing differential equations of the geometrically linear torsion problem) for the element twist and warping, and linear interpolation for the axial displacements along the member reference axis. For the stress-strain description, the second Piola-Kirchhoff (PKII) stress and Green strain are adopted.

The element is developed using a Total Lagrangian–Corotational (TL-CR) approach. The term Total Lagrangian indicates that a single initial configuration is employed as the reference geometry for all of the element responses. In this work, this reference configuration is taken as a straight chord between the element end nodes. The initial curvature relative to this reference configuration is handled as an initial displacement effect. The term corotational indicates that the element is formulated in a

corotational (natural) coordinate frame that rotates with the element chord. The motion of the element is decomposed into two modes: element rigid body motion (taken as the motion of the corotational frame) and displacements that cause element strains, referred to as the natural displacements (Argyris 1982). The strains and the rotations relative to the element chord are assumed to be small. Large rigid-body rotation is accounted for in the transformation between the element natural and global displacements.

The above general-purpose finite element approach captures the effects of horizontal curvature in the following fashion. For members that have a constant horizontal radius of curvature, the element initial end rotations are equal and opposite to one another in the element corotational frame. The corresponding initial transverse displacements relative to the element chord reduce from a cubic function to a quadratic function. In this work, the initial end rotations are computed for this case by matching the peak displacement given by the quadratic function to the circular arc at the middle of the element length. Since AASHTO (2004b) restricts the subtended angle associated with the I-girder unbraced lengths to 0.1 rad within the final constructed configuration, and since generally more than one element is required for each unbraced length, the above quadratic displacement field provides a sufficient description of the curved geometry. For members with a non-constant horizontal radius of curvature, the physical geometry is matched at the element ends and at one-third and two-thirds of the element chord length.

As mentioned in Chapter 1, typically the I-girder cross-section is changed at field splice locations. In the open-section thin-walled beam theory representation of singly-symmetric I-girders, there is a resulting discontinuity in the beam theory warping functions on each side of such a cross-section transition. This is because the warping functions based on Vlasov's theory vary with the location of the shear center, and the shear center location changes with a change in the cross-section dimensions for singly-

symmetric cross-sections. To conquer this problem, cross-section transitions are modeled as a linear taper in the girder cross-section geometry over a short length in this work. The implications of a physical taper in the cross-section geometry, e.g., a variable web depth in nonprismatic members such as haunched girders, on general girder responses are also addressed.

Modeling of the physical depth of bearings as well as the connections between the girders and cross-frame members is an important consideration in the three-dimensional analysis of bridge structural systems. For example, Hall et al (1999) indicate that these considerations are essential to proper calculation of radial reactions at supports. These issues are addressed in this research by the use of rigid offsets in the beam element formulations.

In the following section, the current literature pertaining to curved beam finite elements is briefly reviewed. Then the 3D finite rotation equations are introduced and the transformation between the corotational and global coordinate systems is derived. This is followed by an explanation of the beam finite element formulation within the corotational frame, considering a general singly-symmetric I-shaped cross-section and an assumed linear variation in the cross-section dimensions along the element length, i.e., a linear taper in the cross-section dimensions in a given element. Lastly, the formulation of the rigid offset constraint is introduced. Several benchmark problems are provided at the end of the chapter to demonstrate the correctness and accuracy of the resulting finite element procedures.

2.2 Literature Review

Generally speaking, open-section thin-walled beam finite elements are either based on the kinematics of Vlasov's beam theory, which neglects shear and bi-shear

deformations, or Reissner's beam theory, which includes beam shear deformations and can include consideration of general warping shear deformations.

Several researchers have developed curved finite elements based on the use of a cylindrical coordinate system for description of the strains and displacements, e.g., (Fukumoto and Nishida 1981, Yoshida and Maegawa 1983, and Huang 1996). Pi and Trahair (1996) proposed a curved beam element on the basis of a Cartesian coordinate system. They derived the strain-displacement relations by adopting the curvature expressions from Love (1944) in the context of Green strain. On the other hand, in Simo and Vu-Quoc's (1991) finite element formulation, which includes beam shear and warping shear deformations and is based on the deformation gradient as the strain measure, the curvature effects are handled within an expression for the deformation gradient and by the parameterization of the centroidal reference axis.

Nukala (1997) and Nukala and White (2004) simplify the general kinematic model of Simo and Vu-Quoc (1991) by neglecting the beam shear and warping shear strains and show that curved geometry can be modeled as an initial displacement effect within a Total Lagrangian description, with the reference configuration being taken as a straight configuration. They include finite curvature terms that are comparable to those considered by Pi and Trahair (1996). It is feasible to analyze curved structures with small to moderate curvature by using finite elements that are straight within their reference frame, where the initial curvature is represented as an initial displacement effect. For curved I-girders, the subtended angle L_b/R is limited by (AASHTO 2003 and 2004) to 0.1 rad in the final constructed configuration. Within this limit, and when a corrotational formulation is employed, the finite curvature terms considered by (Nukala and White 2004) and by (Pi and Trahair 1996) may be neglected.

Many successful finite elements have been developed within the past decade, that have the capability for handling large displacements, large rotations and small

strains. These formulations are typically able to address the effects of small to moderate curvature. Izzuddin and Smith (1996), Teh and Clarke (1998) and Alemdar (2001) have used corotational formulations to simplify the strain displacement relations. Alemdar's (2001) research was implemented in the FE++ object-oriented FEA framework, an enhanced version of which is used in this research. Alemdar adopted Crisfield's (1990) algorithm to obtain the geometric stiffness matrix and to handle the transformations between the corotational frame and the global coordinate system. Rankin and Nour-Omid (1988) developed a projector concept that gives improved finite element performance relative to Crisfield's algorithm. The computational overhead of applying the projector concept for the stiffness transformation, including generation of the element geometric stiffness as well as the element state determination, is smaller than that of Crisfield's (1990) algorithm. This is due largely to the fact that the Rankin and Nour-Omid projector concept permits the development of closed form element equations.

I-section girders with variable web depth are used in larger span bridges for reasons of efficiency and economy. The ideal situation is that the cross-section variation matches the girder moment envelope. Several studies of the lateral torsional buckling of tapered I-section beams have been done in the past few decades. Kerensky et al. (1956) analyzed the lateral torsional buckling of a simply supported beam with linearly or parabolically varying flange widths or thicknesses from the midspan to the both ends using the energy method and sinusoidal displacement functions. Kitipornchai and Trahair (1972) mentioned that with this method, the prediction of the critical load is overestimated for a flange-tapered beam. They provided theoretical solutions for simply supported doubly symmetric I-beams with a tapered web and tapered flanges. Furthermore, they provided the theoretical solutions for a beam with a singly symmetric I-section and suggested that the tangent to the shear center line, which is curved for a tapered monosymmetric section, can be used as a convenient reference for measuring

the deflections of the cross section and for calculation of the torque (Kitipornchai and Trahair 1975). Wekezer (1985) developed a general finite element for investigating the buckling of tapered thin-walled bars. Yang and Yau (1987) derived the differential equations of equilibrium for a tapered I-section beam and provided a finite element formulation similar to Wekezer's to investigate doubly-symmetric tapered I-section beams. Ronagh et al. (2000a) adopted a similar concept to Wekezer's to derive a nonlinear finite element for beams of general variable cross-section based on the Green-Lagrange axial strain and the work-conjugate Kirchhoff axial stress. Recently Boissonnade and Maquoi (2005) developed a beam finite element for geometrically and materially nonlinear analysis of general tapered steel I-section members. Also, Andrade and Camotim (2005) have used a Rayleigh-Ritz approach and sinusoidal shape functions for analyzing the lateral torsional buckling behavior of singly symmetric tapered I-section beams with simply supported and cantilever boundary conditions.

2.3 Finite Three-Dimensional Rotation

A finite rotation increment obtained from the global solution may be defined as $\Delta\boldsymbol{\omega} = \Delta\omega_1 e_1 + \Delta\omega_2 e_2 + \Delta\omega_3 e_3 = \Delta\omega\,\mathbf{e}$, where $\Delta\omega = \sqrt{\Delta\omega_1^2 + \Delta\omega_2^2 + \Delta\omega_3^2}$ is the magnitude of the rotation and the unit vector $\mathbf{e}$ is the axis about which the finite rotation occurs (see Figure 2.1(a)). Due to this rotation, the position vector for a general material point changes from $\mathbf{r}_o$ to $\mathbf{r}_n$. The rotation from $\mathbf{r}_o$ to $\mathbf{r}_n$ is given by the orthogonal transformation

$$\mathbf{r}_n = \mathbf{R} \cdot \mathbf{r}_o \tag{2.1}$$

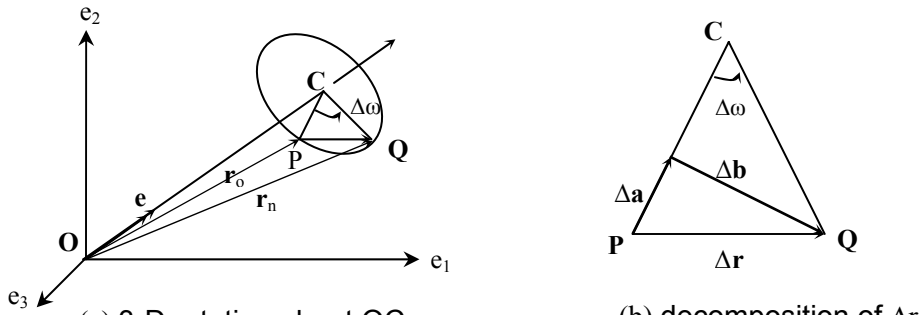

(a) 3-D rotation about OC (b) decomposition of Δr

Figure 2.1 Three-dimensional rotation

The orthogonal finite rotation operator $\mathbf{R}$ can be written in the following form with the aid of Figure 2.1(b) (Crisfield 1997):

$$\mathbf{r}_n = \mathbf{r}_o + \Delta\mathbf{r} = \mathbf{r}_o + \Delta\mathbf{a} + \Delta\mathbf{b} \tag{2.2}$$

or

$$\begin{aligned}\mathbf{r}_n &= \mathbf{r}_o + \frac{1-\cos\Delta\omega}{\Delta\omega^2}(\Delta\boldsymbol{\omega}\times(\Delta\boldsymbol{\omega}\times\mathbf{r}_o)) + \frac{\sin\Delta\omega}{\Delta\omega}(\Delta\boldsymbol{\omega}\times\mathbf{r}_o)\\ &= \left\{\mathbf{I} + \frac{1-\cos\Delta\omega}{\Delta\omega^2}\boldsymbol{\Theta}(\Delta\boldsymbol{\omega})\cdot\boldsymbol{\Theta}(\Delta\boldsymbol{\omega}) + \frac{\sin\Delta\omega}{\Delta\omega}\boldsymbol{\Theta}(\Delta\boldsymbol{\omega})\right\}\cdot\mathbf{r}_o\\ &= \exp(\boldsymbol{\Theta}(\Delta\boldsymbol{\omega}))\cdot\mathbf{r}_o\\ &= \mathbf{R}(\Delta\boldsymbol{\omega})\cdot\mathbf{r}_o\end{aligned} \tag{2.3}$$

in which the matrix $\boldsymbol{\Theta}$ represents the skew-symmetric tensor constructed from $\Delta\boldsymbol{\omega} = \lfloor \Delta\omega_1,\ \Delta\omega_2,\ \Delta\omega_3 \rfloor$. It satisfies the property $\boldsymbol{\Theta}\mathbf{h} = \Delta\omega\times\mathbf{h}$, $\forall\mathbf{h}\in\Re^3$, that is,

$$\boldsymbol{\Theta}(\Delta\boldsymbol{\omega}) = Spin(\Delta\boldsymbol{\omega}) = \Delta\boldsymbol{\omega}\otimes = \begin{bmatrix} 0 & -\Delta\omega_3 & \Delta\omega_2 \\ \Delta\omega_3 & 0 & -\Delta\omega_1 \\ -\Delta\omega_2 & \Delta\omega_1 & 0 \end{bmatrix} \tag{2.4}$$

To obtain the correct geometric stiffness matrix, the proper linearization of the finite rotation equations must be considered. The above rotational vector $\Delta\boldsymbol{\omega}$ (also called

the rotational pseudo-vector (Crisfield 1990)) is non-additive (Alemdar 2001) (see Appendix I). It may be converted to an additive incremental finite rotation quantity so that the following equation is valid:

$$\boldsymbol{\theta}_{new} = \boldsymbol{\theta}_{old} + \Delta\boldsymbol{\theta} \tag{2.5}$$

For a given finite non-additive rotation increment $\Delta\boldsymbol{\omega}$, the corresponding additive finite rotation increment $\Delta\boldsymbol{\theta}$ can be calculated as (Ibrahimbegovic et al. 1995):

$$\Delta\boldsymbol{\theta} = \mathbf{T}^{-1}\left(\boldsymbol{\theta}_{old}\right)\Delta\boldsymbol{\omega} \tag{2.6}$$

in which

$$\mathbf{T}^{-1}(\boldsymbol{\theta}) = \frac{\theta/2}{\tan(\theta/2)}\mathbf{I} - \frac{1}{2}\boldsymbol{\Theta}(\boldsymbol{\theta}) + \frac{1}{\theta^2}\left(1 - \frac{\theta/2}{\tan(\theta/2)}\right)(\boldsymbol{\theta}\otimes\boldsymbol{\theta}) \tag{2.7}$$

and

$$\boldsymbol{\Theta}(\boldsymbol{\theta}) = Spin(\boldsymbol{\theta}) = \boldsymbol{\theta}\otimes = \begin{bmatrix} 0 & -\theta_3 & \theta_2 \\ \theta_3 & 0 & -\theta_1 \\ -\theta_2 & \theta_1 & 0 \end{bmatrix} \tag{2.8}$$

2.4 Transformation between Corotational (Natural) and Global Systems

The transformation of the stiffness matrix between the corotational (natural) and global systems is derived in this section. The derivation is based on the principle of virtual work and follows Rankin and Nour-Omid's (1988) projector concept. As stated by Rankin and Nour-Omid (1988), "the rigid body components of an incremental displacement vector are eliminated when multiplied by the projector (large rigid body rotation components are removed by the projection matrix)."

As shown in Figure 2.2, for a three-dimensional displacement-based beam element, seven degrees of freedom are considered at each element node in the global

system: three displacements u^g, v^g and w^g, three rotations θ_x^g θ_y^g and θ_z^g and a warping degree of freedom ϕ'. In the natural system, where the rigid body modes are removed, the element has nine degrees of freedom: an axial elongation e, three local rotations θ_x^n θ_y^n and θ_z^n relative to the element chord at each node and the same warping degree of freedom ϕ'.

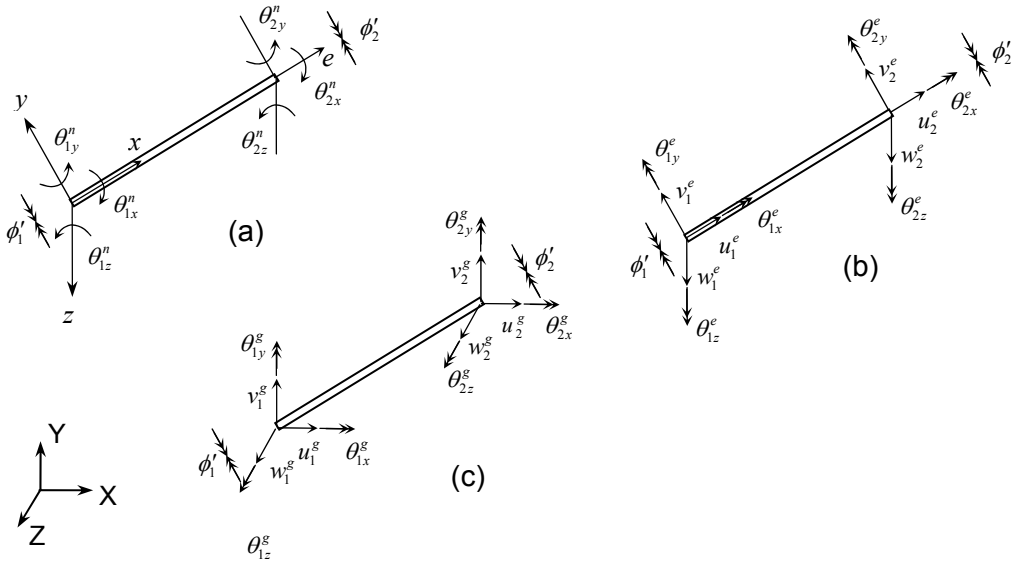

Figure 2.2 The element degrees of freedom in (a) the natural frame, (b) the element frame, and (c) the global frame

The element displacement vectors in the natural frame, element frame and global frame can be expressed as:

$$\mathbf{q}_n^{\,T} = \left\{ e \quad \theta_{1x}^n \quad \theta_{1z}^n \quad \theta_{1y}^n \quad \phi_1' \quad \theta_{2x}^n \quad \theta_{2z}^n \quad \theta_{2y}^n \quad \phi_2' \right\}_{9\times 1} \tag{2.9}$$

$$\mathbf{q}_e^{\,T} = \left\{ u_1^e \quad v_1^e \quad w_1^e \quad \theta_{1x}^e \quad \theta_{1y}^e \quad \theta_{1z}^e \quad \phi_1' \quad u_2^e \quad v_2^e \quad u_2^e \quad \theta_{2x}^e \quad \theta_{2y}^e \quad \theta_{2z}^e \quad \phi_2' \right\}_{14\times 1} \tag{2.10}$$

$$\mathbf{q}_g^{\,T} = \left\{ u_1^g \quad v_1^g \quad w_1^g \quad \theta_{1x}^g \quad \theta_{1y}^g \quad \theta_{1z}^g \quad \phi_1' \quad u_2^g \quad v_2^g \quad u_2^g \quad \theta_{2x}^g \quad \theta_{2y}^g \quad \theta_{2z}^g \quad \phi_2' \right\}_{14\times 1} \tag{2.11}$$

The work conjugate force vectors corresponding to the above displacement vectors are:

$$\mathbf{Q}_n^T = \left\{ P \quad m_{1x}^n \quad m_{1z}^n \quad m_{1y}^n \quad b_1 \quad m_{2x}^n \quad m_{2z}^n \quad m_{2y}^n \quad b_2 \right\}_{9\times 1} \tag{2.12}$$

$$\mathbf{Q}_e^T = \left\{ f_{1x}^e \quad f_{1y}^e \quad f_{1z}^e \quad m_{1x}^e \quad m_{1y}^e \quad m_{1z}^e \quad b_1 \quad f_{2x}^e \quad f_{2y}^e \quad f_{2y}^e \quad m_{2x}^e \quad m_{2y}^e \quad m_{2z}^e \quad b_2 \right\}_{14\times 1} \tag{2.13}$$

$$\mathbf{Q}_g^T = \left\{ f_{1x}^g \quad f_{1y}^g \quad f_{1z}^g \quad m_{1x}^g \quad m_{1y}^g \quad m_{1z}^g \quad b_1 \quad f_{2x}^g \quad f_{2y}^g \quad f_{2z}^g \quad m_{2x}^g \quad m_{2y}^g \quad m_{2z}^g \quad b_2 \right\}_{14\times 1} \tag{2.14}$$

in which P and f represent forces, m represents moments and b represents bi-moment. The variation of $\mathbf{q}_n$ can be written as:

$$\delta\mathbf{q}_n = \left(\frac{\partial \mathbf{q}_n}{\partial \mathbf{q}_e} \right) \delta\mathbf{q}_e = \mathbf{P}\,\delta\mathbf{q}_e = \mathbf{P}\mathbf{G}^T \delta\mathbf{q}_g \tag{2.15}$$

in which $\mathbf{P}$ is the projection operator (or the projector) (Nour-Omid and Rankin 1991) and $\mathbf{G}$ is the coordinate transformation matrix between the element frame and the global frame. The matrix $\mathbf{G}$ is constructed using the element corotational frame (CR frame) basis vectors. The matrix $\mathbf{P}$ maps the absolute element displacement and rotation increments to the corresponding "deformational" or "natural" increments, with all of the terms expressed in element CR coordinates.

Based on work conjugacy

$$\mathbf{Q}_g = \left(\mathbf{P}\mathbf{G}^T\right)^T \mathbf{Q}_n = \mathbf{G}\mathbf{P}^T\mathbf{Q}_n \tag{2.16}$$

Furthermore, the variation of $\mathbf{Q}_g$ may be written as:

$$\delta\mathbf{Q}_g = \mathbf{G}\mathbf{P}^T\delta\mathbf{Q}_n + \mathbf{G}\delta\mathbf{P}^T\mathbf{Q}_n + \delta\mathbf{G}\mathbf{P}^T\mathbf{Q}_n \tag{2.17}$$

in which

$$\delta\mathbf{Q}_n = \left(\frac{\partial \mathbf{Q}_n}{\partial \mathbf{q}_n} \right) \delta\mathbf{q}_n = \mathbf{K}_n\mathbf{P}\mathbf{G}^T\delta\mathbf{q}_g \tag{2.18}$$

$$\delta\mathbf{P}^T\mathbf{Q}_n = \mathbf{K}_{ext1}^e\mathbf{G}^T\delta\mathbf{q}_g \tag{2.19}$$

$$\delta \mathbf{G}\mathbf{P}^T\mathbf{Q}_n = \mathbf{G}\mathbf{K}^e_{ext2}\mathbf{G}^T\delta\mathbf{q}_g \tag{2.20}$$

In Eq. (2.18), $\mathbf{K}_n$ is the element tangent stiffness matrix in the CR frame as introduced in the following section. $\mathbf{K}_{ext1}$ in Eq. (2.19) is the external geometric stiffness matrix contributed by the variation of the projector $\mathbf{P}$ and $\mathbf{K}_{ext2}$ in Eq. (2.20) is the external geometric stiffness matrix contributed by the variation of the transformation matrix $\mathbf{G}$ (see Appendix I). By substituting Eqs. (2.18), (2.19) and (2.20) into Eq. (2.17), Eq. (2.17) becomes

$$\delta\mathbf{Q}_g = \left\{\mathbf{G}\mathbf{P}^T\mathbf{K}_n\mathbf{P}\mathbf{G}^T + \mathbf{G}\left(\mathbf{K}_{ext1} + \mathbf{K}_{ext2}\right)\mathbf{G}^T\right\}\delta\mathbf{q}_g \tag{2.21}$$

Based on the principle of virtual work, the work conjugate relationship in the global frame can be written as

$$\delta\mathbf{q}_g{}^T\mathbf{Q}_g = 0 \tag{2.22}$$

With the aid of Eq. (2.21), the variation in the above virtual work equation can be expressed as:

$$\delta\mathbf{q}_g{}^T\delta\mathbf{Q}_g = \delta\mathbf{q}_g{}^T\left\{\mathbf{G}\mathbf{P}^T\mathbf{K}_n\mathbf{P}\mathbf{G}^T + \mathbf{G}\left(\mathbf{K}_{ext1} + \mathbf{K}_{ext2}\right)\mathbf{G}^T\right\}\delta\mathbf{q}_g = \delta\mathbf{q}_g{}^T\mathbf{K}_g\delta\mathbf{q}_g = 0 \tag{2.23}$$

In Eq.(2.23), $\mathbf{K}_e = \mathbf{P}^T\mathbf{K}_n\mathbf{P} + \mathbf{K}_{ext1} + \mathbf{K}_{ext2}$ is the element tangent stiffness matrix within the element frame. The derivations of the projection operator $\mathbf{P}$ and the external geometric stiffness matrices $\mathbf{K}_{ext1}$ and $\mathbf{K}_{ext2}$ are shown in Appendix I.

Note that the element CR frame basis vectors defined by Rankin and Nour-Omid are obtained based on the rotations at node 1. If the twisting of the element about its chord is such that the cross-section at node 2 undergoes significant rotation relative to the CR frame, the assumption of small rotation in the CR frame is not strictly applicable. In this study, an approximate average rotation of the two end nodes is adopted as the element rigid body rotation. This is similar to the approach taken by Crisfield (1990). This extends the applicability of the small deformation assumption in the CR frame.

As shown in Figure 2.3, the orthogonal rotation tensors $\mathbf{T}$ ($\mathbf{t}_1$, $\mathbf{t}_2$, $\mathbf{t}_3$) and $\mathbf{U}$($\mathbf{u}_1$, $\mathbf{u}_2$, $\mathbf{u}_3$) represent the element nodal triads, and $\mathbf{E}$($\mathbf{e}_1$, $\mathbf{e}_2$, $\mathbf{e}_3$) represents the element base vectors. The base vector $\mathbf{e}_1$ is directed from node 1 to node 2 in the natural configuration, $\mathbf{e}_2$ is approximately the average of $\mathbf{t}_2$ and $\mathbf{u}_2$ (see Appendix I), and $\mathbf{e}_3$ is equal to $\mathbf{e}_1 \times \mathbf{e}_2$. The triads $\mathbf{T}$ and $\mathbf{U}$ are updated by the orthogonal finite rotation operator $\mathbf{R}$ presented in Section 2.2 after obtaining the finite rotation increments $\Delta\boldsymbol{\omega}$ from the global solution. Once the three triads $\mathbf{T}$, $\mathbf{U}$ and $\mathbf{E}$ are updated, the element deformations within the natural frame (Figure 2.2(a)) are calculated by the following equations (Crisfield 1997):

$$\begin{aligned}
\theta_{1x}^n &= \sin^{-1} 0.5(-\mathbf{t}_3^T \mathbf{e}_2 + \mathbf{t}_2^T \mathbf{e}_3) \\
\theta_{1z}^n &= \sin^{-1} 0.5(-\mathbf{t}_2^T \mathbf{e}_1 + \mathbf{e}_2^T \mathbf{t}_1) \\
\theta_{1y}^n &= -\sin^{-1} 0.5(-\mathbf{t}_3^T \mathbf{e}_1 + \mathbf{e}_3^T \mathbf{t}_1) \\
\theta_{2x}^n &= \sin^{-1} 0.5(-\mathbf{u}_3^T \mathbf{e}_2 + \mathbf{u}_2^T \mathbf{e}_3) \\
\theta_{2z}^n &= \sin^{-1} 0.5(-\mathbf{u}_2^T \mathbf{e}_1 + \mathbf{e}_2^T \mathbf{u}_1) \\
\theta_{2y}^n &= -\sin^{-1} 0.5(-\mathbf{u}_3^T \mathbf{e}_1 + \mathbf{e}_3^T \mathbf{u}_1)
\end{aligned} \tag{2.24}$$

and

$$\boldsymbol{\theta}_n = \begin{bmatrix} \theta_{x1}^n & \theta_{z1}^n & \theta_{y1}^n & \theta_{x2}^n & \theta_{z2}^n & \theta_{y2}^n \end{bmatrix}^T \tag{2.25}$$

The axial elongation in the natural frame is calculated as

$$e = L - L_o = \sqrt{\left(\mathbf{X}_{21} + \mathbf{d}_{21}\right)^T \left(\mathbf{X}_{21} + \mathbf{d}_{21}\right)} - \sqrt{\mathbf{X}_{21}^T \mathbf{X}_{21}} = \frac{2}{L + L_o} \left(\mathbf{X}_{21} + \frac{1}{2} \mathbf{d}_{21} \right)^T \mathbf{d}_{21} \tag{2.26}$$

in which L is the final length that connects the two ends of the element in the natural frame, L_o is the initial length of the element and the vector $\mathbf{X}_{21}$ is the position vector between the initial locations of the first and second nodes.

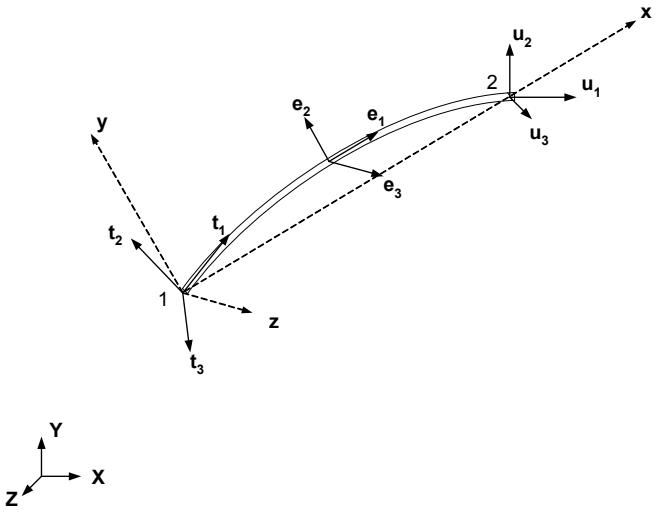

Figure 2.3 Three dimensional beam-column element: element base vectors $\mathbf{E}$ and element nodal triads $\mathbf{T}$ and $\mathbf{U}$

2.5 Open-Section Thin-Walled Beam Element Formulation

The finite element formulation in the corotational frame is derived using the assumption of small deformations. In the following, the calculation of the Green-Lagrange strain is introduced first. The element tangent stiffness matrix is then derived based on the principle of virtual work. The section tangent stiffness matrix is described subsequently.

2.5.1 Green-Lagrange Strain

Based on the assumption of small deformations, the uniaxial element Green-Lagrange strain can be expressed as

$$\varepsilon_x = \frac{1}{2}\left([\mathbf{R}'_n]^T[\mathbf{R}'_n] - [\mathbf{R}'_o]^T[\mathbf{R}'_o]\right) \tag{2.27}$$

in which the “prime” denotes differentiation with respect to the longitudinal X coordinate direction in the reference configuration, the vector $\mathbf{R}_o$ represents the initial position of a

material point in the undeformed geometry and the vector $\mathbf{R}_n$ locates the position in the deformed geometry. The vector $\mathbf{R}_n$ can be expressed as

$$\mathbf{R}_n = \mathbf{R}_o + \mathbf{d} \tag{2.28}$$

in which $\mathbf{d}$ is the displacement vector.

The element reference axis is taken to intersect a given cross-section at an arbitrary point O, located at the mid-thickness of the web. This point is defined as the origin of the cross-section coordinates. In this cross-section coordinate system, three points are defined: the cross-section centroid C with coordinates (y_c , z_c), the shear center S with coordinates (y_s , z_s) and an arbitrary point P located on the mid-thickness of the plate (i.e., flange or web) with coordinates (y, z) as shown in Figure 2.4.

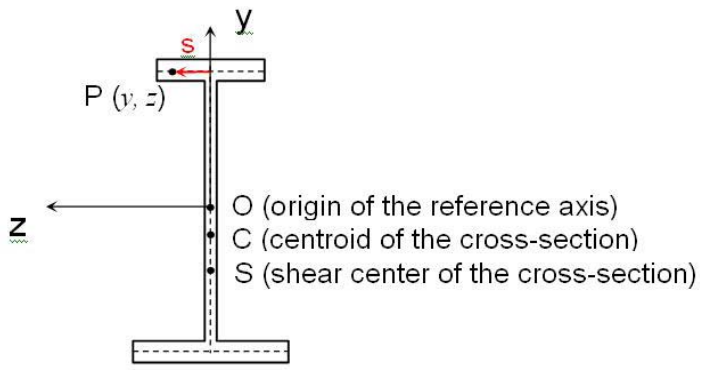

Figure 2.4 A singly-symmetric I-section

Considering a general non-prismatic thin-walled I-section beam, the position of a point P(y, z) on the cross section can be described in terms of the variable x and s, where s is a coordinate tangent to the wall of the cross-section as shown in the figure. That is, $y = y(x,s)$ and $z = z(x,s)$. Given the displacements u, v and w in the cross-section x, y and z directions, Eq. (2.27) can be written explicitly as:

$$\begin{aligned}\varepsilon_x &= \frac{1}{2}\left((1+u')^2+(y'+v')^2+(z'+w')^2-1-y'^2-z'^2\right)\\ &= u'+y'v'+z'w'+\frac{1}{2}\left(u'^2+v'^2+w'^2\right)\end{aligned} \tag{2.29}$$

The square term u'^2 is discarded based on the assumption of small deformations in the CR frame.

The displacements u, v and w at the point P can be expressed in the CR frame as:

$$v = v_o - z\sin\phi - y(1-\cos\phi) \tag{2.30}$$

$$w = w_o + y\sin\phi - z(1-\cos\phi) \tag{2.31}$$

$$u = u_o - (y\cos\phi - z\sin\phi)v_o' - (z\cos\phi + y\sin\phi)w_o' + \varpi\phi' \tag{2.32}$$

in which:

u_o Longitudinal displacement at the reference axis

v_o, w_o Transverse displacements at reference axis

u Longitudinal displacement at any material point P

v, w Transverse displacements at any material point P

ϕ Twist angle of the cross-section

ϖ Warping function (or principal sectorial coordinate), determined with respect to the shear center of the cross-section. For a non-prismatic element, this function varies in $\hat{x}$, $\hat{y}$ and $\hat{z}$, i.e., $\varpi = \varpi(\hat{x},\hat{y},\hat{z})$, in which $\hat{x} = x$, $\hat{y} = y - y_s$ and $\hat{z} = z$.

The first term in Eq. (2.32) is due to the elongation of the reference axis. The second and third terms are due to the bending about z and y axes, respectively. The last term accounts for the warping deformations.

With $\sin\phi$ = ϕ and $\cos\phi$ = 1 based on the small deformation assumption, the derivatives of the displacements *u, v* and *w* can be written as:

$$v' = v'_o - z'\phi - z\phi' \tag{2.33}$$

$$w' = w'_o + y'\phi + y\phi' \tag{2.34}$$

$$\begin{aligned} u' = u'_o &- (y' - z'\phi - z\phi')v'_o - (y - z\phi)v''_o - (z' + y'\phi + y\phi')w'_o \\ &- (z + y\phi)w''_o + \varpi'\phi' + \varpi\phi'' \end{aligned} \tag{2.35}$$

Substituting Eqs. (2.33), (2.34) and (2.35) into Eq. (2.29), and neglecting the high order terms, results in:

$\varepsilon_x = u'_o$	Axial strain due to elongation	
$-(yv''_o + zw''_o)$	Axial strain due to bending about both axes	
$+\varpi\phi''$	Axial strain due to warping	
$+(\varpi' - y'z + z'y)\phi'$	Non-prismatic member effects associated with warping	
$+\frac{1}{2}(v'^2_o + w'^2_o)$	Coupling between axial strain and bending	(2.36)
$+(zv''_o - yw''_o)\phi$	Coupling between axial strain and combined bending and torsion	
$+\frac{1}{2}(y^2 + z^2)\phi'^2$	Wagner effect, coupling between axial strain and torsion	

The variation of Eq. (2.36) can be written as:

$$\begin{aligned} \delta\varepsilon_x = {} & \delta u'_o + v'_o\delta v'_o + w'_o\delta w'_o - y(\delta v''_o + \phi\delta w''_o + w''_o\delta\phi) + z(\phi\delta v''_o - \delta w''_o + v''_o\delta\phi) \\ & + (y^2 + z^2)\phi'\delta\phi' + \varpi\delta\phi'' + (\varpi' - y'z + z'y)\delta\phi' \end{aligned}$$

or

$$\delta\varepsilon_x = \begin{bmatrix} 1 & -y & z & y^2+z^2 & \varpi & \psi \end{bmatrix} \begin{bmatrix} (1, v_o', w_o')(\delta u_o', \delta v_o', \delta w_o') \\ (1, \phi, w_o'')(\delta v_o'', \delta w_o'', \delta\phi) \\ (\phi, -1, v_o'')(\delta v_o'', \delta w_o'', \delta\phi) \\ \phi' \cdot \delta\phi' \\ \delta\phi'' \\ \delta\phi' \end{bmatrix} \tag{2.37}$$

in which

$$\psi = \varpi' - y'z + z'y \tag{2.38}$$

The shear strain due to uniform torsion is expressed as:

$$\gamma = -2\hat{r}\phi' \tag{2.39}$$

in which $\hat{r}$ is the through-thickness distance of the point from the middle surface of the plate. Thus, the variation of the shear strain can be written as

$$\delta\gamma = -2\hat{r}\delta\phi' \tag{2.40}$$

By combining Eqs. (2.37) and (2.40), the variation in the strain may be written as a 2x1 vector:

$$\delta\boldsymbol{\varepsilon} = \begin{Bmatrix} \delta\varepsilon_x \\ \delta\gamma \end{Bmatrix} = \begin{bmatrix} 1 & -y & z & y^2+z^2 & \varpi & \psi \\ 0 & 0 & 0 & 0 & 0 & -2\hat{r} \end{bmatrix} \begin{bmatrix} 1 & v_o' & w_o' & 0 & 0 & 0 & 0 & 0 \\ 0 & 0 & 0 & 1 & \phi & w_o'' & 0 & 0 \\ 0 & 0 & 0 & \phi & -1 & v_o'' & 0 & 0 \\ 0 & 0 & 0 & 0 & 0 & 0 & \phi' & 0 \\ 0 & 0 & 0 & 0 & 0 & 0 & 0 & 1 \\ 0 & 0 & 0 & 0 & 0 & 0 & 1 & 0 \end{bmatrix} \begin{Bmatrix} \delta u_o' \\ \delta v_o' \\ \delta w_o' \\ \delta v_o'' \\ \delta w_o'' \\ \delta\phi_o \\ \delta\phi_o' \\ \delta\phi_o'' \end{Bmatrix}$$

or

$$\delta\boldsymbol{\varepsilon} = \mathbf{SQ}\ \delta\mathbf{v} \tag{2.41}$$

2.5.2 Element Tangent Stiffness Matrix

For the I-section beam, cubic Hermitian interpolation functions are used for the transverse displacements, a linear function is used for the axial displacement and hyperbolic trigonometric functions, based on the analytical geometrically-linear solution of the torsion problem for a straight element, are used for the twist and warping degrees of freedom in the corotational frame. For a rectangular cross-section beam with 12 dofs, the twist degree of freedom is interpolated with linear functions.

Corresponding to the nodal displacements in the natural frame shown in Eq. (2.9), the displacement field in the natural frame can be expressed as

$$u_o(x) = \mathbf{N}_u^T \mathbf{q}_n, \text{ where } \mathbf{N}_u^T = \begin{bmatrix} N_u & 0 & 0 & 0 & 0 & 0 & 0 & 0 & 0 \end{bmatrix} \tag{2.42}$$

$$v_o(x) = \mathbf{N}_v^T \mathbf{q}_n, \text{ where } \mathbf{N}_v^T = \begin{bmatrix} 0 & 0 & N_{v1} & 0 & 0 & 0 & N_{v2} & 0 & 0 \end{bmatrix} \tag{2.43}$$

$$w_o(x) = \mathbf{N}_w^T \mathbf{q}_n, \text{ where } \mathbf{N}_w^T = \begin{bmatrix} 0 & 0 & 0 & N_{w1} & 0 & 0 & 0 & N_{w2} & 0 \end{bmatrix} \tag{2.44}$$

and

$$\phi(x) = \mathbf{N}_\phi^T \mathbf{q}_n, \text{ where } \mathbf{N}_\phi^T = \begin{bmatrix} 0 & N_{\phi1} & 0 & 0 & N_{\phi2} & N_{\phi3} & 0 & 0 & N_{\phi4} \end{bmatrix} \tag{2.45}$$

where

$$N_u(x) = \frac{x}{L} \tag{2.46}$$

$$N_{v1}(x) = -N_{w1}(x) = x - \frac{2x^2}{L} + \frac{x^3}{L^2} \tag{2.47}$$

$$N_{v2}(x) = -N_{w2}(x) = -\frac{x^2}{L} + \frac{x^3}{L^2} \tag{2.48}$$

$$N_{\phi1}(x) = \frac{\tanh(\lambda L/2) \cdot \left[\cosh[\lambda(L-x)] - 1\right] - \sinh[\lambda(L-x)] + \lambda(L-x)}{\lambda L - 2\tanh(\lambda L/2)} \tag{2.49}$$

$$N_{\phi3}(x) = 1 - N_{\phi1}(x) \tag{2.50}$$

$$N_{\phi 2}(x)=\frac{-\dfrac{\sinh(\lambda L)-\lambda L}{\cosh(\lambda L)-1}\left[\cosh[\lambda(L-x)]-1\right]+\sinh[\lambda(L-x)]-\lambda(L-x)}{\lambda\left[2-\lambda L/\tanh(\lambda L/2)\right]} \tag{2.51}$$

$$N_{\phi 4}(x)=\frac{\dfrac{\sinh(\lambda L)-\lambda L}{\cosh(\lambda L)-1}\left[\cosh(\lambda L)-1\right]-\sinh(\lambda L)+\lambda L}{\lambda\left[2-\lambda L/\tanh(\lambda L/2)\right]} \tag{2.52}$$

in which $\lambda=\sqrt{GJ/EC_w}$. It should be noted that the calculation of the hyperbolic trigonometric functions is expensive. However, for each element, they only need to be calculated once at the beginning of the analysis.

With the aid of Eqs. (2.42) to (2.45), the vector $\delta\mathbf{v}$ in Eq. (2.41) can be expressed as $\mathbf{B}\delta\mathbf{q}_n$ so that Eq. (2.41) becomes:

$$\delta\boldsymbol{\varepsilon}=\mathbf{SQB}\ \ \delta\mathbf{q}_n \tag{2.53}$$

in which

$$\mathbf{B}=\begin{bmatrix} N_u' & 0 & 0 & 0 & 0 & 0 & 0 & 0 & 0 \\ 0 & 0 & N_{v1}' & 0 & 0 & 0 & N_{v2}' & 0 & 0 \\ 0 & 0 & 0 & N_{w1}' & 0 & 0 & 0 & N_{w2}' & 0 \\ 0 & 0 & N_{v1}'' & 0 & 0 & 0 & N_{v2}'' & 0 & 0 \\ 0 & 0 & 0 & N_{w1}'' & 0 & 0 & 0 & N_{w2}'' & 0 \\ 0 & N_{\phi 1} & 0 & 0 & N_{\phi 2} & N_{\phi 3} & 0 & 0 & N_{\phi 4} \\ 0 & N_{\phi 1}' & 0 & 0 & N_{\phi 2}' & N_{\phi 3}' & 0 & 0 & N_{\phi 4}' \\ 0 & N_{\phi 1}'' & 0 & 0 & N_{\phi 2}'' & N_{\phi 3}'' & 0 & 0 & N_{\phi 4}'' \end{bmatrix}_{8\times 9} \tag{2.54}$$

The virtual work principle can be written in a general form as:

$$\int_{V_o}\delta\boldsymbol{\varepsilon}^T\boldsymbol{\sigma}\,dV-\delta\,\mathbf{q}_n{}^T\mathbf{Q}_{ext}=0 \tag{2.55}$$

in which $\mathbf{Q}_{ext}$ is a external force vector within the CR frame and $\boldsymbol{\sigma}^T=[\sigma_x\ \ \tau]$ represents the section PKII stresses. By substituting Eq. (2.53) into Eq. (2.55) with $dV=dAdx$, we have:

$$\delta\mathbf{q}_n^T\left(\int_{V_o}\mathbf{B}^T\mathbf{Q}^T\mathbf{D}dV-\mathbf{Q}_{ext}\right)=\delta\mathbf{q}_n^T\mathbf{g}=0 \tag{2.56}$$

$$\mathbf{D} = \int_{A_o} \mathbf{S}^T \boldsymbol{\sigma}\, dA \tag{2.57}$$

in which $\mathbf{D} = \begin{bmatrix} P & M_z & M_y & W & B & T_{sv} \end{bmatrix}^T$ is the stress resultant internal force vector where P is the axial force, M is the moment, W accounts for the Wagner effect, B is the bi-moment, T_{sv} represents the St. Venant torsion, $\mathbf{g}$ is the governing equilibrium equation or the out of balance vector and A_o is the cross section area. A finite increment in the section stresses can be expressed with the incremental form of $\Delta\boldsymbol{\varepsilon}$ as:

$$\Delta\boldsymbol{\sigma} = \mathbf{C}\,\Delta\boldsymbol{\varepsilon} = \mathbf{C}\,\mathbf{S}\mathbf{Q}\mathbf{B}\Delta\mathbf{q}_n \tag{2.58}$$

The matrix $\mathbf{C}$ holds the constitutive relation between the section stresses and the section strains, which is

$$\mathbf{C} = \begin{bmatrix} E & 0 \\ 0 & G \end{bmatrix} \tag{2.59}$$

in which E is Young's modulus and G is the shear modulus. Given Eq. (2.58), the incremental stress resultant internal force vector can be written as

$$\Delta\mathbf{D} = \int_{A_o} \mathbf{S}^T \Delta\boldsymbol{\sigma}\, dA = \int_{A_o} \mathbf{S}^T \mathbf{C}\,\mathbf{S}\, dA\, \mathbf{Q}\mathbf{B}\Delta\mathbf{q}_n = \mathbf{k}_s \mathbf{Q}\mathbf{B}\Delta\mathbf{q}_n \tag{2.60}$$

in which $\mathbf{k_s}$ is the section tangent stiffness, which is introduced in the next section.

To obtain the element tangent stiffness matrix, $\mathbf{g}$ in Eq. (2.56) is linearized as follows:

$$\mathbf{g}^{i+1} \approx \mathbf{g}^i + \left.\frac{d}{d\alpha}\right|_{\alpha,\beta=0} \mathbf{g}\left(\mathbf{q}_n{}^i + \alpha\,\Delta\mathbf{q}_n\right) + \left.\frac{d}{d\beta}\right|_{\alpha,\beta=0} \mathbf{g}\left(\mathbf{Q}_{ext}^i + \beta\,\Delta\mathbf{Q}_{ext}\right) = \mathbf{0} \tag{2.61}$$

After some manipulation, Eq. (2.61) can be written as:

$$\left(\int_0^{L_0} \mathbf{B}^T \mathbf{G}_n\, \mathbf{B} dx + \int_0^{L_0} \mathbf{B}^T\, \mathbf{Q}^T\, \mathbf{k}_s\, \mathbf{Q}\, \mathbf{B}\, dx \right) \Delta\mathbf{q}_n = \mathbf{Q}_{ext}^{i+1} - \mathbf{Q}_{\text{int}}^i \tag{2.62}$$

or

$$\mathbf{k}_n \, \Delta\mathbf{q}_n = \mathbf{Q}_{ext}^{i+1} - \mathbf{Q}_{\text{int}}^{i} \tag{2.63}$$

in which

$$\mathbf{Q}_{\text{int}}^{i} = \int_0^{L_0} \left(\mathbf{Q}^i \mathbf{B}^i\right)^T \mathbf{D}^i \, dx \tag{2.64}$$

$$\mathbf{Q}_{ext}^{i+1} = \mathbf{Q}_{ext}^{i} + \Delta\mathbf{Q}_{ext} \tag{2.65}$$

The first integral in Eq. (2.62) is the element internal geometric stiffness matrix and the second integral is the element elastic stiffness matrix. In addition, $\mathbf{Q}_{ext}^{i+1}$ is the external load vector in the *(i+1)th* iteration and $\mathbf{Q}_{\text{int}}^{i}$ is the element internal (resisting) force vector at the end of the i^{th} iteration. Lastly, the $\mathbf{G}_n$ matrix in Eq. (2.62) is:

$$\mathbf{G}_n = \begin{bmatrix} 0 & 0 & 0 & 0 & 0 & 0 & 0 & 0 \\ 0 & P & 0 & 0 & 0 & 0 & 0 & 0 \\ 0 & 0 & P & 0 & 0 & 0 & 0 & 0 \\ 0 & 0 & 0 & 0 & 0 & M_y & 0 & 0 \\ 0 & 0 & 0 & 0 & 0 & M_z & 0 & 0 \\ 0 & 0 & 0 & M_y & M_z & 0 & 0 & 0 \\ 0 & 0 & 0 & 0 & 0 & 0 & W & 0 \\ 0 & 0 & 0 & 0 & 0 & 0 & 0 & 0 \end{bmatrix} \tag{2.66}$$

The incremental forms of ε and γ are used to obtain the element strains from the element total and incremental displacements in the element state determination algorithm. They can be expressed as:

$$\Delta\varepsilon = \left\{ \begin{array}{l} \mathbf{N}_u'^T + \mathbf{q}_n{}^T \mathbf{N}_v' \mathbf{N}_v'^T + \mathbf{q}_n{}^T \mathbf{N}_w' \mathbf{N}_w'^T - y\mathbf{N}_v''^T - z\mathbf{N}_w''^T + \varpi \, \mathbf{N}_\phi''^T + \\ \psi \, \mathbf{N}_\phi'^T + \left(y^2 + z^2\right)\mathbf{q}_n{}^T \mathbf{N}_\phi' \mathbf{N}_\phi'^T - y\,\mathbf{q}_n{}^T \mathbf{N}_\phi \mathbf{N}_w''^T - y\mathbf{q}_n{}^T \mathbf{N}_w'' \mathbf{N}_\phi{}^T + \\ z\mathbf{q}_n{}^T \mathbf{N}_\phi \mathbf{N}_v''^T + z\mathbf{q}_n{}^T \mathbf{N}_v'' \mathbf{N}_\phi{}^T \end{array} \right\} \Delta\mathbf{q}_n +$$

$$\frac{1}{2}\Delta\mathbf{q}_n{}^T \left\{ \mathbf{N}_v' \mathbf{N}_v'^T + \mathbf{N}_w' \mathbf{N}_w'^T + \left(y^2 + z^2\right)\mathbf{N}_\phi' \mathbf{N}_\phi'^T - 2y\,\mathbf{N}_\phi \mathbf{N}_w''^T + 2z\mathbf{N}_v'' \mathbf{N}_\phi{}^T \right\} \Delta\mathbf{q}_n \tag{2.67}$$

and

$$\Delta\gamma = -2r\, N_{\phi}'^{T}\, \Delta\mathbf{q}_n \tag{2.68}$$

As expressed by Eq. (2.32), the axial displacement at an arbitrary point P may be due to axial displacement (u_o) at the reference axis, bending (v_o', w_o'), torsion (ϕ) and warping (ϕ'). Therefore, with a cubic function for the transverse displacements, linear interpolation of the axial displacement is not sufficient for the element to represent finite inextensional bending. Crisfield (1991) shows that given a cubic function for the transverse displacements, a quintic function for the axial displacements is necessary for the element to be able to represent inextensional bending. This study adopts an ad hoc smoothing of the axial strain suggested by Crisfield (1990) to avoid the need for a quintic axial displacement interpolation, which would be extremely cumbersome. As a consequence, the previous derivations in this section are still valid but the following modifications are applied. Equation (2.37) is replaced with

$$\varepsilon_x = u_o' - (yv_o'' + z\,w_o'') + \varpi\,\phi'' + \psi\,\phi' + \frac{1}{60}\boldsymbol{\theta}_n^T\,\mathbf{X}\boldsymbol{\theta}_n + (zv_o'' - yw_o'')\phi + \frac{1}{2}\left(y^2 + z^2\right)\phi'^2 \tag{2.69}$$

in which $\boldsymbol{\theta}_n$ is the vector containing the element rotational deformations within the natural frame introduced in Eq. (2.25), and

$$\mathbf{X} = \begin{bmatrix} 0 & 0 & 0 & 0 & 0 & 0 \\ 0 & 4 & 0 & 0 & -1 & 0 \\ 0 & 0 & 4 & 0 & 0 & -1 \\ 0 & 0 & 0 & 0 & 0 & 0 \\ 0 & -1 & 0 & 0 & 4 & 0 \\ 0 & 0 & -1 & 0 & 0 & 4 \end{bmatrix}_{6\times 6} \tag{2.70}$$

Therefore, the variation in the axial strain (Eq. (2.38)) becomes

$$\delta\varepsilon_x = \delta u_o' + \frac{1}{30}\boldsymbol{\theta}_n^T\,\mathbf{X}\;\delta\boldsymbol{\theta}_n - y(\delta v_o'' + \phi\delta w_o'' + w_o''\delta\phi) + z(\phi\delta v_o'' - \delta w_o'' + v_o''\delta\phi) + (y^2+z^2)\phi'\delta\phi' + \varpi\delta\phi'' + \psi\delta\phi' \tag{2.71}$$

The corresponding form of the $\mathbf{Q}$ matrix in Eq. (2.41) is then

$$\mathbf{Q} = \begin{bmatrix} 1 & \frac{1}{30}\boldsymbol{\theta}_n^T\,\mathbf{X} & 0 & 0 & 0 & 0 & 0 \\ 0 & 0 & 1 & \phi & w'' & 0 & 0 \\ 0 & 0 & \phi & -1 & v'' & 0 & 0 \\ 0 & 0 & 0 & 0 & 0 & \phi' & 0 \\ 0 & 0 & 0 & 0 & 0 & 0 & 1 \\ 0 & 0 & 0 & 0 & 0 & 1 & 0 \end{bmatrix}_{6\times 12} \tag{2.72}$$

and $\mathbf{B}$ in Eq. (2.53) is

$$\mathbf{B} = \begin{bmatrix} N_u' & 0 & 0 & 0 & 0 & 0 & 0 & 0 & 0 \\ 0 & 1 & 0 & 0 & 0 & 0 & 0 & 0 & 0 \\ 0 & 0 & 1 & 0 & 0 & 0 & 0 & 0 & 0 \\ 0 & 0 & 0 & 1 & 0 & 0 & 0 & 0 & 0 \\ 0 & 0 & 0 & 0 & 0 & 1 & 0 & 0 & 0 \\ 0 & 0 & 0 & 0 & 0 & 0 & 1 & 0 & 0 \\ 0 & 0 & 0 & 0 & 0 & 0 & 0 & 1 & 0 \\ 0 & 0 & N_{v1}'' & 0 & 0 & 0 & N_{v2}'' & 0 & 0 \\ 0 & 0 & 0 & N_{w1}'' & 0 & 0 & 0 & N_{w2}'' & 0 \\ 0 & N_{\phi 1} & 0 & 0 & N_{\phi 2} & N_{\phi 3} & 0 & 0 & N_{\phi 4} \\ 0 & N_{\phi 1}' & 0 & 0 & N_{\phi 2}' & N_{\phi 3}' & 0 & 0 & N_{\phi 4}' \\ 0 & N_{\phi 1}'' & 0 & 0 & N_{\phi 2}'' & N_{\phi 3}'' & 0 & 0 & N_{\phi 4}'' \end{bmatrix}_{12\times 9} \tag{2.73}$$

Also, the incremental form in Eq. (2.68) is changed to

$$\Delta\varepsilon = \begin{Bmatrix} \mathbf{N}_u'^T - y\mathbf{N}_v''^T - z\mathbf{N}_w''^T + \varpi\,\mathbf{N}_\phi''^T + \psi\,\mathbf{N}_\phi'^T \\ +\left(y^2+z^2\right)\mathbf{q}_n^T\mathbf{N}_\phi'\mathbf{N}_\phi'^T - y\mathbf{q}_n^T\mathbf{N}_\phi\mathbf{N}_w''^T - y\mathbf{q}_n^T\mathbf{N}_w''\mathbf{N}_\phi^T \\ +z\mathbf{q}_n^T\mathbf{N}_\phi\mathbf{N}_v''^T + z\mathbf{q}_n^T\mathbf{N}_v''\mathbf{N}_\phi^T \end{Bmatrix}\Delta\mathbf{q}_n + \frac{1}{30}\boldsymbol{\theta}_n^T\,\mathbf{X}\,\Delta\boldsymbol{\theta}_n$$

$$+\frac{1}{2}\Delta\mathbf{q}_n^T\left\{\left(y^2+z^2\right)\mathbf{N}_\phi'\mathbf{N}_\phi'^T - 2y\mathbf{N}_\phi\mathbf{N}_w''^T + 2z\mathbf{N}_v''\mathbf{N}_\phi^T\right\}\Delta\mathbf{q}_n + \frac{1}{60}\Delta\boldsymbol{\theta}_n^T\,\mathbf{X}\Delta\boldsymbol{\theta}_n \tag{2.74}$$

The element formulations in Eqs. (2.61) and (2.65) are the same except the matrix $\mathbf{G}_n$ is changed to

$$\mathbf{G}_n = \begin{bmatrix} 0 & 0 & 0 & 0 & 0 & 0 & 0 & 0 & 0 & 0 & 0 & 0 \\ & 0 & 0 & 0 & 0 & 0 & 0 & 0 & 0 & 0 & 0 & 0 \\ & & \frac{4}{30}P & 0 & 0 & -\frac{1}{30}P & 0 & 0 & 0 & 0 & 0 & 0 \\ & & & \frac{4}{30}P & 0 & 0 & -\frac{1}{30}P & 0 & 0 & 0 & 0 & 0 \\ & & & & 0 & 0 & 0 & 0 & 0 & 0 & 0 & 0 \\ & & & & & \frac{4}{30}P & 0 & 0 & 0 & 0 & 0 & 0 \\ & & & & & & \frac{4}{30}P & 0 & 0 & 0 & 0 & 0 \\ & & & & & & & 0 & 0 & M_y & 0 & 0 \\ & & & & & & & & 0 & M_z & 0 & 0 \\ & & & Sym. & & & & & & 0 & 0 & 0 \\ & & & & & & & & & & W & 0 \\ & & & & & & & & & & & 0 \end{bmatrix} \tag{2.75}$$

2.5.3 Section Tangent Stiffness Matrix

The section tangent stiffness matrix in Eq. (2.60) is given by the term:

$$\mathbf{k}_s = \int_{A_o} \mathbf{S}^T \mathbf{C} \mathbf{S} \, dA \tag{2.76}$$

By expanding the matrix operations, one obtains:

$$\mathbf{S^T C S} = E \cdot \begin{bmatrix} 1 & & & & & & \\ -y & y^2 & & & & Sym. & \\ z & -yz & z^2 & & & & \\ y^2+z^2 & -y(y^2+z^2) & z(y^2+z^2) & (y^2+z^2)^2 & & & \\ \varpi & -y\varpi & z\varpi & (y^2+z^2)\varpi & \varpi^2 & & \\ \psi & -y\psi & z\psi & (y^2+z^2)\psi & \varpi\psi & \psi^2+4G\hat{r}^2/E & \end{bmatrix} \tag{2.77}$$

In Eq. (2.77), y and z are measured from the cross-section reference axis. Also, $\hat{y}$ and $\hat{z}$ in the warping function $\varpi(\hat{x},\hat{y},\hat{z})$ are measured from the shear center of the cross-section.

For an elastic prismatic member, the section tangent stiffness in Eq. (2.77) is constant along the member length and the term ψ. Is equal to zero (see Eq. (2.38)) However, for a general nonprismatic member, the section tangent stiffness varies along the member length and the term ψ. depends on the rate of change of the section dimensions. Figure 2.5 shows a beam element with a singly-symmetric cross-section and a general linear taper in all of its cross-section dimensions. The functions $h_{st}(x)$ and $h_{sb}(x)$ in Figure 2.5 are the dimensions between the shear center (subscript 's') and the centroid of the top (subscript 't') and bottom (subscript 'b') flanges, respectively. The effect of the variation in the cross-section dimensions along the length on the section tangent stiffness may be expressed via the five terms $h'_{st}(x)$, $h'_{sb}(x)$, y_s', b'_{ft} and b'_{fb}.

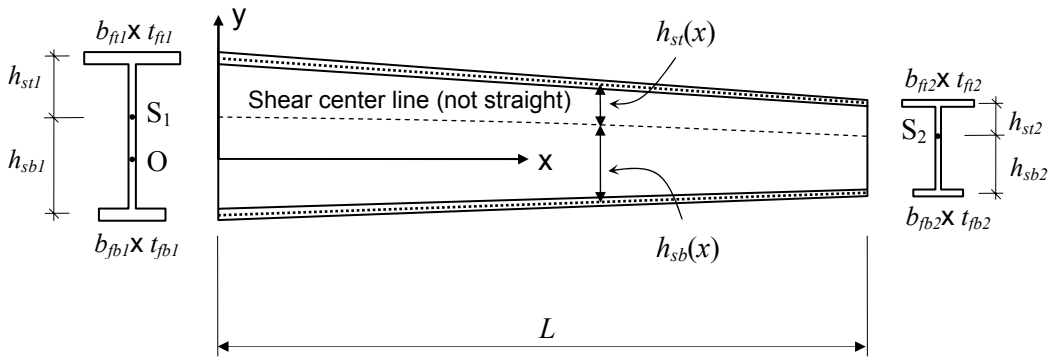

Figure 2.5 Beam element with a singly-symmetric cross-section and a general linear taper in all of its cross-section dimensions

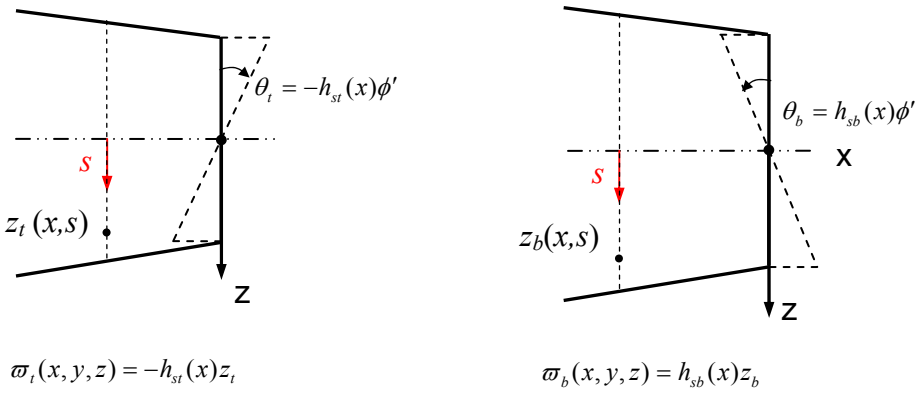

Figure 2.6 Warping functions in top and bottom flanges of a tapered element

After substituting Eq. (2.77) into Eq. (2.76) and performing the integration analytically (see Appendix II), the section tangent stiffness matrix can be expressed as:

$$\mathbf{k} = \begin{bmatrix} EA_o & & \ddots & & \\ -EA_o y_c & EI_{oz} & & Sym & \\ 0 & 0 & EI_{oy} & & \ddots \\ E(I_{oy}+I_{oz}) & k_{42} & 0 & k_{44} & \\ 0 & 0 & 0 & 0 & EC_w \\ 0 & 0 & R_t EI_{ft} + R_b EI_{fb} & 0 & -R_t h_{st} EI_{ft} + R_b h_{sb} EI_{fb} \quad R_t^2 EI_{ft} + R_b^2 EI_{fb} + GJ \end{bmatrix} \tag{2.78}$$

where:

A_o Area of the cross section

I_o Moment of inertia of the cross section with respect to the cross-section reference axes

I_f Moment of inertia of the flange with respect to the y axis

$$R_t = -2h'_{st} - y'_s + y_s \frac{b'_{ft}}{b_{ft}}$$

$$R_b = 2h'_{sb} - y'_s + y_s \frac{b'_{fb}}{b_{fb}}$$

y_s = y coordinate of the shear center line.

The terms $k_{,42}$ and $k_{,44}$ are defined in Appendix II. It should be noted that $h_{st}(x)$, $h_{sb}(x)$, b_{ft} and b_{fb} are cross-section dimensions. Therefore, their derivatives are positive if the dimensions increase with increasing x and are negative if the dimensions decrease with increasing x.

Note that for a doubly symmetric I section, y_c is zero so that the (2, 1) and (4, 2) components in $\mathbf{k}_s$ are zero; for a prismatic element, R_t and R_b are zero so that the (6, 3) and (6, 5) components in $\mathbf{k}_s$ are zero and the component (6, 6) becomes GJ only. For a tapered singly-symmetric beam, the shear center line along the length of an element is not straight. Therefore, the functions $h'_{st}(x)$, $h'_{sb}(x)$ and $y'_s(x)$ are not zero and R_t and R_b are not zero. The values of h'_{st}, h'_{sb} and y'_s are calculated for each segment between two Gauss-Lobatto integration points within an element. The cross-sections at the end integration points use the rates of change between the last two integration points. The intermediate points use the average rate of change of the adjacent segments.

As mentioned in Section 2.2, Kitipornchai and Trahair (1975) suggested that the tangent to the shear center line can be used as a convenient reference for measuring the deflections of the cross section and for calculating the torque. For the current study, a straight line between the shear center locations at the element end nodes is selected as the longitudinal reference axis for all of the element quantities.

It should be noted that the above reference axis is in conflict with the fact that the shear center line along the element length is not straight for a tapered singly-symmetric beam. However, the distance between the straight chord and the shear center line is usually quite small. For the case that the distance between the straight chord and the shear center line is not negligible, the exact solution is obtained as the number of elements along the member length is increased.

2.5.4 State Determination

Once the incremental displacements ($\Delta\mathbf{d}$) and rotations ($\Delta\boldsymbol{\omega}$) are retrieved from the global solution, the element state determination is conducted as follows:

1. Update the translational displacements

$$\mathbf{d}^{i+1} = \mathbf{d}^{i} + \Delta\mathbf{d}$$

2. Update the element nodal triads $\mathbf{T}$ and $\mathbf{U}$ shown in Figure 2.3 with the aid of Eq. (2.3)

$$\mathbf{T}^{i+1} = \mathbf{R}\left(\Delta\boldsymbol{\omega}_1\right)\mathbf{T}^{i}$$

$$\mathbf{U}^{i+1} = \mathbf{R}\left(\Delta\boldsymbol{\omega}_2\right)\mathbf{U}^{i}$$

   in which $\Delta\boldsymbol{\omega}_1$ is the vector containing the incremental non-additive rotations of the first node of the element and $\Delta\boldsymbol{\omega}_2$ is the corresponding vector for the second node of the element.

3. Update the element base vector $\mathbf{E}^{i+1}$ based on $\mathbf{T}^{i+1}$ and $\mathbf{U}^{i+1}$, and calculate the rotations $\boldsymbol{\theta}_n^{i+1}$ (Eq. (2.25)) in the corotational frame using Eq. (2.24), and the corresponding increments for Eq. (2.74):

$$\Delta\boldsymbol{\theta}_n = \boldsymbol{\theta}_n^{i+1} - \boldsymbol{\theta}_n^{i}$$

4. Calculate the axial deformation e in the corotational frame using Eq. (2.26).

5. Update the transformation matrix $\mathbf{G}^{i+1}$ (Eq.(A1.47)) and the projection operator $\mathbf{P}^{i+1}$ (Eq.(A1.53)) based on $\mathbf{T}^{i+1}$, $\mathbf{U}^{i+1}$ and $\mathbf{E}^{i+1}$.
6. Calculate the new state for the element in the natural system.
   a. Calculate the section deformations:

$$\varepsilon^{i+1} = \varepsilon^{i} + \Delta\varepsilon$$

$$\gamma^{i+1} = \gamma^{i} + \Delta\gamma$$

   in which $\Delta\varepsilon$ is calculated from Eq. (2.74) and $\Delta\gamma$ is from Eq. (2.68).

   b. Update the section forces with the use of Eq. (2.60) and calculate the element internal forces in the corotational frame (Eq. (2.64)):

$$\mathbf{Q}_{\text{int}}^{i+1} = \int_0^{L_0} \left(\mathbf{Q}^{i+1}\mathbf{B}^{i+1}\right)^T \mathbf{D}^{i+1}\, dx$$

   c. Calculate the element tangent stiffness matrix in the corotational frame (Eq. (2.62)) and the external geometric stiffness matrix $\mathbf{K}_{ext1}$ (Eq. (A1.65)) and $\mathbf{K}_{ext2}$ (Eq. (A1.70))

$$\mathbf{k}_n = \int_0^{L_0} \mathbf{B}^T \mathbf{G}_n \mathbf{B} dx + \int_0^{L_0} \mathbf{B}^T \mathbf{Q}^T \mathbf{k}_s \mathbf{Q} \mathbf{B}\, dx$$

   d. Calculate the global stiffness matrix $\mathbf{K}_g$ (Eq. (2.21))

$$\mathbf{K}_g = \mathbf{G}\left(\mathbf{P}^T \mathbf{K}_n \mathbf{P} + \mathbf{K}_{ext1} + \mathbf{K}_{ext2}\right)\mathbf{G}^T$$

2.6 Modeling of Rigid Offsets

As described in Sec. 2.2, the rotational vector $\Delta\boldsymbol{\omega}$ is defined as $\Delta\boldsymbol{\omega} = \Delta\omega_1 e_1 + \Delta\omega_2 e_2 + \Delta\omega_3 e_3 = \Delta\omega\,\mathbf{e}$, where $\Delta\omega = \sqrt{\Delta\omega_1^2 + \Delta\omega_2^2 + \Delta\omega_3^2}$ is the magnitude of

the rotation about the axis directed along the unit vector **e**. As shown in Figure 2.1, the point P is rotated about the point C by $\Delta\omega$ to the point Q. The vector from point P to Q can be calculated as:

$$\begin{aligned}\Delta\mathbf{r} &= \Delta\mathbf{a} + \Delta\mathbf{b} \\ &= \frac{1-\cos\Delta\omega}{\Delta\omega^2}\boldsymbol{\Theta}(\Delta\boldsymbol{\omega})\boldsymbol{\Theta}(\Delta\boldsymbol{\omega})\mathbf{r}_o + \frac{\sin\Delta\omega}{\Delta\omega}\boldsymbol{\Theta}(\Delta\boldsymbol{\omega})\mathbf{r}_o) \\ &= \left\{-\frac{1-\cos\Delta\omega}{\Delta\omega^2}\boldsymbol{\Theta}(\Delta\boldsymbol{\omega})\cdot\boldsymbol{\Theta}(\mathbf{r}_o) - \frac{\sin\Delta\omega}{\Delta\omega}\boldsymbol{\Theta}(\mathbf{r}_o)\right\}\cdot\Delta\boldsymbol{\omega} \\ &= \mathbf{R}_{off}\cdot\Delta\boldsymbol{\omega}\end{aligned} \tag{2.79}$$

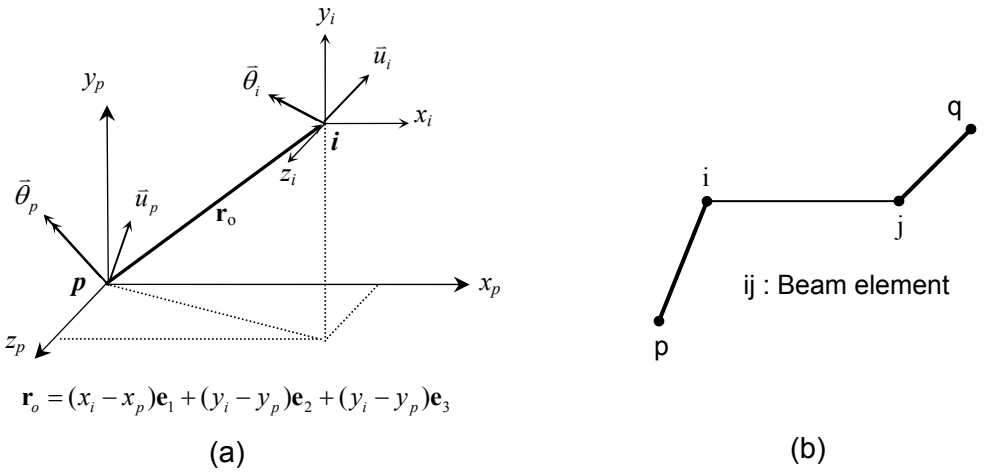

Figure 2.7 Rigid offset: (a) translation of axes, (b) beam element with rigid offsets

With the aid of the rotation matrix $\mathbf{R}_{off}$, the displacements at node ***i*** can be expressed in terms of the displacements at node ***p*** as follows (see Figure 2.7(a)): (Note that to simplify the notation, the subscript '*off*' is omitted in the following equations)

$$\mathbf{u}_i = \begin{Bmatrix} \vec{u}_i \\ \vec{\theta}_i \end{Bmatrix} = \begin{bmatrix} \mathbf{I} & \mathbf{R}_{ip} \\ \mathbf{0} & \mathbf{I} \end{bmatrix} \cdot \begin{Bmatrix} \vec{u}_p \\ \vec{\theta}_p \end{Bmatrix} \Rightarrow \mathbf{u}_i = \mathbf{T}_{ip} \cdot \mathbf{u}_p \tag{2.80}$$

The subscript "ip" means transforming the displacements from node $\boldsymbol{p}$ to node $\boldsymbol{i}$. Based on work conjugacy, the forces at node $\boldsymbol{i}$ must be related to the forces at node $\boldsymbol{p}$ as:

$$\mathbf{f}_p = \begin{Bmatrix} \vec{f}_p \\ \vec{m}_p \end{Bmatrix} = \mathbf{T}_{ip}^{\ T}\, \mathbf{f}_i \quad \Rightarrow \quad \mathbf{f}_i = \mathbf{T}_{ip}^{\ -T}\, \mathbf{f}_p \tag{2.81}$$

Therefore, for a beam element with rigid offsets at both ends as shown in Figure 2.7(b), one can transform the responses from ($\boldsymbol{i}$, $\boldsymbol{j}$) to ($\boldsymbol{p}$, $\boldsymbol{q}$) by using following equations:

$$\mathbf{q}_{ij} = \begin{Bmatrix} \mathbf{u}_i \\ \mathbf{u}_j \end{Bmatrix} = \begin{bmatrix} \mathbf{T}_{ip} & \mathbf{0} \\ \mathbf{0} & \mathbf{T}_{jq} \end{bmatrix} \cdot \begin{Bmatrix} \mathbf{u}_p \\ \mathbf{u}_q \end{Bmatrix} \quad \Rightarrow \quad \mathbf{q}_{ij} = \mathbf{T}_B \cdot \mathbf{q}_{pq} \tag{2.82}$$

$$\mathbf{Q}_{ij} = \begin{Bmatrix} \mathbf{f}_i \\ \mathbf{f}_j \end{Bmatrix} = \begin{bmatrix} \mathbf{T}_{ip}^{\ -\mathrm{T}} & \mathbf{0} \\ \mathbf{0} & \mathbf{T}_{jq}^{\ -\mathrm{T}} \end{bmatrix} \cdot \begin{Bmatrix} \mathbf{f}_p \\ \mathbf{f}_q \end{Bmatrix} \quad \Rightarrow \quad \mathbf{Q}_{ij} = \mathbf{T}_B^{\ -\mathrm{T}} \cdot \mathbf{Q}_{pq} \tag{2.83}$$

in which

$$\mathbf{T}_{ip}^{\ -\mathrm{T}} = \begin{bmatrix} \mathbf{I} & \mathbf{R}_{ip} \\ \mathbf{0} & \mathbf{I} \end{bmatrix}^{-\mathrm{T}} = \begin{bmatrix} \mathbf{I} & -\mathbf{R}_{ip} \\ \mathbf{0} & \mathbf{I} \end{bmatrix}^{\mathrm{T}} = \begin{bmatrix} \mathbf{I} & \mathbf{0} \\ -\mathbf{R}_{ip} & \mathbf{I} \end{bmatrix} \tag{2.84}$$

Note that the above equations are both written in the global coordinate system. With the aid of Eq. (2.84), the transformation of the global (denoted by subscript "G") tangent stiffness matrix between a beam element with nodes $\boldsymbol{i}$ and $\boldsymbol{j}$ and its rigid offset system with nodes $\boldsymbol{p}$ and $\boldsymbol{q}$ can be expressed as:

$$\mathbf{K}_{G,pq} = \mathbf{T}_B^{\ \mathrm{T}} \mathbf{K}_{G,ij} \mathbf{T}_B \quad \text{where} \quad \mathbf{T}_B = \begin{bmatrix} \mathbf{I} & \mathbf{R}_{ip} & \mathbf{0} & \mathbf{0} \\ \mathbf{0} & \mathbf{I} & \mathbf{0} & \mathbf{0} \\ \mathbf{0} & \mathbf{0} & \mathbf{I} & \mathbf{R}_{jq} \\ \mathbf{0} & \mathbf{0} & \mathbf{0} & \mathbf{I} \end{bmatrix} \tag{2.85}$$

The coordinates of the nodes $\boldsymbol{p}$ and $\boldsymbol{i}$ in Figure 2.7(a) are updated during the process of the state determination. Therefore, the vector $\mathbf{r}_o$ needs to be updated and the matrix $\mathbf{R}_{off}$ in Eq. (2.79) needs to be recalculated resulting in new transformation matrix $\mathbf{T}_B$ in Eq. (2.85) for the next iteration.

2.7 Benchmark Solutions

This section provides several benchmark problems targeted for verification of the capabilities of the beam finite element in handling the monosymmetry of the cross-section, initial horizontal curvature and tapered geometry along the member length.

2.7.1 Elastic Lateral Torsional Buckling of Singly-Symmetric Prismatic I-Section Beams

An elastic lateral torsional buckling solution is presented to validate the singly-symmetric I-section beam element developed in this research. The model is a torsionally simply-supported straight prismatic beam with a singly-symmetric I-section subjected to uniform bending as shown in Figure 2.8. The eigenvalue solutions are compared to the analytical elastic lateral torsional buckling solutions.

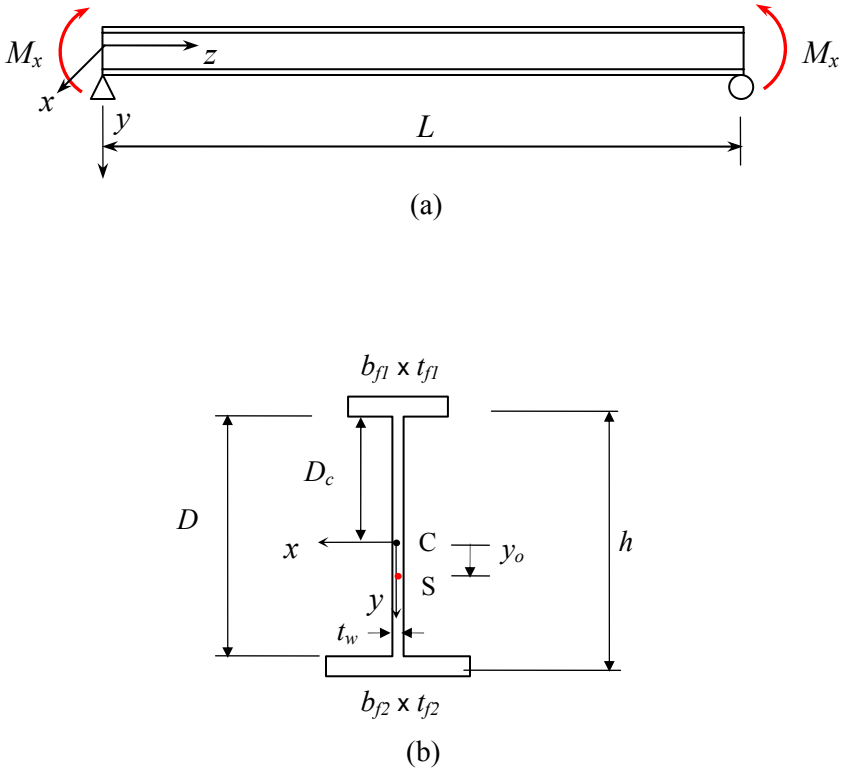

Figure 2.8 Simply supported singly-symmetric I-section beam: (a) loading condition; (b) cross-section dimension

The governing differential equations for minor axis bending and torsion of this model are given by Kitipornchai et al. (1986):

$$EI_y \frac{d^2u}{dz^2} = -M_x\phi \tag{2.86}$$

$$(GJ + M_x\beta_x)\frac{d\phi}{dz} - EC_w\frac{d^3\phi}{dz^3} = M_x\frac{du}{dz} \tag{2.87}$$

in which M_x is the bending moment about the x-axis, ϕ is the axial rotation, u is the lateral deflection and 'β_x' is the monosymmetry parameter, which is defined as:

$$\beta_x = \frac{1}{I_x}\left(\int_A y(x^2+y^2)dA\right) - 2y_o$$
$$= \frac{1}{I_x}\left[\left(\frac{b_{f2}^3}{12}(D-D_c)t_{f2} + \frac{b_{t2}^3}{24}t_{f2}^2 + b_{f2}t_{f2}(D-D_c)^3 + 1.5b_{f2}(D-D_c)^2t_{f2}^2 + b_{f2}(D-D_c)t_{f2}^3 + \frac{b_{f2}}{4}t_{f2}^4\right)\right.$$
$$-\left(\frac{b_{f1}^3}{12}D_c t_{f1} + \frac{b_{f1}^3}{24}t_{f1}^2 + b_{f1}t_{f1}D_c^3 + 1.5b_{f1}D_c^2t_{f1}^2 + b_{f1}D_c t_{f1}^3 + \frac{b_{f1}}{4}t_{f1}^4\right)$$
$$\left.+\left(\frac{(D-D_c)^4}{t}t_w + \frac{(D-D_c)^2}{24}t_w^3 - \frac{D_c^4}{4}t_w - \frac{D_c^2}{24}t_w^3\right)\right] - 2y_o \qquad (2.88)$$

in which y_o is the coordinate of the shear center when the centroid of the cross-section is the origin of the reference axis as in Figure 2.8.

The monosymmetry parameter β_x accounts for the coupling between axial strain and torsion. For a doubly symmetric I-section beam, the torque components due to the compressive and tensile stresses are balanced and β_x is zero. However, for a singly-symmetric I-section beam, the stresses are unbalanced and the resultant torque causes a change in the effective torsional stiffness. When the smaller flange is in compression, β_x is negative, which means there is a reduction in the effective torsional stiffness (Kitipornchai et al., 1980).

The boundary conditions are given by:

$$\phi = u = \frac{d^2\phi}{dz^2} = \frac{d^2u}{dz^2} = 0 \qquad \text{at } z = 0 \text{ and } L \qquad (2.89)$$

The analytical solution for the elastic critical moment of this problem may be expressed as (White and Jung, 2003):

$$M_{cr} = \frac{\pi^2 EI_y}{2L_b^2}\left\{\beta_x + \sqrt{\beta_x^2 + 4\left[\frac{C_w}{I_y} + \frac{GJL_b^2}{\pi^2 EI_y}\right]}\right\} \qquad (2.90)$$

The cross-section of girder G2 in the composite test bridge (see Section 3.5) is used for the current study. The cross-section dimensions are: top flange 36.04 cm x 2.23 cm (14.19 in x 0.88 in), bottom flange 56.31 cm x 2.55 cm (22.17 in x 1.00), and web

122.06 cm x 0.82 cm (48.06 x 0.32). To reach the elastic lateral torsional buckling when the beam is subjected to the uniform bending as in Figure 2.8(a), the length of the beam must be longer than L_r (White and Jung 2003):

$$L_r = \frac{1.38}{S_{xc}} \frac{E}{F_{yr}} \sqrt{I_y J} \sqrt{2.6\beta_x \frac{F_{yr}}{E} \frac{S_{xc}}{J} + 1 + \sqrt{\left[2.6\beta_x \frac{F_{yr}}{E} \frac{S_{xc}}{J} + 1\right]^2 + 27 \frac{C_w}{I_y} \left[\frac{F_{yr}}{E} \frac{S_{xc}}{J}\right]^2}} \quad (2.91)$$

in which $F_{yr} = 0.7\ F_{yc}$ and F_{yc} is the specified minimum yield stress of the compression flange with the unit ksi. For the current benchmark problem, the required length of the beam with a larger compression flange, for elastic lateral torsional buckling to control, is at least 13.28 m (43.57 ft). Therefore, a length 15.24 m (50.00 ft) is used for the study. Tables 2.1 and 2.2 show the analysis results based on the beam element and the analytical solution from the Eq. (2.90).

Table 2.1 Critical bending moment for the beam with the larger flange in compression (The analytical solution is 1,224.59 kN-m (903.21 kips-ft))

Number of Elements	Critical bending moment Proposed beam element kN-m (kips-ft)	% Difference compared to analytical solution
2	1,174.70 (866.41)	-4.07 %
4	1,208.27 (891.17)	-1.33 %
6	1,216.97 (897.59)	-0.62 %

Table 2.2 Critical bending moment for the beam with the larger flange in tension (The analytical solution is 4,123.34 kN-m (3,041.22 kips-ft))

Number of Elements	Critical bending moment Proposed beam element (kN-cm)	% Difference compared to analytical solution
2	3,563.92 (2,628.61)	-13.57 %
4	3,940.58 (2,906.42)	-4.43 %
6	4,037.48 (2,977.89)	-2.08 %
8	4,074.23 (3,005.00)	-1.19 %
12	4,101.49 (3,025.11)	-0.53 %

2.7.2 Curved Singly-Symmetric I-Section Beams

In this subsection, two fundamental geometrically-linear benchmark problems and their analytical solutions are presented.

The first benchmark problem is shown in Figure 2.9. This is a torsionally simply-supported curved I-girder with a singly-symmetric cross section (the cross-section from girder G2 of the composite test bridge is used (see Section 3.5)). The warping and twist displacements are constrained at both ends and the member is subjected to uniform major-axis bending. The applied moments are such that the maximum flange stress is equal to the yield stress F_y (taken equal to 50 ksi). The analytical solution for the bi-moment is shown in Eqs. (2.92) to (2.99), in which R is the radius of curvature, L_b is the unbraced length and h is the depth between the centroids of the flanges.

$$M_l(t) = h\left(A\cosh\alpha\, t + B\sinh\alpha\, t + C\cos\theta\, t + D\sin\theta\, t\right) \tag{2.92}$$

in which:

$$A = \frac{\left(\frac{\alpha}{\theta}C\tanh\frac{\alpha}{2} + \frac{\alpha D}{\sinh\alpha} - D\right)(\cos\theta - 1) + \left(\frac{\alpha}{\theta}D\tanh\frac{\alpha}{2} - \frac{\alpha C}{\sinh\alpha} + C\right)\sin\theta - \alpha D\tanh\frac{\alpha}{2}}{\theta\left(1 - \frac{2}{\alpha}\tanh\frac{\alpha}{2}\right)} \tag{2.93}$$

$$B = \frac{\left(D\tanh\frac{\alpha}{2} - \frac{\alpha}{\theta}C\right)(\cos\theta - 1) - \left(C\tanh\frac{\alpha}{2} + \frac{\alpha}{\theta}D\right)\sin\theta + \alpha D}{\theta\left(1 - \frac{2}{\alpha}\tanh\frac{\alpha}{2}\right)} \tag{2.94}$$

$$C = \frac{M}{Rh(\frac{1}{R^2} + \frac{1}{a^2})} \tag{2.95}$$

$$D = \frac{M}{Rh(\frac{1}{R^2} + \frac{1}{a^2})}\frac{1-\cos\theta}{\sin\theta} \tag{2.96}$$

$$a = \sqrt{EC_w/GJ} \tag{2.97}$$

$$\alpha = L_b/a \tag{2.98}$$

$$t = \frac{s}{L_b}, \quad \theta = \frac{L_b}{R} \tag{2.99}$$

A comparison of the top flange lateral bending stresses between the analytical solution and the results from finite element analysis with four and six curved elements is shown in Figure 2.10. At the midspan, the flange lateral bending stress produced by the 4-element model is 12.6% greater than the analytical solution while the 6-element model reduces the difference to 5.4%. At the ends, the maximum flange lateral bending stress from the 4-element model is 7.0% smaller than the analytical solution while the 6-element model reduces the difference to 3.4%. A similar analysis has been conducted by Huang (1996) except his benchmark assumes a doubly-symmetric cross-section.

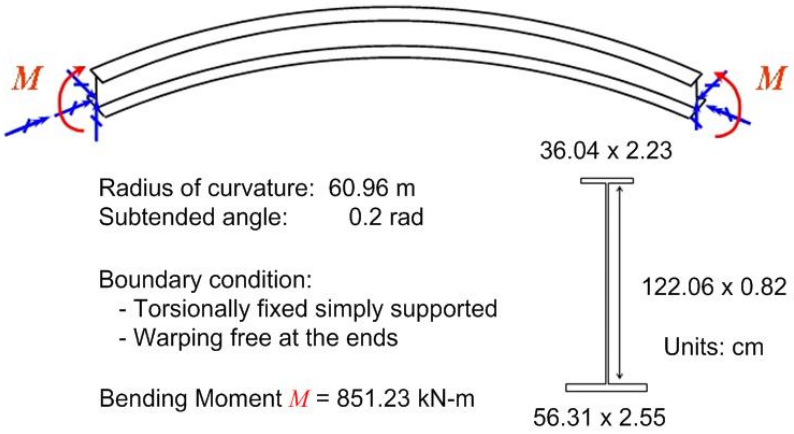

Figure 2.9 The first benchmark problem – a curved singly-symmetric I-section beam under uniform major-axis bending

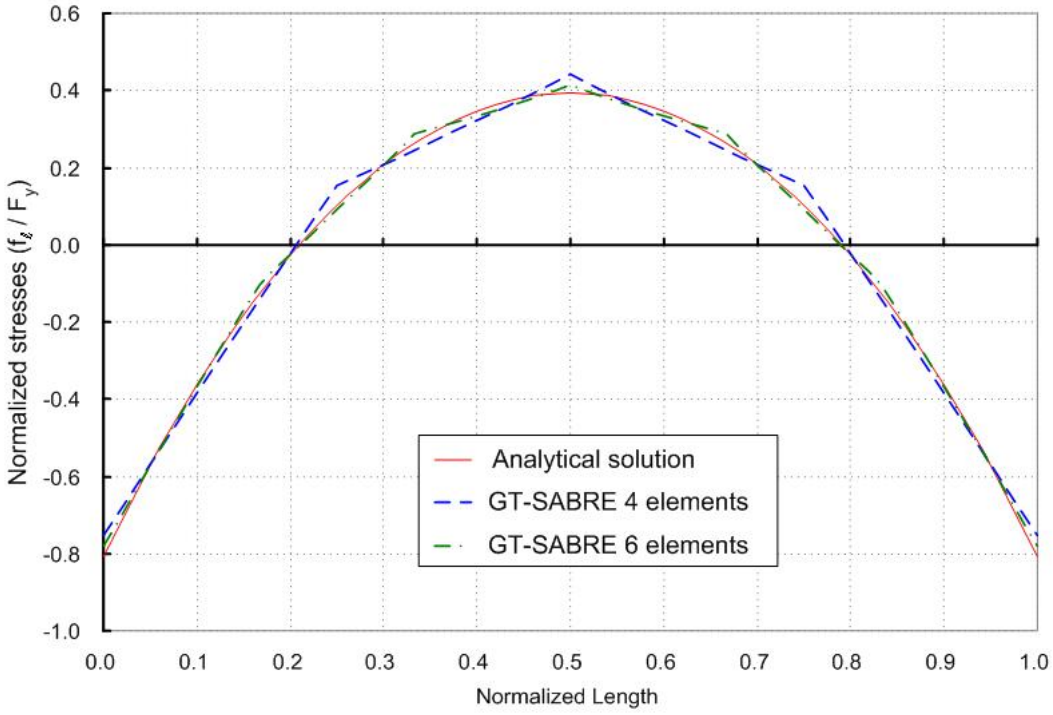

Figure 2.10 The results of the benchmark problem in Figure 2.9: top flange lateral bending stresses

The second benchmark problem is shown in Figure 2.11. This example has the same geometry and boundary conditions as the example of Figure 2.9, except warping is free at both ends, and an eccentric vertical concentrated load is applied at the midspan. This problem is similar to the experimental test setup used by Mozer and Culver (1970). The load is applied eccentrically to counteract the tendency of the member to twist and the top flange to bend laterally. The analytical solution for the bi-moment $B(t)$ is (Mozer and Culver 1970):

$$B(t) = \frac{PR^2}{2}\left[\frac{\frac{e}{R}(1-\eta)+\eta}{\frac{R}{a}}\frac{\sinh \alpha\, t}{\cosh \frac{\alpha}{2}t} + (\frac{e}{R}-1)\eta\frac{\sin \theta\, t}{\cos \frac{\theta}{2}}\right] \tag{2.100}$$

in which

$$\eta = \frac{1}{1+(R/a)^2} \tag{2.101}$$

The comparison of the top flange lateral bending stresses between the analytical solution and finite element analysis results is shown in Figure 2.12. In this case, more elements are required to capture the variation in the flange lateral bending stresses near the midspan.

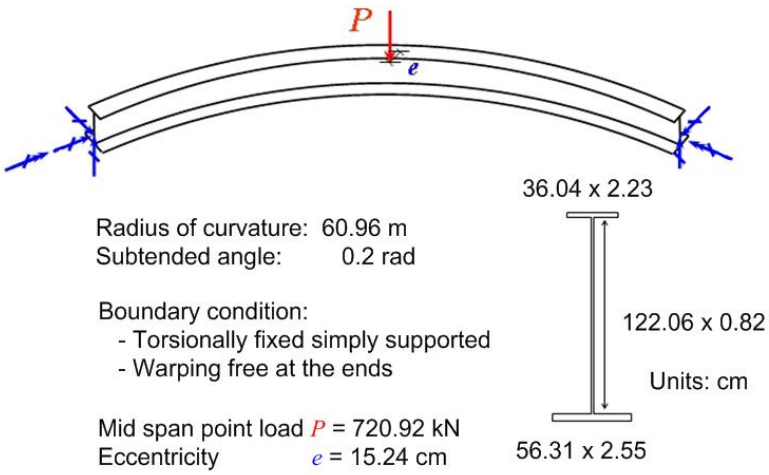

Figure 2.11 The second benchmark problem – a curved singly-symmetric I-section beam under midspan eccentric vertical concentrated load

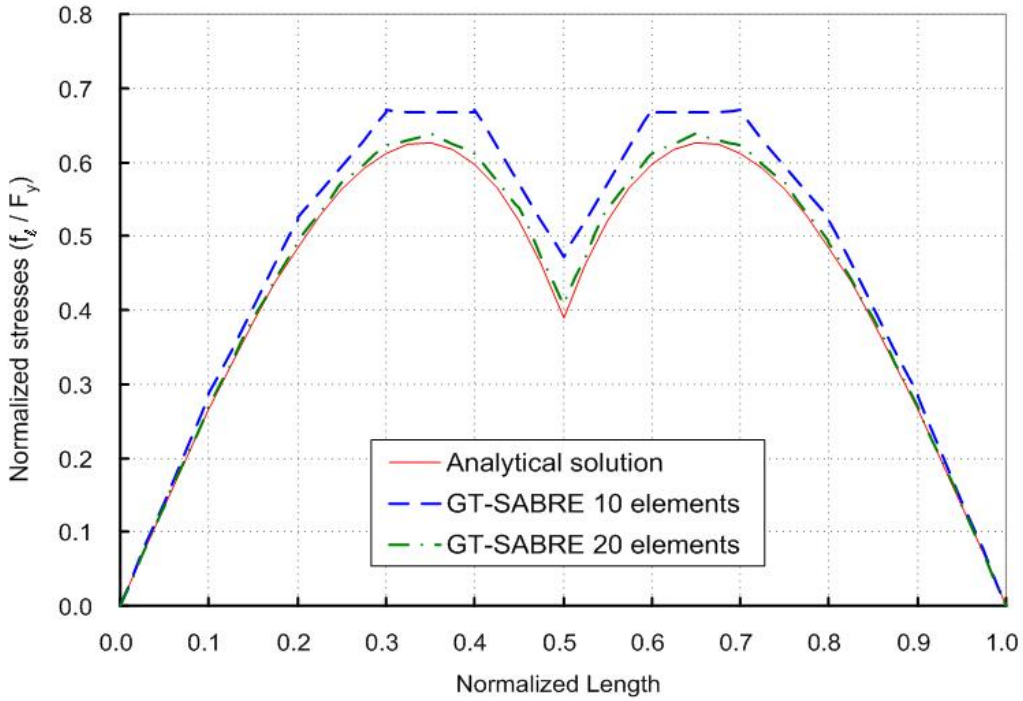

Figure 2.12 The results of the benchmark problem in Figure 2.11: top flange lateral bending stresses

2.7.3 Tapered I-Section Beams

In this subsection, three benchmark problems are solved to demonstrate the capability of the proposed beam finite element for the analysis of tapered I-section members. The first problem involves the lateral torsional buckling of the straight simply-supported beam with doubly-symmetric tapered section shown in Figure 2.13. This problem has been studied by Yang and Yau (1987) and Andrade and Camotim (2005). The second and third problems are curved web-tapered cantilever beams using the singly-symmetric I-section shown in Figure 2.15. These benchmarks are created for the further verification of the beam finite element for combined cross-section monosymmetry, cross-section taper and initial horizontal curvature. These are new benchmarks not previously solved in the literature. The analysis results are compared to the results from a refined shell finite element solution.

2.7.3.1 Lateral Torsional Buckling Analysis

Figure 2.13 shows a torsionally simply supported web-tapered beam with a doubly symmetric I section. Both ends are free to warp. A concentrated load is applied at the mid web-depth at midspan. Figure 2.14 shows the comparison among the results based on the proposed beam finite element, the solution by Yang and Yau (1987) and the solution by Andrade and Camotim (2005).

The analysis results based on the proposed beam element tend to agree more closely with Yang and Yau's solution. The results from Andrade and Camotim (2005) are higher than the other two solutions especially when the taper ratio α is less than 0.5. These investigators used a number of sinusoidal functions with the Rayleigh-Ritz method to achieve convergence when the taper ratio is small (e.g.,12 for α=0.3).

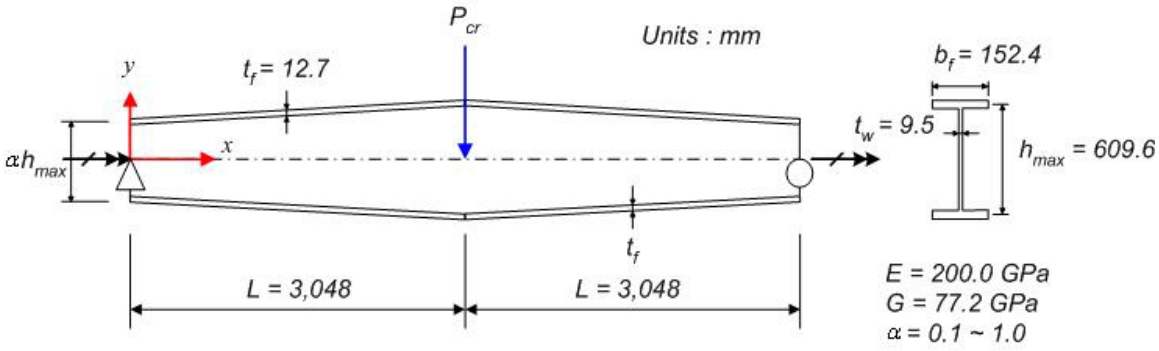

Figure 2.13 Web-tapered simply supported beam for LTB analysis

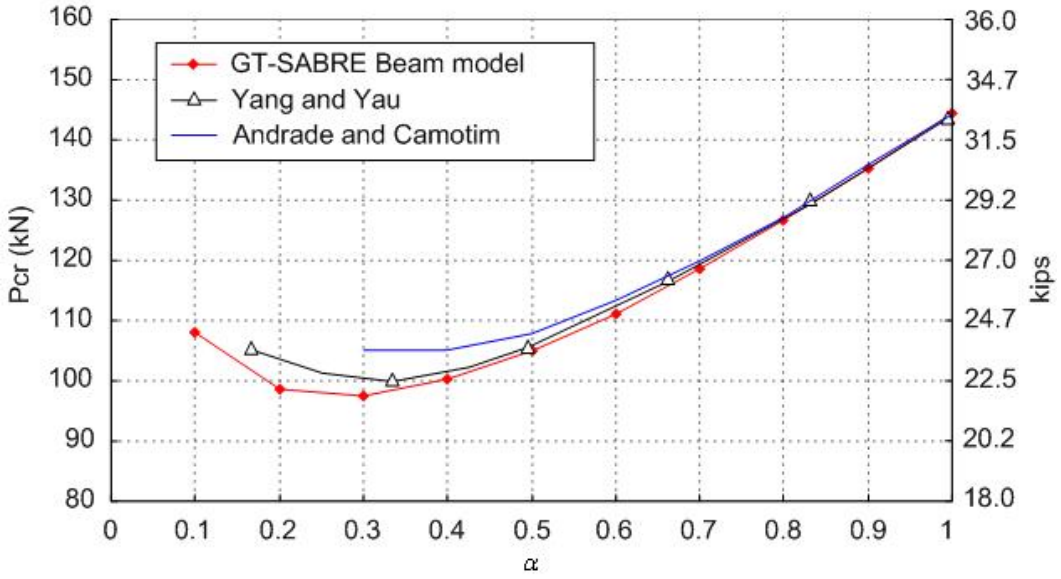

Figure 2.14 Variation of critical load P_{cr} with taper ratio α – of the simply supported beam in Figure 2.13 from the proposed beam element solution, Yang and Yau (1987) and from Andrade and Camotim (2005)

2.7.3.2 Cantilever Benchmark with Large Flange Lateral Bending

In this subsection, a cantilever beam with a web-tapered, singly-symmetric I-section and horizontal curvature is analyzed to validate of the derived beam element formation. Both first- and second-order analyses are performed.

As shown in Figure 2.15, the arc length of the curved girder is 10.97 m. The subtended angle is set as 22.5 degree (0.393 rad) with a corresponding radius of curvature of 29.74 m. It is noted that this large unbraced length relative to the web-depth may exist during steel erection. The web slenderness ratio is varied from 128 to 96. The flange slenderness ratios $b_f/2t_f$ are 6 for the top flange and 5.33 for the bottom flange. The downward point load is applied to the top web-flange juncture at the free end. The magnitude of the applied load is 46.57 kN (10.47 kips) and is such that the maximum flange stress is equal to the yield stress F_y (= 482.63 MPa or 70 ksi) based on the first order analysis performed by shell-beam model created in ABAQUS (HKS 2005).

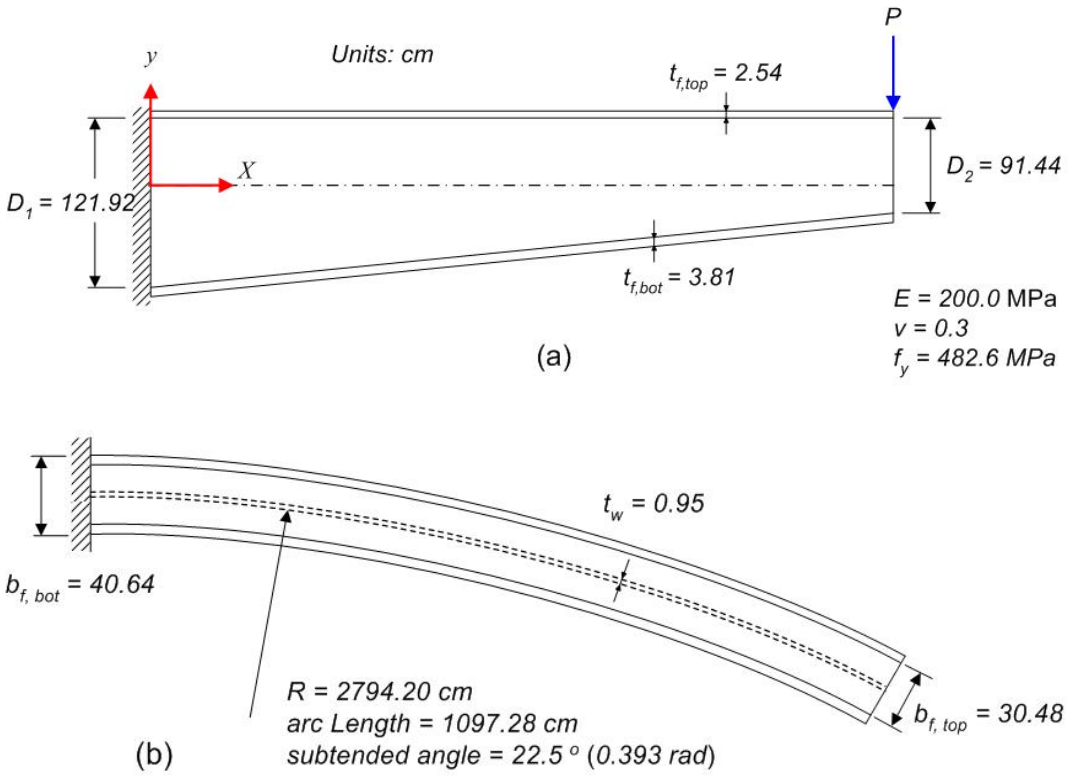

Figure 2.15 (a) Elevation of the curved web-tapered cantilever beam with singly-symmetric I section (b) Plan view of the curved web-tapered cantilever beam with singly-symmetric I section

For the shell-beam model, the girder tapered web is modeled with four-node shell elements (S4R) and the flanges are modeled with beam elements (B31). A bearing stiffener modeled with beam elements is added to the free end.

As shown in Figures 2.16 to 2.19, the flange stresses determined using the open-section thin-walled beam element are in good agreement with the results from the shell-beam model. The flange major-axis bending stresses are much smaller than the flange lateral bending stresses in this case. In other words, the beam response is dominated by warping torsion. The two models match well for both the top and bottom flange major-axis bending stresses based on both the first- and second-order analyses. No significant second-order effect is observed for the flange major-axis bending stresses. Based on the first-order analysis, the difference of the flange lateral bending stresses between two models is less than 1%. For the second-order analysis, the maximum flange lateral bending stress from the beam model is 1.2% higher than that from shell-beam model at the top flange and 0.1% smaller at the bottom flange.

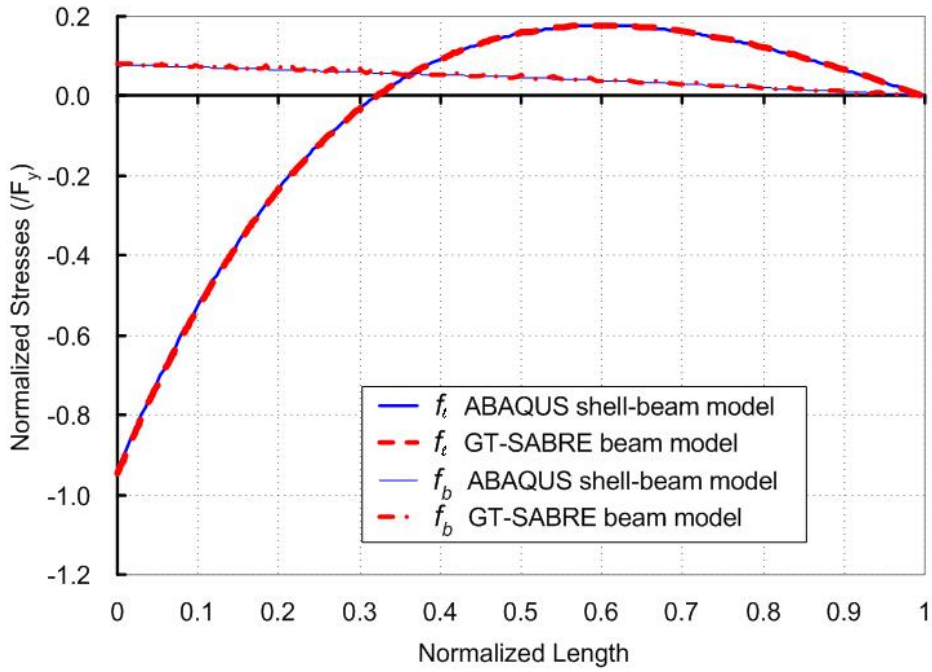

Figure 2.16 Top flange stresses based on the first order analysis

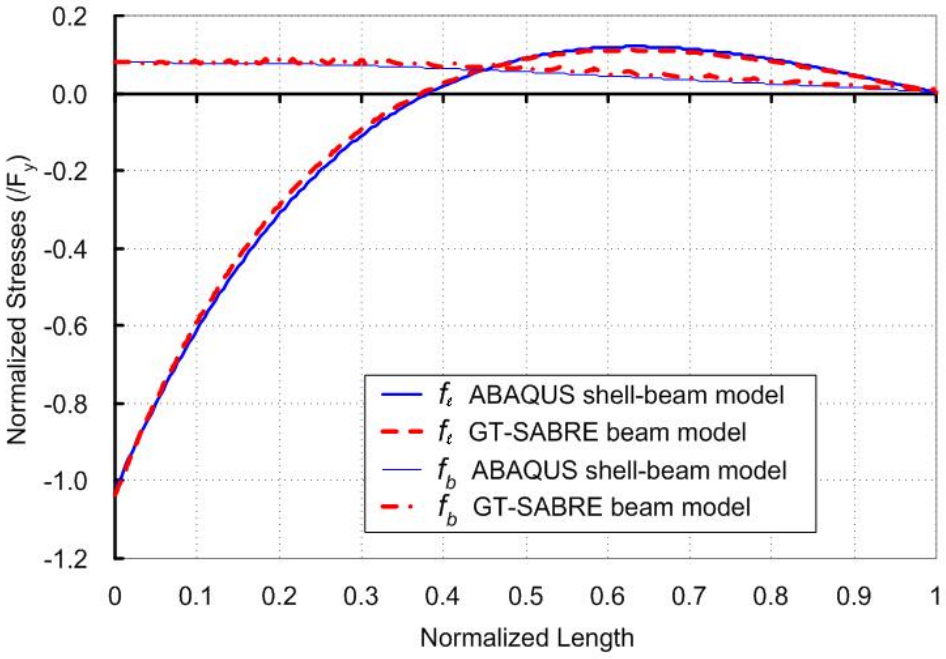

Figure 2.17 Top flange stresses based on the second order analysis

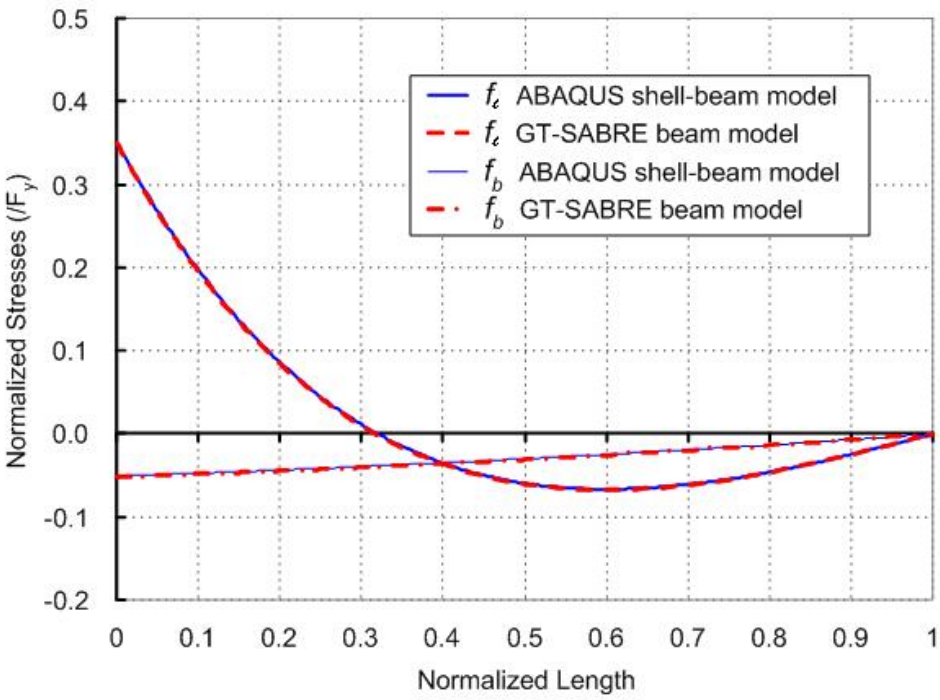

Figure 2.18 Bottom flange stresses based on the first order analysis

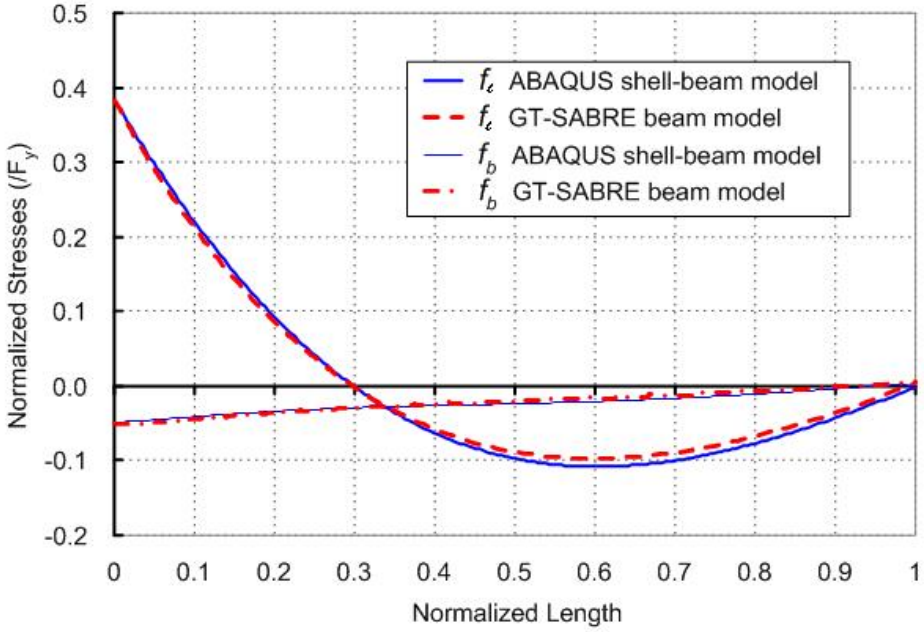

Figure 2.19 Bottom flange stresses based on the second order analysis

The maximum lateral bending stresses at both the top and bottom flanges are increased about 9.0% in both the beam and the shell-beam models due to the second order effects. The second order amplification is larger around the midspan. The shell-beam model shows an increase of about 63% for the maximum bottom flange lateral bending stress (Figure 2.18 and 2.19) and a reduction of about 44% for the maximum top flange lateral bending stress (Figure 2.16 and 2.17) around the midspan due to the second-order effects. However, these values are of a smaller magnitude than the flange lateral bending stresses near the fixed end.

2.7.3.3 Cantilever Benchmark with Large Amplification of Flange Lateral Bending Stresses

Another cantilever beam with the combination of the web-tapered, singly-symmetric I-section and horizontal curvature is utilized for further validation of the derived beam finite element formation in this subsection. In contrast to the above example, which has a subtended angle of 0.393 rad (22.5^o), the girder subtended angle in this example is set to 0.05 rad to magnify the second order effect. Also, the radius of curvature is changed to 57.15 m (187.5 ft), the width of the top flange is changed to 38.10 cm (15.0 in) and the web depth is varied from 95.25 cm (37.5 in) to 76.20 cm (30.0 in) such that the web slenderness ratio D/t_w varies from 100 to 80.

The magnitude of the applied load is 1,032 kN (232 kips) and is such that the maximum flange stress is equal to the yield stress F_y (= 482.63 MPa or 70 ksi) based on a first order analysis performed using the beam model developed in this research. The shell-beam model of this example is created in ABAQUS in the same fashion as the above example.

Figure 2.20 shows the top flange lateral bending stresses based on a first and second order analysis using the beam finite element model with 10 elements along the

length. The maximum top flange lateral bending stress increases 51.7% due to the second-order effect. The influence of the second-order effect on flange major-axis bending stresses is not significant.

Figure 2.21 shows plots of the applied load versus maximum top flange lateral bending stress at the fixed end from the beam finite element and the shell-beam models based on second-order analysis. The beam finite element solution agrees with the shell beam model solution until the applied load reaches about 0.675P. When the applied load is larger than this level, the maximum top flange lateral bending stress of the shell-beam model is increased due to web-distortion effects, which can not be accounted for by the beam finite element.

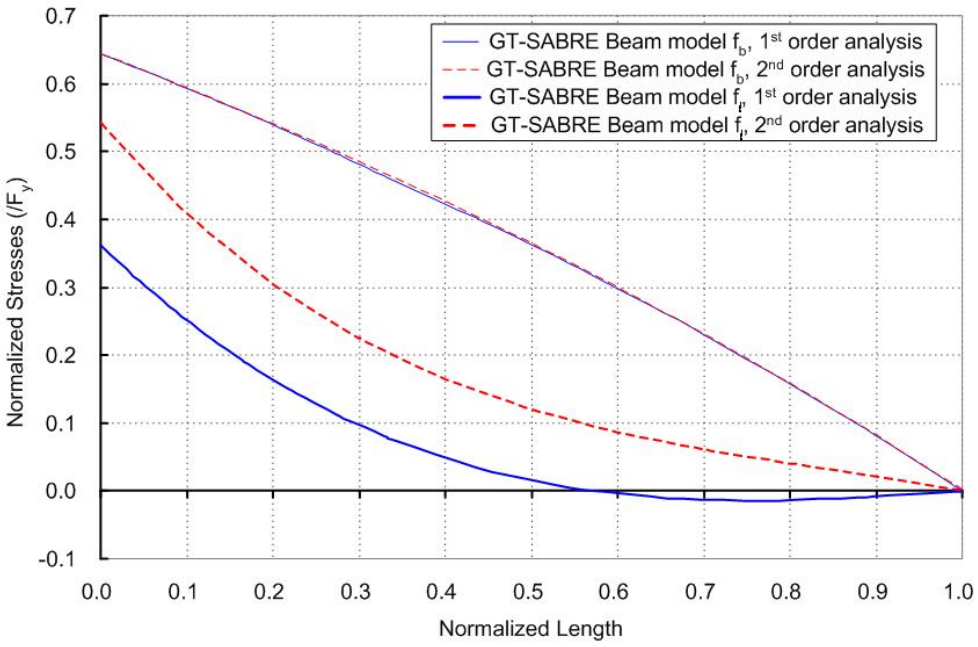

Figure 2.20 Top flange lateral bending stresses from beam model based on the second-order analysis

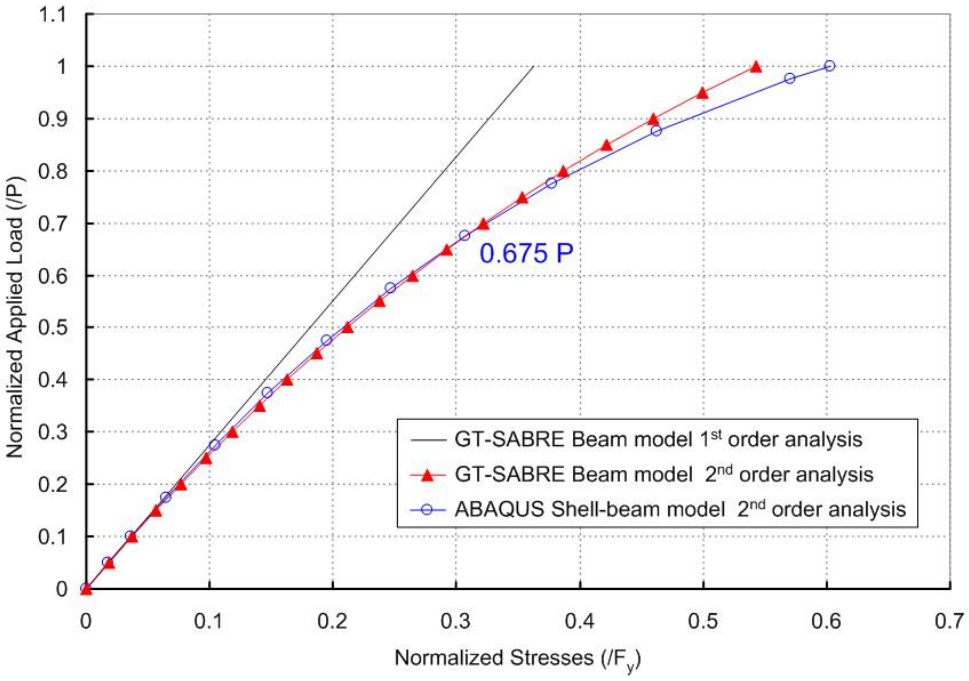

Figure 2.21 The curves of applied load vs. top flange maximum lateral bending stress from beam model and shell-beam model based on the second-order analysis

CHAPTER 3

MODELING OF COMPOSITE CURVED I-GIRDER BRIDGES

This chapter provides an investigation on the qualities and limitations of various modeling strategies for design analysis of composite curved I-girder bridge structural systems. The targeted analysis approaches include line girder analysis combined with the V-load method, grillage methods and general finite element methods. Results from a full-scale composite I-girder bridge tested at the Federal Highway Administration (FHWA) Turner-Fairbank Highway Research Center (TFHRC) are used as a basis for the comparison of the different analysis methods. The test bridge is designed to accentuate a number of the characteristics of curved I-girder bridges within the specific context of a three-girder simply-supported span with a constant radius of curvature, radial supports and radial cross-frames.

3.1 Component Responses of Curved I-Girder Bridge Systems

Hall et al. (1999) explain that the response of curved I-girder bridges is comprised of the four components illustrated by Figure 3.1. The various analysis methods can be categorized by considering their ability to represent each of these components. Components 1 through 3 are contributions to the girder major-axis bending moments. Component 1 is the moment due to loads assumed to be applied directly through the individual girder shear centers, assuming that each of the girders is independent from the rest of the structure and that twisting is prevented. The Component 2 moments are caused by the transfer of load from girders with larger Component 1 deflections to the adjacent girders, such that the differences in their vertical deflections are mitigated,

assuming that twisting is prevented. The Component 3 moments are due to the larger reactions on the outside girders and the corresponding smaller reactions on the inside girders required for torsional equilibrium of a horizontally curved bridge (see Figure 1.1). Also, the internal twisting restraint provided to the I-girders from the slab and the cross-frames causes vertical forces (i.e., the V-loads) in these elements. These V-loads cause load to be shifted to the exterior girder(s) and away from the interior girder(s). The Component 3 moments are due to these internal vertical loadings from the slab and the cross-frames (see Figure 1.3). Component 4 is the flange lateral bending (or warping) associated with non-uniform torsion of the I-girders (see Figure 1.4). For typical bridge geometries, the I-girder torsional responses tend to be dominated by non-uniform or warping torsion. However, particularly within the final constructed composite system, the I-girder webs are not sufficiently stiff to maintain the shape of the cross-section profiles. The torsional response of the I-girders is influenced heavily by web distortion. The importance of web distortion on the torsional response is well recognized for straight composite I-section members (e.g., see Bradford and Gao (1992)), but has not received much attention in the context of curved composite I-girders.

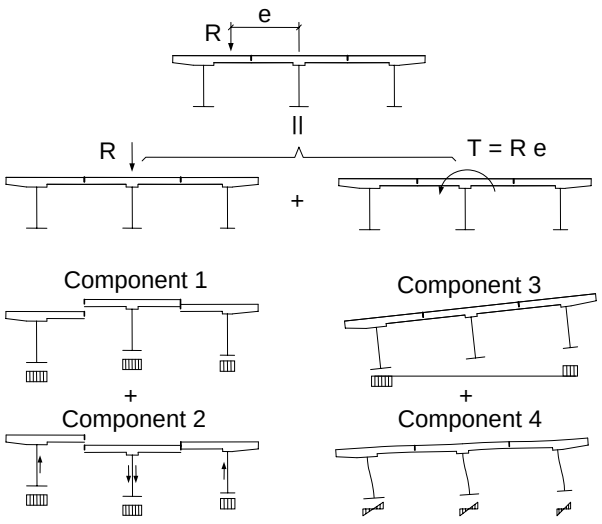

Figure 3.1 Longitudinal member component responses.

3.2 General Modeling Considerations

3.2.1 Girder Web Distortion Effects

The I-girder behavior in a typical composite bridge involves significant web distortion. Web distortion causes additional lateral displacements and lateral bending stresses at the girder bottom flanges. As noted in Chapter 1, this research applies open-section thin-walled beam theory for modeling of curved steel I-girders. Since beam element kinematics does not capture the effects of web distortion, it is important to determine if approximations using open-section thin-walled beam theory can be utilized that provide an adequate representation of this physical behavior.

3.2.2 Cross-Frame Modeling

Cross-frames connect the girders to each other and provide torsional restraint and lateral stability to the girders. In this study, cross-frames are modeled with truss and/or beam elements. Rigid offset constraints are implemented between the ends of the cross-frame elements and the girder reference axes. Beam elements are necessary to model the bottom chord of cross-frames such as the one shown in Figure 3.2. If truss elements were used for the bottom chord in this example, there is no resistance to deflection in the out-of-plane direction at the middle of the bottom chord. Bottom chord beam elements are required to resist longitudinal movement at the juncture of the chord with the cross-frame diagonals.

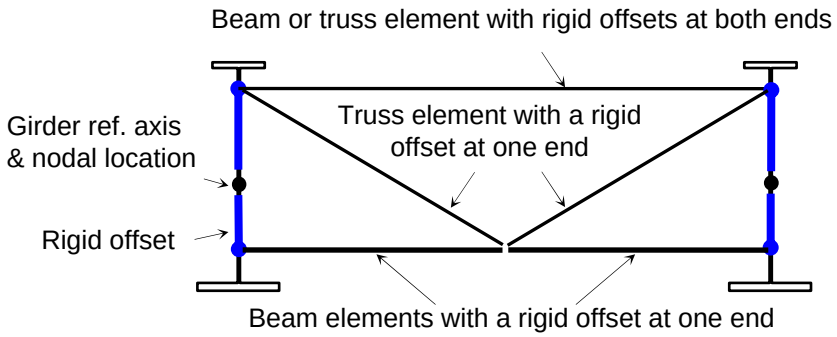

Figure 3.2 Cross-frame model

3.2.3 Modeling of Supports, Load Height

When modeling curved I-girder bridges, it is generally important also to include the actual elevation of the girder supports. The horizontal forces generated at bearing locations can depend significantly on the vertical position of these reactions. Figure 3.3 shows a rigid offset constraint used to model the elevation of a bearing. Also, to handle the potential uplift at certain bearing locations, a compression-only gap element is used. In addition, the elevation of the applied loads from the wet concrete, etc. should be accounted for. Loads such as the weight of the slab cause a tipping effect on the I-girders.

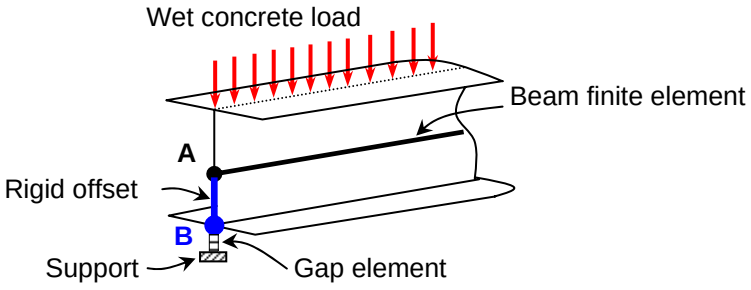

Figure 3.3 Bearing offset and load-height effects

3.2.4 Displacement Compatibility between Girders and Slab

If a shell-beam model is employed (shell elements for the slab and beam elements for the girders) for a bridge structure, the displacement fields in the shell and beam elements need to be compatible with each other. For example, with the use of a 9-node shell element (degenerated from a 3D solid), 3-node beam elements based on Reissner-Mindlin beam theory should be adopted to avoid compatibility problems. In as such, the displacement field approximation is quadratic in both the beam and the shell elements. If a comparable 4-node shell element is used, a two-node Reissner-Mindlin beam element is necessary for compatibility reasons.

3.3 Investigation of Approximate Procedures for Capture of Web Distortion Effects Using Open-Section Thin-Walled Beam Element

The significance of the web distortional flexibility on the response and the investigation of approximate procedures for capture of web distortion effects using open-section thin-walled beam elements for the steel I-girders are presented in this section. Curved I-girder bridges and their component members are subjected to coupled torsion and bending. In this study, a straight composite girder subjected to a uniformly distributed torque is considered first to focus on the fundamental responses. The torsional loading and boundary conditions in this study are equivalent to those of an isolated curved I-girder with a constant horizontal radius of curvature subjected to uniform bending and having symmetry boundary conditions at the cross-frame locations. In other words, the straight girder is subjected to a uniformly distributed torque along the length of the member and the boundary conditions are fully-fixed at its ends.

Regarding the above issues, an equivalent open-section thin-walled beam section of a straight composite girder proposed by Heins and Kuo (1972) and utilized by

Huang (1996) is used for comparison purposes (see Figure 3.4). Closed form analytical solutions are presented using this model.

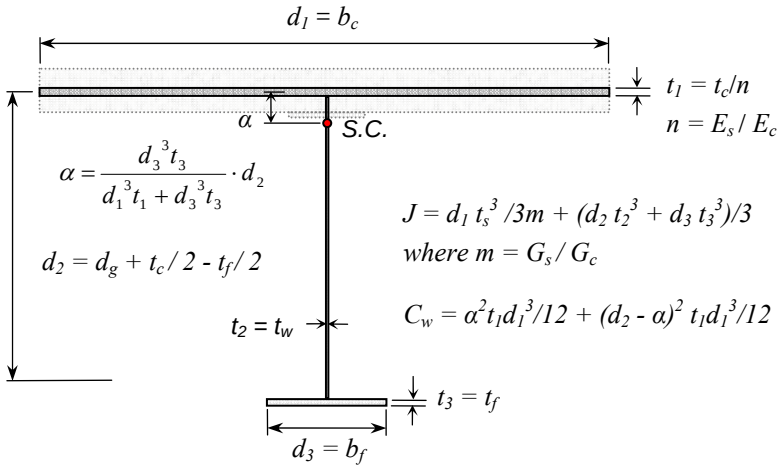

Figure 3.4 Heins and Kuo's idealized composite section (Model c1) and approximate equations for torsional properties

3.3.1 Models Using Shell Elements For The Girder Webs

To investigate the web distortion effects in composite bridge I-girders, four different geometrically linear benchmark FEA models shown in Table 3.1 and Figures 3.5 and 3.6 have been studied using the ABAQUS software system (ABAQUS 2005). In all cases the web is modeled using the S4R shell element and the flanges and the slab are modeled using B31 elements. The Girder G2 cross-section from the composite test bridge introduced later in Section 3.5.1 is used. The length between the supports is taken equal to the unbraced length along the arc between the cross-frames in the test bridge.

Table 3.1 Four different benchmark models for investigating web distortion effects

Model (a1):	The slab is modeled explicitly; the shell-element web is constrained to remain straight;
Model (a2):	The slab is modeled explicitly; the shell-element web is unstiffened (the web's distortional flexibility is considered);
Model (b1):	The slab is not included in the FEA model; all components of the displacement and rotation except the torsional rotation are restrained at the centerline of the top flange; the shell-element web is constrained to remain straight;
Model (b2):	The slab is not included in the FEA model, but all components of the displacement and rotation are restrained at the centerline of the top flange; the shell-element web is unstiffened (the web's distortional flexibility is considered).

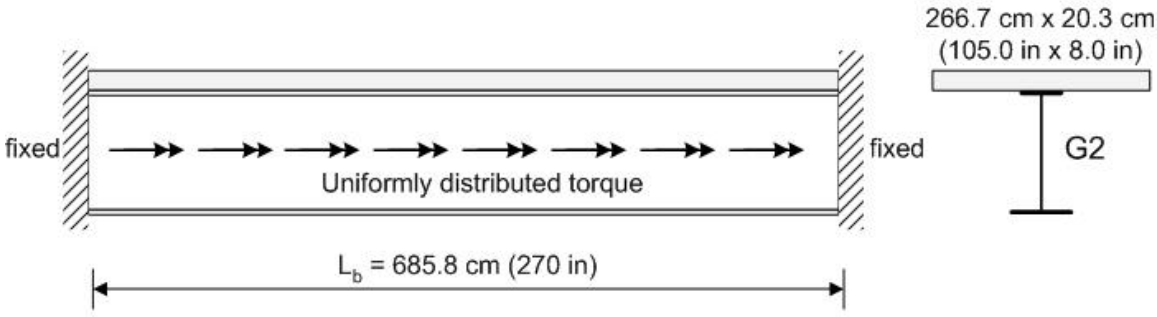

Figure 3.5 Shell-web models for investigating web distortion effects – (a) straight composite I-girder: model (a1) NO web distortion; model (a2) Web distortion allowed

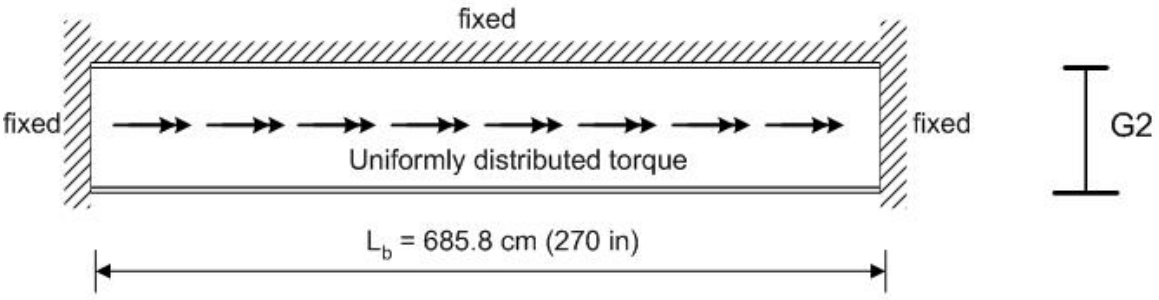

Figure 3.6 Shell-web models for investigating web distortion effects – (b) Model (a) with rigid slab: model (b1) NO web distortion, torsional restraint released at the top flange; model (a2) Web distortion allowed

In the above cases where the slab is modeled explicitly, a beam element representation of the slab is used with the concrete modulus E_c. In all cases, a uniformly distributed torque is applied as an equivalent distributed force couple along the length of the member such that the maximum stress at the bottom flange from the analytical solution based on Heins and Kuo's Model, which is referred to as Model (c1), is equal to $0.6F_y$ (F_y = 50 ksi).

The results for the flange lateral bending stresses are summarized in Figures 3.7 and 3.8. Model (a2) is considered to be the most rigorous of the above models. However, Models (b1) and (b2) give essentially the same results as Model (a2). Conversely, Models (a1) and (c1) give predicted displacements and bottom flange lateral bending stresses that are significantly smaller than Model (a2). The bottom flange lateral bending stresses match closely between Models (a1) and (c1) but the lateral bending displacements at the bottom flange are slightly smaller in Model (c1). The larger displacements and bottom flange lateral bending stresses in Model (a1) are due to web distortion. The following conclusions may be drawn from these results:

1) Due to the distortional flexibility of the web, the torsional restraint provided by the slab has essentially zero effect on the bottom flange displacements and stresses.

2) The equivalent I-girder model developed by Heins and Kuo (1972) generally underestimates the bottom flange lateral bending displacements and stresses.

3) The fact that Model (b1) gives results that are practically identical to Model (a2) indicates that Girder G2 can be modeled accurately using an open-section thin-walled beam element for the steel section while using a separate finite element representation for the slab. However, a specialized constraint must be employed between the slab and the steel I-section. The torsional and lateral bending restraint provided by the slab to the steel I-secton at the slab-beam interface must be released. If these restraints are included within the finite element model, the bottom flange lateral bending displacements and lateral bending stresses are significantly underpredicted (as indicated by Model (a1)).

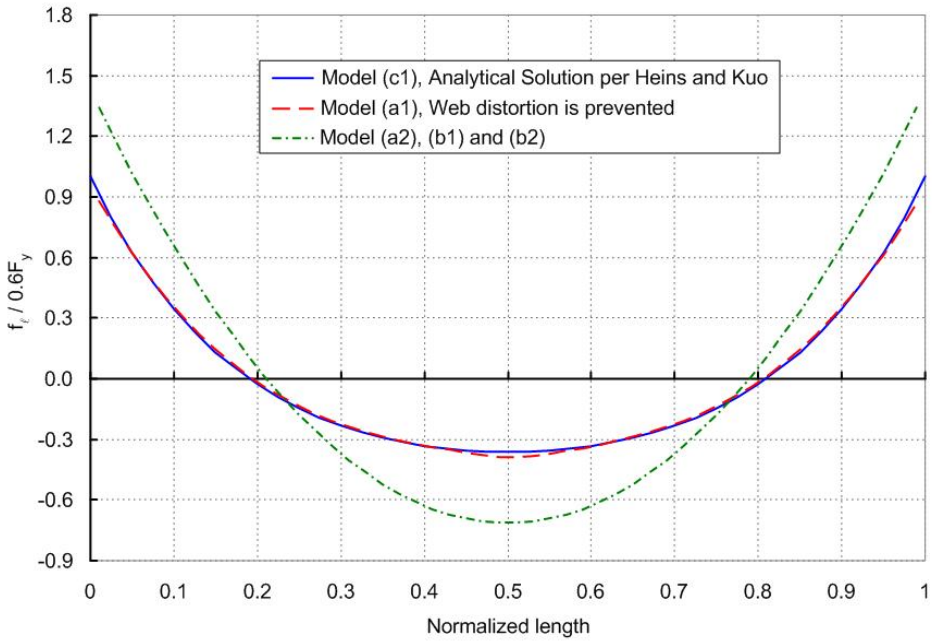

Figure 3.7 Linear analysis results of the models in Figures 3.5 and 3.6 – Lateral bending stresses at bottom flange

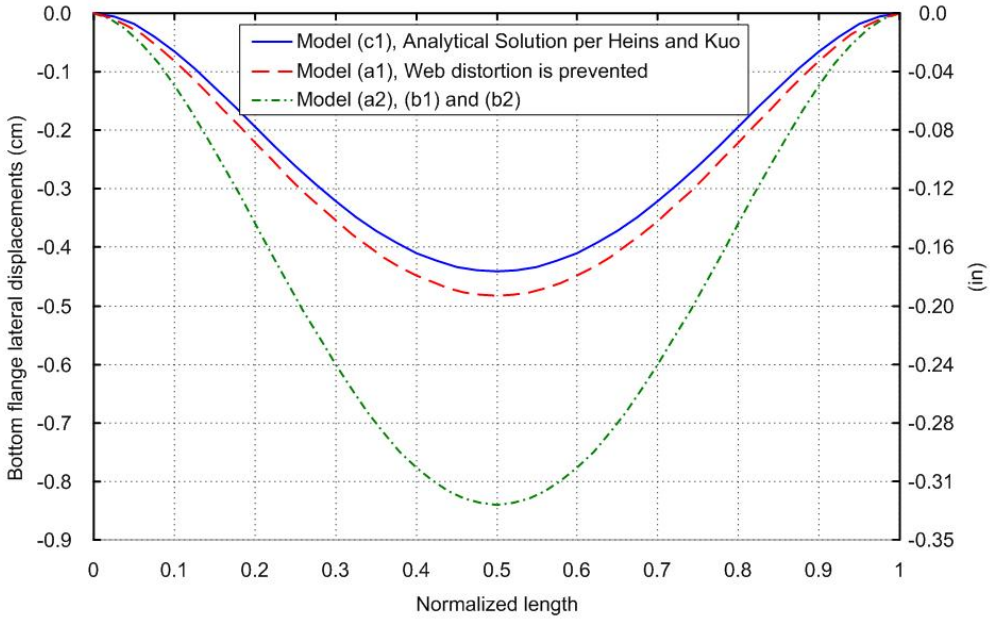

Figure 3.8 Linear analysis results of the models in Figures 3.5 and 3.6 – Lateral displacement at bottom flange

In this study, Girder G2 has a slender web. The slenderness ratio of the web is $D/t_w = 153.6$. To investigate the web distortion effects for a girder with a stocky web that is more representative of rolled I-section proportions, the web in all the above Models is made three times thicker and the girders are reanalyzed. As a result, the corresponding modified web slenderness is representative of typical rolled wide-flange shapes (although the girder is still singly-symmetric). The results are essentially the same as the results summarized above.

In many cases in practice, intermediate transverse stiffeners are employed within curved steel I-girders. These stiffeners may help stiffen the web. However, plastic hinging can occur at the tops of typical transverse stiffeners prior to the I-girders reaching their maximum strength (Jung 2006). Special checks would be necessary in general if the Engineer were to rely on intermediate transverse stiffeners to assist the slab in restraining bottom flange lateral displacements.

3.3.2 Models Using Open-Section Thin-Walled Beam Elements For the I-Girders

As indicated in previous Section, the composite Girder G2 can be modeled accurately using an open-section thin-walled beam element for the steel section. Therefore in this Section, the girder is modeled using open-section thin-walled beam elements with the reference axis located at the steel I-girder shear center (S.C.). Two specific models are considered. These models are referred to as Models (a3) and (b3) and are described in Table 3.2 and Figure 3.9.

Table 3.2 Benchmark models a3 and b3 for investigating web distortion effects

Model (a3):	The slab is modeled explicitly using conventional beam elements; the open-section thin-walled beam element model of the girder and the slab model are connected by rigid offsets with hinges at the girder top flange;
Model (b3):	The slab is not included in the FEA model, the open-section thin-walled beam element model of the girder is implemented with rigid offset constraints to the nodes at the top flange; all translational degrees of freedom are restrained at the top flange nodes, but the rotations are not restrained

The concrete slab only constrains the I-girder top flange. However, if a rigid offset constraint is applied between the slab and open-section thin-walled beam representation of the girder, the lateral bending in the bottom flange is also constrained by the slab. This significantly over-constrains the bottom flange displacements. Therefore, as noted previously, the torsional and lateral bending rotations are released at the top flange nodes in both Models (a3) and (b3). For the purpose of simplification,

all rotational degrees of freedom are released at this location. The results show that the lateral bending stresses and lateral displacements in the bottom flange of the I-girders in Models (a3) and (b3) match closely with those of Model (a2). In addition, with the use of this modeling technique, the rotation about the vertical axis at the girder top flange, due to lateral bending and warping, is compatible with the rotation of the slab throughout the girder length.

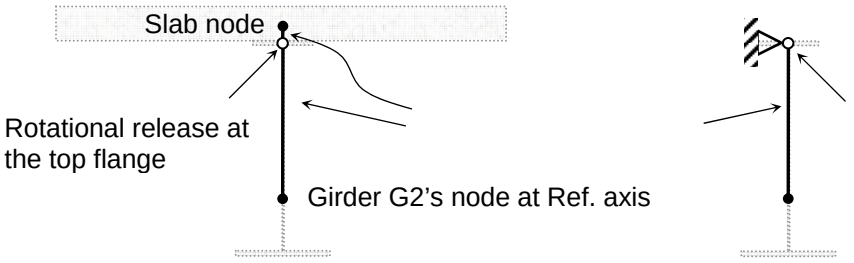

(a) Model (a3) Straight composite I-girder using ABAQUS B31OS element for the girders and B31 for the slab

(b) Model (b3) Straight I-girder using ABAQUS B31OS element

Figures 3.9 Beam models for capturing the web distortion effects

3.4 Overview of Analysis Methods

3.4.1 Line-Girder Analysis Combined with Distribution and Modification Factors

AASHTO (1993) provides equations for a set of factors that can be applied to the major-axis moments from a line girder analysis to estimate the girder major-axis and flange lateral bending moments in curved bridge structural systems. These factors contain implicitly a host of assumptions and idealizations invoked in the parametric

studies on which they are based, e.g., constant radius of curvature and similar behavior of the interior and exterior girders. They give estimates of average responses from a limited number of idealized bridge systems and provide little insight into the structural behavior. The Engineer simply enters a few parameters (girder spacing, span length, and radius of curvature) and the equations produce a multiplier to be applied to the line-girder analysis moments. Since only limited accuracy can be achieved with this type of approach, and also since there is no information within the equations themselves for the Engineer to intuitively check the correctness of the resulting calculations, these equations are no longer included within AASHTO (2003 & 2004).

3.4.2 Line-Girder Analysis Combined with the V-Load Method

The V-Load method (NSBA 1996) is a widely used approximate procedure for analyzing horizontally-curved I-girder bridges. The method assumes that the twisting of the I-girders due to the horizontal curvature is resisted by self-equilibrating sets of shears (the V-loads) located solely within the cross-frames. The V-loads are calculated using an idealized model in which the girder major-axis moments are assumed to be uniform within the unbraced lengths adjacent to a given cross-frame location and equal to the calculated moments at this location. The method assumes a linear distribution of the V-loads across the bridge cross-section; thus, the girders should have roughly the same vertical stiffness. The V-load method does not account for the general torsional flexibility of I-section members; therefore, estimation of vertical and lateral deflections using line-girder analyses supplemented by V-loads is unreliable. Also, the V-load method has no mechanism for handling general effects such as reverse curvature bending, staggered piers, and/or bracing systems located in a horizontal plane. Furthermore, line-girder analysis necessitates the use of lateral load distribution factors to determine the base loads acting on the included girders. The AASHTO (2004) factors

were developed for straight bridges without cross-frames, and therefore they tend to be less accurate for typical curved I-girder bridges. The idealizations and simplifications associated with the V-load method are such that AASHTO (2004) suggests this method should be limited to preliminary design. As the horizontal curvature of the bridge increases, and as other characteristics ignored by the method become important, the V-load approach can err substantially.

The base line-girder analysis of the V-load method accounts only for the Component 1 effects discussed in Section 3.1. Component 2 is handled only in a generalized way, via load distribution factors. The V-loads are an approximation of Component 3. Lastly, Component 4 is addressed typically by calculating the flange lateral bending moments as

$$M_\ell = \frac{ML_b^2}{NRD} \tag{3.1}$$

where M is the maximum major-axis moment within the unbraced segment, L_b is the unbraced length between the cross-frames, R is the girder radius, D is the web depth, and N is a constant taken as 10 or 12 in practice (AASHTO 2004). Eq. (3.1) can be derived by assuming a radial load on the flange equal to the approximate flange force $F = M/D$ divided by the radius of the girder, and analyzing the flange as a continuous beam on rigid intermediate supports. The assumption of symmetric boundary conditions at the cross-frames gives N = 12. For situations that deviate significantly from these idealized boundary conditions, e.g., highly nonuniform cross-frame spacing or significant skew, alternate calculations should be considered. The fact that Eq. (3.1) is based on the assumption of constant major-axis bending moment compensates to some extent for any unconservatism in the above idealizations.

3.4.3 Grid (or Grillage) Methods

Grid (or grillage) methods can provide improved accuracy relative to line girder analyses, by increasing the dimensionality of the model. However, as noted previously, there are many different types of grid methods. Options include the following:

- The use of conventional beam elements for all of the idealized grid members. The cross-sections are assumed to remain planar and only St. Venant torsion is recognized. This approach can be contrasted with the use of open-section thin-walled beam or frame elements for the I-girders, which typically include an additional nodal degrees of freedom representing the cross-section warping displacements. Also, the cross-frames may be modeled using equivalent beam elements to represent the entire cross-frame, or they can be modeled explicitly using beam and truss elements with rigid offsets for the individual cross-frame members. Conventional grid models use only three nodal degrees of freedom: the vertical displacement and the rotations within a horizontal plane. Also, these models typically locate the reference axis of all the grid elements within a single plane and neglect the section depth after determining the section properties. The flange lateral bending stresses in the physical I-girders are estimated using expressions such as Eq. (3.1), given the calculated major-axis moments. If the I-girders are modeled using open-section thin-walled beam elements, the flange lateral bending stresses are obtained directly.
- The level of refinement in the grid discretization. Conventional grid models may use either a coarse grid, where each girder and the corresponding effective width of the slab is represented by a longitudinal grid member, and the transverse actions of the cross-frames and the slab are represented by transverse grid members solely at the cross-frame locations. Alternately, a fine grid may be used in which the longitudinal and transverse actions of the slab are represented by additional beam elements

between the above coarse grid members. When open-section thin-walled beam elements are used to model the I-girders, the corresponding grid models typically use the above coarse idealization.

- Selection of a reference axis or plane and application of 2D constraints. As noted above, conventional grid models typically do not consider any displacements within the horizontal plane of the analysis model, or rotations about a normal to this plane. The reference axis of the grid members is often taken as the mid-thickness of the slab. One must be cautious when these types of models are extended by the use of open-section thin-walled beam elements for the I-girders. In particular, the warping displacements, lateral displacements, twist rotations and vertical axis rotations are generally coupled in open-section thin-walled beam elements. Therefore, application of planar grid constraints to these types of elements can lead to a significant under-prediction of certain displacements and stresses. Furthermore, curved bridges generally have non-negligible radial deflections at the slab level as well as at the centroidal depths of the I-girders. Therefore, none of these locations is particularly good for imposing the planar grid idealization. If the Engineer wishes to conduct a thermal analysis of the bridge system, inclusion of in-plane degrees of freedom is essential. Also, for bridges where significant lateral forces or displacements may be induced at the bearings, modeling of the actual height of the bearings is important. For all of the above reasons, it is recommended that grid models utilizing open-section thin-walled beam elements should include all the 3D and warping nodal degrees of freedom.
- Determination of equivalent composite cross-section properties. Several aspects of the calculated composite I-girder cross-section properties are key in general to obtaining accurate solutions using grid models. One approach that is used commonly for approximate calculation of girder cross-section properties is the one originally

proposed by Heins and Kuo (1972) and shown in Figure 3.4. This figure illustrates the transformed cross-section associated with this idealization and lists the equations for the torsional properties J and C_w. The contribution of the slab to the St. Venant torsional constant J in these equations is typically quite large compared to the contributions from the steel plates. As discussed in Section 3.3.1, the flange lateral bending stresses predicted by this model often are underestimated significantly due to web distortion effects. A factor 0.5 is suggested in AASHTO 2004 to reduce the J calculated from the Heins and Kuo equation. However, the calculation of J solely from the steel plates, neglecting the contribution of the slab, is recommended in this work. Also, the full tributary width is recommended for the slab effective width in most cases based on the studies by Chiewanichakorn (2005) and Chen et al. (2005). That is, the total width from the summation of the widths from all the longitudinal slab elements above each girder is equal to the width of the bridge deck. Furthermore, for the recommended coarse-grid approach using open-section thin-walled beam elements for the I-girders, an effective width of the transverse grid elements should be selected for modeling the transverse bending actions of the slab. A value of 0.3S is used for the effective rectangular concrete slab transverse member at the cross-frame locations in this work, based on Huang (1996), where S is the spacing between the longitudinal members. These slab elements are tied to the I-girder reference axes by rigid offsets.

Grid methods directly capture Components 1, 2 and 3 discussed previously. Component 4 is captured by the use of open-section thin-walled beam elements, or by the use of formulas such as Eq. (3.1) in conventional grid models. However, the representation of the slab using a tributary width in each of the isolated girder models (Figure 3.4) does not capture the true vertical and lateral bending stiffness of the slab. In other words, there is an incompatibility in the calculated slab displacements between the

adjacent girder models. The shear center of the girder models is typically slightly below the slab mid-thickness. However, the shear center of the bridge cross-section is above the slab. Fortunately, the slab warping deformations in the recommended 3D grid approach are relatively small. Therefore, this model can still provide accurate results.

3.4.4 General Finite Element Methods

The most realistic way to capture the slab actions and their influence on the overall response of a curved I-girder bridge is to model the slab explicitly using shell finite elements. Furthermore, the use of shell finite elements for the I-girder webs gives the most realistic representation of the effects of web distortion on the I-girder torsional responses. Conventional beam elements (6 dofs per node) can still be used quite effectively to represent the I-girder flanges, and rigid offsets can be used to tie the top-flange beam elements to the slab elements and to tie explicit beam and/or truss representations of the cross-frames to the I-girders. A number of commercial systems exist that provide these capabilities. Jung (2006) discusses the modeling details of and strength analysis results from a model of this type for the FHWA composite test bridge. A linear elastic version of this model is used in this study as a base for evaluation of the results from the various simplified methods. Obviously, this model captures all of the four component effects outlined at the beginning of this section. In the subsequent solutions, this model is referred to as the S-BS approach (Shell elements for the slab, Beam and Shell elements for the I-girders).

Generally, it is important *not* to include intermediate transverse stiffeners in the model when the above approach is used for design analysis. This is because intermediate transverse stiffeners typically are not sufficient to develop the torsional restraint from the slab under Strength loading conditions without forming plastic hinges at their tops. As a result, the restraint these elements provide against bottom flange

lateral bending may exist only partially at Strength load levels. Rather than applying torsional bracing design principles to the proportioning of the intermediate transverse stiffeners, it is better simply to neglect the elastic restraint they provide to the bottom flange within the analysis model. This ensures a conservative design of the I-girders. Bearing stiffeners and connection plates should be included in the model however. Otherwise, the results can be influenced significantly by localized distortions at the cross-frame and support locations.

There is one other approach the Engineer can use that is intermediate in refinement between grid analysis and the above general method: use of open-section thin-walled beam elements to model the I-girders, combined with shell elements for the slab, and explicit beam and truss elements for the cross-frames. This approach also can be configured to capture the full dimensionality of the bridge system, including the modeling of support elevations, by the use of rigid offsets to reference axes. At first blush, the Engineer might choose to tie the girder open-section thin-walled section beam elements to the slab nodes by a rigid offset type constraint. This model is referred to as the S-B approach (Shell elements for the slab, open-section thin-walled beam elements for the I-girders). However, this is a mistake. If the open-section thin-walled beam elements are constrained to the slab in this way, the torsional and lateral bending stiffness of the slab will over-constrain the girder twisting and bottom flange lateral bending as discussed in Section 3.3.2. This problem is similar to the issue discussed in Section 3.4.3 with respect to applying the 2D plane grid constraint to open-section thin-walled beam elements. Furthermore, although it is not possible strictly to represent web distortion effects by the kinematics of open-section thin-walled beam theory, web distortion effects can be modeled conservatively and the over-constraint of the I-girder deflections can be avoided by adopting the approach indicated in Section 3.3.2. This approach is illustrated in Figure 3.10. In this approach, the various structural

components are connected together at the centroid of the steel girder top flange. The cross-frame and I-girder elements are tied to this location by rigid offsets. Furthermore, the slab elements are tied to this location by a rigid offset, but with a rotational release in all directions at the top flange. As concluded in Section 3.3.2, this idealization maintains the full displacement compatibility of the open-section thin-walled beam model of the I-girders and the shell model of the slab at the top flange, while also allowing the I-girders to rotate freely about this location, violating the twisting compatibility between the top flange and the slab and providing a simple approximation of web distortion effects. This model is referred to subsequently as the S-BR model (Shell elements for the slab and Beam elements for the I-girders, with a rotational Release at the top flange).

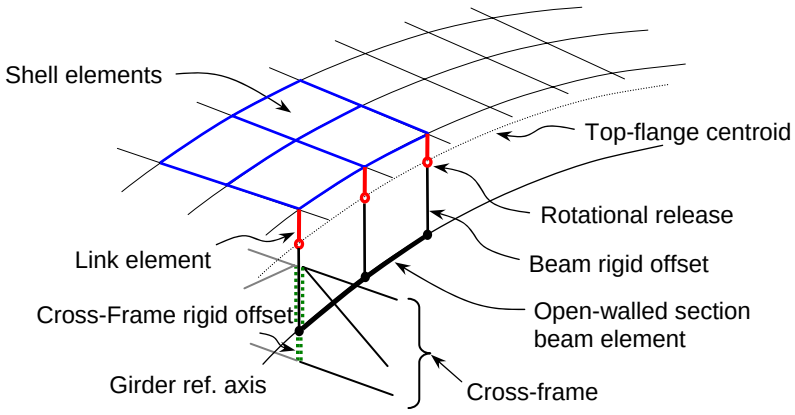

Figure 3.10 The S-BR model for a composite I-girder bridge structural system

The S-BR model can be simplified by modeling the bridge slab with a coarse grid instead of shell elements. This grid system is modeled with conventional 6-dof beam elements. This model is referred to as the B-BR model. In section 3.5, the results from the models S-BR and B-BR are compared to the S-B model (i.e., the model in which the

rigid offset constraints are applied without any rotational release. All aspects of the section depth are included in all of the above models, including the support elevations.

One additional issue that must be considered in the context of the above methods is the general inter-element compatibility within the analysis model. Caution must be used if one wishes to combine displacement-based elements that do not have compatible displacements, for instance a 3D beam element based on cubic Hermitian interpolation and a shell finite element with comparable nodal degrees of freedom but different displacement fields. Compatible displacement-based beam and shell elements are employed within the S-BS, S-BR and S-B solutions demonstrated in this work. ABAQUS (HKS 2005) is the specific analysis system employed in generating these solutions, and the specific elements used are the B31 and B31OS beam elements and the S4R shell element. These are general purpose elements degenerated from a 3D solid. The 2D- and 3D-Grid solutions are conducted in the software system developed in this research, GT-SABRE, using the rectangular section (6 dofs per node) and open-section thin-walled beam (7 dofs per node) elements developed in this research, respectively. Also, the B-BR solution is conducted in GT-SABRE. The width of the longitudinal slab elements is taken equal to the tributary width of the slab. The transverse slab elements are located only at the cross-frame locations. Their effective width is modeled as 0.3 times the girder spacing as in Huang's grillage representation.

3.5 Analysis of the FHWA Composite Test Bridge

3.5.1 Description of the Composite Test Bridge

Figure 3.11 shows the girder cross-section, bridge cross-section and plan views of the composite curved I-girder bridge recently tested at the FHWA Turner-Fairbank

Highway Research Center. The reader is referred to Jung (2006) for the detailed analysis and design of this bridge, and for assessment of the test results along with full nonlinear FEA solutions. The reader is Beshah (2006) for additional experimental data. The test bridge consists of three prismatic I-girders spaced radially at 2.67 m (8.75 ft). The measured flange and web dimensions are detailed in the figure. The radius of curvature is 63.63 m (208.75 ft) for the outside girder (G3), 60.96 m (200 ft) for the middle girder (G2) and 58.29 m (191.25 ft) for the inside girder (G1). The span of G2 is 27.43 m (90 ft) along its arc length. A709 Grade 50 steel is used for all the steel plates with the exception of the bottom flange of G3, which is HPS 70W. The steel elastic modulus E is taken as 204 GPa (29,600 ksi) (Jung 2006).

The bridge slab is a conventional 203 mm (8 in) thick cast-in-place concrete slab (average measured thickness of 205 mm (8.06 in); only a minor variation in thickness over the slab area) with 76 mm (3 in) haunches and 914 mm (3 ft) overhangs. Wood forms are used for the concrete casting, to simplify interpretation of the slab responses. The forms are attached to the I-girders by a typical strap detail, the flexibility of which precludes any significant lateral restraint of the top flanges during the slab casting operations. The average concrete cylinder strength (f_c') is 33.58 MPa (4.87 ksi) at 28 days and 33.85 MPa (4.91 ksi) at 298 days (just prior to the start of strength testing). The concrete elastic modulus for the design analysis is taken as 27,786 MPa (4,030 ksi) using the first of these values and the AASHTO (2004) equation for normal density concrete. The slab reinforcing is set approximately at the base requirements of the AASHTO (2004) empirical method. Composite action between the slab and the steel I-girders is provided by 15.2-cm x 1.9-cm (6-in x ¾-in) studs designed conservatively for fatigue using AASHTO (2004).

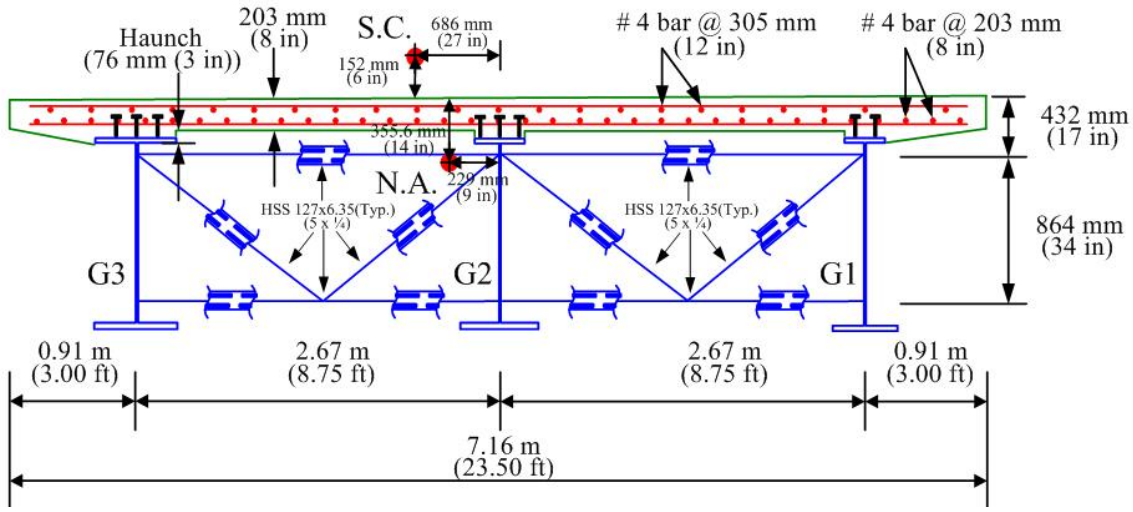

(a)

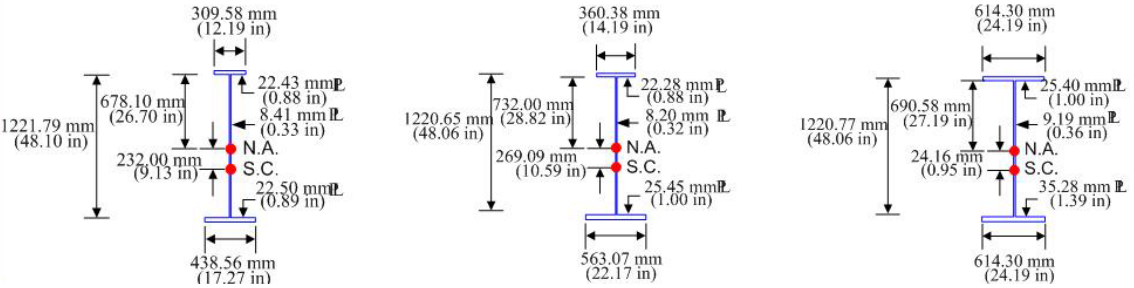

(b) **(c)** **(d)**

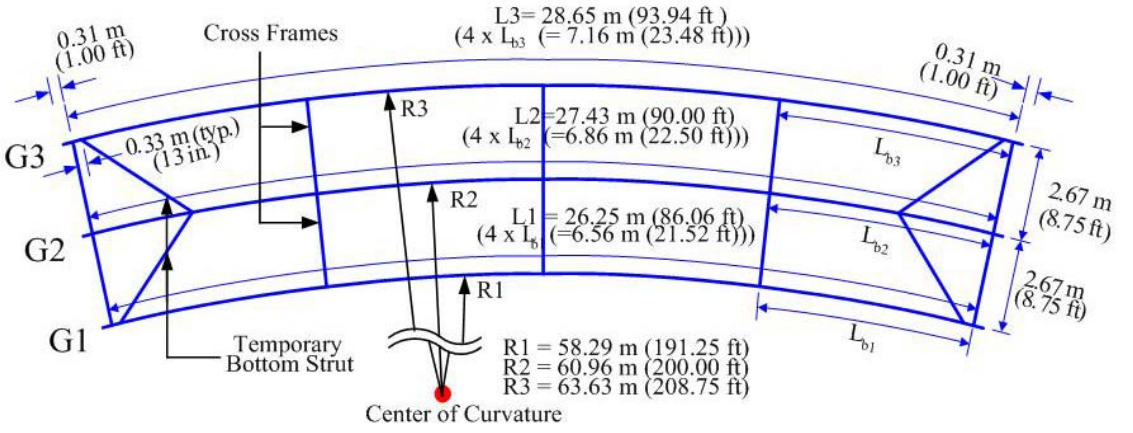

(e)

Figures 3.11 Test bridge Geometry: (a) bridge cross-section, (b) girder G1 cross-section, (c) girder G2 cross-section, (d) girder G3 cross-section, (e) plane view

The test bridge has five equally-spaced K-shaped cross-frame locations. Except as noted otherwise, the cross-frame members are 127 mm (5 in) diameter circular tubes with 6.4 mm (¼ in) wall thickness and F_y = 503 MPa.(73 ksi). They are connected to the K-joint and the girder connection plates by double gussets. These members have the same axial stiffness as more typical cross-frame members. Tubes are used within the test bridge to facilitate measurement of internal forces. The cross-frame members are sized to remain below their proportional limit throughout the development of the ultimate strength of the composite bridge. For ultimate strength testing, the diagonals between G2 and G3 at the mid- and quarter-span locations are reinforced by splitting and welding 6 in x ¼ in tubes around the outside of the 127 mm (5 in) tubes. Also, the bottom chord of these cross-frames is reinforced in the same fashion between the connection to G3 and the K joint. This variation in the cross-frame member areas has little to no influence on the displacements and distribution of forces within the bridge system. In this study, the cross-frame properties at the time of the strength test are used in all the calculations.

Key characteristics of the test bridge pertinent to this study are: (1) There are only three internal cross-frame locations, resulting in a subtended angle between the cross-frames of L_b/R = 0.1125 (or 6.45^o). (2) The slenderness ratio of the I-girder webs (D/t_w) ranges from 133 to 149. Also, a relatively wide stiffener spacing is used within the girders, ranging from $d_o \cong D$ close to the ends of G3 (with the exception of the end panels, which are designed to anchor the shear tension field), to $d_o \cong 2.4D$ close to the ends of G1 and $d_o \cong 3D$ near the midspan of all three girders. (3) All the girders are designed close to various maximum limits of the AASHTO (2004) Specifications. (4) The radii of the girders are reasonably close to the AASHTO (2003) minimum R of 30.5 m (100 ft). These characteristics accentuate a number of the important 3D responses of

the structure, and thus make the test bridge ideal for evaluating the capabilities of different analysis methods.

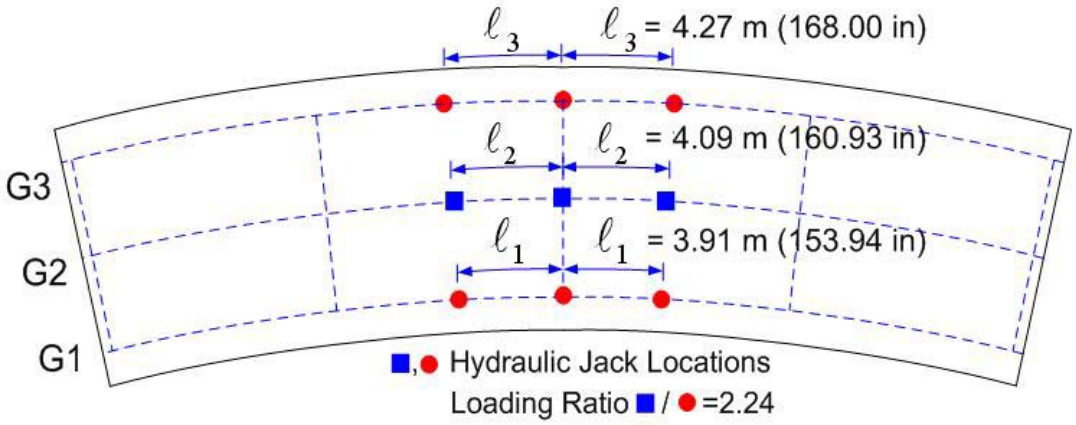

Figure 3.12 Test bridge loading condition

3.5.2 Analysis Results

Tables 3.3 through 3.9 summarize the results from various linear analyses of the composite test bridge for the loading shown in Figure 3.12. Figure 3.12 shows the specific laboratory loadings, which are approximately equivalent to two lane loads plus two design vehicles placed at the middle of the bridge for maximum flexural effect on G3. The experimental data shows that the bridge still behaves in a linear elastic fashion when the total applied load reaches load level A (Jung 2006), which is equal to the total factored AASHTO design live load (2,415 kN (543 kips), two trucks + two lanes, dynamic allowance factor of 1.33 on trucks, load factor of 1.75, multiple presence factor of 1.0). In Tables 3.3 through 3.9, quantities with differences relative to the S-BS model larger than 15 % are shown in bold.

Table 3.3 Sum of girder end reactions (kN (kips))

Model	**G2**	% error[1]	**G3**	% error
S-BS	699.30 (157.21)		1,529.57 (343.86)	
Experimental	685.03 (154.00)	-2.0%	1,570.22 (353.00)	2.7%
S-B	681.25 (153.15)	-2.6%	1,538.64 (345.90)	0.6%
S-BR	692.72 (155.73)	-0.9%	1,532.90 (344.61)	0.2%
B-BR	706.14 (158.75)	1.0 %	1,525.70 (342.99)	-0.3%
V-Load Method	**1,276.55 (286.98)**	**82.5%**	**1,199.46 (269.65)**	**-21.6%**
2D-Grid Conv.	667.72 (150.11)	-4.5%	1,551.90 (348.88)	1.5%
2D-Grid w/ J_1[2]	726.97 (163.43)	4.0%	1,516.31 (340.88)	-0.9%
2D-Grid w/ J_2[3]	721.46 (162.19)	3.2%	1,519.07 (341.50)	-0.7%
2D-Grid w/ J_3 - 1[4]	713.58 (160.42)	2.0%	1,523.03 (342.39)	-0.4%
2D-Grid w/ J_3 - 2[5]	662.56 (148.95)	-5.3%	1,548.32 (348.12)	1.2%
3D-Grid w/ J_1	729.24 (163.94)	4.3%	1,515.20 (340.63)	-0.9%
3D-Grid w/ J_2	723.41 (162.63)	3.4%	1,518.09 (341.28)	-0.8%
3D-Grid w/ J_3	700.68 (157.52)	0.2%	1,529.48 (343.84)	0.0%

[1] Percentage error relative to the S-BS model

[2] J_1: St. Venant torsion constant specified by Heins and Kuo (1972)

[3] J_2: St. Venant torsion constant is equal to a half of J_1

[4] J_3-1: St. Venant torsion constant determined solely from the I-girder steel plates, reference plane at the average of the centroids of composite girders

[5] J_3-2: St. Venant torsion constant determined solely from the I-girder steel plates, reference plane at the mid-thickness of the slab

Table 3.4 Midspan vertical deflection (cm (in)) at the outside tip of the bottom flange (positive downward)

Model	**G2**	% error[(1)]	**G3**	% error
S-BS	8.28 (3.26)		11.46 (4.51)	
Experimental	8.48 (3.34)	2.0%	12.17 (4.79)	6.2%
S-B	7.49 (2.95)	-9.5%	10.26 (4.04)	-10.5%
S-BR	8.00 (3.15)	-3.4%	11.02 (4.34)	-3.7%
B-BR	7.83 (3.08)	-5.4%	10.87 (4.28)	-5.1%
V-Load Method	---		---	
2D-Grid Conv.	**5.23 (2.06)**	**-36.7%**	**7.29 (2.87)**	**-36.4%**
2D-Grid w/ J_1[(2)]	7.70 (3.03)	-7.1%	10.67 (4.20)	-6.9%
2D-Grid w/ J_2[(3)]	7.87 (3.10)	-5.0%	11.13 (4.38)	-2.9%
2D-Grid w/ J_3 - 1[(4)]	8.10 (3.19)	-2.2%	11.73 (4.62)	2.4%
2D-Grid w/ J_3 - 2[(5)]	**5.69 (2.24)**	**-31.2%**	**7.98 (3.14)**	**-30.4%**
3D-Grid w/ J_1	7.80 (3.07)	-6.0%	10.82 (4.26)	-5.6%
3D-Grid w/ J_2	7.98 (3.14)	-3.9%	11.28 (4.44)	-1.5%
3D-Grid w/ J_3	8.15 (3.21)	-1.6%	11.79 (4.64)	2.8%

(1) Percentage error relative to the S-BS model

(2) J_1: St. Venant torsion constant specified by Heins and Kuo (1972)

(3) J_2: St. Venant torsion constant is equal to a half of J_1

(4) J_3-1: St. Venant torsion constant determined solely from the I-girder steel plates, reference plane at the average of the centroids of composite girders

(5) J_3-2: St. Venant torsion constant determined solely from the I-girder steel plates, reference plane at the mid-thickness of the slab

Table 3.5 Midspan radial deflection (cm (in)) at the slab mid-thickness (positive toward center of curvature)

Model	G2	G3
S-BS	0.168 (0.066)	0.163 (0.064)
Experimental	---	0.150 (0.059)
S-B	0.150 (0.059)	0.142 (0.056)
S-BR	0.178 (0.070)	0.170 (0.067)
B-BR	0.221 (0.087)	0.224 (0.088)
V-Load Method	---	---
2D-Grid Conv.	0.00	0.00
2D-Grid w/ J_1[(2)]	-0.018 (-0.007)	-0.056 (-0.022)
2D-Grid w/ J_2[(3)]	-0.020 (-0.008)	-0.061 (-0.024)
2D-Grid w/ J_3 - 1[(4)]	-0.023 (-0.009)	-0.069 (-0.027)
2D-Grid w/ J_3 - 2[(5)]	0.00	0.00
3D-Grid w/ J_1	0.076 (0.030)	0.025 (0.010)
3D-Grid w/ J_2	0.076 (0.030)	0.018 (0.007)
3D-Grid w/ J_3	0.333 (0.131)	0.315 (0.124)

(2) J_1: St. Venant torsion constant specified by Heins and Kuo (1972)

(3) J_2: St. Venant torsion constant is equal to a half of J_1

(4) J_3-1: St. Venant torsion constant determined solely from the I-girder steel plates, reference plane at the average of the centroids of composite girders

(5) J_3-2: St. Venant torsion constant determined solely from the I-girder steel plates, reference plane at the mid-thickness of the slab

Table 3.6 Midspan radial deflection (cm (in)) at bottom flange (positive toward center of curvature)

Model	**G2**	% error[(1)]	**G3**	% error
S-BS	2.26 (0.89)		2.39 (0.94)	
Experimental	2.26 (0.89)	0.0%	2.41 (0.95)	1.1%
S-B	**1.85 (0.73)**	**-18.1%**	**1.93 (0.76)**	**-19.2%**
S-BR	2.21 (0.87)	-3.1%	2.29 (0.90)	-3.5%
B-BR	2.35 (0.92)	3.8 %	2.35 (0.93)	-1.5%
V-Load Method	---		---	
2D-Grid Conv.	**1.12 (0.44)**	**-51.0%**	**1.65 (0.65)**	**-30.6%**
2D-Grid w/ J_1[(2)]	**1.32 (0.52)**	**-41.5%**	**1.37 (0.54)**	**-42.1%**
2D-Grid w/ J_2[(3)]	**1.45 (0.57)**	**-36.2%**	**1.50 (0.59)**	**-36.7%**
2D-Grid w/ J_3 - 1[(4)]	**1.60 (0.63)**	**-29.3%**	**1.68 (0.66)**	**-29.9%**
2D-Grid w/ J_3 - 2 [(5)]	**1.47 (0.58)**	**-35.2%**	**1.55 (0.61)**	**-34.5%**
3D-Grid w/ J_1	**1.45 (0.57)**	**-36.7%**	**1.50 (0.59)**	**-37.5%**
3D-Grid w/ J_2	**1.55 (0.61)**	**-31.2%**	**1.63 (0.64)**	**-32.0%**
3D-Grid w/ J_3	2.49 (0.98)	10.2%	2.59 (1.02)	9.2%

[(1)] The values in parenthesis () are the percentage error relative to the S-BS model

[(2)] J_1: St. Venant torsion constant specified by Heins and Kuo (1972)

[(3)] J_2: St. Venant torsion constant is equal to a half of J_1

[(4)] J_3-1: St. Venant torsion constant determined solely from the I-girder steel plates, reference plane at the average of the centroids of composite girders

[(5)] J_3-2: St. Venant torsion constant determined solely from the I-girder steel plates, reference plane at the mid-thickness of the slab

Table 3.7 Maximum bottom flange major-axis bending stress (MPa (ksi))

Model	**G2**	% error[1]	**G3**	% error
S-BS	167.4 (24.28) [165.5 (24.00)] [6]		215.2 (31.21) [213.1 (30.90)]	
Experimental	[177.2 (25.70)]	7.1%	[223.7 (32.45)]	5.0%
S-B	170.2 (24.69)	1.7%	208.6 (30.25)	-3.1%
S-BR	164.9 (23.92)	-1.5%	217.2 (31.50)	0.9%
B-BR	170.5 (24.74)	1.9%	219.9 (31.90)	2.2%
V-Load Method	**284.1 (41.20)**	**69.5%**	199.9 (29.00)	-7.1%
2D-Grid Conv.	162.7 (23.60)	-2.7%	199.9 (29.00)	-7.1%
2D-Grid w/ J_1[2]	166.4 (24.14)	-0.6%	225.5 (32.71)	4.8%
2D-Grid w/ J_2[3]	165.3 (23.97)	-1.3%	231.9 (33.64)	7.8%
2D-Grid w/ J_3 - 1[4]	163.8 (23.75)	-2.2%	240.4 (34.86)	11.7%
2D-Grid w/ J_3 - 2 [5]	156.0 (22.63)	-6.8%	218.2 (31.65)	1.4%
3D-Grid w/ J_1	165.5 (24.00)	-1.1%	226.4 (32.83)	5.2%
3D-Grid w/ J_2	164.2 (23.82)	-1.9%	232.9 (33.78)	8.2%
3D-Grid w/ J_3	161.6 (23.44)	-3.4%	217.5 (31.54)	1.0%

[1] The values in parenthesis () are the percentage error relative to the S-BS model

[2] J_1: St. Venant torsion constant specified by Heins and Kuo (1972)

[3] J_2: St. Venant torsion constant is equal to a half of J_1

[4] J_3-1: St. Venant torsion constant determined solely from the I-girder steel plates, reference plane at the average of the centroids of composite girders

[5] J_3-2: St. Venant torsion constant determined solely from the I-girder steel plates, reference plane at the mid-thickness of the slab

[6] The stresses shown in square brackets [] are taken at the same location as in experiment

Table 3.8 Maximum bottom flange lateral bending stress (MPa (ksi))

Model	**G2**	% error[1]	**G3**	% error
S-BS	119.1 (17.28) [84.8 (12.3)][6]		135.0 (19.58) [95.8 (13.9)]	
Experimental	[77.9 (11.3)]	-8.1%	[79.3 (11.5)]	-17.3%
S-B	**13.9 (2.02)**	**-88.3 %**	**34.6 (5.02)**	**-74.4 %**
S-BR	119.4 (17.32)	0.3 %	136.0 (19.72)	0.7%
B-BR	124.1 (18.00)	4.2 %	134.7 (19.53)	-0.3 %
V-Load Method	**269.6 [7] (39.10)**	**126.0%**	**169.6 (24.60)**	**25.5%**
2D-Grid Conv.	**160.6 [7] (23.30)**	**34.8%**	**178.6 (25.90)**	**32.1%**
2D-Grid w/ J_1[2]	**77.8 (11.28)**	**-34.7%**	**103.9 (**15.07**)**	**-23.0%**
2D-Grid w/ J_2[3]	**98.2 (14.24)**	**-17.6%**	122.0 (17.70)	-9.6%
2D-Grid w/ J_3 - 1[4]	132.2 (19.17)	10.9%	147.0 (21.32)	8.6%
2D-Grid w/ J_3 - 2 [5]	129.8 (18.82)	8.9%	154.9 (22.46)	14.7%
3D-Grid w/ J_1	**78.9 (11.44)**	**-33.8%**	**103.6 (15.03)**	**-23.3%**
3D-Grid w/ J_2	**99.4 (14.41)**	**-16.6%**	121.8 (17.66)	-9.8%
3D-Grid w/ J_3	133.4 (19.35)	12.0%	149.7 (21.71)	10.9%

[1] The values in parenthesis () are the percentage error relative to the S-BS model

[2] J_1: St. Venant torsion constant specified by Heins and Kuo (1972)

[3] J_2: St. Venant torsion constant is equal to a half of J_1

[4] J_3-1: St. Venant torsion constant determined solely from the I-girder steel plates, reference plane at the average of the centroids of composite girders

[5] J_3-2: St. Venant torsion constant determined solely from the I-girder steel plates, reference plane at the mid-thickness of the slab

[6] The stresses shown in bracket [] are taken at the same location as in experiment

[7] Based on Eq. (3.1) with N = 12

Table 3.9 Cross-frame forces, midspan between G2 and G3 (kN (kips))

Model	**Bottom Chord Compression**	% error[1]	**Shear Force**	% error
S-BS	705.44 (158.59)		311.91 (70.12)	
Experimental	695.26 (156.30)	-1.4 %	274.01 (61.60)	-12.2%
S-B	**385.35 (86.63)**	**-45.4%**	**126.06 (28.34)**	**-59.6%**
S-BR	**860.60 (193.47)**	**22.0%**	357.68 (80.41)	14.7%
B-BR	781.37 (175.66)	10.8%	355.74 (79.97)	14.1%
V-Load Method	**662.34 (148.90)** [8]	**-34.7%**	280.24 (63.00)	-9.6%
2D-Grid Conv.	**259.78 (58.40)**	**-63.2%**	**88.52 (19.90)**	**-71.6%**
2D-Grid w/ J_1[2]	691.03 (155.35)	-2.0%	318.00 (71.49)	2.0%
2D-Grid w/ J_2[3]	739.47 (166.24)	4.8%	335.89 (75.51)	7.7%
2D-Grid w/ J_3 - 1[4]	799.92 (179.83)	13.4%	358.17 (80.52)	14.8%
2D-Grid w/ J_3 - 2 [5]	**816.78 (183.62)**	**15.8%**	**366.53 (82.40)**	**17.5%**
3D-Grid w/ J_1	692.45 (155.67)	-1.8%	316.40 (71.13)	1.4%
3D-Grid w/ J_2	742.01 (166.81)	5.2%	334.42 (75.18)	7.2%
3D-Grid w/ J_3	807.89 (181.62)	14.5%	359.24 (80.76)	15.2%

[1] The values in parenthesis () are the percentage error relative to the S-BS model

[2] J_1: St. Venant torsion constant specified by Heins and Kuo (1972)

[3] J_2: St. Venant torsion constant is equal to a half of J_1

[4] J_3-1: St. Venant torsion constant determined solely from the I-girder steel plates, reference plane at the average of the centroids of composite girders

[5] J_3-2: St. Venant torsion constant determined solely from the I-girder steel plates, reference plane at the mid-thickness of the slab

[8] Top chord force assumed located at slab mid-thickness

The analysis strategies considered in Tables 3.3 through 3.9 are the S-BS, S-B, S-BR and B-BR models, line-girder analyses combined with the V-load method, a fine (5x21) conventional 2D-grid analysis (2D-Grid Conv.), four versions of a coarse (3x5) 2D-grid analysis using open-section thin-walled beam elements for the I-girders, and three versions of the recommended coarse (3x5) 3D-grid analysis method.

The latter 2D- and 3D-grid models differ in the St. Venant torsional constant for the I-girder cross-sections and the selected reference plane. The first version uses the J formula specified originally by Heins and Kuo (1972), denoted by the symbol J_1. The second version uses only a half of J_1, which is suggested by AASHTO 2004 and is denoted by the symbol J_2. The third version uses only the I-girder steel plates (neglecting any contribution from the slab) for the calculation of J. This is denoted by the symbol J_3. In addition, for the 2D-grid models with the use of J_3, the influence of different reference planes (different elevations where the horizontal displacements are taken equal to zero) is investigated.

The conventional 2D-grid solution uses the same cross-section property idealizations as in the Barker and Puckett (1997) straight-bridge examples, except that the cross-frame members are modeled explicitly and are tied to the reference axes at the slab mid-thickness by rigid offsets. In fact, the cross-frame members are modeled explicitly in all the solutions shown in Table 3.3. Truss elements with rigid offsets are employed for the cross-frame members with the exception of the bottom chords, where beam elements are employed such that the K-joints have a stiffness in the longitudinal direction. The conventional grid model represents the slab by one additional longitudinal element between each of the I-girders and by four additional transverse elements between the cross-frames. The width of the transverse elements is taken as the tributary length along an arc at the mid-distance between the I-girders. The 2D-grid solutions that utilize open-section thin-walled beam elements for the I-girders use a reference axis at

the average centroidal depth of the composite girders. The deflections within and the rotation about the normal to a horizontal plane are constrained at this level. These models use the coarse grid idealization described previously, i.e., a longitudinal grid member is positioned at each of the I-girders and a transverse slab member of width 0.3S with a rigid offset to the reference axes plus the above cross-frame idealization is placed at the cross-frame locations.

As discussed previously, the 3D-grid solutions do not use any planar grid constraints. Also, as mentioned in Section 2.5.3, to correctly account for the torsional behavior of a singly-symmetric I-section member, the longitudinal reference axis needs to be the shear center line along the element length. In this study, although the slab mid-thickness is defined as the reference axis in the model input file, GT-SABRE will automatically transfer the user defined longitudinal reference axis to the shear center line along the element length. As a result, the 3D-grid solutions are independent of the choice of reference axis. The elevation of the transverse slab elements in these models is the same as the physical elevation of the slab.

Generally, the S-BS model provides the most accurate representation of the experimental responses. The match between the S-BS solution and the experimental results is reasonably good for all the responses shown in the Tables. Therefore, the S-BS model is taken as the base solution for evaluation of the different approaches considered in this study. The S-B model gives a reasonable fit to the S-BS results except that it dramatically underestimates the bottom flange lateral bending stresses and the cross-frame forces. The B-BR model, which is adopted in the following Chapters for curved steel I-girder bridge analyses, and S-BR model give significantly better results. except that the S-BR model overestimates the cross-frame forces somewhat. The V-Load method dramatically overestimates the reactions and major-axis bending stresses on G2 while it underestimates these responses on G3. Eq. (3.1) gives moderately

conservative flange lateral bending results for G3 and substantially conservative results for G2.

In Table 3.5, the midspan radial deflection at the slab mid-thickness tends toward the center of curvature in the S-BS model. However, in the 2D-grid model with the reference plane at the average centroid of the three composite girders, the slab deflects away from the center of curvature. Therefore, locating the reference plane at the slab mid-thickness is recommended for 2D-grid models. The conventional 2D-Grid model significantly underestimates the bottom flange vertical and radial displacements as well as the cross-frame forces. However, it gives a good prediction of the reactions and the major-axis bending stresses. The use of J_3 leads to similar or improved predictions in the coarse 2D- and 3D-Grid models relative to the use of J_1 and J_2, except that the major-axis bending stresses and the cross-frame forces are slightly less accurate based on J_3. The 3D-Grid model based on J_3 gives the best overall results of the Grid models.

CHAPTER 4

CONSTRUCTION SIMULATION METHODOLOGY

This chapter discusses prototype capabilities for calculation of the construction requirements, the structural responses during construction, and the final dead load state (stresses, deflections, forces and reactions) in general curved steel I-girder bridges. Emphasis is placed on the fundamental requirements for correctness of the calculations. The primary design-analysis capabilities, which have been implemented in GT-SABRE (Chang 2006), are based on beam theory idealizations. Steel detailing practices are addressed in Section 4.1. Section 4.2 discusses the concepts and conditions for uniqueness of the analysis results. The specific construction simulation capabilities implemented in this research are summarized in Section 4.3.

4.1 Steel Detailing Practices

Steel I-girders are practically always fabricated with a vertical camber to compensate for their vertical dead load deflections. Furthermore, in straight skewed bridges and in horizontally curved bridges with or without skewed supports, the torsional rotations of the I-girders may or may not be compensated for in the fabrication of the structural steel. The simplest practice is to fabricate the I-girders such that their webs are vertical or plumb when they are fully-supported (i.e., blocked) in their no-load geometry. Also, the simplest practice is to fabricate the cross-frames such that they fit-up with the cambered no-load geometry of the I-girders without inducing any deformations and internal stresses due to lack-of-fit. This type of detailing is referred to in this work as *No-Load Fit* or *NLF*. In this case, the final constructed state under the steel dead loads can

be analyzed simply by building a model in the idealized no-load geometry and then "turning on" the steel dead loads.

Bridges that are detailed for no-load fit necessarily have out-of-plumb webs in their steel or total dead load conditions, due to the torsional rotations of the structure under these loadings. Also, the final in-plan dead-load position of the slab is deflected from the ideal no-load geometry, and dead load rotations occur that must be accommodated at the bridge bearings. As long as these deflections do not influence the performance in any significant way, NLF detailing is generally the preferred approach. However, in structures where these deviations from the ideal geometry are larger than acceptable tolerances, other options must be considered. In the context of the AASHTO (2004) elastic analysis and design procedures, the only strength performance consideration in setting the above tolerances, for bridges detailed for *NLF*, is whether a second-order elastic analysis should be conducted to determine the dead load stresses. All of the relevant strength issues are addressed within the AASHTO (2004) resistance equations as long as the computed second-order elastic stresses are sufficiently accurate. In many cases, the second-order elastic amplification of the bridge dead load responses is small. In these situations, a first-order analysis for the steel dead load, using a model of the complete structure, and simply "turning on" the load, followed by a first-order analysis of the structure accounting for any effects of staged slab construction and satisfying the AASHTO (2004) requirements for modeling of the concrete, results in an accurate design for the dead load effects. Unfortunately, rigorous guidelines for when first-order analysis is not sufficient do not exist.

Incidentally, the detailing of I-girder bridges for NLF requires that either all the girder connection plates (option 1), or all the cross-frames (option 2) must be detailed differently. For the first option as shown in Figure 4.1, the bolt holes in the connection plates must be at different distances from the flanges. For the second option as shown in

Figure 4.2, the cross-frames must be detailed to account for the different cambers. These differences also occur due to superelevation, and therefore their handling does not present any special problem. AASHTO/NSBA (2006) indicates that option 2 is preferred, since this allows the connection plates to be stack drilled or multiple punched, and since the changes in the geometry of the cross-frames to account for the differences in the connection elevations can be handled easily by moving one side of a jig. These suggestions are in the context of one-piece shop-welded X or K type cross-frames, which are recommended over multiple-piece knocked-down cross-frames.

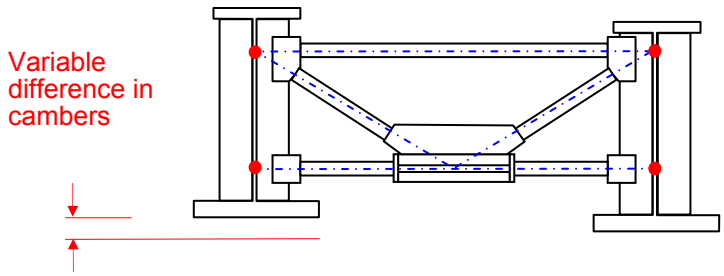

Figure 4.1 NLF option 1 – all the connection plates are detailed differently

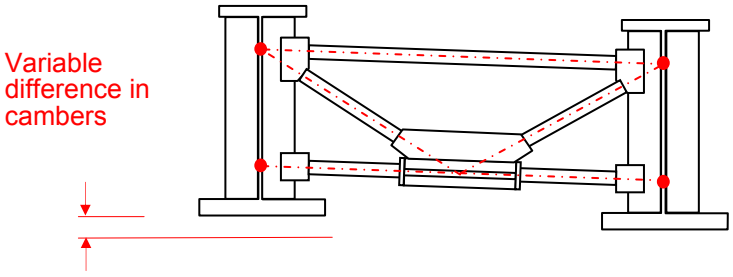

Figure 4.2 NLF option 2 – all the cross-frames are detailed differently

In cases where displacements other than the vertical deflections must be compensated for, a common practice is to detail the cross-frames to fit-up with the I-girders in their idealized web-plumb but vertically deflected positions under either the steel dead load only or under the total dead load. These detailing practices are referred to in this research as *Steel Dead Load Fit (SDLF)* and *Total Dead Load Fit (TDLF)*. SDLF allows the erector to target a web plumb condition at the end of the steel erection. However, achieving a perfectly plumb web condition is obviously an unnecessary requirement. Also, since TDLF targets a web plumb condition in the final state of the structure, implying a shared responsibility among the steel erector and the concrete contractor, its practical implementation can be problematic.

Under SDLF or TDLF detailing, the cross-frames do not fit-up with the I-girders in the ideal zero-stress condition of the structure (see Figure 4.3). As shown in Figure 4.4, the girders must be twisted (i.e., their flanges must be pushed and/or pulled radially, thus changing their radius of curvature) to connect the cross-frames in the idealized no-load position. This lack-of-fit in the no-load geometry, and the resistance of the flanges to changes in their radii, induces additional "locked-in" stresses throughout the structure and influences the vertical, horizontal and twist deflections of the system. AASHTO (2004) states that the Engineer may need to consider these lack-of-fit stresses in the girder flanges or the cross-frames or diaphragms, but that the decision as to when these stresses should be evaluated is currently a matter of engineering judgment. As noted previously, the AASHTO (2004) resistance equations generally provide a sufficient strength assessment as long as the second-order elastic stresses are accurately calculated. With SDLF and TDLF detailing, these stresses should include the influence of the lack of fit when the lack-of-fit stresses are a significant fraction of the total stresses. However, any potential definition of what fraction is significant (or non-incidental) should consider the beneficial inelastic redistribution that occurs under

incidental overloads, deviation from support elevation tolerances, etc. in all types of steel bridge structures. These attributes are factors in the development of the AASHTO provisions for elastic analysis and design. The above types of incidental stresses are not included in the elastic analysis and design calculations other types of steel bridges.

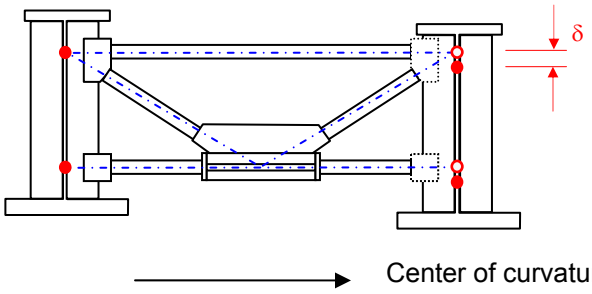

Figure 4.3 SDLF or TDLF concept 1 – lack of fit between girders and cross-frames in no-load geometry

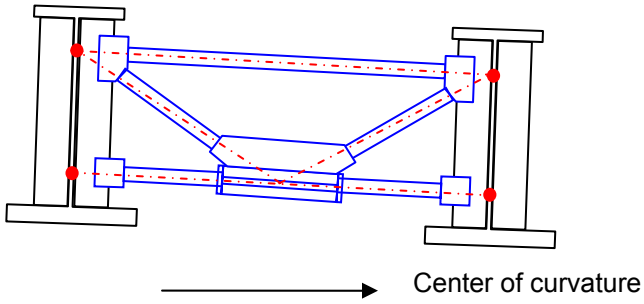

Figure 4.4 SDLF or TDLF concept 2 –forcing/twisting of the girders into position to connect the cross-frames

AASHTO (2004) describes one other method of steel detailing, but points out that it has limited use since it is generally more costly. In this method, referred to here as

Twist Camber Fit or *TCF*, the girder top and bottom flanges are fabricated with a different radius of curvature to compensate for the twist rotations under the steel or the total dead load, in addition to cambering to offset the vertical deflections. It is anticipated that the flanges are then twisted and welded to the girder webs such that the girder webs are flat and perpendicular to the flanges within each of the cross-section profiles. Correspondingly, the cross-frames are detailed to fit to the ideal twist cambered geometry without inducing any lack-of-fit stresses in the structure.

4.2 Conditions for Uniqueness of the Analysis Results

Another key to addressing construction simulation for curved steel I-girder bridges is an understanding of when the analysis solutions are unique, or in other words, when the analysis results are independent of the order of the component assembly or load application. Basically, the conditions for uniqueness of the analysis can be stated as follows. The solution for the displacements, internal stresses, and reactions is unique for any sequence of assembly and/or loading when:

1) The no-load geometry of the structural components is the same for any sequence,
2) The connections are made ideally with zero tolerance,
3) The structure is maintained in an elastic condition, and
4) The final displacement boundary conditions at the supports are independent of the sequence.

The first three conditions are essential for simplifying the consideration of connection assembly procedures. Otherwise, the details of how even a minor joint is bolted up must be accounted for in determining the state of the structure. All four conditions are also essential for allowing the Engineer to use a model of the complete structure to analyze for the final responses in certain cases without the need to consider

the erection sequence. For example, the final response of the structure under steel dead load only, or under total dead load when the slab is cast in one continuous stage.

Under the above four conditions, the bridge model is a conservative elastic system. The second-order elastic deflections, stresses and reactions are independent of the sequence of the assembly and/or loading. Obviously, if a slab is cast in successive stages, the hypothetical no-load geometry of the various portions of the slab depends on the slab casting sequence. Each stage of the slab is typically assumed to harden into its no-load geometry in the current deformed configuration at the time of the casting. Each stage of the slab is instantiated on the current deformed geometry of the structure.

It appears that in the use of a number of commercial programs in current practice, Engineers typically instantiate new steel elements on the deformed geometry of the structure. This leads to a false dependency of the solution on the steel erection sequence. All of the steel components must be defined in their original no-load geometry to obtain a correct analysis result. This geometry must then be subjected to its own self weight (where the self-weight deflections and/or stresses are significant) and assembled into the current deformed geometry of the loaded partially completed structure to determine the construction requirements (e.g., crane forces, temporary tower reactions, come-along forces, etc.) accurately. One should note that if SDLF or TDLF detailing is employed, the analysis solution for the steel dead load is still unique once the specifics of the detailing and the resulting lack-of-fit in the idealized no-load geometry are defined.

The second of the above conditions relates to an important general consideration in controlling the erected geometry of curved bridges. Oversize or slotted holes should be used rarely (if ever) to facilitate the erection of the structure. Use of this practice introduces a variable that may be difficult to control in achieving the desired final geometry.

The fourth condition relates to factors such as simple support conditions that are subsequently made continuous, or cases where a constraint is introduced along a certain degree of freedom at a support such that the final support displacement boundary conditions are a function of the construction sequence.

4.3 Specific GT-SABRE Capabilities for Construction Simulation

Given a fundamental understanding of the above detailing practices and the conditions for uniqueness of the structural analysis, it is possible to focus on a meaningful discussion of desirable capabilities for simulating curved I-girder bridge construction. Important construction simulation capabilities implemented in this work are discussed in the following sections.

4.3.1 Modeling of Open-Section Thin-Walled Members, Tracking and Displaying of the 3D Deformed Geometry

The primary focus of this research is on the use of open-section thin-walled beam theory for modeling of the I-girders. The cross-frames or diaphragms are modeled with truss and/or beam elements. Rigid offset connections are implemented between the ends of the cross-frame elements and the corresponding girder nodal positions, and between the girder nodal positions and bearing elevations. The solutions from the resulting grillage models are compared to those of more rigorous models using shell finite elements for the slab and the girder webs. The visualization of the 3D deformed geometry is essential regardless of the underlying analysis approach. GT-SABRE draws the deformed geometry of the I-girder components, including the warping of the flanges, using a surface rendering of the flange and web plates.

4.3.2 Precise Definition and Modeling of the No-Load Geometry

In this work, the vertically curved and/or cambered girder geometries are defined by curve fitting between specified locations using a combined Bezier and B-spline approach. Also, it is assumed that the finite connection tolerances between the cross-frames and the girders, between the two girders at splice locations, and between the girders and their supports have a negligible influence on the bridge responses. Girder vertical curves are defined generally to handle changes in grade and superelevation along the bridge. Girder vertical cambers are defined to compensate for expected (predicted) vertical displacements in the structural system.

The Bezier and B-spine formulations are two methods for representing curves. A Bezier curve is defined by four control points and blending (basis) functions, which are cubic polynomial functions. That is, each point on the curve is determined by scaling each control point by the corresponding blending function using the following equation:

$$\mathbf{Q}(u) = \mathbf{P}_0\,(1-u)^3 + \mathbf{P}_1\,3u(1-u)^2 + \mathbf{P}_2\,3u^2(1-u) + \mathbf{P}_3\,u^3 = \sum_{i=0}^{3} \mathbf{P}_i\,\mathrm{B}_i(u) \qquad (4.1)$$

in which $0 \le u \le 1$ (Watt 2000). The curve passes through its first and last control points $\mathbf{P}_0$ and $\mathbf{P}_3$ when u is equal to 0 and 1, respectively. The vector $\overrightarrow{\mathbf{P}_0\mathbf{P}_1}$ and $\overrightarrow{\mathbf{P}_2\mathbf{P}_3}$ are the tangent vectors of the curve at the end points. Therefore, when joining two Bezier curves, the first order continuity C^1 (tangential continuity) is achieved if the slope of each curve at the connecting point is the same. A composite Bezier curve description can be constructed by adding one curve segment at a time with this condition. However, changing one of the control points influences only the part of the curve closest to it. This property is called localness. In other words, there is no relationship that extends through all the curve segments.

The B-spline approach conquers the above problem. B-spline curves have the property of non-localness. That is, in addition to influencing the part of the curve close to a control point, changing a control point also has some effects on the entire curve. This is because a B-spline curve achieves positional, first derivative (C^1) and second derivative (C^2) continuity (curvature continuity) due to the fact that the blending functions are themselves C^2 piecewise polynomials. The non-localness property can be useful in obtaining a smooth representation of the overall geometry. However, the B-spline curve does not pass through any of its control points unless a control point is repeated three times. Triplicating a control point makes the curve non-smooth at the control point point (Watt 2000).

To fit the camber design, a curve must at least pass through all the specified camber values. Typically, girder cambers are specified at an interval such as 1/10 of the span length. More generally, it is desired to fit a curve through the precise girder no-load geometry due to the vertical curve plus the vertical camber. In this work, it is assumed that this vertical position of the girders is determined and specified at an interval such as 1/10 of the span length. A curve is fit through these vertical positions that has both the positive characteristic of the Bezier curve approach in fitting exactly through the specified positions as well as non-localness property associated with the B-spline approach. This is achieved by:

1. Using a Bezier curve description between each of the above specified vertical positions, and
2. Using the B-spline approach to enforce C^1 and C^2 continuity between these Bezier curve descriptions. The locations of the interior control points $\mathbf{P}_1$ and $\mathbf{P}_2$ in Eq. (4.1) are detemined for each of the Bezier curve segments based this continuity requirement plus some special handling of the end segments discussed below.

This approach results in a smooth curve through all the specified vertical positions.

In the above approach, the tangent vector at the end points and at the two interior control points of each Bezier curve segment need to be defined or calculated. Based on the constraint of C^2 continuity, the tangent vectors at all the end points (i.e., the locations where the vertical positions are specified) are related to each other. Only the tangent vectors at the end points of the entire curve need to be specified. The other tangent vectors can be solved for based on the specified points at the ends of the Bezier curve segments and the specified tangent vectors at the end points of the entire curve. The algorithm for determining the tangent vectors is as follows:

The first and second derivatives of Eq. (4.1) can be written as

$$\mathbf{Q}'(u) = \frac{d\mathbf{Q}(u)}{du} = 3(\mathbf{P}_1 - \mathbf{P}_0)(1-u)^2 + 6(\mathbf{P}_2 - \mathbf{P}_1)u(1-u) + 3(\mathbf{P}_3 - \mathbf{P}_2)u^2 \tag{4.2}$$

$$\mathbf{Q}''(u) = \frac{d^2\mathbf{Q}(u)}{du^2} = 6(\mathbf{P}_2 - 2\mathbf{P}_1 + \mathbf{P}_0)(1-u) + 6(\mathbf{P}_3 - 2\mathbf{P}_2 + \mathbf{P}_1)u \tag{4.3}$$

In Figure 4.5, points P_0, P_1 and P_2 are specified points (based on the specified vertical positions of the girder geometry and the corresponding location in plan) and $\mathbf{d}_{ij}$ is the tangent vector at each of these points (to be determined). The subscript 'i' in $\mathbf{d}_{ij}$ represents the Bezier curve segment number and the subscript 'j' represents the associated specified point. The C^1 and C^2 continuity of the two Bezier curves $\mathbf{Q_1}(\mathrm{u})$ and $\mathbf{Q_2}(\mathrm{u})$ at point P_1 can be expressed as:

$$\mathbf{Q}_1'(1) = \mathbf{Q}_2'(0) \quad \Rightarrow \quad -\mathbf{d}_{11} = \mathbf{d}_{21} \tag{4.4}$$

$$\mathbf{Q}_1''(1) = \mathbf{Q}_2''(0) \quad \Rightarrow \quad \mathbf{d}_{10} - 2\mathbf{d}_{11} + 2\mathbf{d}_{21} - \mathbf{d}_{22} = \mathbf{P}_2 - \mathbf{P}_0 \tag{4.5}$$

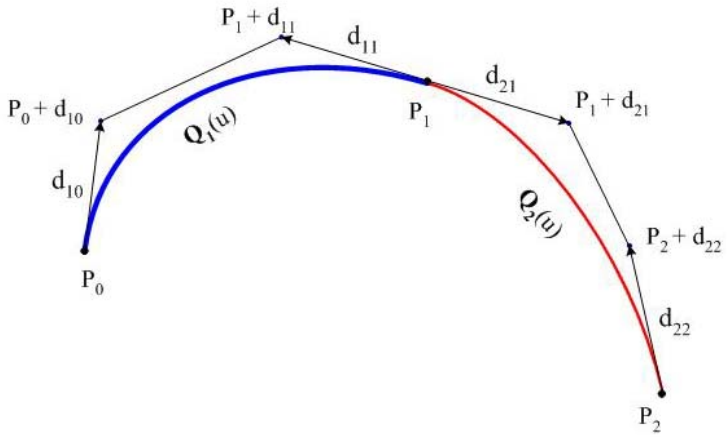

Figure 4.5 Two Bezier curves with C^2 continuity

To simplify the notation, the tangent vectors d_{10}, d_{21} and d_{22} are denoted by d_0, d_1 and $-d_2$. Therefore, Eq. (4.5) can be written as

$$\mathbf{d}_0 + 4\mathbf{d}_1 + \mathbf{d}_2 = \mathbf{P}_2 - \mathbf{P}_0 \tag{4.6}$$

Based on Eq. (4.6) for N successive Bezier curves, the requirement of C^2 continuity results in N linear equations:

$$4\mathbf{d}_1 + \mathbf{d}_2 = \mathbf{P}_2 - \mathbf{P}_0 - \mathbf{d}_0$$

$$\mathbf{d}_1 + 4\mathbf{d}_2 + \mathbf{d}_3 = \mathbf{P}_3 - \mathbf{P}_1$$

$$\ldots \qquad \ldots$$

$$\mathbf{d}_i + 4\mathbf{d}_{i+1} + \mathbf{d}_{i+2} = \mathbf{P}_{i+2} - \mathbf{P}_i$$

$$\ldots \qquad \ldots$$

$$\mathbf{d}_{N-2} + 4\mathbf{d}_{N-1} = \mathbf{P}_N - \mathbf{P}_{N-2} - \mathbf{d}_N$$

The above equations can be written succinctly as:

$$\mathbf{d}_i = \mathbf{A}_i + B_i\, \mathbf{d}_{i+1}\,, \qquad i = 1\,,\, 2\,,\, \ldots\,,\, N{-}1 \tag{4.7}$$

where

$$\mathbf{A}_1 = (\mathbf{P}_2 - \mathbf{P}_0 - \mathbf{d}_0)/4 \tag{4.8}$$

$$B_1 = -1/4 \tag{4.9}$$

$$\mathbf{A}_i = (\mathbf{P}_{i+1} - \mathbf{P}_{i-1} - \mathbf{A}_{i-1})/(4 + B_{i-1}) \tag{4.10}$$

$$B_i = -1/(4 + B_{i-1}) \tag{4.11}$$

After calculating all the $\mathbf{A}_i$ and B_i values from Eqs. (4.8) through (4.11), $i = 1$ to $N-1$ one can find $\mathbf{d}_{N-1}$ and $\mathbf{d}_i$ successively by substitution in reverse order as

$$\mathbf{d}_{N-1} = \mathbf{A}_{N-1} + B_{N-1}\,\mathbf{d}_N \tag{4.12}$$

$$\mathbf{d}_i = \mathbf{A}_i + B_i\,\mathbf{d}_{i+1}\,, \quad i = N\text{-}2, N\text{-}3, \ldots 1 \tag{4.13}$$

In the current study, the end-point tangent vectors are initially directed from the end points to the nearest specified point. Also, the norm of each vector is set to be one-third of the vector length between these points. The vector $\mathbf{v_0}$ in Figure 4.6 is one of these vectors. Once the tangent vectors of all the interior end points of the Bezier curve segments (such as $\mathbf{v_1}$ in Figure 4.6) are calculated, the end-point tangent vectors are adjusted such that each end curve segment is symmetric to the mirror line of the two points P_0 and P_1 as shown in Figure 4.6.

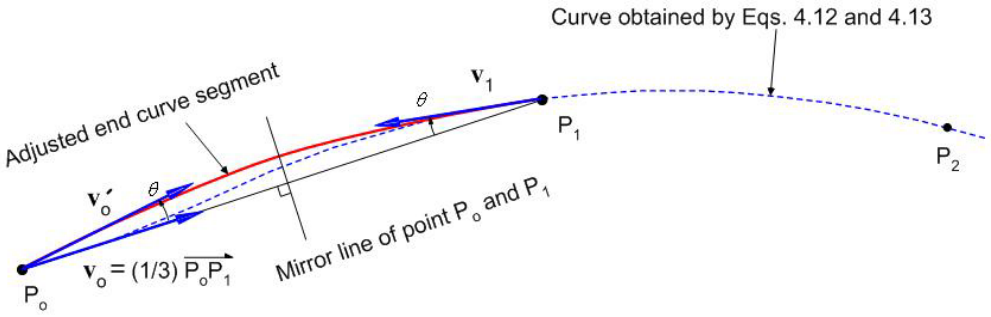

Figure 4.6 Illustration of the adjustment of the end curve segment

4.3.3 Handling of Potentially Significant Geometric Nonlinearities

In horizontally curved I-girder bridges, the geometric nonlinearity is potentially important during construction because of the flexibility of I-girders in torsion and lateral bending. Also, one should note that in modeling steel erection operations, compatibility must be achieved between connecting points on the deformed structure and/or structural components. This necessitates the consideration of equilibrium on the deformed geometry, i.e., a geometrically nonlinear analysis. All the analyses pertaining to construction simulation presented in this research are geometrically nonlinear. It should be noted that the uniqueness considerations discussed above are not influenced by the geometric nonlinearity.

4.3.4 Solution for Deflected Geometry of Unconstrained Components and Subassemblies

The steel erection process can be subdivided into two parts:

(1) Positioning: lifting a steel group and placing it in a desired position, and

(2) Assembly: connecting the lifted groups with supports and other portions of the structure that are already in place.

A “group” is defined as any portion of the bridge that is fabricated and/or assembled before being lifted. The group positioning involves two actions: (1) lifting the group and (2) rigid-body motion of the group to the desired position. If the Engineer is not interested in the responses due to the positioning and assembly of a given group, the group model may be inserted into the structure in a simplified fashion, and the group’s gravity load can be simply “turned on.” The solutions during lifting and rigid-body motion are discussed in more detail below. The assembly process is discussed in Section 4.3.5

4.3.4.1 Lifting

As mentioned in Section 1.2, the best scheme for lifting a single curved girder (resulting in the smallest induced stresses) is to lift by cables at two locations separated by a spreader beam, and to attach the cables at the intersection of a line through the member center of gravity (Davidson 1996). In this research, the crane system is modeled with cable and truss elements (the spreader beam is modeled by a truss element) as shown in Figure 4.7 Generally, when a group is lifted, its center of gravity changes due to the group deformations. Therefore, the group experiences some rigid-body motion such that the resultant of the lifting forces passes through the center of gravity of its deformed geometry. To analyze the group and crane system under its self-weight, artificial spring constraints are placed on the model such that it is structurally stable. As shown in Figure 4.7, translational spring constraints are placed at nodes A, B, C, D and E in the global X and Z directions, and additional rotational spring constraints are placed at nodes D and E in both the global X and Z directions. The Y-direction spring S_{Aty} at node A is used to control the elevation of the girder by applying a vertical force at node A. This spring is called the elevation control spring. The other spring forces at nodes B, C, D and E need to be driven to be zero within a specified tolerance in order to obtain the girder responses during the lifting. This produces the rigid-body displacements required for alignment of the self-weight and the cable force resultants.

The algorithm for driving the spring forces to zero is as follows. The artificial spring constants are specified such that the entire structure, i.e., a girder and its crane system, is stable under its self-weight (based on judgment and trial-and-error). During the state determination, the artificial springs at nodes B, C, D and E are assumed to have zero force. This causes an out-of-balance between the internal and external forces. These out-of-balance forces are driven to zero within a specified equilibrium tolerance in GT-SABRE, using standard iterative FEA global nonlinear solution procedures. These

artificial springs are removed from the model once the group is stably connected to its supports and/or the other portions of the structure.

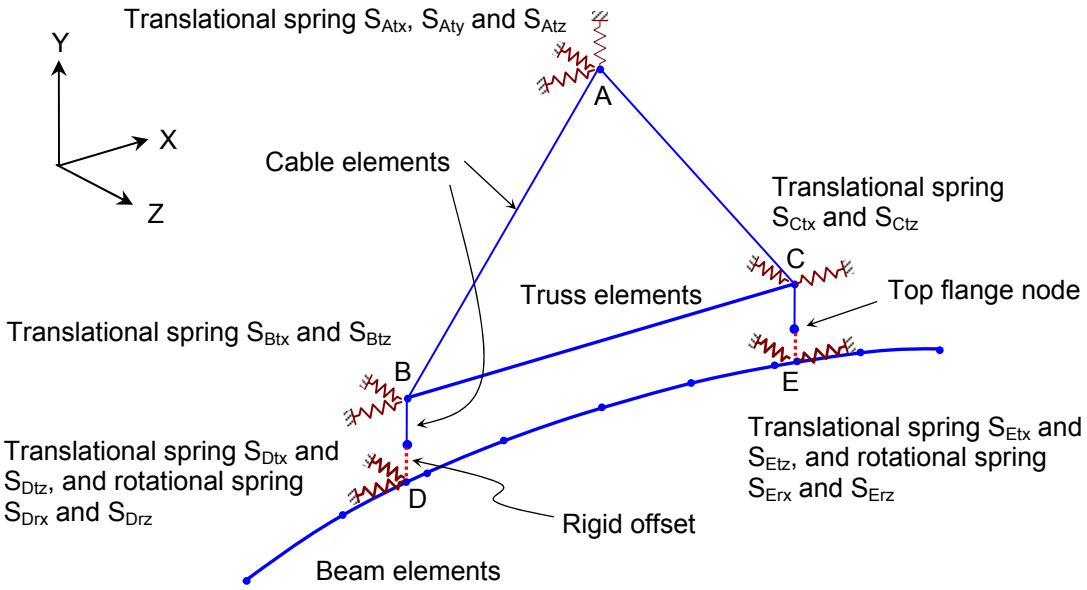

Figure 4.7 Finite element model for a single-girder with a crane system

4.3.4.2 Rigid Body Displacement

During the rigid-body motion operation, the deformed steel group is moved to a desired position where it is brought into contact with the erected structure and/or the supports at specific locations. A connection is then established between the appropriate dofs at these contact points, i.e., the nodal dofs on the lifted group and the nodal dofs at the corresponding point on the model of the erected structure or at a support are made the same. This is the initial step in the assembly process. Other subsequent assembly operations are necessary in general to complete the other connections of the group to the structure.

4.3.5 Assembly Process

The assembly process is accomplished in the physical structure by seating the lifted group on the bearings, and/or by bolting or welding to the erected structure. These processes are modeled in GT-SABRE by solving for the forces required at selected nodal locations, representing cranes, jacks, come-alongs or other construction equipment, to achieve compatibility at the same or other nodal positions that are to be connected at a given erection stage. Given *n* degrees of freedom (dofs) where compatibility is to be established at one or more nodes, *n* dofs can be selected at which the software can solve for the applied forces required to achieve the desired compatibility. Given the vector of the selected displacement incompatibilities, **D**, i.e., the difference in the positions and/or the angles of orientation for the selected dofs, and given the selected unknown vector of forces that are to be applied, **P**, a corresponding *n* x *n* tangent flexibility matrix, **F** is determined. This flexibility matrix represents the consistently linearized solution for the displacements at each of the dofs of **D** due to unit forces at each of the dofs of **P** for the structure in its current state. Next, the matrix equation **D = F P** is solved to determine a linearized estimate of the forces **P** necessary to achieve the compatibility. The forces **P** are then applied to the finite element model of the partially completed structure. Due to any geometric nonlinearity, this **P** does not bring the separate parts of the structure completely into contact at the dofs of **D**. Therefore, the remaining incompatibility is determined and the above equations are solved repeatedly (using Newton iteration at the level of the flexibility equations, given the specified **D** and the unknown **P**) until the connection satisfies the condition that the norm of the displacement incompatibility vector $\mathbf{D}_i$ is equal or less than a specified solution tolerance, in which the subscript 'i' represents for the i^{th} compatibility iteration. The FEA global solution for the incremental displacement due to a given estimated total incremental **P** in effect becomes the state determination for the above process. In some

cases, the forces are determined to displace the group on the erected structure to a certain position, e.g., to achieve a certain elevation at a point along a girder or to "close" a certain fraction of the displacement incompatibility. The above iteration process for steel assembly is summarized as follows:

1. Select the displacement control points, the corresponding connecting points, the force control points and the force control dofs,
2. Calculate the displacement incompatibility vector $\mathbf{D}_{R,i}$ between the displacement control points and the corresponding connecting points, in which the subscript 'i' represents for the i^{th} compatibility iteration.
3. Calculate the tangent flexibility matrix **F,**
4. Solve for the incremental forces $\mathbf{P} = \mathbf{F}^{-1} \bullet \mathbf{D}_R$.
5. Impose the total incremental force **P** (i.e., the sum of the **P** values obtained from the prior iterations during this increment) on the global finite element model of the partially completed structure and solve for the structural state due to this loading.
6. Repeat steps 2~5 until $\| \mathbf{D}_{R,i} \| \leq$ specified connection tolerance

In the physical erection of a bridge, generally crane, jacking, and come-along forces are introduced along with temporary supports to bring the desired connection points into close proximity. This is followed by localized forcing of the pieces together using drift pins and partial bolting combined with other local or global "jimmying" of the force and displacement boundary conditions to accomplish the connections. These operations are modeled by modifying the force vector **P** at selected steps of the simulation. It is generally difficult to achieve complete compatibility at a selected connection based solely on the application of crane forces at other locations. Typically,

local forces, e.g., forces representing local jacking, come-along or pinning/bolting operations, are required to completely close the incompatibility.

There are three principal assembly operations once a group has been brought into contact with the erected structure and/or the supports: (1) seating of the girders or groups on their supports, (2) girder splicing, and (3) cross-frame, diaphragm and/or bracing installation. The following subsections discuss these operations in detail.

4.3.5.1 Seating of the Girders or Groups on Their Supports

Once a girder or group is brought into contact with its supports at specific locations, typically it is lowered further until a desired rotational orientation is achieved at the bearings, the girder or group is brought into contact with additional supports, and/or the girder or group is positioned at an elevation that facilitates further assembly. The above general flexibility solution procedure is used to vary the crane forces, etc. such that the desired displacements are achieved. When a physical girder or group is being seated on its supports, the erector may tie-down the group at a specific support at a certain stage of the process, to prevent further translation or rotation in certain directions at this point. Such tie-downs are modeled with displacement constraints at the corresponding support dofs. These tie-downs must be released at some point in subsequent stages of the assembly to avoid introducing unwanted restraints or locked-in stresses in the system.

4.3.5.2 Girder Splicing

Girders are spliced typically by pinning and bolting in three steps: (1) one flange is pinned; (2) the web splice is pinned progressively from the pinned flange to the other flange; (3) the other flange is pinned and the entire splice is aligned (AISC 1994). In the

current study, the girder splicing is achieved in four steps as shown in Figures 4.8: (1) translational continuity is enforced at the girder top flange, (2) translational continuity is enforced at the girder bottom flange, (3) nodal rotational continuity is enforced and (4) warping continuity is established. It should be noted that the overlaps in the 3D geometry at the splice connections (in this section) and at support points (discussed in the previous section) are neglected based on the assumption that they do not have a significant effect on the construction requirements. Also, once the complete compatibility of the degrees of freedom is achieved at a given position, the response is independent of the prior solution history.

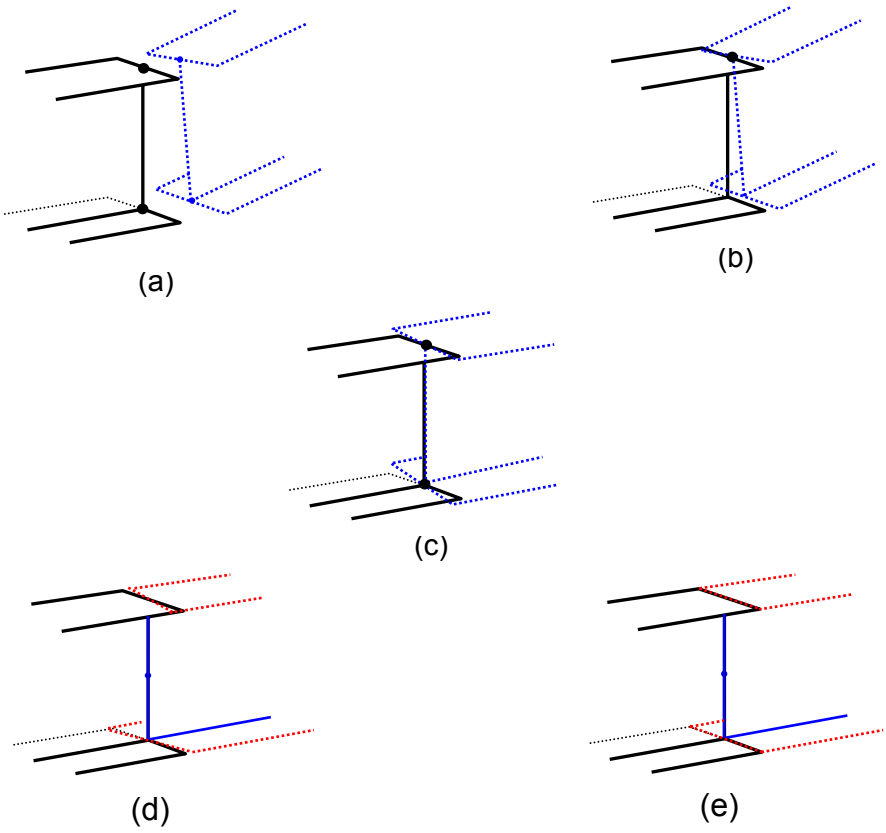

Figure 4.8 Girder splicing (a) initial position; (b) translational continuity at the top flange; (c) translational continuity at the bottom flange; (d) rotational and (e) warping continuities

One should note that the above solutions take advantage of an understanding of the previously discussed concepts of uniqueness. The above approach does not allow for the calculation of the detailed local forces required during the actual assembly of the splice in the field. In fact, the Engineer generally cannot possibly know this amount of detail about how the structure is erected, and certainly cannot prescribe this level of detail on the erector. However, this approach does allow for estimation of the global forces required for the erection operations. The approach relies on the fact that the final solution is unique once the splice connection is completed.

The locations of girder field splices typically depend on handling and shipping limitations in addition to other requirements. For continuous bridges, the splice locations are often selected near the points of dead load contraflexure to minimize the splice design moment. Typically the girder cross-sections are changed at the splice locations (see Figure 4.9).

In a finite element model using open-section thin-walled beam elements, there is a discontinuity in the warping functions if the two elements with different shear center elevation are connected to each other. This is because the warping functions depend on the shear center elevation as shown in Figure 2.6.

To conquer this problem, the cross-section transition at the splice location is modeled using tapered elements as shown in Figure 4.10. Tapered elements are used on both sides of the splice. The length of each tapered element is taken to be the largest flange width at the splice location. Conservatively, the cross-section dimensions can be tapered only on the side with the larger elements. The taper length also can be based on the Whitmore section rule (AISC 2005).

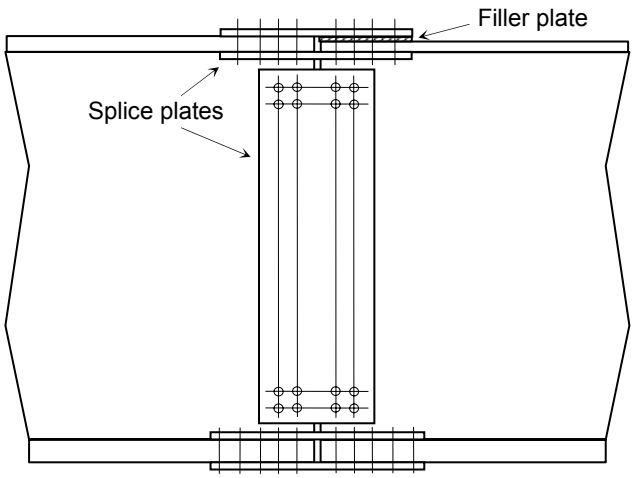

Figure 4.9 Cross section transition at girder splice location

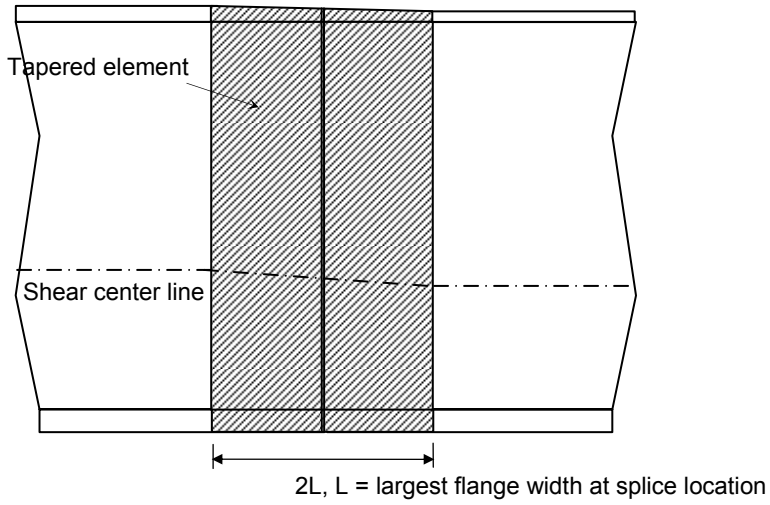

Figure 4.10 Finite element model for the cross section transition at girder splice location

4.3.5.3 Cross-Frame, Diaphragm and Bracing Installation

Figure 4.11 illustrates one possible cross-frame installation sequence. The cross-frame is first connected to the girder on the left. Then point P_1 is connected to P_1' on the

right-hand girder. Finally, P_2 is connected to P_2'. The chords of the cross-frame are modeled using beam elements. Initially, full continuity of rotations and displacements is assumed between the girder on the left and the cross-frame chords, with the cross-frame installed in the correct no-load orientation relative to the left-hand girder. This is to prevent rigid-body rotation of the cross-frame about the web of the left-hand girder prior to completing its installation. As noted previously, a rigid offset is defined between the connection points and the corresponding girder nodes once the connections are achieved. However, a rotational release is defined at the P_1 end of the top chord, when P_1 is connected to P_1', to allow free rotation in this connection during the last step of assembling P_2 to P_2'.

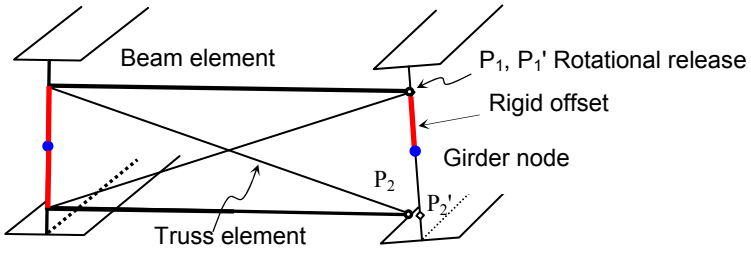

Figure 4.11 Cross-frame installation.

In the above, only displacement continuity is enforced between P_1 and P_1' and P_2 and P_2' (i.e., a rotational release is also inserted at P_2 when its connection is accomplished). After the displacement continuity between the above points is achieved, the rotational continuity is also released between the chords and the left-hand girder. This gives a model in which all the members are represented effectively by truss elements in the subsequent steps of the analysis. In the case of K-shaped cross-

frames, beam elements are still needed for the chord in which the diagonal members are connected at the mid-length.

Since the cross-frame is held by a crane during the installation, the self-weight of the cross-frame is neglected in this work until the cross-frame is fully installed and the crane is removed. The cross-frame self weight is then “turned on.” Locations are specified for crane forces, jacks and/or come-alongs to bring the points P_1-P_1' and P_2-P_2' together. The previously discussed flexibility algorithm is used to solve for the forces necessary to establish the continuity at these points.

The final state of the structure associated with the cross-frame installation is independent of the assembly sequence. If desired, the six forces required to achieve compatibility in the six displacement dofs at P_1-P_1' and P_2-P_2' can be determined in one step.

4.3.6 Instantiation of Slab Elements on the Deformed Geometry

The concrete slab elements are instantiated on the deformed girder geometry as illustrated in Figure 4.12. First for a girder node N_i, a new node N_{i1} is created at the top web-flange juncture along the Y direction of the nodal triad. Another new node N_{i2} is then created directly above N_{i1} (in the global Y direction) at a height above N_{i1} equal to the haunch depth plus one-half of the slab thickness. As noted previously, the slab elements are instantiated at the dead-load deformed geometry for each stage of the slab construction. The loads from the wet concrete are applied to interior I-girders based on tributary widths and to facia girders based on the lever rule (AASHTO 2004). In the targeted 3D grid analysis approach, 6-dof beam elements are used to represent the slab. The slab is modeled by a grillage of beam elements.

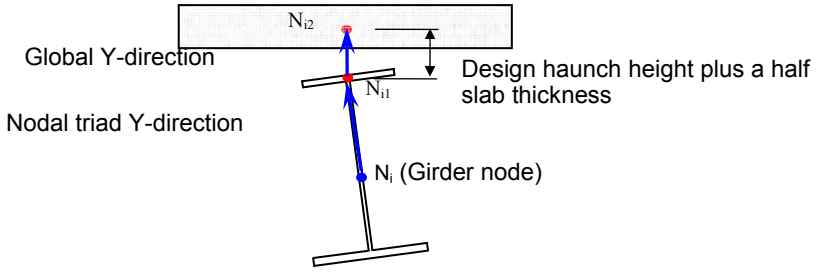

Figure 4.12 New node creation for slab elements

The concrete slab may not be cast in one stage due to the large volume of concrete. In this case, the casting sequence is subdivided into several stages. Concrete in early stages may gain strength and contribute stiffness to the structure. It is assumed that the portions of the bridge corresponding to previous stages behave compositely[1]. New elements are created to model the hardened concrete slab based on the current girder geometry at the end of each stage. After the completion of the slab construction, the entire bridge is considered to act compositely. The slab overhang support brackets are removed, the weight of forming removed from the bridge is released, and any temporary bracing is removed. The self-weight of parapets, sidewalks, barriers and/or other components that contribute dead weight, but are placed after casting of the slab, are applied at their actual location in the composite model. The position of the bridge deck is then checked with target values. If necessary, the initial camber of the girders is modified and the above processes are repeated (including the erection simulation).

[1] Typically, it is not considered necessary for the software to be able to represent a continuous strength and stiffness gain of the concrete slab. The concrete may be considered to be fluid at the instant that a particular portion of the slab is poured. If set may occur at portions of the bridge deck previously poured within a continuous casting sequence, this may be represented approximately by subdividing the continuous casting sequence into stages, and assuming that the earlier stages act compositely.

It should be noted that for continuous-span bridges, the casting typically does not proceed monotonically from one end of the bridge to the other. Generally the slab in positive moment regions is cast earlier to alleviate slab tensile stresses in the negative moment regions.

Also, it should be noted that when the bridge is under the steel plus partial wet concrete load, the slab elements based on the new generated nodes generally will not have the same curvature along the corresponding girder length. The curve-fitting algorithm presented in Section 4.3.2 can be used to find a curve passing through all the new generated nodes and to calculate the initial rotation at the end of each element to instantiate the curved slab elements. Alternatively, the slab nodes can be instantiated directly above the corresponding girder flange nodal location and the slab elements can be instantiated as straight elements between the slab nodes. The curvature of the slab is typically small enough and the slab is stiff enough such that this chorded representation of the slab geometry gives essentially the same results as the above more refined approach. The slab is modeled using straight elements between the slab nodes in all the examples presented in this research.

4.3.7 Consideration of Induced Stresses Due to Lack-of-Fit

When cross-frames are detailed based on either SDLF or TDLF, a lack-of-fit exists between the girders and cross-frames at their connection points under the no-load condition. This lack-of-fit induces stresses in both the cross-frames and girders when the cross-frames are installed. These induced stresses generally need to be considered.

In this study, two methods are provided to include the induced stresses due to lack-of-fit in the model of the bridge structure. The first method is to install all the cross-frames sequentially based on the assembly process introduced in Section 4.3.5. The required forces for the cross-frame installation are calculated and then applied to cross-

frames (and girders) to make the connection. Based on the uniqueness concepts and conditions described in Section 4.2, once all the cross-frames are installed, the induced stresses due to lack-of-fit are automatically included. This method is time-consuming. An easier way to handle the induced stresses (and deformations) due to lack-of-fit is as follows.

For the case that cross-frames are detailed with TDLF, the non-cambered girders and cross-frames are initially fitted together under the no-load condition. Then the girders are displaced vertically to their cambered positions without twisting. The cross-frames are displaced vertically due to the girder cambering. As a result, internal cross-frame member forces are induced due to the deformation. These forces are considered as initial internal cross-frame member forces for subsequent analysis. For the SDLF detailing method, the process is the same as above except that the cross-frames are fit to the girders in their concrete dead load cambered positions (i.e., the positions associated with the total camber minus the steel dead load camber). Then the girders are displaced vertically to their total cambered positions without twisting to induce the forces in the cross-frames due to the lack-of-fit.

CHAPTER 5

APPLICATION 1: COMPOSITE TEST BRIDGE

5.1 Introduction

The finite element methodology introduced in Chapter 4 has been implemented in the software system GT-SABRE (Chang 2006). In this Chapter, three examples are presented to demonstrate the approaches addressed in Chapter 4 and the capabilities of GT-SABRE. The full-scale composite I-girder bridge tested at the Federal Highway Administration (FHWA) Turner-Fairbank Highway Research Center (TFHRC) and introduced in Section 3.5 is utilized for these examples. All the examples are performed using an elastic geometric nonlinear analysis.

The first example demonstrates that the solution for the steel erection is unique, i.e., independent of the construction sequence, as stated in Section 4.1. Solutions based on both the No-Load Fit (NLF) and the Total Dead Load Fit (TDLF) detailing methods are considered. The influence of the lack-of-fit associated with the TDLF method on the girder responses is investigated. The second example evaluates the performance of GT-SABRE by comparison of the analysis results based on the beam-grillage model created in GT-SABRE to a refined Shell-Beam-Shell finite element model (shell elements for the slab, beam elements for the girder flanges and connection plates, and shell elements for the girder webs, referred to as the S-BS model in Section 3.4.4) using ABAQUS (HKS 2005). These analyses are conducted for the noncomposite total dead load (steel self-weight + wet concrete load). The third example serves to demonstrate the suggested modeling technique for composite bridges using open-section thin-walled beam elements as discussed in Chapter 3. The slab elements are instantiated based on the girder geometries under the total dead load. The experimental loading condition

described in Figure 3.12 is applied to the bridge model for the third example. Summary observations are provided based on these analysis results.

5.2 Example I: Beam Grillage Solutions for the Composite Test Bridge

The focus of this example is on (1) the demonstration of the uniqueness concept discussed in Section 4.2, and (2) the influence of the lack-of-fit associated with TDLF detailing on the girder responses. Four test bridge finite element models are created in GT-SABRE for these purposes. These models are based on the NLF and TDLF detailing methods. The girder cambers determined based on NLF detailing are used for all of the models discussed in this section. The analyses are conducted using two different approaches to illustrate the uniqueness of the solution given a particular detailing method.

.

5.2.1 Model Description

The geometry and material properties of the composite test bridge are introduced in Section 3.5. The steel curved I-girders are modeled using the displacement-based open-section thin-walled beam element introduced in Chapter 2. For the cross-frame members, in order for the model to be stable when only one side of cross-frame is connected to a girder, the top and bottom chords are modeled with traditional 6-dof beam elements. The diagonal members are modeled with truss elements. The final displacement boundary conditions are a vertical restraint at each bearing, radial restraints at the G2 bearings, and a longitudinal restraint at the G2 midspan (preventing rigid body longitudinal displacements while maintaining symmetry of the analysis deflections on each side of the midspan). The weights of the cross-frames and connection plates are lumped at the associated girder nodes. The weights of stiffeners

are included in the uniformly distributed girder self-weight. The wet concrete load within the tributary width of each girder is applied as a uniform line load to the top web-flange juncture of each girder. In addition, the torsion on the facia girders from the cantilever brackets supporting the deck overhangs is accounted for by applying work equivalent nodal torques to the facia girder nodes along the girder lengths.

The first type of analysis approach considered in this section is referred to as the "Instantaneously Instantiated Model" or IIM approach. In this approach, all the steel members are assembled in their no-load condition at the beginning of the analysis and then the gravity load is simply "turned on". The other type of analysis approach is called a "Sequentially Assembled Model" or SAM approach. In this method, the erection of the structure is explicitly simulated. In the current study, the SAM approach follows the steel erection sequence conducted in the FHWA Lab, which is explained in Figures 5.1 to 5.8. The NLF and TDLF detailing methods are studied using both of these analysis approaches.

For the NLF detailing, the workpoints for the cross-frame connections are all located precisely at the mid-thickness of the girder webs. Also, the work points for the top and bottom chord connections are located at the same top and bottom distances from the top flange in all of the girders. Therefore, for all the steel members to fit together in the no-load condition, every cross-frame must have a different geometry. This is due to the different girder cambers shown in Table 5.1. The above approach is referred to as the NLF detailing option 2 in Figure 4.2.

For the TDLF detailing, all the cross-frames have identical geometry. Also all the cross-frame connection top and bottom work points are located at the same top and bottom locations for all the girders. This causes a lack-of-fit between the girders and the cross-frames in their no-load geometry. Therefore, additional stresses are induced by the assembly of the girders and cross-frames.

The test bridge construction sequence in the laboratory and in the finite element model is explained in Figures 5.1 to 5.9.

Table 5.1 Designed cambers of the test bridge girders based on NLF

Normalized Length	0.0	0.1	0.2	0.3	0.4	0.5	0.6	0.7	0.8	0.9	1.0
G1 (cm (in))	0.0	1.189 (0.468)	2.240 (0.882)	3.068 (1.208)	3.592 (1.414)	3.754 (1.478)	3.592 (1.414)	3.068 (1.208)	2.240 (0.882)	1.189 (0.468)	0.0
G2 (cm (in))	0.0	2.253 (0.887)	4.237 (1.668)	5.804 (2.285)	6.800 (2.677)	7.125 (2.805)	6.800 (2.677)	5.804 (2.285)	4.237 (1.668)	2.253 (0.887)	0.0
G3 (cm (in))	0.0	3.421 (1.347)	6.469 (1.547)	8.867 (3.491)	10.391 (4.091)	10.922 (4.300)	10.391 (4.091)	8.867 (3.491)	6.469 (1.547)	3.421 (1.347)	0.0

Figure 5.1 Test bridge steel erection sequence step 1: (a) G1, G2, and G3 are blocked to their camber profiles on the lab floor; (b) holes are drilled and cross-frames are assembled; (c) bottom flange diagonals are attached between G1 and G2; (d) cross-frames are disassembled between G2 and G3.

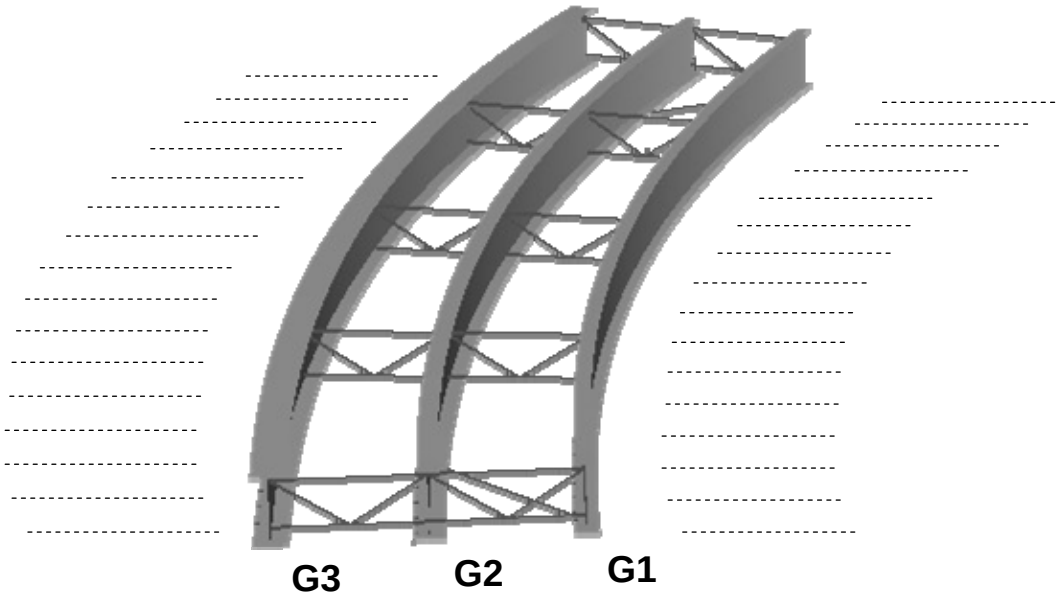

Figure 5.2 Corresponding FEA model of the test bridge steel erection sequence, step 1

Figure 5.3 Test bridge steel erection sequence, step 2: (a) G1-G2 pair is set on the abutments; (b) G3 is left blocked in its camber profile.

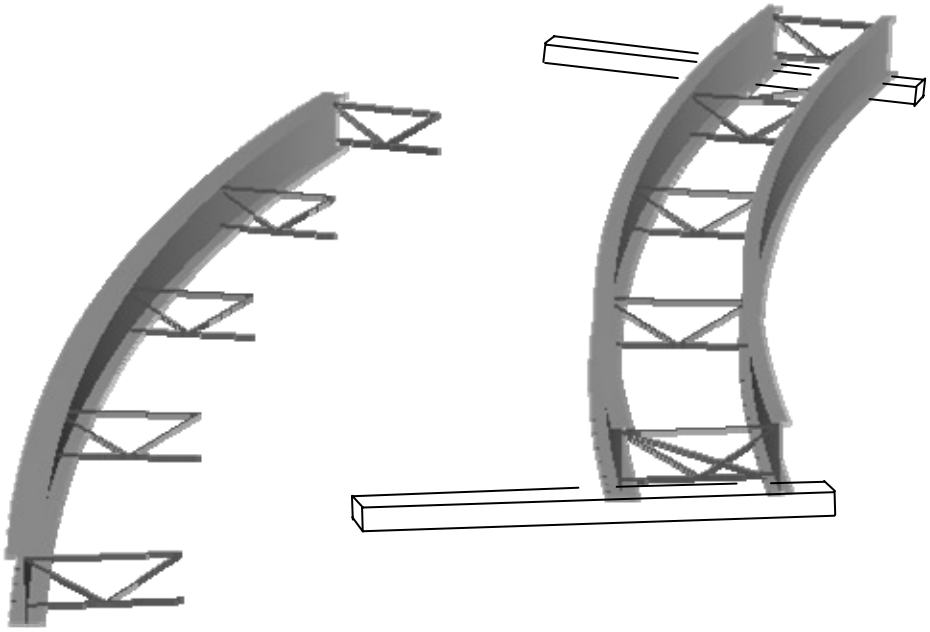

Figure 5.4 Corresponding FEA model of the test bridge steel erection sequence, step 2

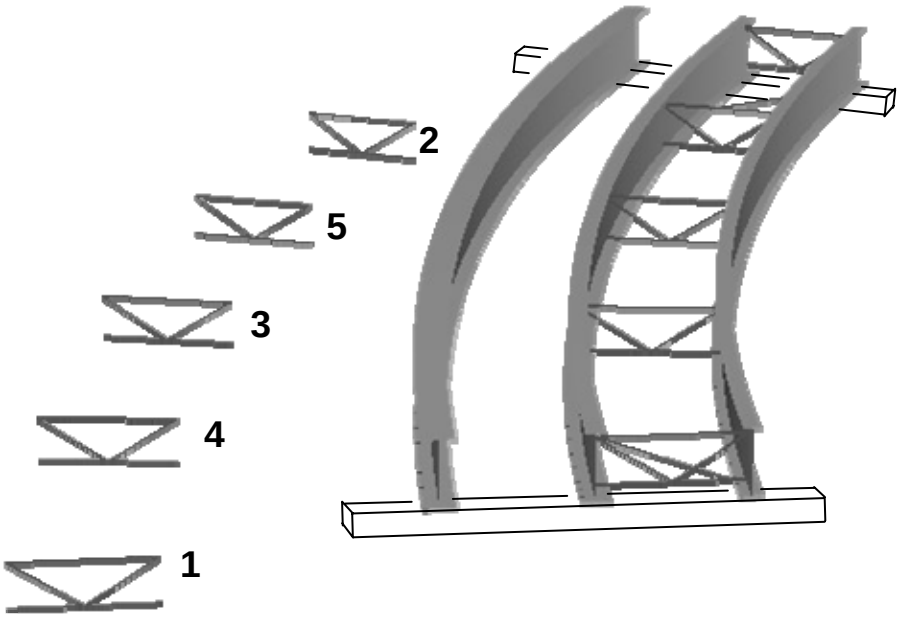

Figure 5.5 Test bridge steel erection sequence, step 3 (FEA model): (a) girder G3 is set on the abutments and held with the crane; (b) cross-frames are installed in the order of 1, 2, 3, 4 and 5; (c) bottom flange diagonals are attached between G2 and G3.

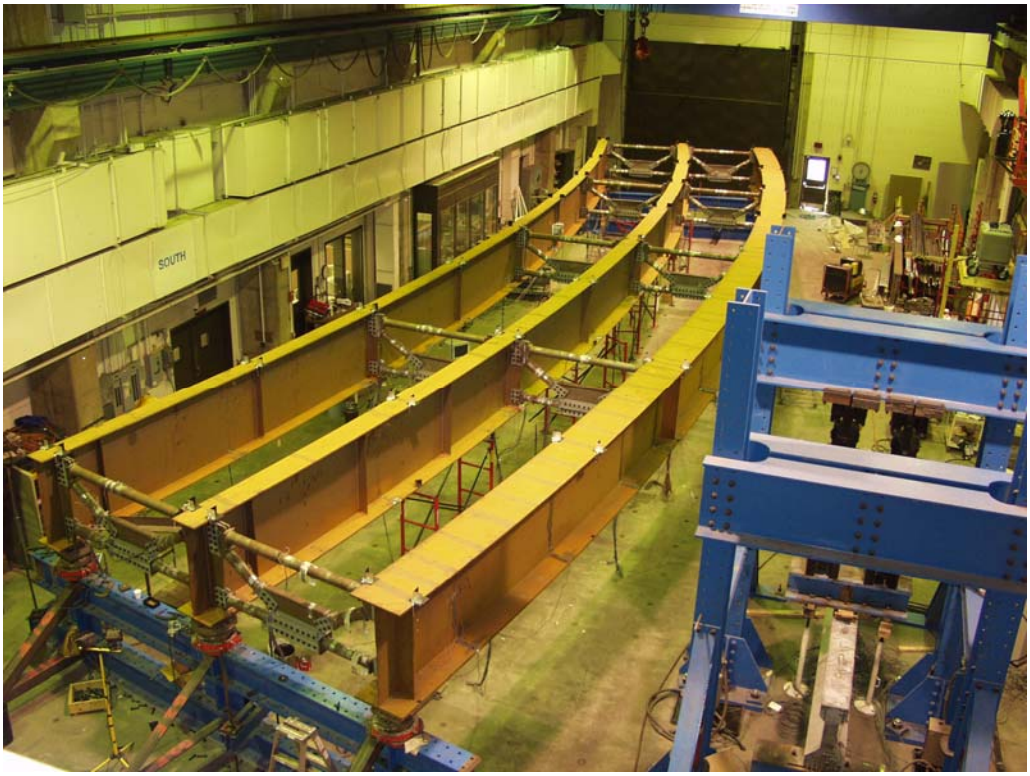

Figure 5.6 Test bridge steel erection sequence, step 4: Release all cranes.

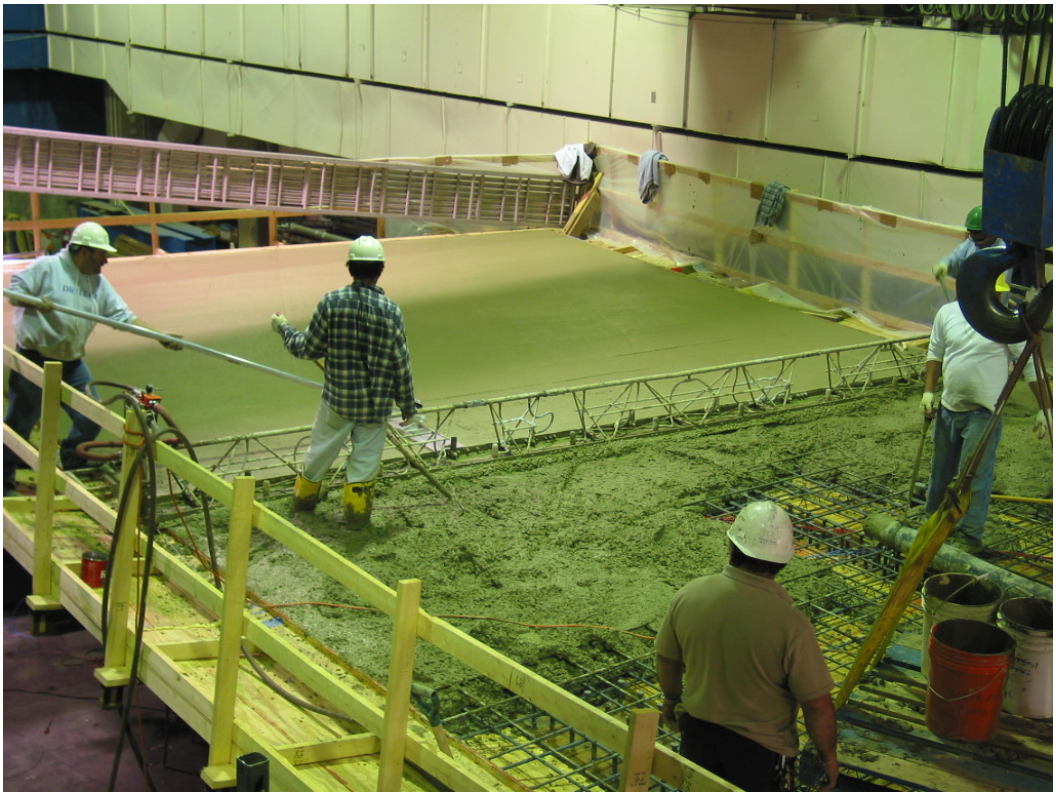

Figure 5.7 Test bridge slab casting: the slab is cast in one continuous stage

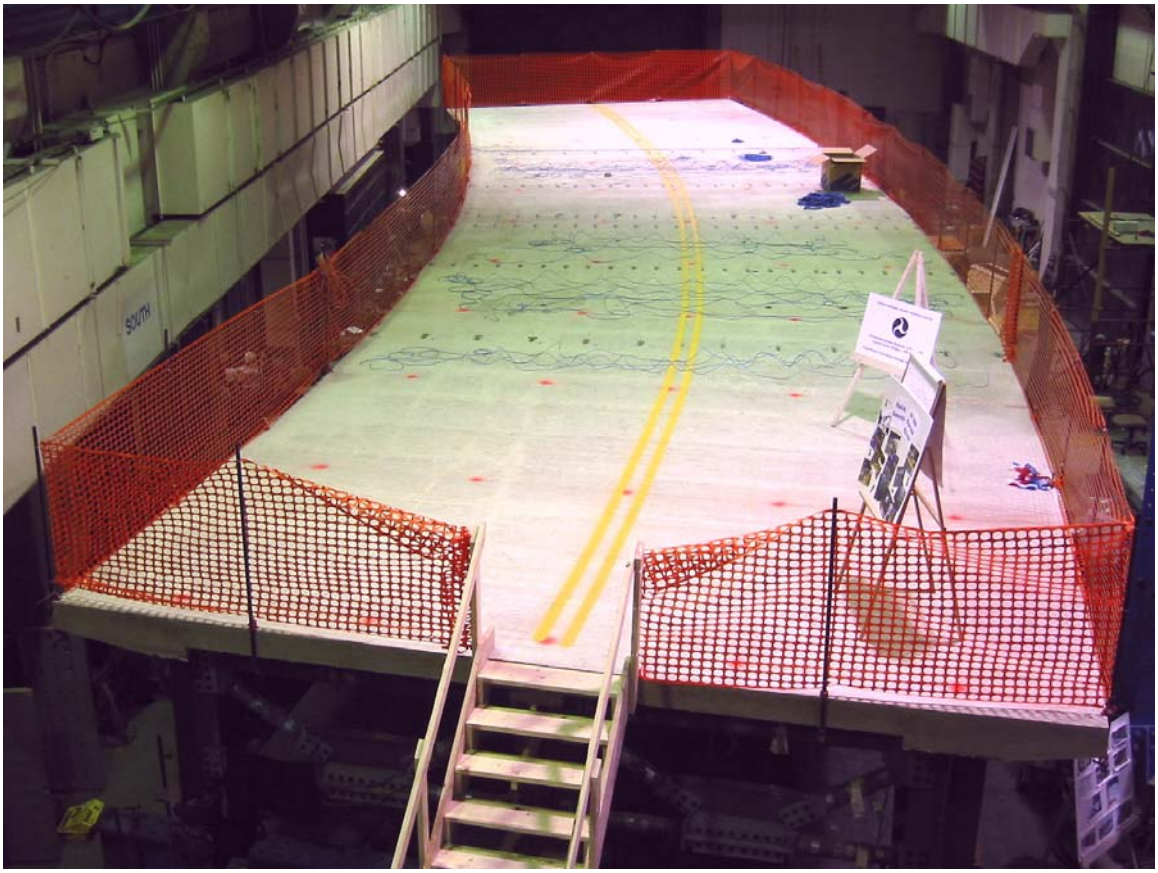

Figure 5.8 Test bridge slab casting: formwork and bottom flange diagonals are removed

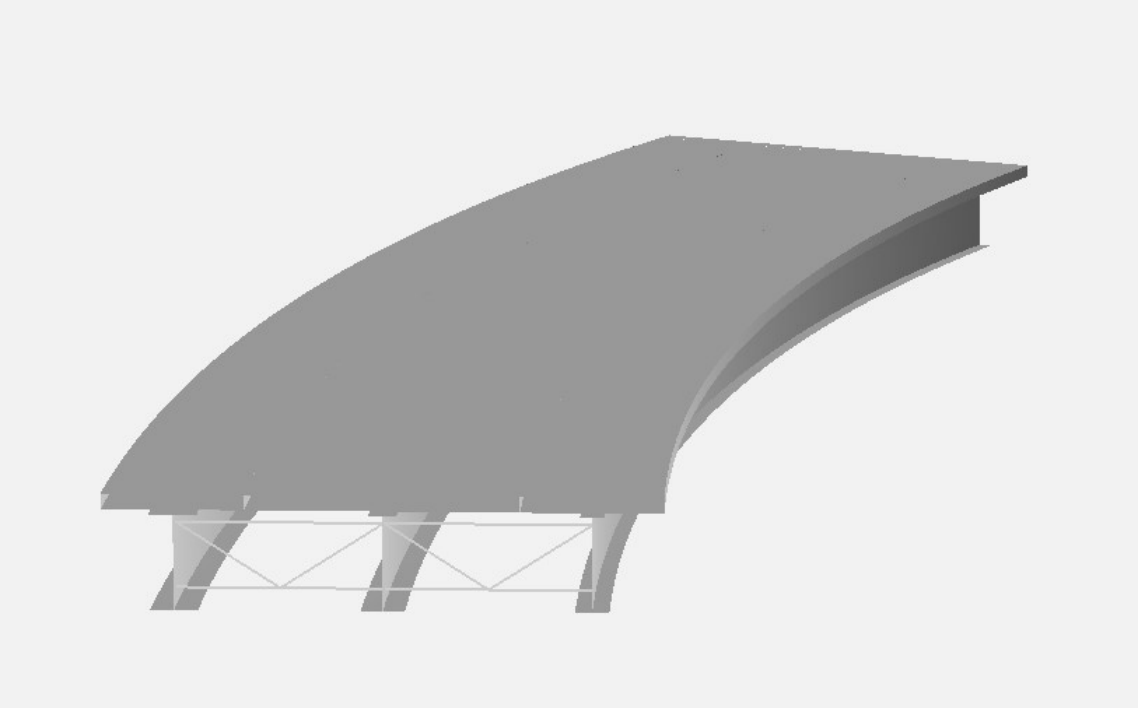

Figure 5.9 Corresponding FEA model of the test bridge slab casting

It should be noted that for the K-shaped cross-frames used in the test bridge, the bottom chord needs to be modeled with at least two beam elements. Based on the algorithm introduced in Section 4.3.7, the two exterior nodes of the bottom chord are simply moved vertically along with the girder cambering. However, if the cross-section and/or the material property of each of the cross-frame members are not the same, then the interior node at K-joint can not be simply moved vertically to the position such that it is collinear with the two exterior nodes. The stiffness of each cross-frame member needs to be considered for the calculation of the correct movement of the interior node. Currently GT-SABRE is not able to handle this case. Therefore, the IIM-TDLF model of the test bridge is actually constructed as a simplified SAM model as described below.

In the IIM-TDLF model, all the cross-frames are created based on the girder non-cambered no-load position and have the same geometry. The bottom flange diagonals

between girders G1 and G2 are instantiated first. Then the cross-frames between girders G1 and G2 are attached to G2, and the cross frames between girders G2 and G3 are attached to G3 using rigid offset constraints. This results in the lack-of-fit shown in Figure 4.3. Then the cross-frames between girders G1 and G2 are connected to girder G1 and the cross-frames between girders G2 and G3 are connected to girder G2 using the algorithm in Section 4.3.5.3 without considering the gravity load. During the connection process, the girder nodes corresponding to the cross-frame locations are temporarily fully restrained such that no stress is induced in the girders.

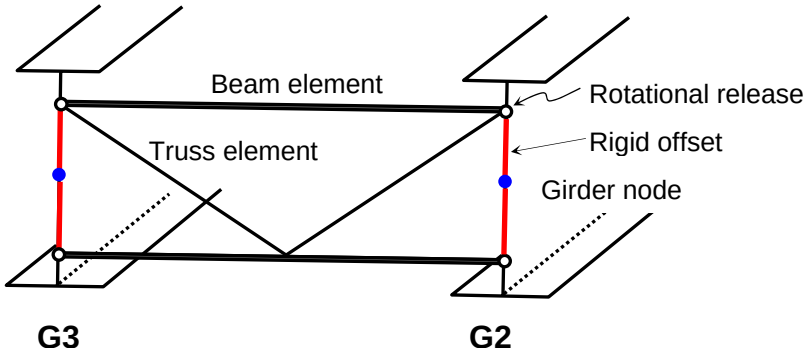

Figure 5.10 All rotational degrees of freedom at the connecting points are released after the cross-frame is connected to the girders

When all the cross-frames are installed and all the rotational degrees of freedom at the connecting points are released, all the girders remain non-stressed and the stress in each cross-frame member is the induced stress due to lack-of-fit. The temporary restraints on the girder nodes are then released. Due to the rotational release at the cross-frame members, the girder G3 is unstable under the final boundary condition until

the bottom flange diagonals between girders G2 and G3 are not installed. Therefore, a temporary longitudinal restraint is placed at the G3 midspan.

The steel dead load is then applied to this bare girder system. Then, as in the steel physical erection sequence in the lab, the bottom flange diagonals between girders G2 and G3 are instantiated in this deformed geometry without inducing any internal stress in the girders and the temporary restraint at the G3 midspan is removed. Finally, the wet concrete load is applied including the torque on the facia girders G1 and G3.

Unlike the IIM-TDLF model, the IIM-NLF model of the entire bridge is simply instantiated in the assembled condition at one time since there is no lack-of-fit.

In the SAM approach, the steel components between girders G1 and G2 are installed in the same way as in the above IIM-TDLF model for the TDLF case. However, for the NLF case, these two girders are created all at once along with the cross-frames between them, and then lifted as a pair onto their bearings. This represents the assembly of these components on the lab floor and the lifting of the G1-G2 pair as a single unit. The crane system introduced in Figure 4.7 is attached to the girder G3, the gravity load is turned on, and G3 is placed on its bearings. The cross-frames between girders G2 and G3 are then installed based on the sequence in Figure 5.5. The cross-frame self-weight is applied to the girders immediately after each installation. After installing the bottom flange diagonals between girders G2 and G3, the wet concrete load is then applied to the assembled structure.

It is noted that the algorithm in Section 4.3.5.3 for the cross-frame installation achieves the displacement compatibility within a specified tolerance. For the IIM-TDLF and SAM models considered in this section, the connection tolerance is set to a small number (e.g., 0.00025 cm (0.0001 in)) to ensure high precision of the analysis results. It is important to note that the convergence criterion for the global nonlinear solution algorithm must be set tighter than the above tolerance. Otherwise, the compatibility

iterations may not converge. Another potential factor that can affect the analysis results is the locked in stresses due to forcing the cross-frames and girders together when a rotational continuity of the cross-frame members and the girders has already been specified at some of the completed the cross-frame connection points. The rotational continuity at certain completed connection points is necessary for stability of the cross-frames during the erection simulation. To remove the associated locked-in forces in the bridge, all the rotational degrees of freedom at the connecting points are released after the cross-frame is connected to the girders as shown in Figure 5.10 such that the top and bottom chord beam elements of the cross-frame behave as truss elements. In fact, this is a common way to model the cross-frame.

5.2.2 Analysis Results

5.2.2.1 Demonstration of Uniqueness – Comparison Between Instantaneously Instantiated and Sequentially Assembled Models

The solutions for the maximum major-axis bending and lateral bending stresses in all the girder flanges are effectively identical (less than 0.1 % difference) using either the IIM or the SAM approach. One set of identical solutions is obtained for the case where the cross-frames are assumed to be detailed by the NLF method, and another set of identical solutions is obtained for the case where the cross-frames are assumed to be detaied by the TDLF method. Figure 5.11 compares the girder G2 bottom flange lateral bending stresses for TDLF detailing obtained by the IIM and SAM procedures. The percentage differences for the girder displacement solutions by the IIM and SAM approaches are smaller than 0.05 % for both the No-Load Fit (NLF) and Total Dead Load Fit (TDLF) detailing methods. This is expected, since the accuracy of the

displacements is always better than the accuracy of the displacement derivatives for displacement-based finite element solutions.

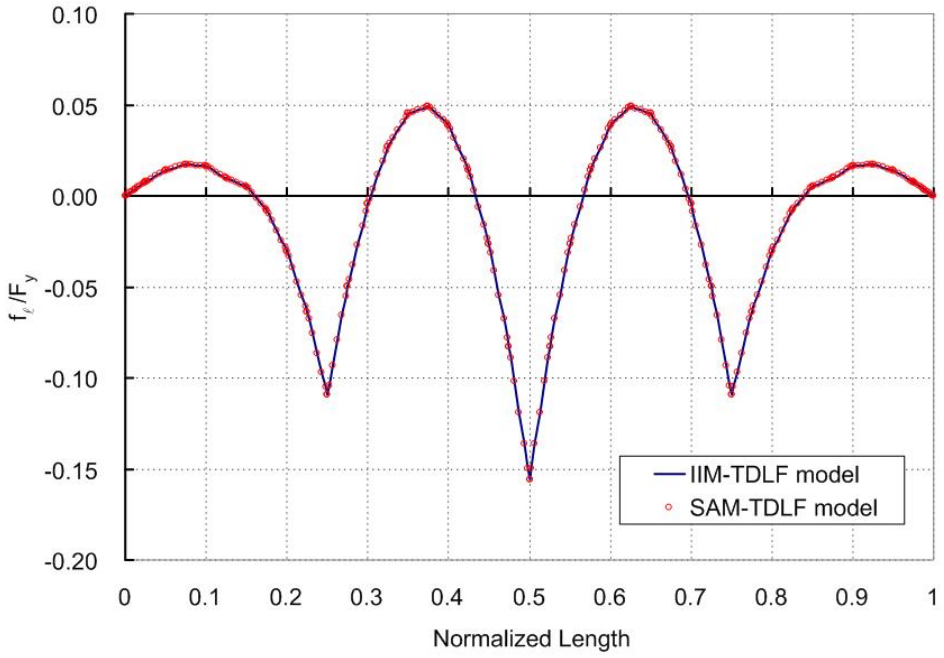

Figure 5.11 Comparison of Girder G2 bottom flange lateral bending stress solutions obtained by the IIM and SAM approaches, TDLF detailing

Tables 5.2 and 5.3 show the girder end reactions from the IIM and SAM models for both the NLF and TDLF steel detailing methods. The percentage differences between IIM and SAM models are less than 0.1 % for NLF case and less than 0.6 % for TDLF cases. Tables 5.4 and 5.5 show the cross-frame member forces of the cross-frame CF8. Figures 5.12 and 5.13 show the numbering of the test bridge cross-frames and cross-frame members, respectively. The percentage differences between IIM and SAM models are 0.1 % or lower for both NLF and TDLF cases except for the cross-frame member 5. The larger error for this member is because the force magnitude is small. The differences in the above solutions is due to the finite tolerance of 0.00025 cm (0.0001 in) on the residual relative displacements at the connection of the cross-frames CF6

through CF10 to Girder G2 in the SAM and IIM-TDLF solutions. The residual relative displacements are zero in the IIM-NLF solutions; the accuracy of these solutions depends only on the global nonlinear FEA solution tolerances for a given finite element discretization.

Table 5.2 Girder end reactions (kN (kips)) for IIM-NLF and SAM-NLF models (Girder cambers based on NLF)

Girders / Models	G1	G2	G3
IIM- NLF	100.35 (22.56)	173.57 (39.02)	411.06 (92.41)
SAM- NLF	100.40 (22.57)	173.61 (39.03)	410.97 (92.39)
% Difference	0.048 %	0.024 %	-0.022 %

Table 5.3 Girder end reactions (kN (kips)) for IIM-TDLF and SAM-TDLF models (Girder cambers based on TDLF)

Girders / Models	G1	G2	G3
IIM- TDLF	102.58 (23.06)	172.06 (38.68)	410.35 (92.25)
SAM- TDLF	103.07 (23.17)	171.03 (38.45)	410.84 (92.36)
% Difference	0.500 %	-0.588 %	0.123 %

Table 5.4 Cross-frame member forces (kN (kips)) of the cross-frame CF8 in Figure 5.12. The cross-frame member numbers are shown in Figure 5.13. (Girder cambers based on NLF, cross-frames detailed based on NLF)

CF members / Models	1	2	3	4	5
IIM- NLF	248.61 (55.89)	220.05 (49.47)	-213.52 (-48.002)	-430.32 (-96.74)	-66.19 (-14.88)
SAM-NLF	248.52 (55.87)	220.01 (49.46)	-213.50 (-47.997)	-430.19 (-96.71)	-66.15 (-14.87)
Difference %	-0.042 %	-0.011 %	-0.010 %	-0.030 %	-0.134 %

Table 5.5 Cross-frame member forces (kN (kips)) of the cross-frame CF8 in Figure 5.12. The cross-frame member numbers are shown in Figure 5.13. (Girder cambers based on NLF, cross-frames detailed based on NLF)

CF members / Models	1	2	3	4	5
IIM-TDLF	245.68 (55.23)	220.54 (49.58)	-216.76 (-48.73)	-426.41 (-96.86)	-59.16 (-13.30)
SAM-TDLF	245.81 (55.26)	220.32 (49.53)	-216.54 (-48.68)	-426.36 (-95.86)	-59.47 (-13.37)
Difference %	0.04 %	-0.086 %	-0.090 %	-0.004 %	0.521 %

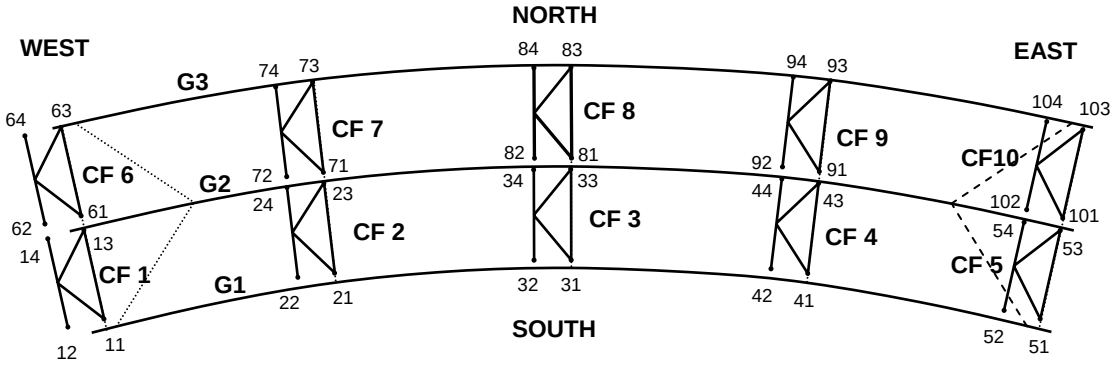

Figure 5.12 Numbering of the test bridge cross-frames and node numbers of each cross-frame members

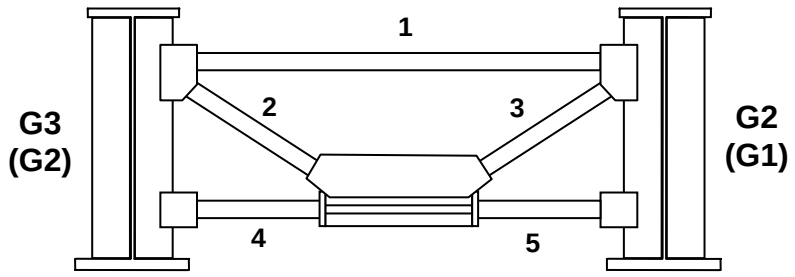

Figure 5.13 Member numbers for the test bridge cross-frames

5.2.2.2 Influence of Lack-of-Fit on Girder Responses : Comparison Between the Results for No-Load Fit (NLF) and Total Dead Load Fit (TDLF) Detailing

The analysis results from the above NLF and TDLF solutions are compared in this Section. In the TDLF solution, the lack-of-fit between the girders and cross-frames induces stresses in both the cross-frame members and girders. Figures 5.14 to 5.16 show the influence of these stresses on the girder elevations. The girders are deflected upward and twisted in the opposite direction from the dead load torsional deformations due these induced stresses. As a result, the girder elevations are above their desired locations under the total dead load (the desired location is a perfectly flat geometry for the test bridge). Table 5.6 compares the girder elevations, twist angles and flange radial deflections at the midspan of each girder. It can be observed that the girder twist angles (or out-of-plumbness) and flange radial deflections are smaller in the TDLF model. Also the vertical deflections are smaller in the TDLF model such that the corresponding final elevations are higher.

Table 5.6 Girder elevations, twist angles (at neutral axis), and flange radial deflections at midspan for cross-frames NLF and TDLF (Girder cambers based on NLF)

Girder	Load Condition	Elevation (cm (in))	Twist Angle (degree)	Radial Deflection (cm (in)) top / bottom flanges
G1	No-load cambered position	3.75 (1.48)	0.000˚	0.000
	Total dead load (NLF)	0.07 (*0.03*)	*-0.773˚*	*-2.92 (1.15) / -1.21 (-0.48)*
	Total dead load (TDLF)	**1.65** (**0.65**)	**0.023˚**	**-0.97 (-0.38)** / **-1.02 (-0.40)**
G2	No-load cambered position	7.13 (2.81)	0.000˚	0.000
	Total dead load (NLF)	-0.03 (*-0.01*)	*-0.841˚*	*-3.01 (-1.19) / -1.15 (0.45)*
	Total dead load (TDLF)	**1.89** (0.74)	**-0.040˚**	**-1.03 (-0.41)** / **-0.95 (-0.37)**
G3	No-load cambered position	10.92 (4.30)	0.000˚	0.000
	Total dead load (NLF)	-0.15 (0.06)	*-1.017˚*	*-3.23 (-1.27) / -0.96 (-0.38)*
	Total dead load (TDLF)	**1.70** (0.67)	**-0.213˚**	**-1.22 (-0.48)** / **-0.74 (-0.29)**

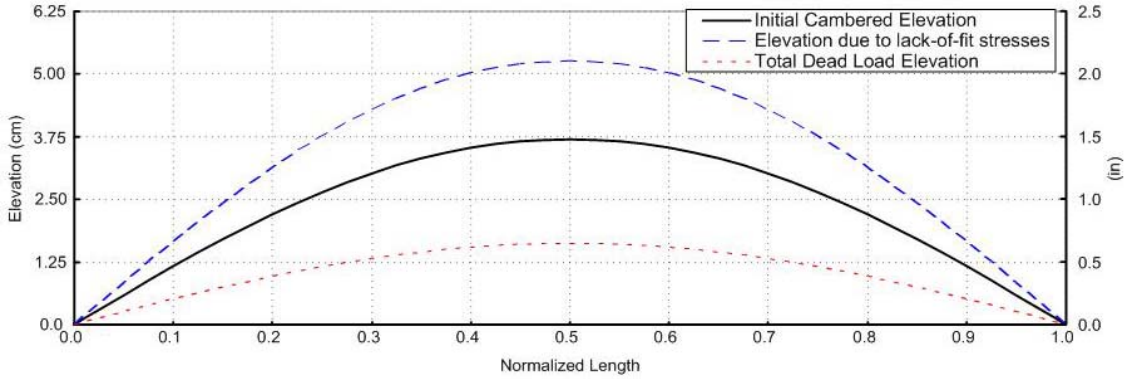

Figure 5.14 Girder G1 elevations at neutral axis for use of TDLF detailing (cambers set based on NLF detailing)

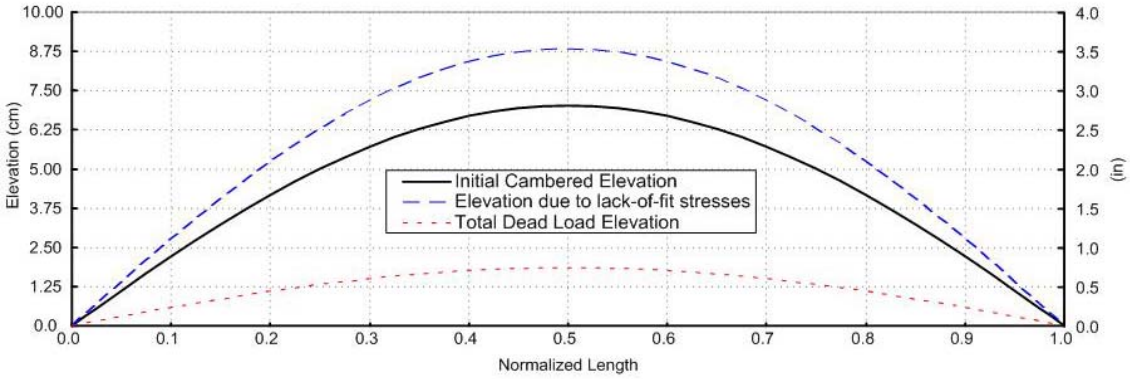

Figure 5.15 Girder G2 elevations at neutral axis for use of TDLF detailing (cambers set based on NLF detailing)

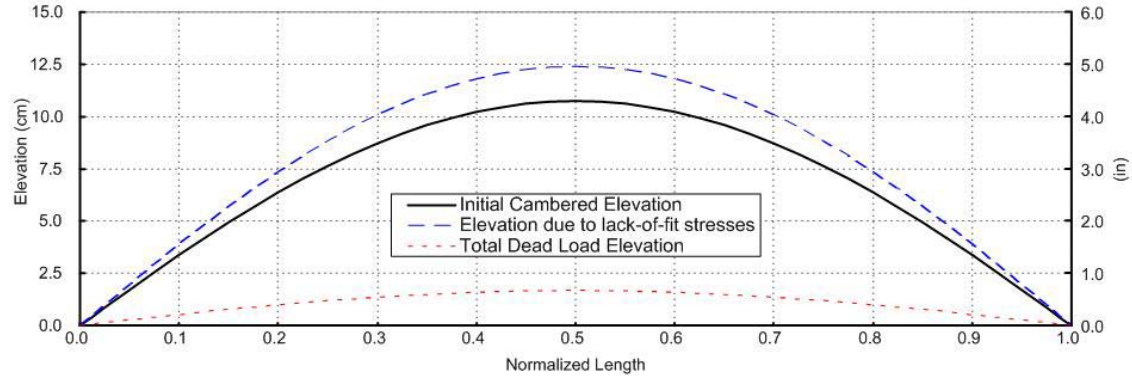

Figure 5.16 Girder G3 elevations at neutral axis for use of TDLF detailing (cambers set based on NLF detailing)

Figures 5.17 and 5.18 compare the girder G3 top flange stresses for the above TDLF and NLF designs. The flange stresses derived from the measured experimental strains on the test bridge, which was designed as NLF, are also inserted in these figures. One can observe that the method of cross-frame detailing has essentially no influence on the girder major-axis bending stresses. The locked-in stresses on the girders due to lack-of-fit are approximately the difference between two curves in Figures 5.18. The induced girder major-axis bending stresses due to lack-of-fit are essentially zero for the test bridge model. The flange lateral bending stress at the midspan in the TDLF design is about 15 % higher than in NLF design. It should be noted that use of NLF analysis for the camber design but TDLF detailing for the cross-frames is a common practice.

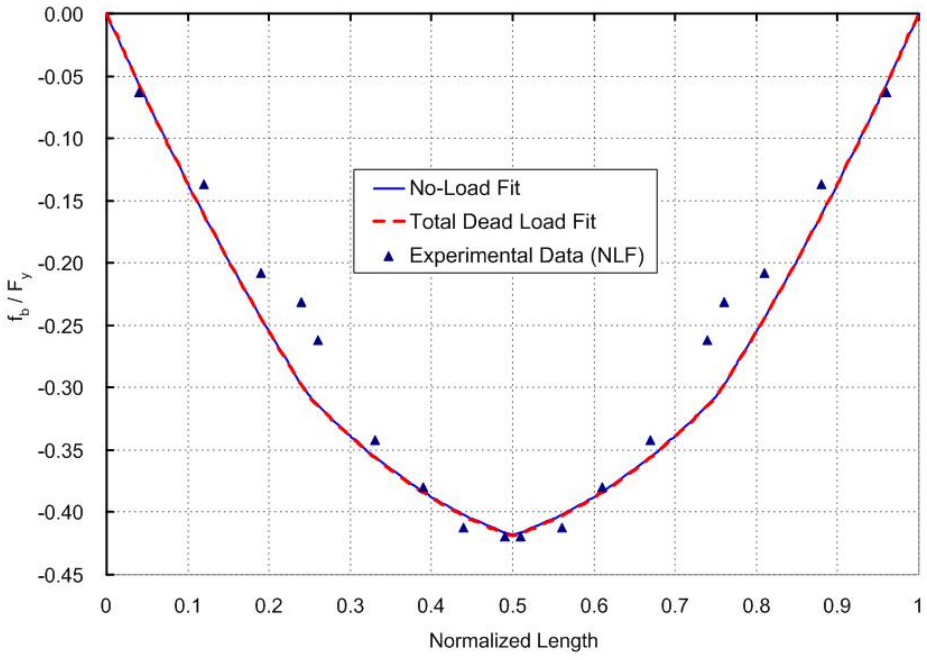

Figure 5.17 Comparison of girder G3 top flange major axis bending stresses from the NLF and TDLF analyses and from the stresses derived from the experimentally measured flange strains (cambers set based on the NLF detailing)

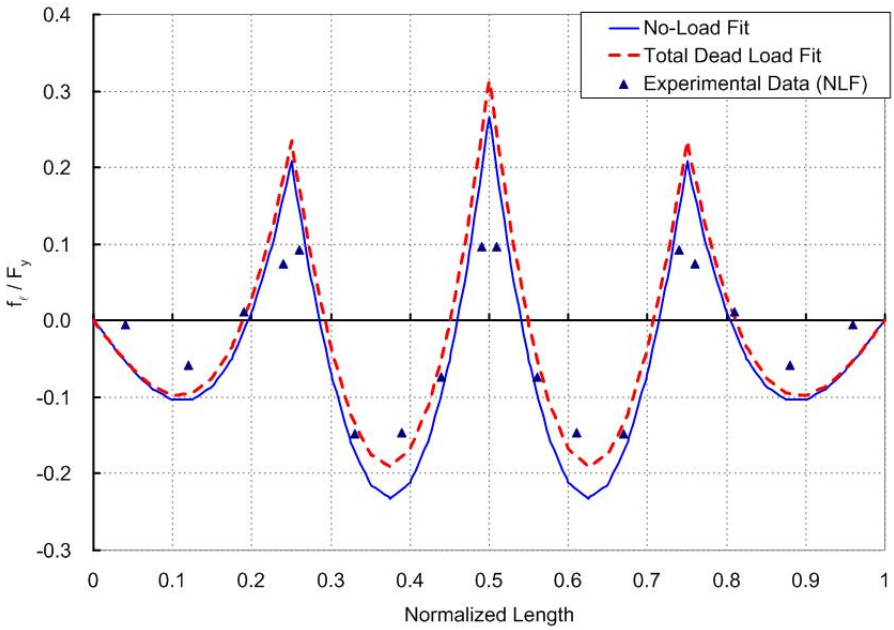

Figure 5.18 Comparison of girder G3 top flange lateral bending stresses from the NLF and TDLF analyses and from the stresses derived from the experimentally measured flange strains (cambers set based on the NLF detailing)

5.3 Example II: Comparison of Beam Grillage Model and Refined Shell-Beam-Shell (S-BS) Model – Non-Composite Bridge under Total Dead Load

This section highlights the GT-SABRE capabilities for progressively assembling components into a partially erected curved I-girder bridge structure accounting for the spatial deformations, displacements and rotations in the components being assembled as well as in the partially erected structure at intermediate stages of construction. In this section, the analysis results for an updated IIM-TDLF solution from the open-section thin-walled beam grillage model built in GT-SABRE are compared to the results from a refined shell-beam model (Shell elements for the slab, Beam and Shell elements for the I-girders or S-BS model mentioned in Section 3.4.4) created in ABAQUS (HKS 2005). It should be noted that the IIM solution is the preferred solution if the checking of the construction requirements is not desired. The author is not aware of any commercial or

research software system that is able to progressively assemble components into a partially erected structure, i.e., to obtain the SAM solution. The ABAQUS IIM solutions are generated by the approach discussed in Section 5.3.1.

In Section 5.2, the girder cambers are designed based on NLF detailing. As a result, when the cross-frames are detailed for TDLF, the girder final vertical displacements are less than the cambered displacements (i.e., the girder final elevations are higher than in NLF detailing had been used). In this Section, the girder cambers are redesigned as follows. The reversed vertical deflections of each girder in the TDLF model in Section 5.2 are set as the initial camber diagrams for a new model of the test bridge. Then the total dead load is applied to this model to determine the vertical deflections of each girder. The TDLF camber design in Table 5.7 for the test bridge is obtained with two iterations.

Table 5.7 Cambers of the test bridge girders based on TDLF

Normalized Length	0.0	0.1	0.2	0.3	0.4	0.5	0.6	0.7	0.8	0.9	1.0
G1 (cm (in))	0.0	0.765 (0.301)	1.443 (0.568)	1.979 (0.779)	2.314 (0.911)	2.418 (0.952)	2.314 (0.911)	1.979 (0.779)	1.443 (0.568)	0.765 (0.301)	0.0
G2 (cm (in))	0.0	1.501 (0.591)	2.822 (1.111)	3.858 (1.519)	4.516 (1.778)	4.727 (1.861)	4.516 (1.778)	3.858 (1.519)	2.822 (1.111)	1.501 (0.591)	0.0
G3 (cm (in))	0.0	2.936 (1.156)	5.555 (2.187)	7.617 (2.999)	8.936 (3.518)	9.380 (3.693)	8.936 (3.518)	7.617 (2.999)	5.555 (2.187)	2.936 (1.156)	0.0

5.3.1 Model Description

To create a IIM-TDLF test bridge model using ABAQUS, the following steps are employed (Jung 2006):

1. To determine the cambered girder geometry and the induced cross-frame member forces, an initial model of the steel superstructure is constructed that is flat in plan. The bottom diagonals between girders G2 and G3 are not instantiated yet. The radial deflections at the top and bottom flanges of each girder are restrained in addition to the desired final displacement boundary condition. The ABAQUS displacement control analysis is then applied to this bare girder model such that the specified TDLF camber control points in each girder reach their cambered positions. At this time, the geometry of the steel girders and the induced forces at all cross-frame members are recorded.
2. To determine the geometry of the girders due to the lack-of-fit between the girders and the cross-frames in the initial no-load geometry, a new model of the steel superstructure is created in which the geometry in the previous step is imported. Again, the bottom diagonals between girders G2 and G3 are not instantiated yet. The displacement boundary conditions are set as the physical support boundary conditions for the bridge. The induced cross-frame member forces obtained in the first step are then applied to this model.
3. To include the steel dead load effects, the self-weight of the steel superstructure is applied to the FEA model generated in step 2. These loads are applied from the state of the above model at the end of step 2.
4. To include the concrete dead load effects, the bottom flange bracing diagonals between girders G2 and G3 and between girders G1 and G2 are added to the FEA model from step 3 (using the MODEL CHANGE command). Then the concrete dead loads, including the eccentric bracket loads on the facia girders, are applied to the above model, starting from its state at the end the instantiation of the bottom flange diagonals.

5.3.2 Analysis Results

Table 5.8 compares the girder reactions between the GT-SABRE beam grillage model and ABAQUS S-BS model. The maximum percentage difference is approximately 2 %, corresponding to girder G2. There are some differences in the cross-frame member forces as shown in Table 5.9. This may be because the shell-element model of the web in ABAQUS accounts for distortion of the girder webs. These effects do not have a significant influence on the girder stress responses as shown in Figures 5.19 to 5.22, which show good agreements between the results from the beam grillage model and the S-BS model.

Table 5.10 shows the girder final elevation, twist angles and flange radial deflections for the beam grillage and S-BS models. The vertical deflections in the S-BS model are slightly larger than in the beam grillage model. The difference may due to the shear deformation that is not accounted for by the Vlasov-type beam element as well as minor web distortion that may occur in the S-BS model. The twist angles in the S-BS model are somewhat larger than in beam grillage model. This may be attributed to the same effects.

One can compare the analysis results of the beam grillage models in Table 5.10 (girder cambers based on TDLF) and Table 5.6 (girder cambers based on NLF), to find that for the TDLF models based on either of the camber designs, the twist angles and flange radial deflections are quite similar. However, the final elevations are quite different. The girders with the smaller camber diagrams (determined considering the influence of the TDLF detailing) result in less lack-of-fit between the girders and the cross-frames. As a consequence, it can be expected that the required forces for the cross-frame installation are reduced.

Table 5.8 Girder end reactions (kN (kips)) for beam grillage model and S-BS model (Girder cambers based on TDLF)

Models \ Girders	G1	G2	G3
Beam Grillage Model	112.86 (25.37)	151.91 (34.15)	420.18 (94.46)
S-BS Model	110.85 (24.92)	155.15 (34.88)	418.71 (94.13)
Difference %	-1.77 %	2.14 %	-0.35 %

Table 5.9 Cross-frame member forces (kN (kips)) of the cross-frame CF8 in Figure 5.12 for beam grillage model and S-BS model. The cross-frame member numbers are shown in Figure 5.13 (Girder cambers based on TDLF)

Models \ CF members	1	2	3	4	5
Beam Grillage Model	245.14 (55.11)	231.80 (52.11)	-228.02 (-51.26)	-435.21 (-97.84)	-49.11 (-11.04)
S-BS Model	245.27 (55.14)	269.34 (60.55)	-270.59 (-60.83)	-469.42 (-105.53)	-16.10 (-3.62)

Table 5.10 Girder midspan elevations, twist angles and flange radial deflections for the beam grillage model and S-BS model (Girder cambers based on TDLF)

Girder	Load Condition	Elevation (cm)	Twist Angle (degree)	Radial Deflection (cm) top / bottom flanges
G1	No-load cambered position	2.42 (0.95)	0.000˚	0.000
	Total dead load (Beam)	-0.057 (-0.02)	0.008˚	-0.67 (-0.26) / -0.69 (-0.27)
	Total dead load (S-BS)	-0.13 (-0.05)	-0.043˚	-0.79 (-0.31) / -0.70 (-0.27)
G2	No-load cambered position	4.73 (1.86)	0.000˚	0.000
	Total dead load (Beam)	0.12 (0.05)	-0.040˚	-0.72 (-0.28) / -0.63 (-0.25)
	Total dead load (S-BS)	-0.11 (-0.04)	-0.094˚	-0.86 (-0.34) / -0.65 (-0.26)
G3	No-load cambered position	9.38 (3.69)	0.000˚	0.000
	Total dead load (Beam)	-0.04 (-0.02)	-0.214˚	-0.91 (-0.36) / -0.43 (-0.17)
	Total dead load (S-BS)	-0.34 (-0.13)	-0.279˚	-1.09 (-0.43) / -0.47 (-0.19)

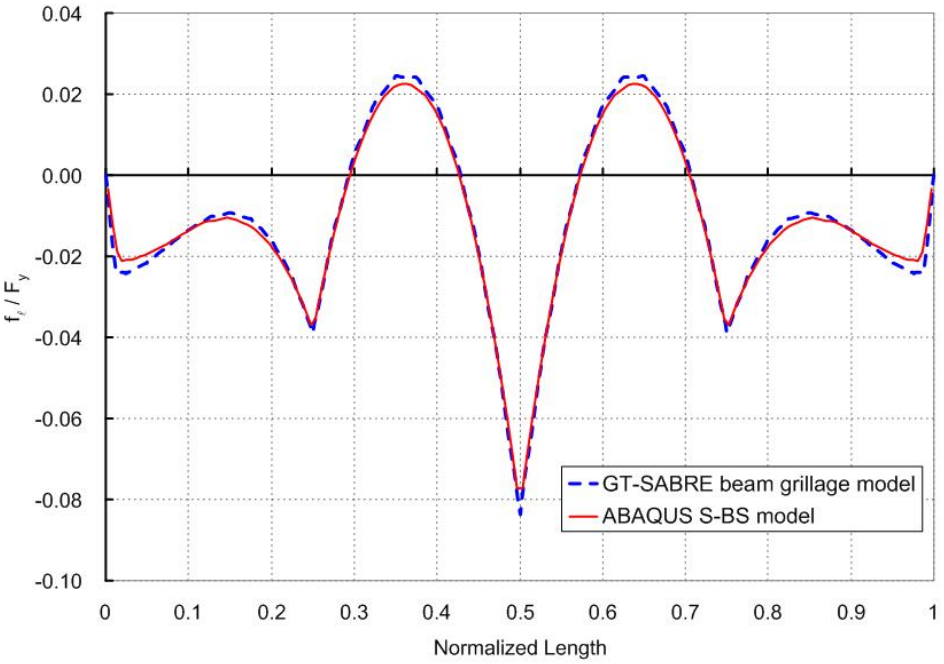

Figure 5.19 Comparison of girder G1 bottom flange lateral bending stresses between GT-SABRE beam grillage model and ABAQUS S-BS model

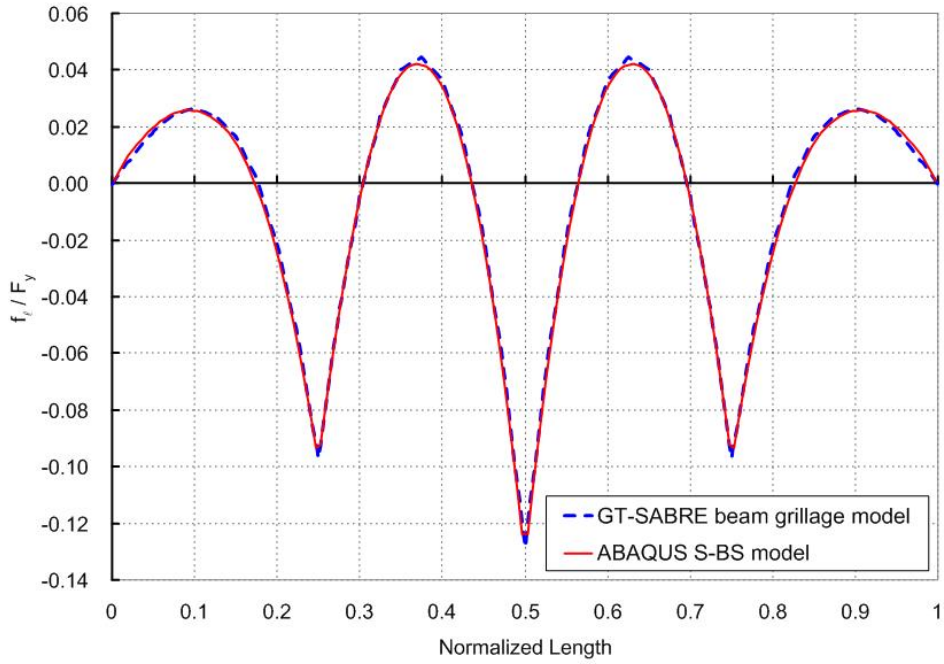

Figure 5.20 Comparison of girder G2 bottom flange lateral bending stresses between GT-SABRE beam grillage model and ABAQUS S-BS model

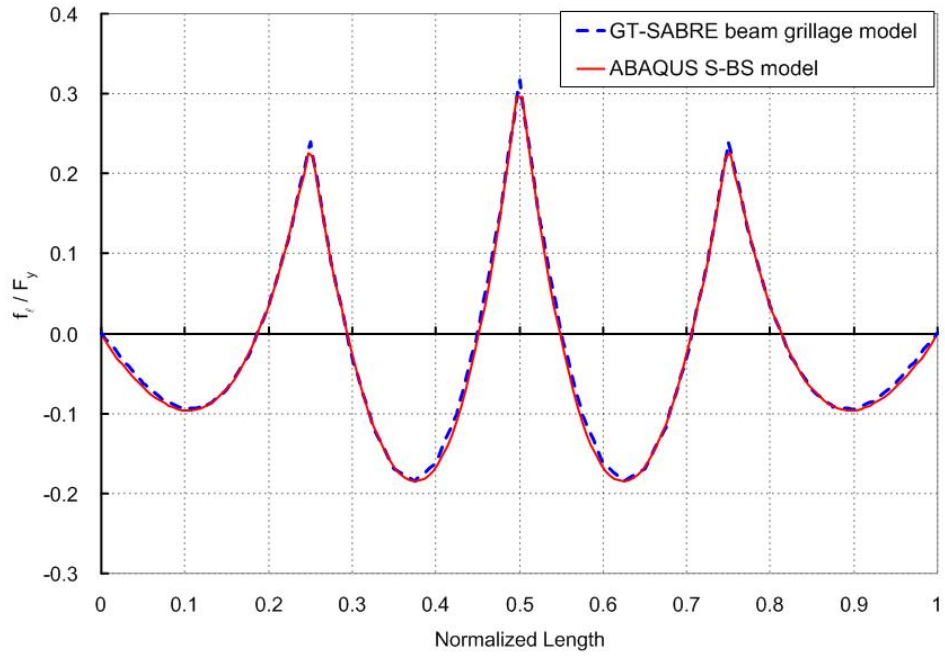

Figure 5.21 Comparison of girder G3 top flange lateral bending stresses between GT-SABRE beam grillage model and ABAQUS S-BS model

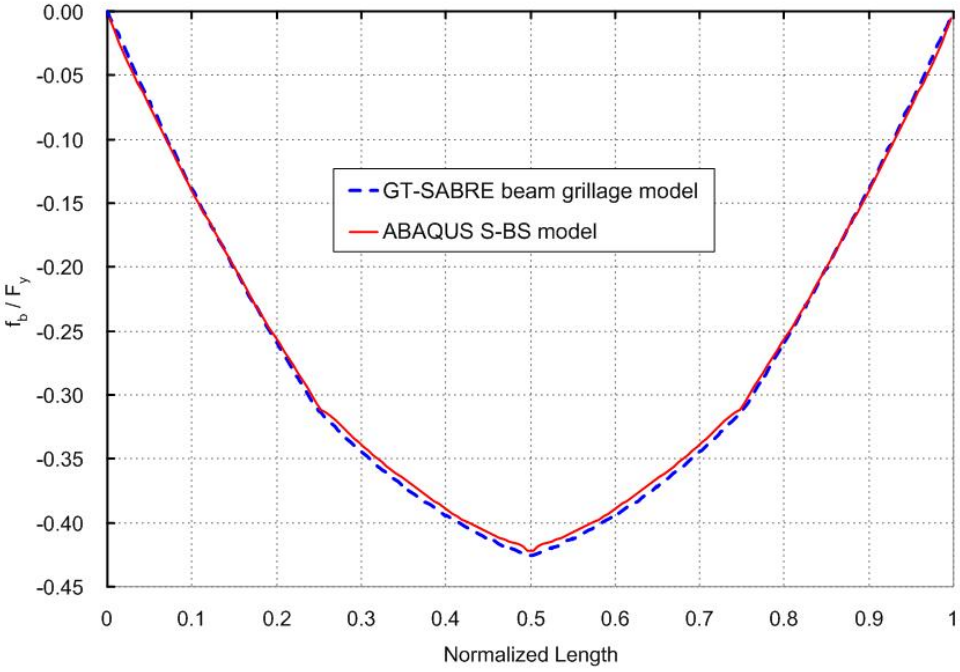

Figure 5.22 Comparison of girder G3 top flange major-axis bending stresses between GT-SABRE beam grillage model and ABAQUS S-BS model

5.4 Example III: Comparison of Beam Grillage Model and Refined Shell-Beam-Shell (S-BS) Model – Composite Bridge under Experimental Load

In this section, slab elements are added to the IIM-NLF non-composite bridge model from Section 5.2 using the method introduced in Section 4.3.6. The experimental loading condition shown in Figure 3.12 is applied to the resulting composite bridge model. The suggested modeling technique for the composite bridge using open-section thin-walled beam elements (the B-BR model discussed in Section 3.4.4) is evaluated. The results from the beam grillage models are compared to the results from a refined S-BS model (Jung 2006), which shows a good match with the experimental data.

5.4.1 Model Description

The girder camber and cross-frame detailing are based on NLF for the solutions shown in this section. This is the same as the camber design and cross-frame detailing used for the composite test bridge. All the slab nodes and the nodes at girder top flanges are created based on the deformed non-composite girder geometry under the steel dead load as described in Section 4.3.6. Since the entire concrete casting operation lasted less than 5 hours, the concrete slab elements are instantiated all at once after the total dead load is applied.

Two beam-grillage models of the composite test bridge are analyzed for the experimental loading pattern with a total applied load of 4,448.2 kN (1000 kips). The difference between these two models is in the definition of the concrete slab grid. For both models, the longitudinal slab elements are modeled such that the full tributary width is included for the slab effective width as indicated in Section 3.4.3 and shown in Figure 5.23. For the transverse slab elements in the first model, in addition to defining transverse slab elements at the cross-frame locations, one additional slab element is placed between the slab elements above the cross-frames. The total width of the

transverse elements is taken as the tributary length along an arc at the mid-distance between the I-girders. In the second model, transverse slab elements are used only at the cross-frame locations. A value of 0.3S is used for these effective transverse slab members as suggested by Huang (1996), where S is the spacing between the longitudinal members. The thickness of all the slab elements is 20.32 cm (8.00 in). All the slab elements are connected to the I-girder top flanges by link elements as explained in Section 3.4.4. The rotational degrees of freedom are released at each top flange node as suggested in Section 3.4.4. The models are similar to the one shown in Figure 3.10 except that the slab elements are modeled with 6-dof displacement-based beam elements.

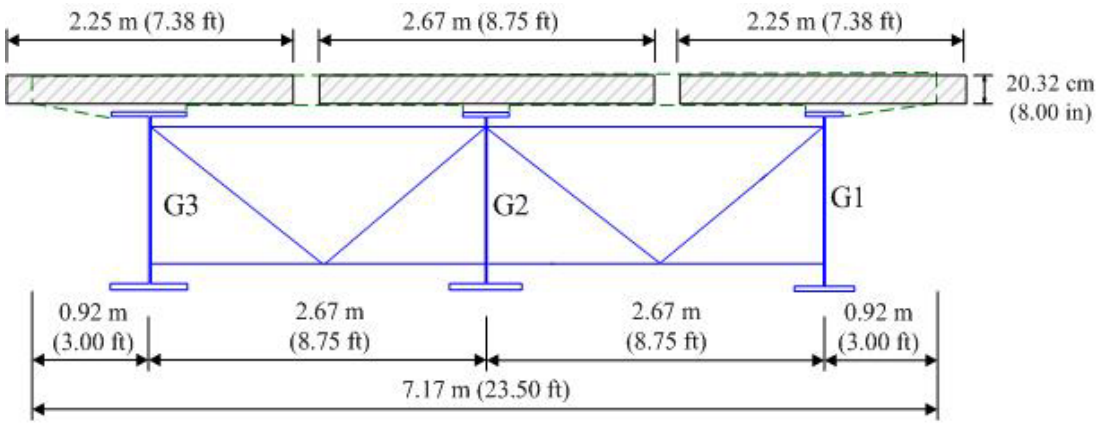

Figure 5.23 Width and thickness of the longitudinal slab elements at each girder

5.4.2 Analysis Results

Figures 5.24 to 5.29 show the analysis results from the two beam grillage models and from the refined Shell-Beam-Shell (S-BS) model (Jung 2006). The beam grillage models are performed with geometric nonlinear analysis while the S-BS model is

performed with full nonlinear analysis. The geometric nonlinearity of the composite bridge behavior is insignificant. The deviation between the curves at higher load levels is due predominantly to the onset of some yielding in the S-BS model.

Figure 5.24 shows the girder G3 vertical deflections at the midspan bottom web-flange juncture under the applied loading on the composite bridge. The girder deflections are the same in both the beam grillage models 1 and 2 and are slightly smaller than in the S-BS model. One of the reasons may be because the Vlasov-type beam element can not account for the shear deformation. Figures 5.25 to 5.27 show the midspan internal moments in each girder. It is found that the load transferred to girder G1 is slightly larger and the load transferred to girder G3 is slightly smaller in the beam grillage model 1, which has a larger number of transverse slab elements than in the beam grillage model 2. As a result, the deflection and the internal moment in girder G3 are slightly smaller in beam grillage model 1 than in beam grillage model 2.

Figures 5.28 and 5.29 show the major-axis and lateral bending stresses at the girder G3 bottom flange from the experiment, the S-BS model and the beam grillage model due to the live load level A, where the total applied load is 2,415 kN (543 kips) as described in Section 3.5.2. The test bridge response is entirely elastic at this load level (Jung 2006). The results from the two beam grillage models are essentially the same and are shown as one curve in Figures 5.28 and 5.29. The flange major-axis bending stresses along the girder length from the beam grillage models are close to the experimental data. The flange lateral bending stresses from the beam grillage models are a reasonably close fit to both the experimental results and to the S-BS model results at this load level.

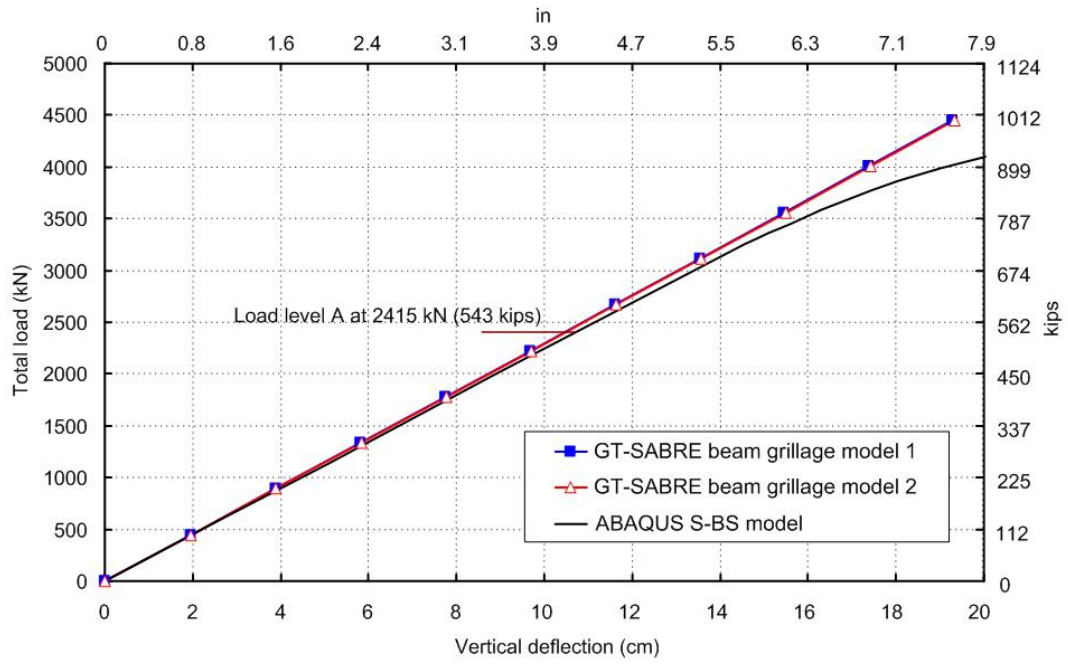

Figure 5.24 Girder G3 vertical deflections at midspan bottom web-flange juncture for beam grillage models and S-BS model subjected to the applied experimental load

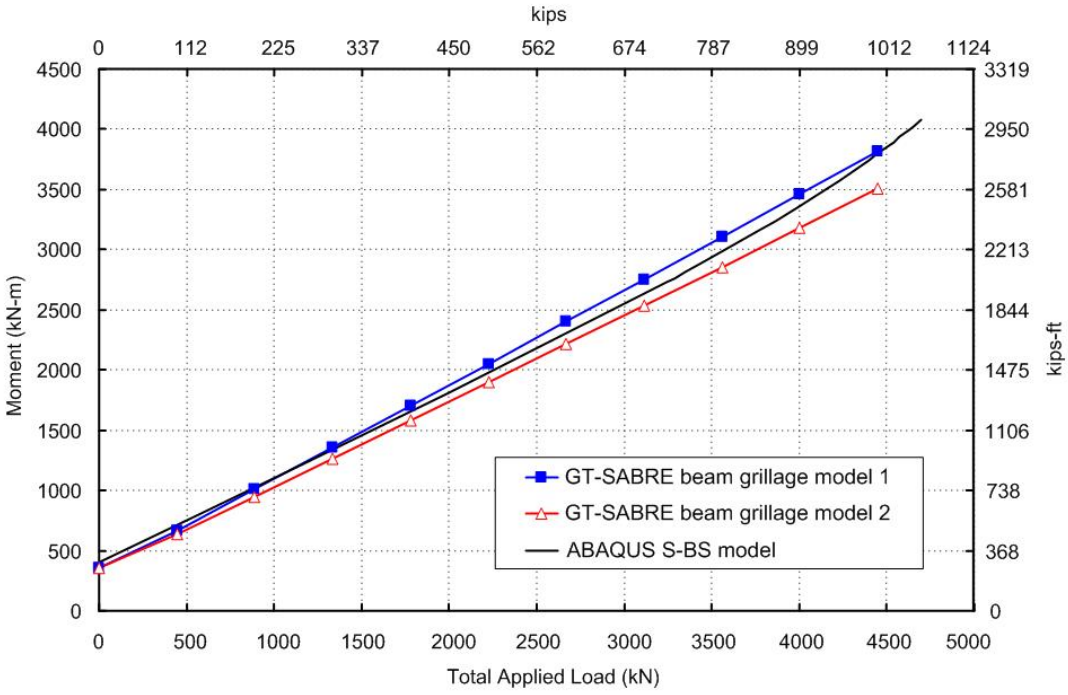

Figure 5.25 Girder G1 internal moment at midspan for beam grillage models and S-BS model subjected to the applied experimental load

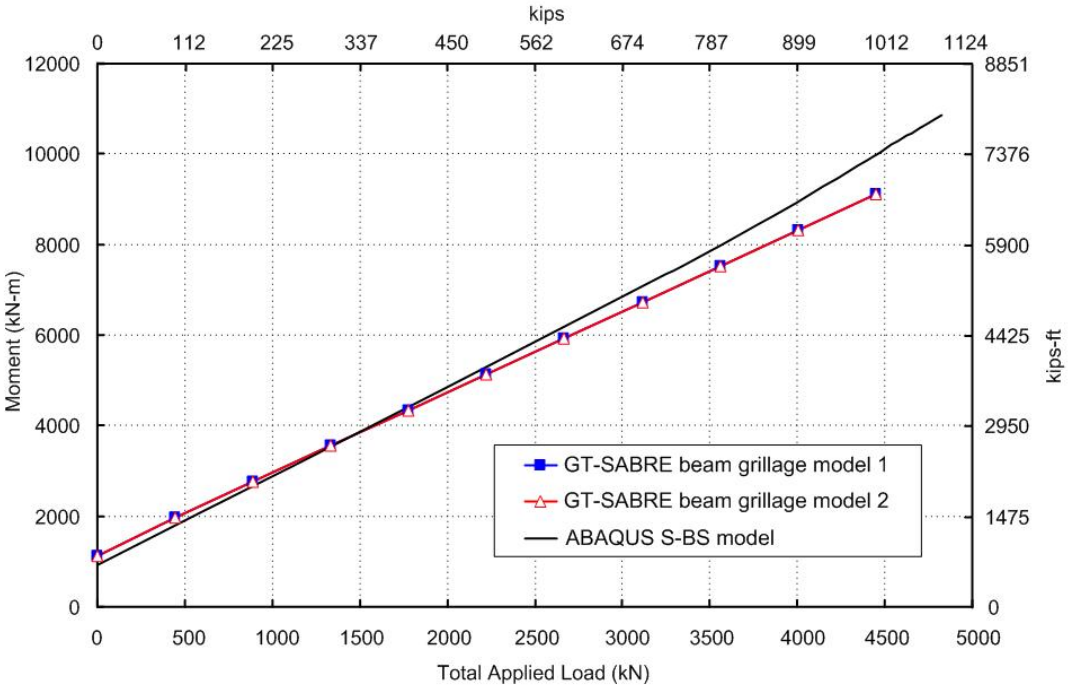

Figure 5.26 Girder G2 internal moment at midspan for beam grillage models and S-BS model subjected to the applied experimental load

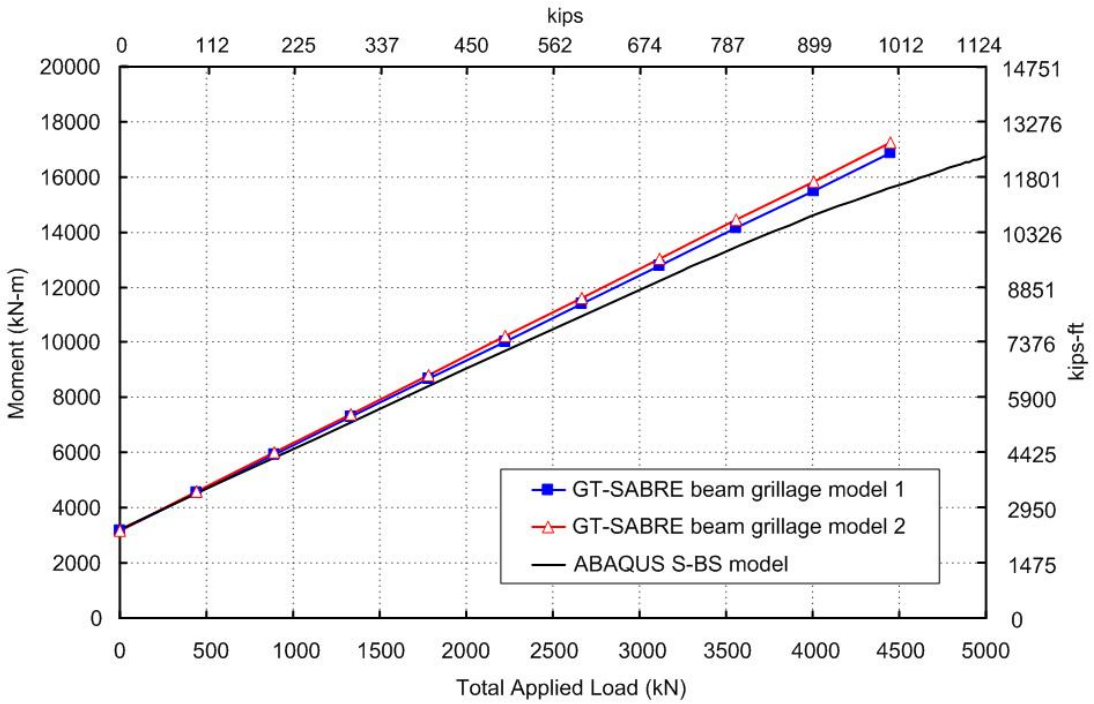

Figure 5.27 Girder G3 internal moment at midspan for beam grillage models and S-BS model subjected to the applied experimental load

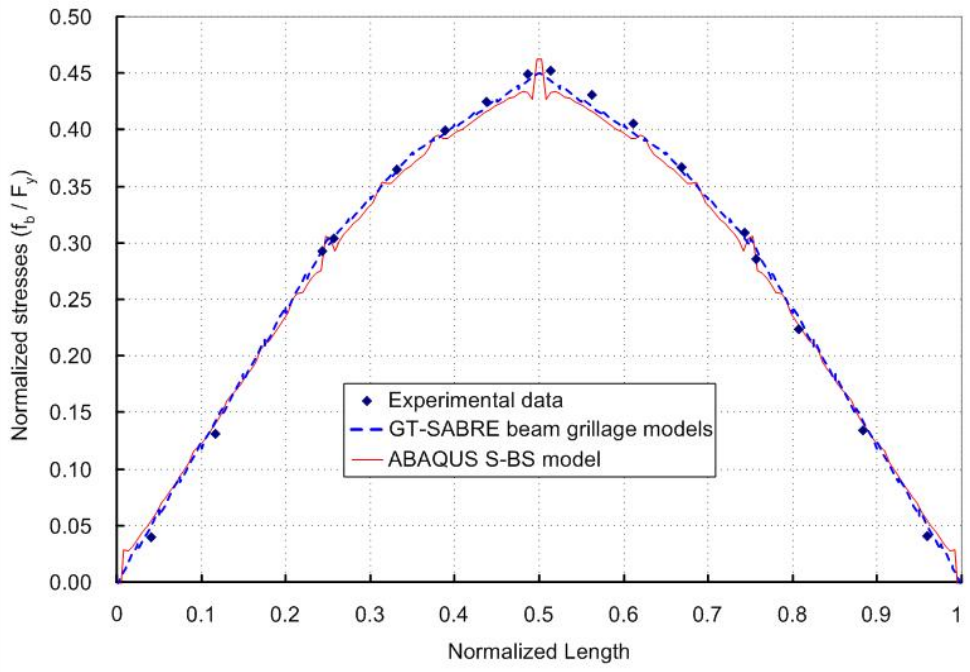

Figure 5.28 Girder G3 bottom flange major-axis bending stresses due to live load (load level A) from experiment, S-BS model and beam grillage model (F_y = 493 MPa (71.5 ksi))

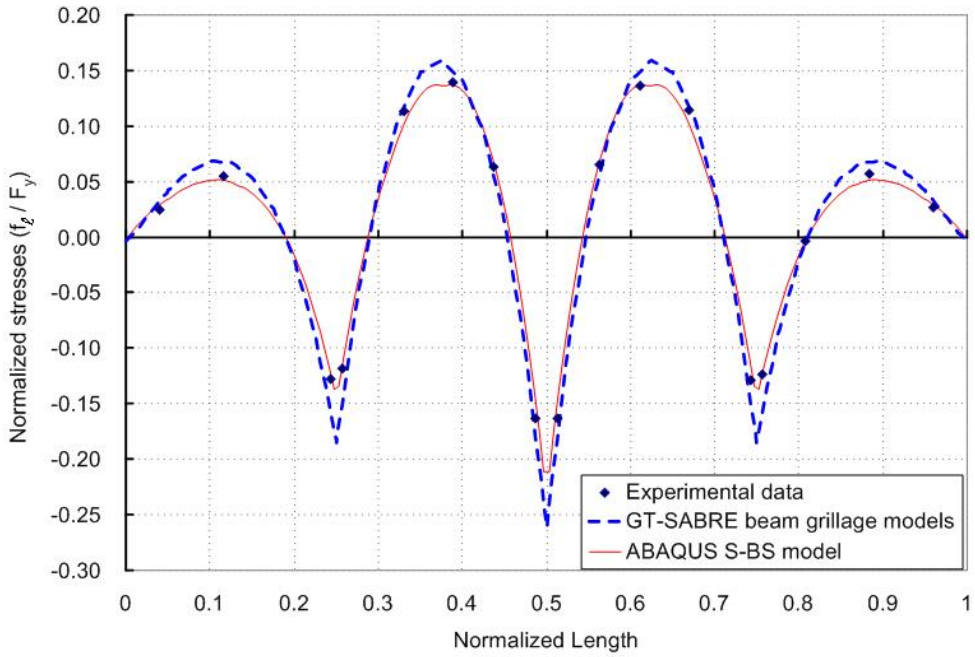

Figure 5.29 Girder G3 bottom flange lateral bending stresses due to live load (load level A) from experiment, S-BS model and beam grillage model (F_y = 493 MPa (71.5 ksi))

CHAPTER 6

APPLICATION 2: THE FORD CITY BRIDGE

6.1 Introduction

The finite element methodologies for the analysis of steel I-girder bridge construction introduced in Chapter 4 have been demonstrated in Chapter 5 by applying them to a full-scale composite I-girder bridge tested at the FHWA TFHRC. In this chapter, a long-span bridge – The Ford City Bridge (PennDOT 1998, Chavel and Earls 2001, 2006a & b) – is utilized for the further demonstration of the proposed finite element methodologies and the capabilities of GT-SABRE. This chapter focuses on the demonstration and evaluation of the staged slab construction analysis capabilities, and the analysis and simulation of an example steel erection sequence. The required crane capacities are investigated in addition to the responses of the bridge components during construction.

Section 6.2 gives an overview of the Ford City Bridge. A description of the finite element model of the Ford City Bridge is provided in Section 6.3. This is followed by studies of the staged slab construction and the influence of different cross-frame detailing methods. The last example of the chapter studies a steel erection sequence for the curved span of the Ford City Bridge. The chapter ends with a summary and concluding remarks.

6.2 Overview of the Ford City Bridge

The Ford City Bridge, shown in Figure 6.1, is a three-span continuous bridge with a total length of 323 m (1060 ft). This bridge was completed in July 2000 to carry

Pennsylvania State Route 128 over the Allegheny River. The Ford City Bridge consists of four I-girders with a web-depth of 4.275 m (14 ft) spaced at 4.1 m (13.5 ft). The width of the bridge deck is 14.7 m (48.2 ft) including two vehicular lanes and a pedestrian walkway. The bridge girders are divided into 11 field sections (FS) with 44 individual girder sections as shown in Figures 6.2 and 6.3. The northernmost span of the Ford City Bridge, which is called the first span in the following, is a curved span with a radius of curvature of 156 m (511 ft) along the bridge center line. The curved length extends about 89 m (292 ft) from the north abutment (bearing abutment I) and then continues with a straight part with 8.8 m (28.8 ft) to the north pier (bearing pier I). The center span (span II) and the southernmost span (span III) are straight and have lengths of 127 m (416.4 ft) and 98 m (321.3 ft), respectively. Figures 6.2 and 6.3 show the plan views of the Ford City Bridge. It should be noted that the distances denoted in Figures 6.2 and 6.3 are the horizontal dimensions of the structure. The actual lengths of the components differ from these lengths due to the grade of the bridge. The design grade of the bridge is -3.0% from the bearing abutment I to a location close to the bearing pier II and then changes to -5.98% for the rest of the bridge.

HPS70W steel is used for the webs and flanges in the negative moment regions over the piers and grade 50 weathering steel is used for the rest of the structure. X-shaped cross-frames are utilized for the entire bridge. Figure 6.4 shows the erected steel superstructure of the Ford City Bridge.

Figure 6.1 The completed Ford City Bridge, Pennsylvania, July 2000
(Courtesy of Pennsylvania DOT)

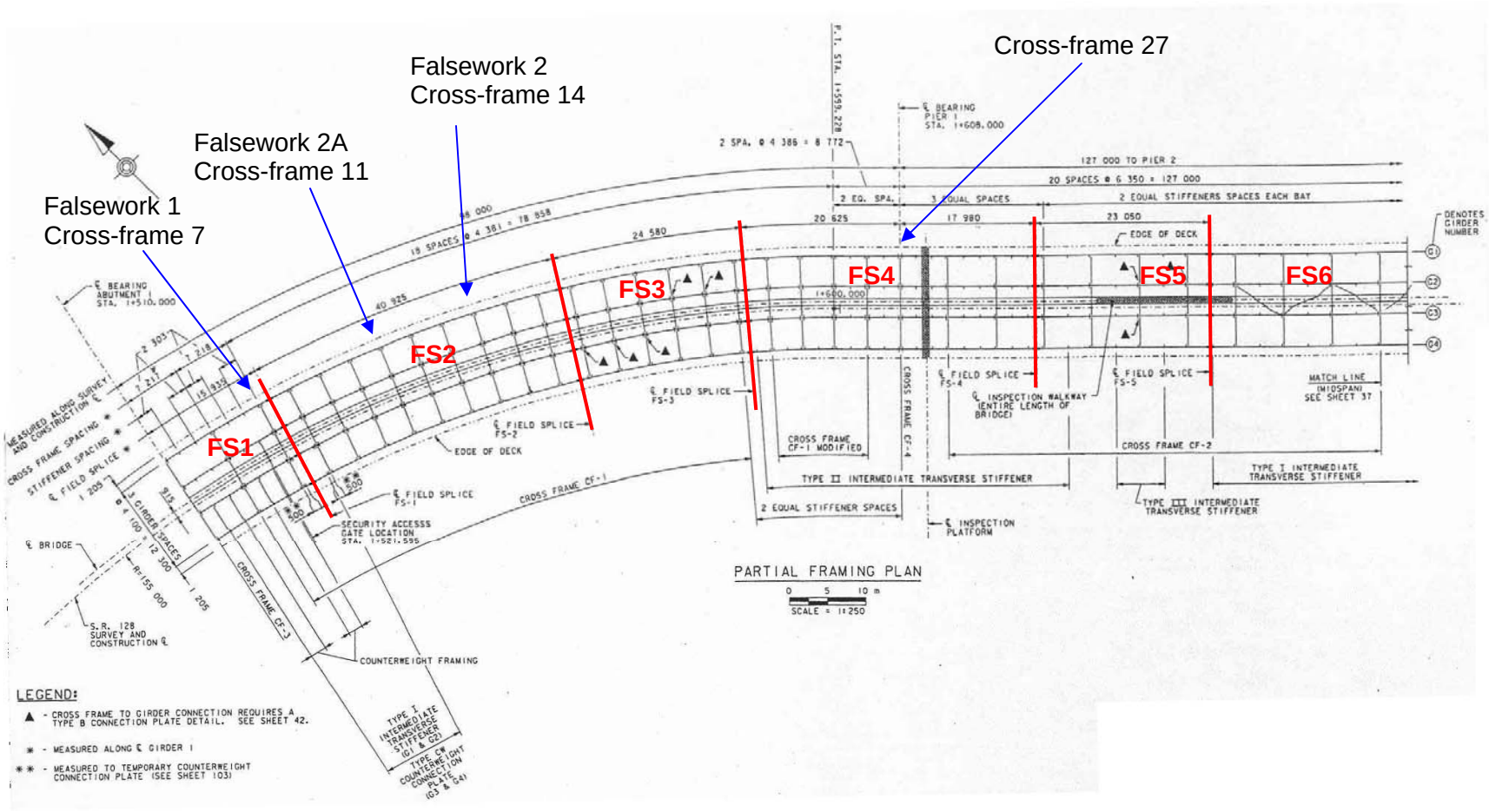

Figure 6.2 Plan view of the Ford City Bridge, all dimensions in mm (Sheet 1) (Courtesy of John Yadlosky, HDR Engineering Inc.)

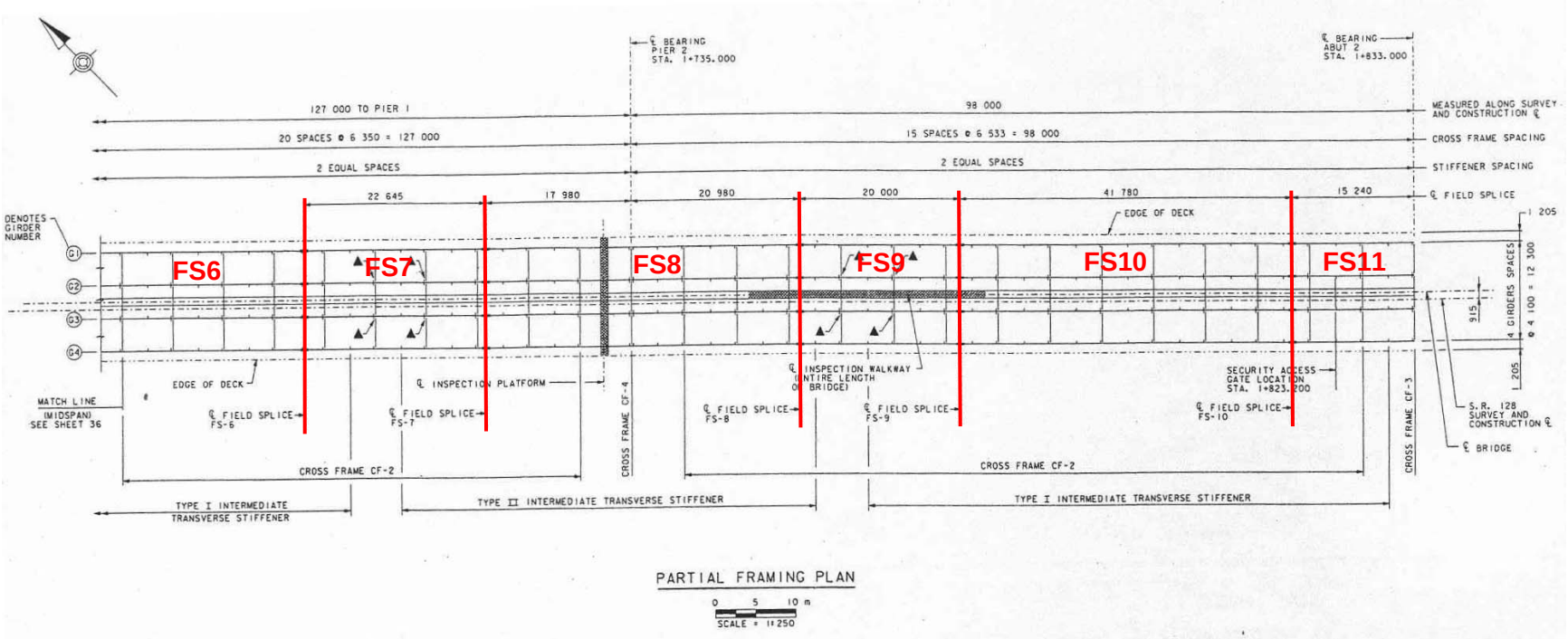

Figure 6.3 Plan view of the Ford City Bridge, all dimensions in mm (Sheet 2) (Courtesy of John Yadlosky, HDR Engineering Inc.)

Figure 6.4 The steel superstructure of the Ford City Bridge (reprinted with permission from Chavel and Earls (2001))

6.2.1 I-Girder and Cross-Frame Details

Most of the girder sections in the Ford City Bridge are singly-symmetric. Also, the girder web depth remains constant at 4.275 m (14 ft) throughout the structure. However, the flange dimensions and web thicknesses of each girder section are usually different from one section to another. The constant radii of curvature of the girders from outside girder to inside girder in the curved span are 162.1 m (531.7 ft), 158.0 (518.3 ft), 153.9 m (504.8 ft) and 149.8 m (491.4 ft). The subtended angle of the complete curved length is 0.5757 radians (32.98 degrees). Figures 6.5 to 6.8 show the elevations of girders G1, G2, G3 and G4. The distances denoted in Figures 6.5 to 6.8 represent the horizontal

distances rather than the actual lengths of the girders. Typical bridge sections are shown in Figure 6.9.

The cross-frame spacing is not uniform along the entire bridge length but is equal within certain lengths as shown in Figures 6.2 and 6.3. There are four different cross-frame sizes used in the bridge as shown in Figures 6.10 to 6.13. All of the cross-frames were assembled and their connections were pre-drilled at the fabrication shop (Chavel and Earls 2001).

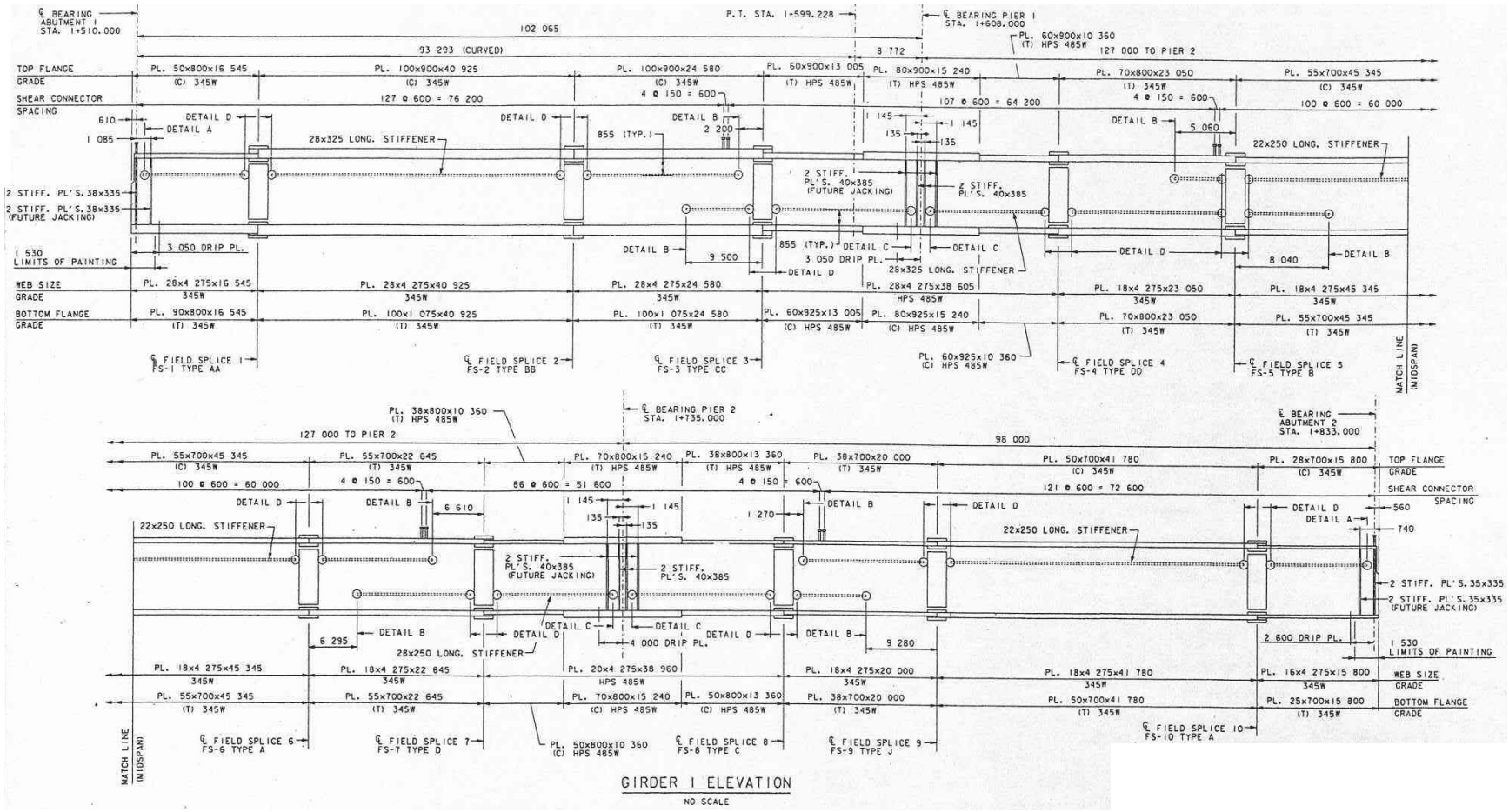

Figure 6.5 The Ford City Bridge girder G1 elevation, all dimensions in mm (Courtesy of John Yadlosky, HDR Engineering Inc.)

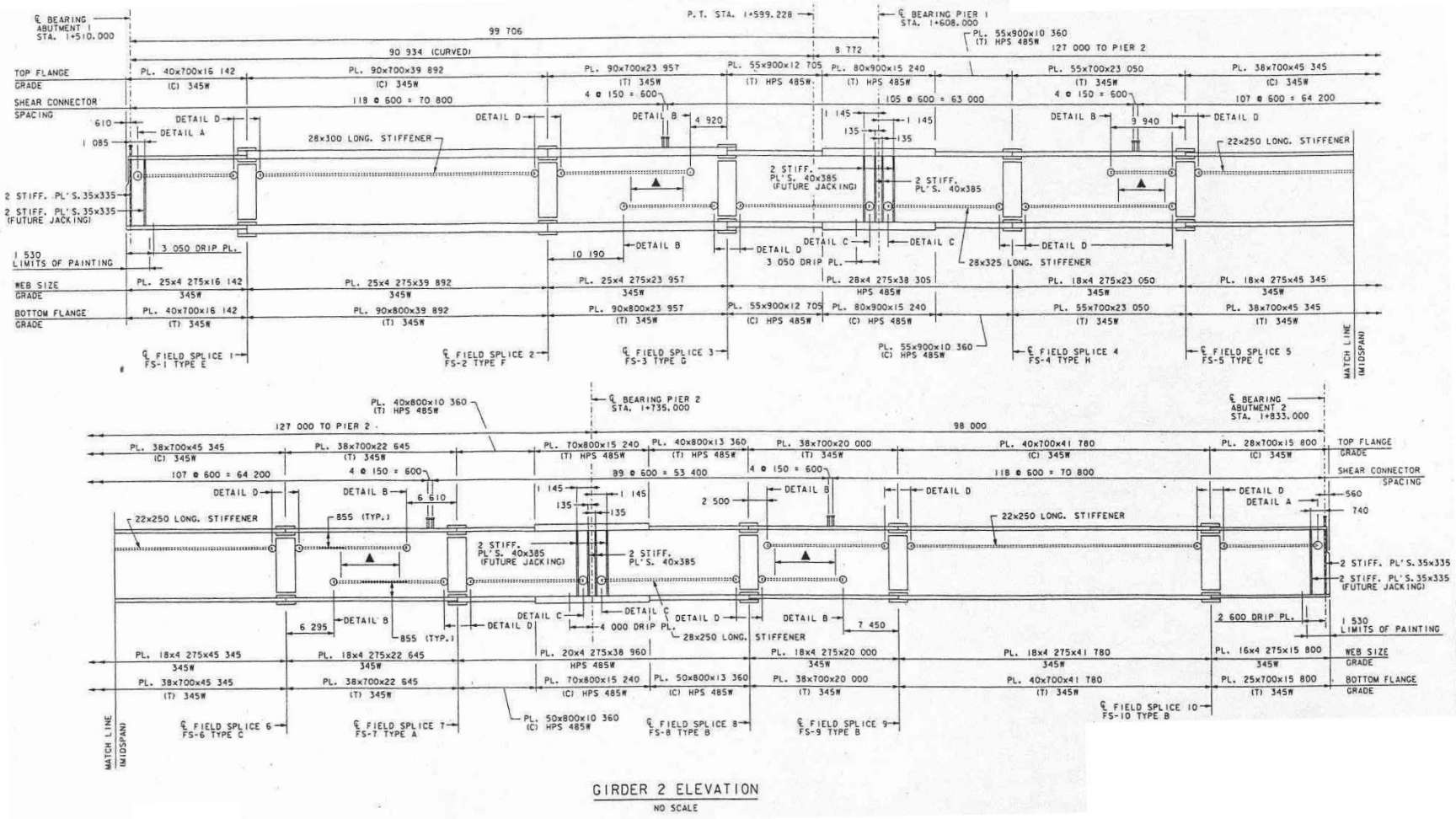

Figure 6.6 The Ford City Bridge girder G2 elevation, all dimensions in mm (Courtesy of John Yadlosky, HDR Engineering Inc.)

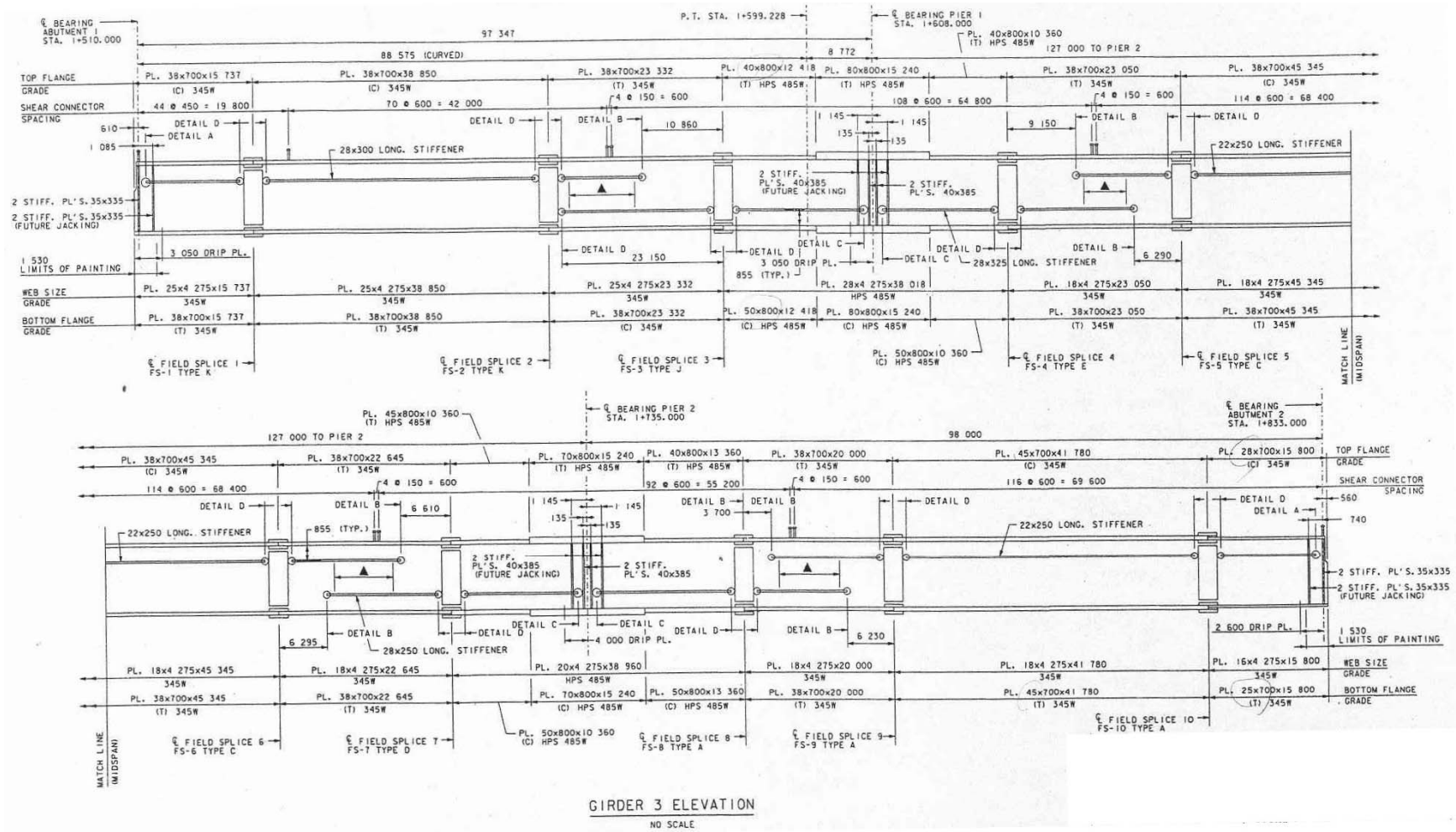

Figure 6.7 The Ford City Bridge girder G3 elevation, all dimensions in mm (Courtesy of John Yadlosky, HDR Engineering Inc.)

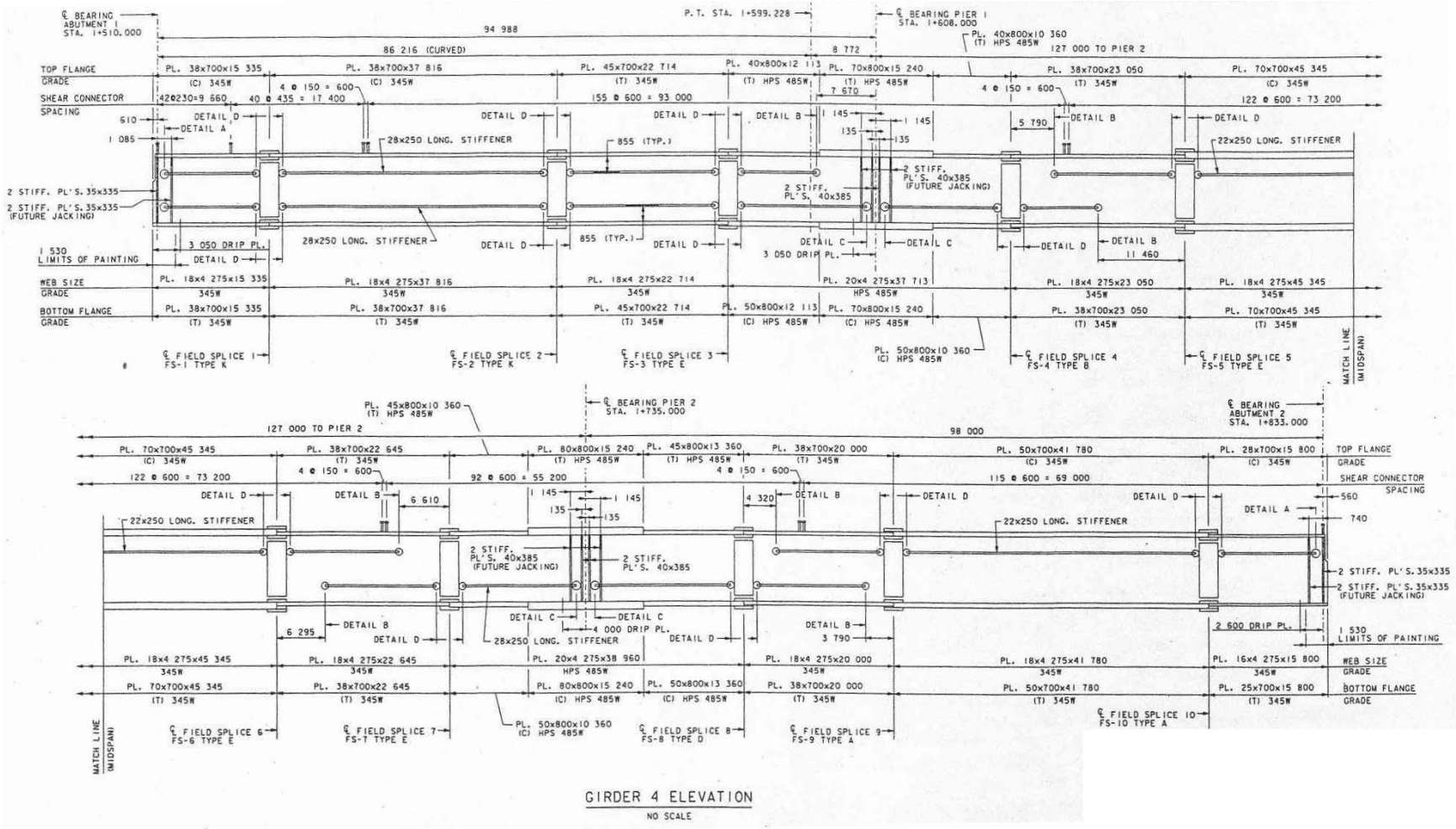

GIRDER 4 ELEVATION

NO SCALE

Figure 6.8 The Ford City Bridge girder G4 elevation, all dimensions in mm (Courtesy of John Yadlosky, HDR Engineering Inc.)

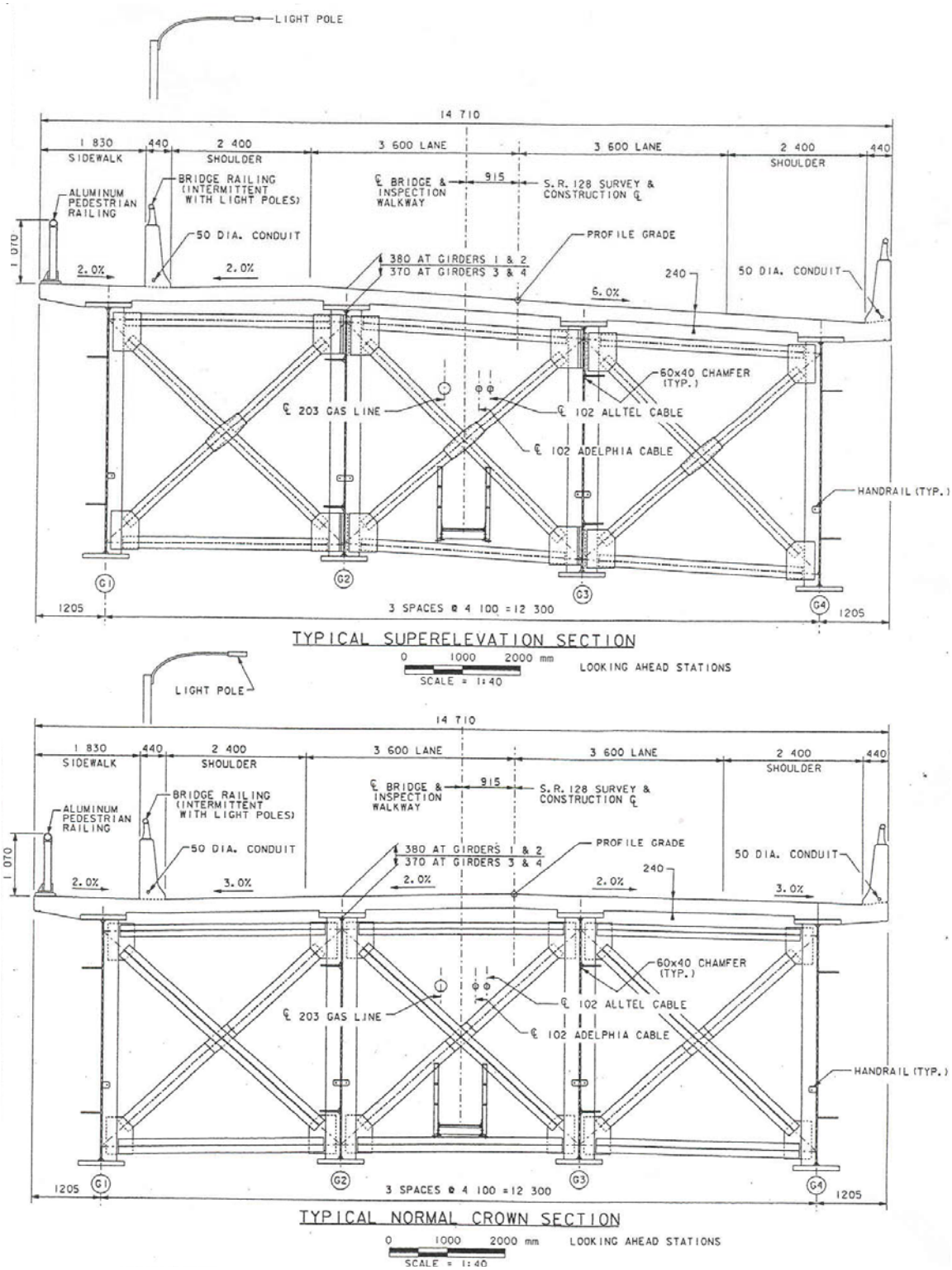

Figure 6.9 Typical bridge sections and girder ratings of the Ford City Bridge, all dimensions in mm (Courtesy of John Yadlosky, HDR Engineering Inc.)

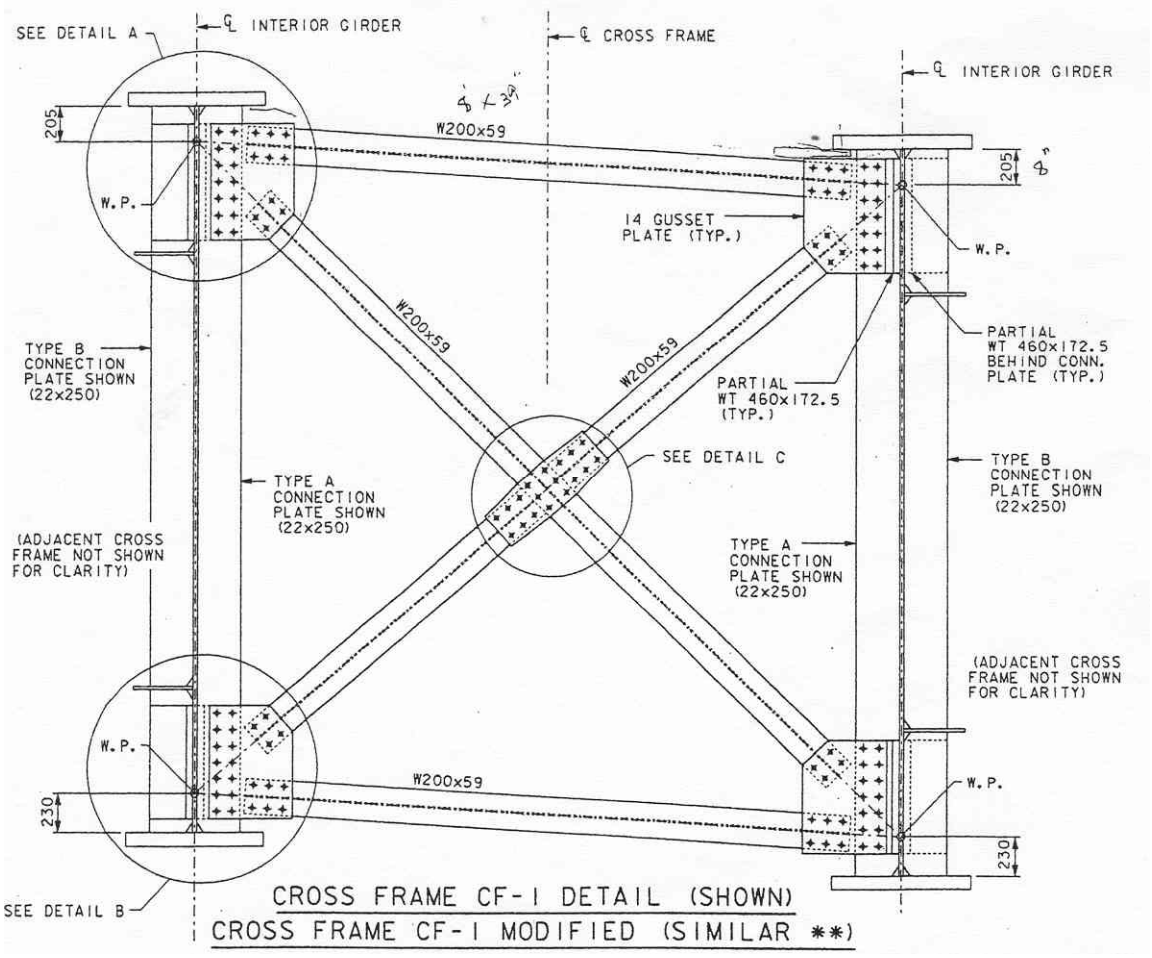

Figure 6.10 The Ford City Bridge cross-frame CF-1 detail, all dimensions in mm (Courtesy of John Yadlosky, HDR Engineering Inc.)

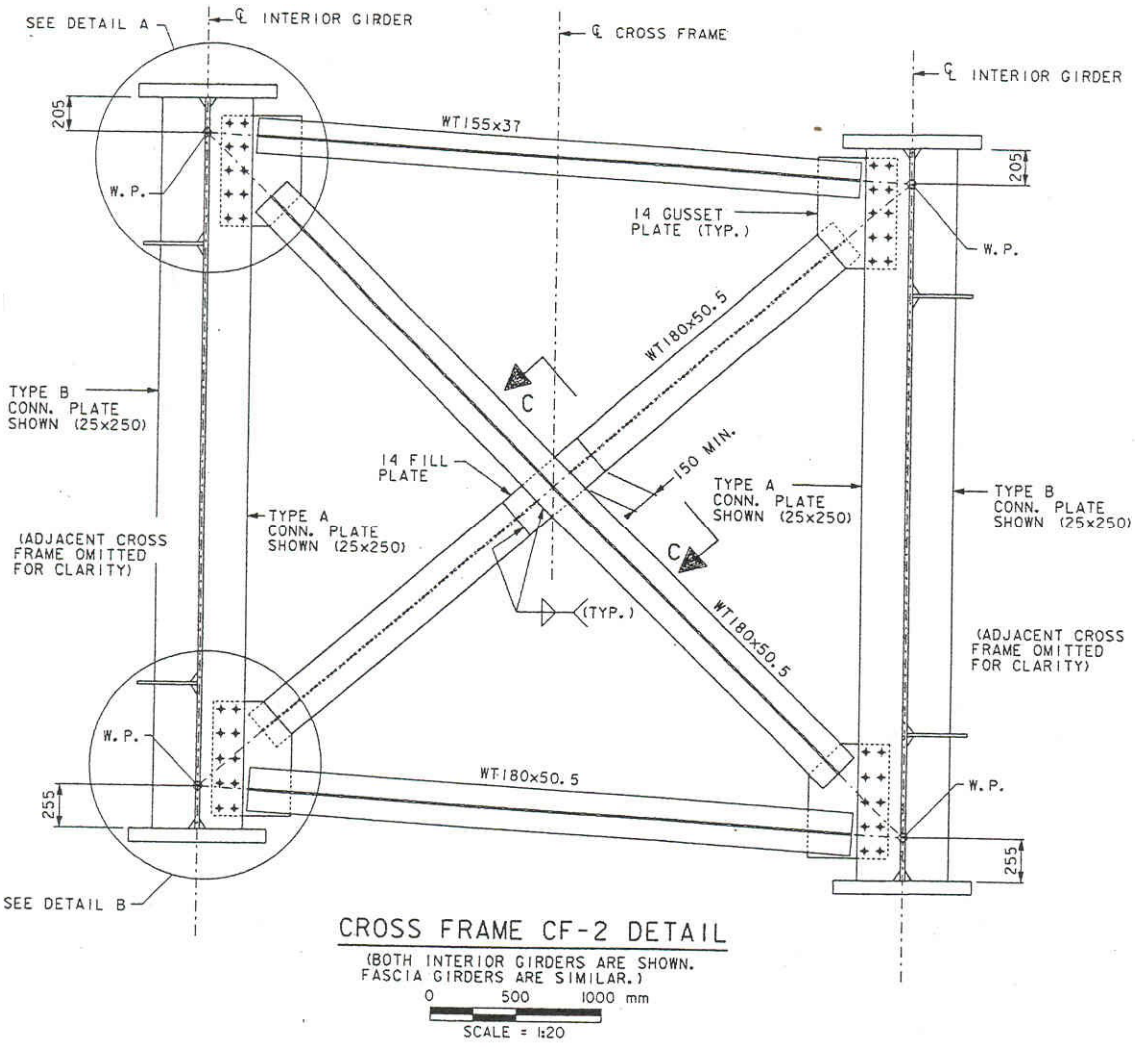

Figure 6.11 The Ford City Bridge cross-frame CF-2 detail, all dimensions in mm (Courtesy of John Yadlosky, HDR Engineering Inc.)

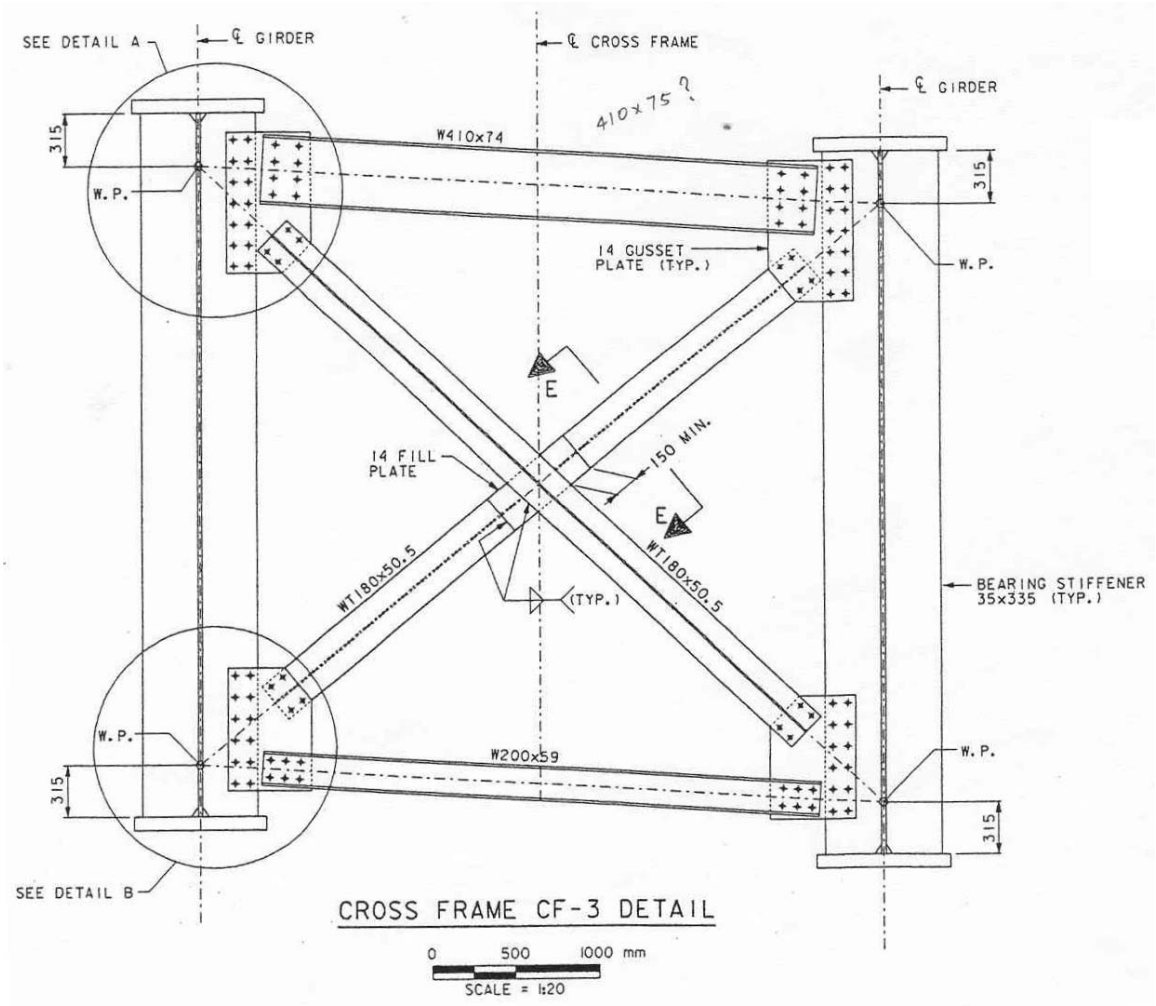

Figure 6.12 The Ford City Bridge cross-frame CF-3 detail, all dimensions in mm (Courtesy of John Yadlosky, HDR Engineering Inc.)

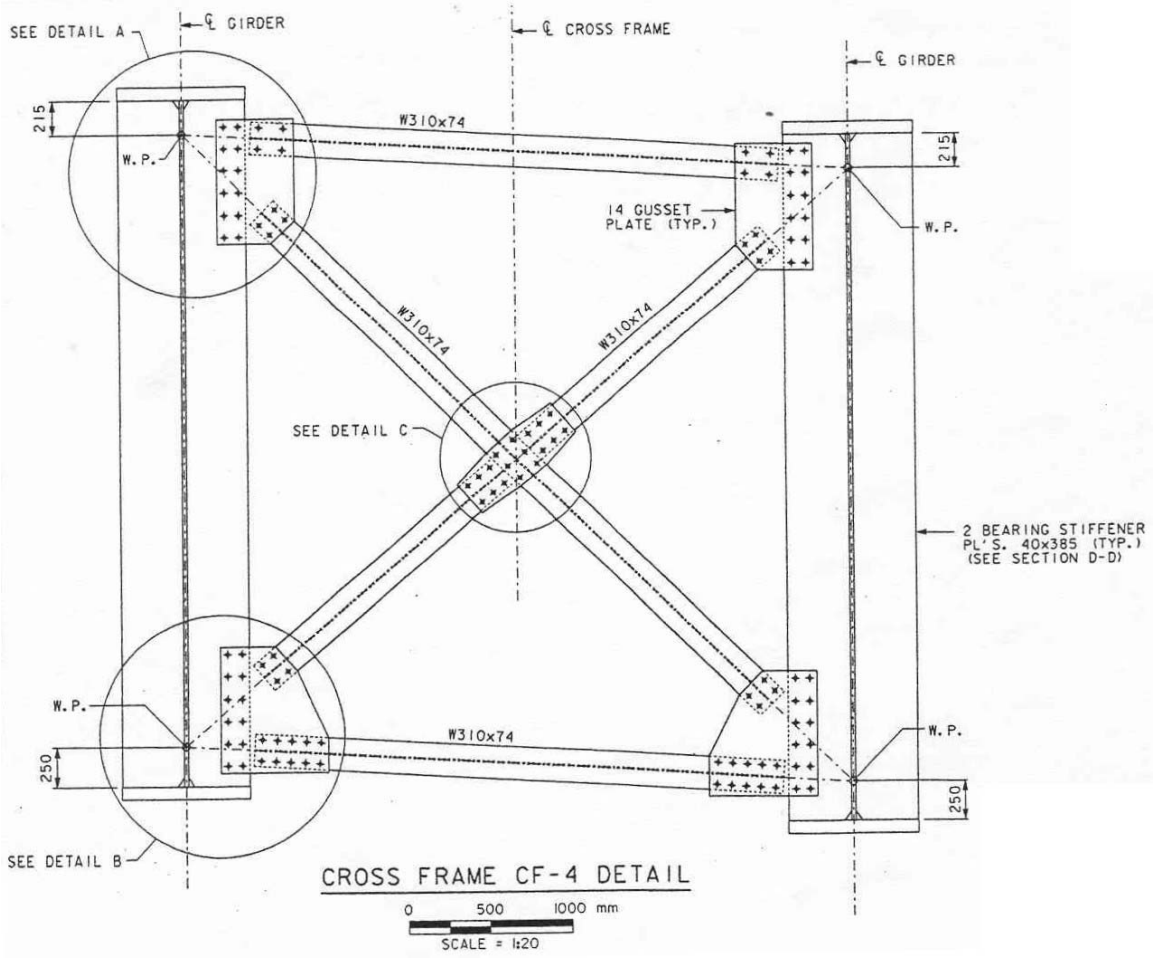

Figure 6.13 The Ford City Bridge cross-frame CF-4 detail, all dimensions in mm (Courtesy of John Yadlosky, HDR Engineering Inc.)

6.2.2 Miscellaneous Characteristics

Falseworks (temporary supports) were placed within the end spans (span I and III) to control the girder deflections and stabilize the girders during the steel erection. There were three falseworks within the curved span. Falsework 1 was located below cross-frame 7, falsework 2A was below cross-frame 11 and falsework 2 was placed at

cross-frame 14 location as shown in Figure 6.2. Also, brackets were utilized at the piers to stabilize the girder sections during the erection.

Field-splices were used to connect two of the field sections during the steel erection. The girder cross-sections are usually different from one girder section to another in the Ford City Bridge.

Lateral bracing was used between the top flanges of the two interior girders (G2 and G3) to limit the lateral displacements due to wind loads. Field-drilled connections were utilized to install the lateral bracing.

The bridge slab is a 24.0 cm (9.4 in) thick cast-in-place concrete slab with 14.0 cm (5.5 in) haunches for the outside two girders G1 and G2 and 13.0 cm (5.1 in) haunches for the inside two girders G3 and G4. The slab overhangs have a width of 120.5 cm (47.4 in) and the girder spacing is 4.1 m (13.45 ft). The total width of the bridge deck is 14.7 m (48.2 ft). The girders are composite with the slab throughout the structure. A typical concrete deck profile is shown in Figure 6.14.

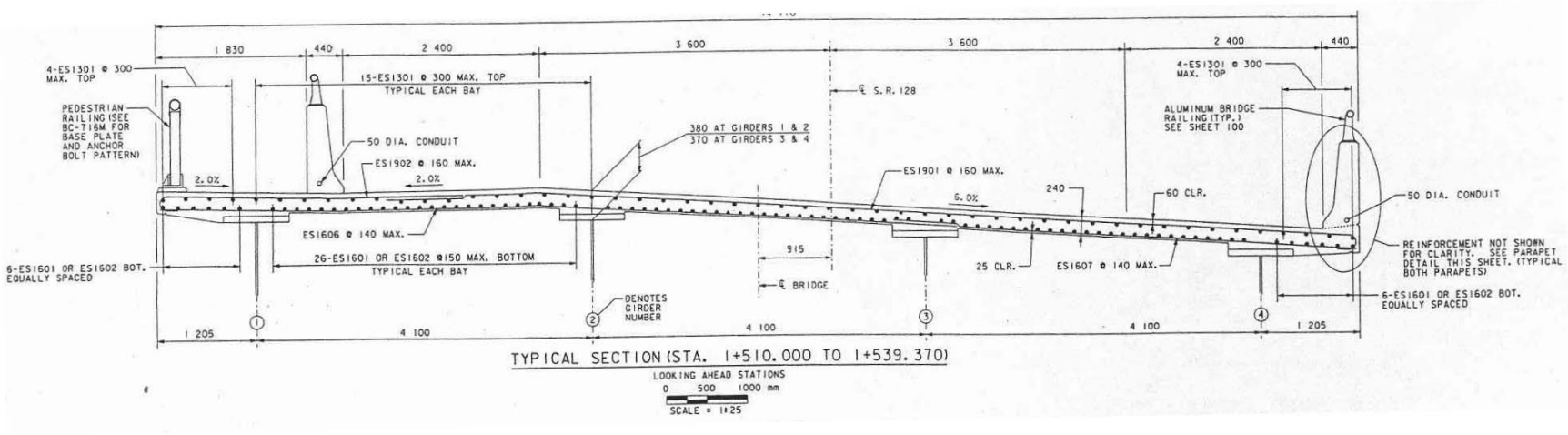

Figure 6.14 Typical concrete deck profile of the Ford City Bridge, all dimensions in mm (Courtesy of John Yadlosky, HDR Inc.)

6.3 Finite Element Model of the Ford City Bridge

6.3.1 General Model Description

The I-girders of the Ford City Bridge are modeled with the open-section thin-walled beam elements derived in Chapter 2. The initial curvature associated with the horizontal curvature, the vertical curve of the girders and the vertical camber is handled as an initial displacement effect as discussed in Section 2.1. Cross-section transitions are modeled using tapered elements as indicated in Section 4.3.5.2 and in Figures 4.9 and 4.10. Tapered elements are used on both sides of the splice location. The length of each tapered element is taken to be the largest flange width at the splice location.

The cross-frames are modeled using truss elements for the diagonals and the top chord, and using the 6-dof beam element based on the Chapter 2 developments for the bottom chords. It should be noted that as discussed in Section 5.2 (see also Section 4.3.5.3), when simulating the cross-frame installation, the top chord of a cross-frame is modeled with a beam element and the rotation at the end of the chord first attached to a girder is constrained to the corresponding girder degrees of freedom (to prevent the cross-frame from swinging about the connection point to the girder). The rotational degrees of freedom are released after the installation is completed such that the beam element then behaves as a truss element. The bottom chord of a cross-frame is modeled with a beam element. In addition, in order to compare the analysis results from the SAM (Sequentially Assembled Model) and IIM (Instantaneously Instantiated Model), all the rotational continuities at the connections between the girders and cross-frame bottom chords are released at the last step of the installation to avoid bending due to changes in orientation at the connecting points as discussed in Section 5.2.1. That is,

the cross-frame members are idealized as truss elements (no local bending) within the final constructed geometry.

The slab elements are modeled with the 6-dof displacement-based elements. The width of longitudinal slab elements is equal to the tributary width. Transverse slab elements in the grid model of the slab are placed only over the top of each cross location. The width of the transverse slab elements are taken as 0.3 of the girder spacing as suggested by Huang (1996).

The overall modeling considerations for composite I-girder bridges have been introduced in Section 3.3. The cross-frame members are connected to the girder nodes by rigid offset connections. A rigid offset constraint is used to model the elevation of the bearing supports. Also, a gap element is used to handle potential uplift at certain bearing locations. The boundary conditions for the entire Ford City Bridge are shown in Figure 6.15. In addition to the vertical restraint at the abutments and piers, radial/lateral restraints are placed at the girder G3 bottom flange at each bearing location. Furthermore, longitudinal restraints are placed on all four girder bottom flanges at pier I. Figure 6.15 also labels the slab casting sequence for the Ford City Bridge, discussed subsequently.

The dead loads considered in this study include the steel and concrete weights. The torsional forces on the facia girders from the deck cantilever brackets supporting the slab overhangs during construction of the slab are accounted for by equivalent torques applied to the facia girder nodes along the girder lengths. These equivalent torques are removed at the end of the slab casting sequence. A steel density of 0.077 N/cm^3 (7.85 x 10^3 kg/m^3, or 0.490 kip/ft^3) is used to estimate the steel dead load. The concrete unit weight w'_c is taken as 0.0228 N/cm^3 (2.30 x 10^3 kg/m^3, or 0.145 kip/ft^3). The steel modulus of elasticity E is taken as 2.0 x 10^7 N/cm^2 (29,000 ksi). The concrete modulus

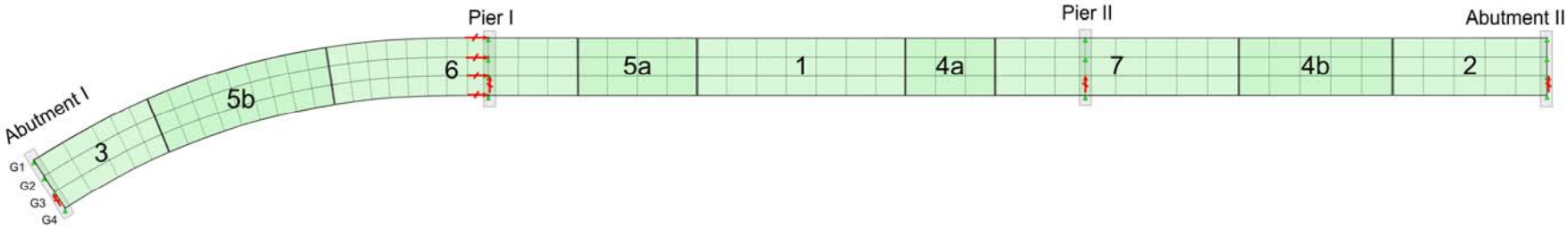

Figure 6.15 The Ford City Bridge boundary conditions and slab casting sequence

of elasticity E_c is calculated based on the AASHTO (2004) equation:

$$E_c = 33{,}000\, K_1\, w_c^{1.5} \sqrt{f_c'} \quad \text{(ksi)}$$

In which K_1 is the correction factor for source of aggregate and is taken as 1.0, and f'_c is the compressive strength of concrete and is taken as 4.5 ksi. With w'_c = 0.145 kcf, E_c becomes 3,865 ksi or 2.665 x 10^6 N/cm^2. The wet concrete load is applied at the girder top flange.

6.3.2 Girder Geometry

6.3.2.1 Designed Girder Final Geometry

As discussed in Secton 1.2, generally the overall structural plan geometry is shown for the cross section in its flat position (Gaylord et al 1997). To define the girder final geometry, the grade and superelevation need to be considered. For the Ford City Bridge, it is possible to define the girder final geometries using the flat structural geometry and the provided grade and superelevation. However, it is more precise and straightforward to define the final geometry based on the designed deck contours and elevations, which are based on the specified grade and superelevation. In the current study, the designed girder final geometry is calculated based on the specified deck contours and elevations. The point at station I+608.0 (bearing pier 1) on the profile grade line on the deck surface and the centerline of the bridge is selected as the origin of the global Cartesian coordinate system. The elevation at the origin of the global Cartesian coordinate system is taken as the reference elevation. Tables 6.1 and 6.2 show the designed elevations of the slab top surface and the calculated elevations of the girder mid-web depth along the bridge length relative to the reference elevation.

The calculated relative elevation of the girder mid-web depth to the reference elevation is treated as an initial displacement of the girder from the idealized flat position. Figures 6.16 to 6.19 indicate that the modeled girder final geometry in GT-SABRE closely matches the designed girder final geometry. It is emphasized that the final geometry is the desired geometry of the bridge girders after the camber has been taken out by the vertical deflections under the total dead load. The next section addresses the handling of the girder vertical cambers. It should be noted that no attempt is made in this research to compare the calculated girder geometries to the actual geometries of the Ford City Bridge girders. To the author's knowledge, this precise information is not available. The focus in this research is on the demonstration and evaluation of the capabilities developed in GT-SABRE utilizing the engineering drawings for the Ford City Bridge and approaching the calculations as the construction engineering problem for a bridge yet to be built. The camber design is also addressed in this work. That is, the required cambers are calculated using the GT-SABRE software. Furthermore, the detailing of the cross-frames, discussed subsequently, is approached from the perspective of the engineering for a bridge yet to be constructed.

6.3.2.2 Designed Girder Initial Geometry – Consideration of Cambers

As discussed previously in Section 5.3.2, the required vertical camber is influenced by the type of detailing selected for the cross-frames. Also, the dead loads calculated in this research based on the available information may not be precisely the dead loads assumed in the original calculation of the girder cambers specified on the engineering drawings. Therefore, the girder cambers are redesigned based on the author's calculated steel and concrete weights for the current study. The girder camber design is considered both with and without staged slab casting. The superimposed dead loads including parapets, pedestrian railing, utilities, etc. are not included in the

calculation of the cambers. The load-height effects of the wet concrete load are considered. Further discussion of the camber design is provided in Section 6.4.2.

Table 6.1 Ford City Bridge designed girder final elevations of Segment 1 (Sta. I+510.0 m ~ I+647.0 m)

Station (m)	Elevation of the slab top surface (m)				Normalized Length	Elevation of the girder mid-web depth (m)				Elevation of girder mid-web-depth relative to the reference elevation (m)			
	G1	G2	G3	G4		G1	G2	G3	G4	G1	G2	G3	G4
510.000	263.780	263.769	263.523	263.277	**0.000**	261.263	261.252	261.016	260.770	**0.6525**	**0.6415**	**0.4055**	**0.1595**
512.848	263.695	263.683	263.437	263.191	0.021	261.178	261.166	260.930	260.684	0.5675	0.5555	0.3195	0.0735
515.696	263.609	263.598	263.352	263.106	0.042	261.092	261.081	260.845	260.599	0.4815	0.4705	0.2345	-0.0115
518.544	263.524	263.513	263.267	263.021	0.062	261.007	260.996	260.760	260.514	0.3965	0.3855	0.1495	-0.0965
521.392	263.439	263.427	263.181	262.935	0.083	260.922	260.910	260.674	260.428	0.3115	0.2995	0.0635	-0.1825
					0.100	Interpolation				**0.2418**	**0.2306**	**-0.0054**	**-0.2514**
524.240	263.353	263.342	263.096	262.850	0.104	260.836	260.825	260.589	260.343	0.2255	0.2145	-0.0215	-0.2675
527.088	263.268	263.256	263.010	262.764	0.125	260.751	260.739	260.503	260.257	0.1405	0.1285	-0.1075	-0.3535
529.936	263.182	263.171	262.925	262.679	0.146	260.665	260.654	260.418	260.172	0.0545	0.0435	-0.1925	-0.4385
532.784	263.097	263.085	262.839	262.593	0.166	260.580	260.568	260.332	260.086	-0.0305	-0.0425	-0.2785	-0.5245
535.632	263.011	263.000	262.754	262.508	0.187	260.494	260.483	260.247	260.001	-0.1165	-0.1275	-0.3635	-0.6095
					0.200	Interpolation				**-0.1693**	**-0.1803**	**-0.4163**	**-0.6623**
538.480	262.926	262.915	262.669	262.423	0.208	260.409	260.398	260.162	259.916	-0.2015	-0.2125	-0.4485	-0.6945
541.328	262.840	262.829	262.583	262.337	0.229	260.323	260.312	260.076	259.830	-0.2875	-0.2985	-0.5345	-0.7805
544.177	262.755	262.744	262.498	262.252	0.249	260.238	260.227	259.991	259.745	-0.3725	-0.3835	-0.6195	-0.8655
547.025	262.670	262.658	262.412	262.166	0.270	260.153	260.141	259.905	259.659	-0.4575	-0.4695	-0.7055	-0.9515
549.873	262.584	262.573	262.327	262.081	0.291	260.067	260.056	259.820	259.574	-0.5435	-0.5545	-0.7905	-1.0365
					0.300	Interpolation				**-0.5801**	**-0.5916**	**-0.8276**	**-1.0736**
552.721	262.499	262.487	262.241	261.995	0.312	259.982	259.970	259.734	259.488	-0.6285	-0.6405	-0.8765	-1.1225
555.569	262.413	262.402	262.156	261.910	0.333	259.896	259.885	259.649	259.403	-0.7145	-0.7255	-0.9615	-1.2075
558.417	262.328	262.316	262.070	261.824	0.353	259.811	259.799	259.563	259.317	-0.7995	-0.8115	-1.0475	-1.2935
561.265	262.242	262.231	261.985	261.739	0.374	259.725	259.714	259.478	259.232	-0.8855	-0.8965	-1.1325	-1.3785
564.113	262.157	262.146	261.900	261.654	0.395	259.640	259.629	259.393	259.147	-0.9705	-0.9815	-1.2175	-1.4635
					0.400	Interpolation				**-0.9912**	**-1.0022**	**-1.2382**	**-1.4842**
566.961	262.071	262.060	261.814	261.568	0.416	259.554	259.543	259.307	259.061	-1.0565	-1.0675	-1.3035	-1.5495
569.809	261.986	261.975	261.729	261.483	0.437	259.469	259.458	259.222	258.976	-1.1415	-1.1525	-1.3885	-1.6345
572.657	261.901	261.889	261.643	261.397	0.457	259.384	259.372	259.136	258.890	-1.2265	-1.2385	-1.4745	-1.7205
575.505	261.815	261.804	261.558	261.312	0.478	259.298	259.287	259.051	258.805	-1.3125	-1.3235	-1.5595	-1.8055
578.353	261.730	261.718	261.472	261.226	0.499	259.213	259.201	258.965	258.719	-1.3975	-1.4095	-1.6455	-1.8915
					0.500					**-1.4019**	**-1.4139**	**-1.6499**	**-1.8959**
581.201	261.644	261.633	261.387	261.141	0.520	259.127	259.116	258.880	258.634	-1.4835	-1.4945	-1.7305	-1.9765
584.049	261.559	261.547	261.301	261.055	0.541	259.042	259.030	258.794	258.548	-1.5685	-1.5805	-1.8165	-2.0625
586.897	261.473	261.462	261.216	260.970	0.561	258.956	258.945	258.709	258.463	-1.6545	-1.6655	-1.9015	-2.1475
589.745	261.388	261.377	261.131	260.885	0.582	258.871	258.860	258.624	258.378	-1.7395	-1.7505	-1.9865	-2.2325
					0.600	Interpolation				**-1.8128**	**-1.8246**	**-2.0606**	**-2.3066**
592.593	261.303	261.291	261.045	260.799	0.603	258.786	258.774	258.538	258.292	-1.8245	-1.8365	-2.0725	-2.3185
595.441	261.217	261.206	260.960	260.714	0.624	258.700	258.689	258.453	258.207	-1.9105	-1.9215	-2.1575	-2.4035
598.298	261.132	261.120	260.874	260.628	0.645	258.615	258.603	258.367	258.121	-1.9955	-2.0075	-2.2435	-2.4895
599.220	261.103	261.092	260.846	260.600	0.651	258.586	258.575	258.339	258.093	-2.0245	-2.0355	-2.2715	-2.5175
602.000	260.992	260.985	260.754	260.521	0.672	258.475	258.468	258.247	258.014	-2.1355	-2.1425	-2.3635	-2.5965
605.000	260.872	260.870	260.655	260.436	0.693	258.355	258.353	258.148	257.929	-2.2555	-2.2575	-2.4625	-2.6815
					0.700	Interpolation				**-2.2915**	**-2.2920**	**-2.4925**	**-2.7070**
608.000	260.752	260.755	260.555	260.351	0.715	258.235	258.238	258.048	257.844	-2.3755	-2.3725	-2.5625	-2.7665
611.000	260.632	260.639	260.455	260.266	0.737	258.115	258.122	257.948	257.759	-2.4955	-2.4885	-2.6625	-2.8515
614.000	260.512	260.524	260.356	260.180	0.759	257.995	258.007	257.849	257.673	-2.6155	-2.6035	-2.7615	-2.9375
617.000	260.391	260.408	260.256	260.095	0.781	257.874	257.891	257.749	257.588	-2.7365	-2.7195	-2.8615	-3.0225
					0.800	Interpolation				**-2.8405**	**-2.8192**	**-2.9473**	**-3.0962**
620.000	260.271	260.293	260.157	260.010	0.803	257.754	257.776	257.650	257.503	-2.8565	-2.8345	-2.9605	-3.1075
623.000	260.151	260.178	260.057	259.925	0.825	257.634	257.661	257.550	257.418	-2.9765	-2.9495	-3.0605	-3.1925
626.000	260.031	260.062	259.958	259.839	0.847	257.514	257.545	257.451	257.332	-3.0965	-3.0655	-3.1595	-3.2785
629.000	259.911	259.947	259.858	259.754	0.869	257.394	257.430	257.351	257.247	-3.2165	-3.1805	-3.2595	-3.3635
632.000	259.792	259.833	259.764	259.666	0.891	257.275	257.316	257.257	257.159	-3.3355	-3.2945	-3.3535	-3.4515
					0.900	Interpolation				**-3.3862**	**-3.3430**	**-3.3925**	**-3.4905**
635.000	259.675	259.721	259.674	259.576	0.912	257.158	257.204	257.167	257.069	-3.4525	-3.4065	-3.4435	-3.5415
638.000	259.558	259.609	259.584	259.486	0.934	257.041	257.092	257.077	256.979	-3.5695	-3.5185	-3.5335	-3.6315
641.000	259.441	259.496	259.494	259.396	0.956	256.924	256.979	256.987	256.889	-3.6865	-3.6315	-3.6235	-3.7215
644.000	259.324	259.384	259.404	259.306	0.978	256.807	256.867	256.897	256.799	-3.8035	-3.7435	-3.7135	-3.8115
647.000	**259.214**	**259.278**	**259.314**	**259.216**	**1.000**	**256.697**	**256.761**	**256.807**	**256.709**	**-3.9135**	**-3.8495**	**-3.8035**	**-3.9015**

Table 6.2 Ford City Bridge designed girder final elevations of Segment 2 (Sta. I+647.0 m ~ I+833.0 m)

Station (m)	Elevation of the slab top surface (m)				Normalized Length	Elevation of the girder mid-web depth (m)				Elevation of girder mid-web-depth relative to the reference elevation (m)			
	G1	G2	G3	G4		G1	G2	G3	G4	G1	G2	G3	G4
647.000	**259.214**	**259.278**	**259.314**	**259.216**	**1.000**	**256.697**	**256.761**	**256.807**	**256.709**	**-3.9135**	**-3.8495**	**-3.8035**	**-3.9015**
650.000	259.124	259.188	259.224	259.126	1.016	256.607	256.671	256.717	256.619	-4.0035	-3.9395	-3.8935	-3.9915
653.000	259.034	259.098	259.134	259.036	1.032	256.517	256.581	256.627	256.529	-4.0935	-4.0295	-3.9835	-4.0815
656.000	258.944	259.008	259.044	258.946	1.048	256.427	256.491	256.537	256.439	-4.1835	-4.1195	-4.0735	-4.1715
659.000	258.854	258.918	258.954	258.856	1.065	256.337	256.401	256.447	256.349	-4.2735	-4.2095	-4.1635	-4.2615
662.000	258.764	258.828	258.864	258.766	1.081	256.247	256.311	256.357	256.259	-4.3635	-4.2995	-4.2535	-4.3515
665.000	258.674	258.738	**258.774**	258.676	1.097	256.157	256.221	256.267	256.169	-4.4535	-4.3895	-4.3435	-4.4415
					1.100	Interpolation							**-4.4715**
668.000	258.584	258.648	258.684	258.586	1.113	256.067	256.131	256.177	256.079	-4.5435	-4.4795	-4.4335	-4.5315
671.000	258.494	258.558	258.594	258.496	1.129	255.977	256.041	256.087	255.989	-4.6335	-4.5695	-4.5235	-4.6215
674.000	258.403	258.466	258.503	258.404	1.145	255.886	255.949	255.996	255.897	-4.7245	-4.6615	-4.6145	-4.7135
677.000	258.309	258.372	258.409	258.311	1.161	255.792	255.855	255.902	255.804	-4.8185	-4.7555	-4.7085	-4.8065
680.000	258.214	258.277	258.314	258.215	1.177	255.697	255.760	255.807	255.708	-4.9135	-4.8505	-4.8035	-4.9025
683.000	258.116	258.180	258.216	258.118	1.194	255.599	255.663	255.709	255.611	-5.0115	-4.9475	-4.9015	-4.9995
					1.200	Interpolation							**-5.0511**
686.000	258.017	258.080	258.117	258.019	1.210	255.500	255.563	255.610	255.512	-5.1105	-5.0475	-5.0005	-5.0985
689.000	257.916	257.979	258.016	257.918	1.226	255.399	255.462	255.509	255.411	-5.2115	-5.1485	-5.1015	-5.1995
692.000	257.813	257.876	257.913	257.814	1.242	255.296	255.359	255.406	255.307	-5.3145	-5.2515	-5.2045	-5.3035
695.000	257.708	257.771	257.808	257.709	1.258	255.191	255.254	255.301	255.202	-5.4195	-5.3565	-5.3095	-5.4085
698.000	257.601	257.664	257.701	257.603	1.274	255.084	255.147	255.194	255.096	-5.5265	-5.4635	-5.4165	-5.5145
701.000	257.492	257.555	257.592	257.494	1.290	254.975	255.038	255.085	254.987	-5.6355	-5.5725	-5.5255	-5.6235
					1.300	Interpolation							**-5.7021**
704.000	257.381	257.445	257.481	257.383	1.306	254.864	254.928	254.974	254.876	-5.7465	-5.6825	-5.6365	-5.7345
707.000	257.269	257.332	257.369	257.270	1.323	254.752	254.815	254.862	254.763	-5.8585	-5.7955	-5.7485	-5.8475
710.000	257.154	257.217	257.254	257.156	1.339	254.637	254.700	254.747	254.649	-5.9735	-5.9105	-5.8635	-5.9615
713.000	257.038	257.101	257.138	257.039	1.355	254.521	254.584	254.631	254.532	-6.0895	-6.0265	-5.9795	-6.0785
716.000	256.919	256.982	257.020	256.921	1.371	254.402	254.465	254.512	254.414	-6.2085	-6.1455	-6.0977	-6.1965
716.000	256.919	256.982	257.020	256.921	1.371	254.402	254.465	254.512	254.414	-6.2085	-6.1455	-6.0977	-6.1965
719.000	256.799	256.862	256.899	256.800	1.387	254.282	254.345	254.392	254.293	-6.3285	-6.2655	-6.2185	-6.3175
					1.400	Interpolation							**-6.4261**
722.000	256.677	256.740	256.777	256.678	1.403	254.160	254.223	254.270	254.171	-6.4505	-6.3875	-6.3405	-6.4395
725.000	256.552	256.616	256.652	256.554	1.419	254.035	254.099	254.145	254.047	-6.5755	-6.5115	-6.4655	-6.5635
728.000	256.426	256.490	256.526	256.428	1.435	253.909	253.973	254.019	253.921	-6.7015	-6.6375	-6.5915	-6.6895
731.000	256.298	256.362	256.398	256.300	1.452	253.781	253.845	253.891	253.793	-6.8295	-6.7655	-6.7195	-6.8175
734.000	256.168	256.232	256.268	256.170	1.468	253.651	253.715	253.761	253.663	-6.9595	-6.8955	-6.8495	-6.9475
735.000	256.125	256.188	256.225	256.126	1.473	253.608	253.671	253.718	253.619	-7.0025	-6.9395	-6.8925	-6.9915
737.000	256.037	256.100	256.137	256.038	1.484	253.520	253.583	253.630	253.531	-7.0905	-7.0275	-6.9805	-7.0795
740.000	255.903	255.966	256.003	255.904	**1.500**	253.386	253.449	253.496	253.397	**-7.2245**	**-7.1615**	**-7.1145**	**-7.2135**
743.000	255.767	255.831	255.867	255.769	1.516	253.250	253.314	253.360	253.262	-7.3605	-7.2965	-7.2505	-7.3485
746.000	255.630	255.693	255.730	255.631	1.532	253.113	253.176	253.223	253.124	-7.4975	-7.4345	-7.3875	-7.4865
749.000	255.490	255.553	255.590	255.492	1.548	252.973	253.036	253.083	252.985	-7.6375	-7.5745	-7.5275	-7.6255
752.000	255.349	255.412	255.449	255.350	1.565	252.832	252.895	252.942	252.843	-7.7785	-7.7155	-7.6685	-7.7675
755.000	255.205	255.269	255.305	255.207	1.581	252.688	252.752	252.798	252.700	-7.9225	-7.8585	-7.8125	-7.9105
758.000	255.060	255.124	255.160	255.062	1.597	252.543	252.607	252.653	252.555	-8.0675	-8.0035	-7.9575	-8.0555
					1.600	Interpolation							**-8.0969**
761.000	254.913	254.976	255.013	254.915	1.613	252.396	252.459	252.506	252.408	-8.2145	-8.1515	-8.1045	-8.2025
764.000	254.764	254.827	254.864	254.766	1.629	252.247	252.310	252.357	252.259	-8.3635	-8.3005	-8.2535	-8.3515
767.000	254.613	254.676	254.713	254.615	1.645	252.096	252.159	252.206	252.108	-8.5145	-8.4515	-8.4045	-8.5025
770.000	254.460	254.512	254.560	254.462	1.661	251.943	251.995	252.053	251.955	-8.6675	-8.6155	-8.5575	-8.6555
773.000	254.305	254.369	254.405	254.307	1.677	251.788	251.852	251.898	251.800	-8.8225	-8.7585	-8.7125	-8.8105
776.000	254.148	254.212	254.248	254.150	1.694	251.631	251.695	251.741	251.643	-8.9795	-8.9155	-8.8695	-8.9675
					1.700	Interpolation							**-9.0427**
779.000	253.990	254.053	254.090	253.991	1.710	251.473	251.536	251.583	251.484	-9.1375	-9.0745	-9.0275	-9.1265
782.000	253.829	253.893	253.929	253.831	1.726	251.312	251.376	251.422	251.324	-9.2985	-9.2345	-9.1885	-9.2865
785.000	253.667	253.730	253.767	253.668	1.742	251.150	251.213	251.260	251.161	-9.4605	-9.3975	-9.3505	-9.4495
788.000	253.502	253.566	253.602	253.504	1.758	250.985	251.049	251.095	250.997	-9.6255	-9.5615	-9.5155	-9.6135
791.000	253.336	253.399	253.436	253.338	1.774	250.819	250.882	250.929	250.831	-9.7915	-9.7285	-9.6815	-9.7795
794.000	253.168	253.231	253.268	253.170	1.790	250.651	250.714	250.761	250.663	-9.9595	-9.8965	-9.8495	-9.9475
					1.800	Interpolation							**-10.0615**
797.000	252.998	253.061	253.098	252.999	1.806	250.481	250.544	250.591	250.492	-10.1295	-10.0665	-10.0195	-10.1185
800.000	252.826	252.889	252.926	252.827	1.823	250.309	250.372	250.419	250.320	-10.3015	-10.2385	-10.1915	-10.2905
803.000	252.652	252.715	252.752	252.653	1.839	250.135	250.198	250.245	250.146	-10.4755	-10.4125	-10.3655	-10.4645
806.000	252.476	252.539	252.576	252.477	1.855	249.959	250.022	250.069	249.970	-10.6515	-10.5885	-10.5415	-10.6405
809.000	252.298	252.361	252.398	252.300	1.871	249.781	249.844	249.891	249.793	-10.8295	-10.7665	-10.7195	-10.8175
812.000	252.119	252.182	252.219	252.120	1.887	249.602	249.665	249.712	249.613	-11.0085	-10.9455	-10.8985	-10.9975
					1.900	Interpolation							**-11.1629**
815.000	251.926	252.003	252.048	251.971	1.903	249.409	249.486	249.541	249.464	-11.2015	-11.1245	-11.0695	-11.1465
818.000	251.731	251.823	251.878	251.826	1.919	249.214	249.306	249.371	249.319	-11.3965	-11.3045	-11.2395	-11.2915
821.000	251.536	251.644	251.708	251.680	1.935	249.019	249.127	249.201	249.173	-11.5915	-11.4835	-11.4095	-11.4375
824.000	251.342	251.465	251.539	251.535	1.952	248.825	248.948	249.032	249.028	-11.7855	-11.6625	-11.5785	-11.5825
827.000	251.150	251.286	251.371	251.390	1.968	248.633	248.769	248.864	248.883	-11.9775	-11.8415	-11.7465	-11.7275
830.000	250.970	251.109	251.211	251.240	1.984	248.453	248.592	248.704	248.733	-12.1575	-12.0185	-11.9065	-11.8775
833.000	**250.791**	**250.932**	**251.051**	**251.090**	**2.000**	**248.274**	**248.415**	**248.544**	**248.583**	**-12.3365**	**-12.1955**	**-12.0665**	**-12.0275**

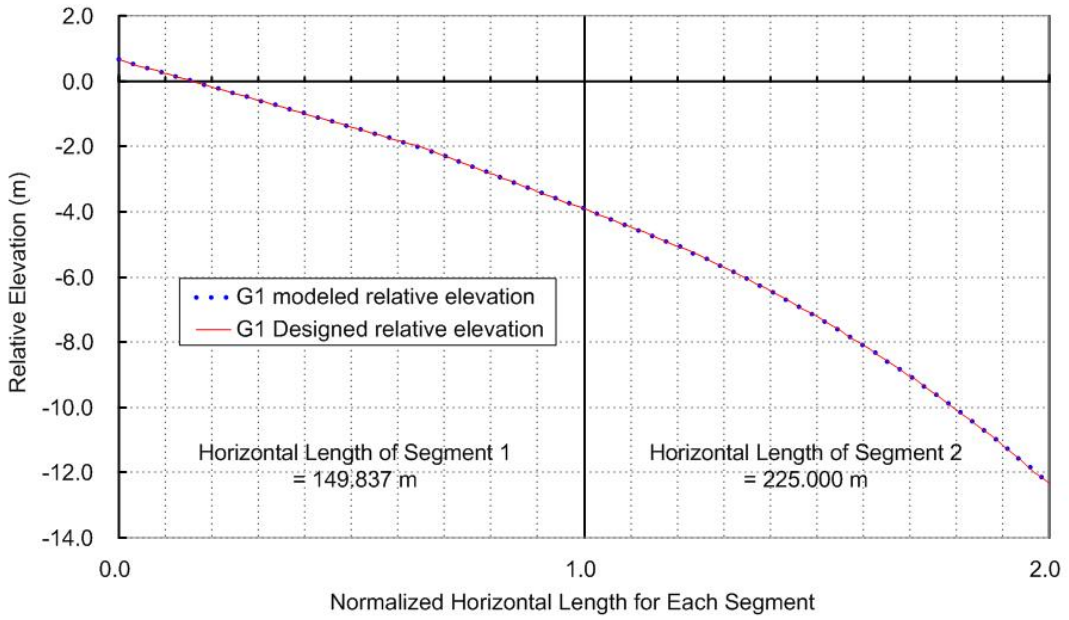

Figure 6.16 Comparison of girder G1 designed and modeled relative elevations

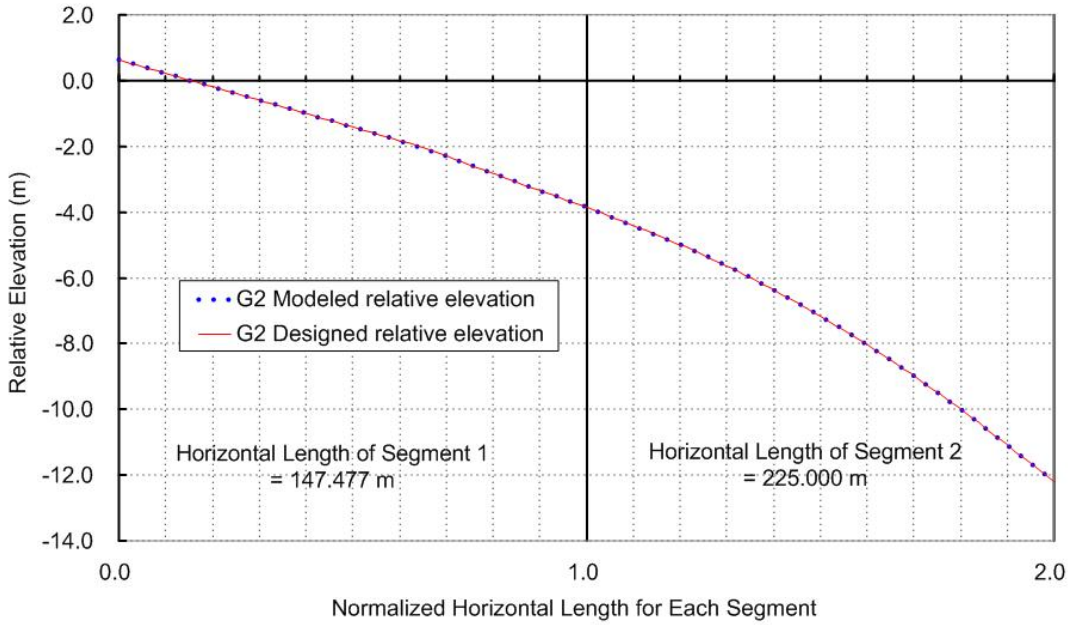

Figure 6.17 Comparison of girder G2 designed and modeled relative elevations

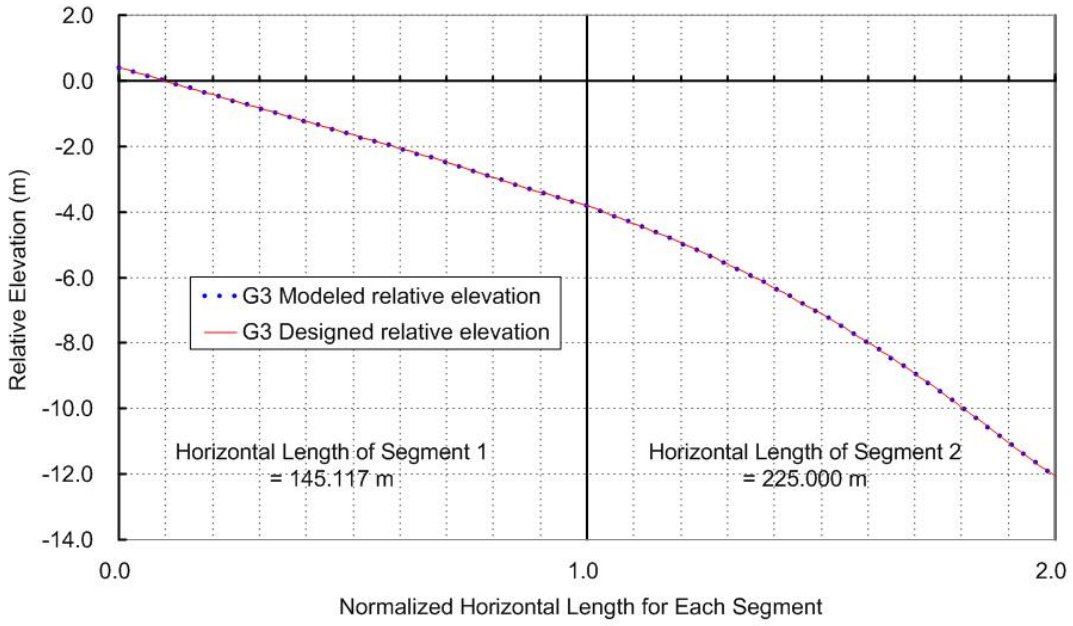

Figure 6.18 Comparison of girder G3 designed and modeled relative elevations

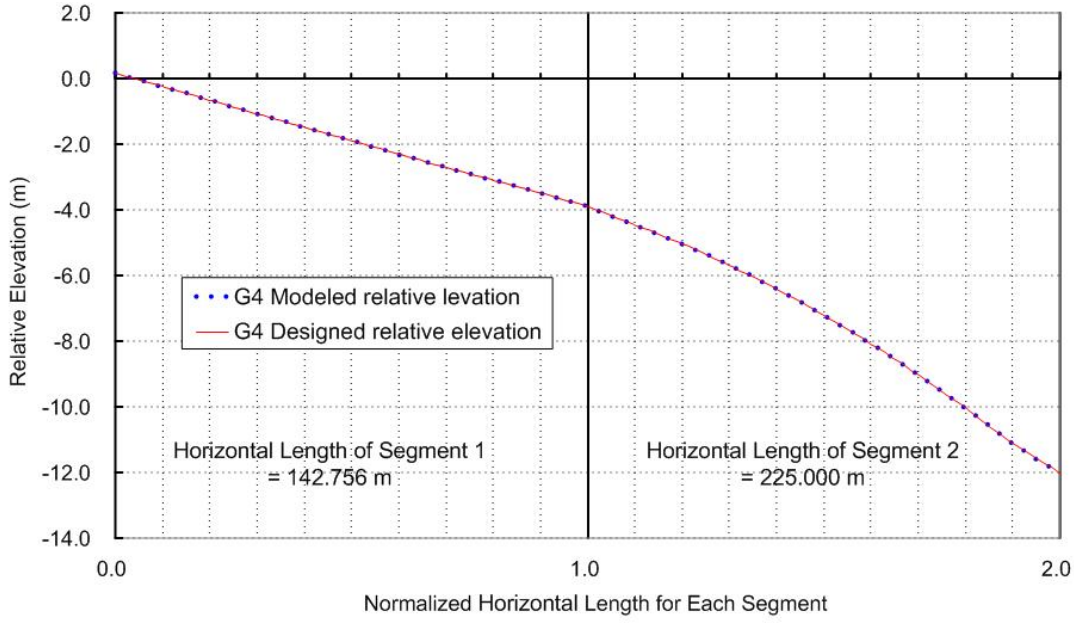

Figure 6.19 Comparison of girder G4 designed and modeled relative elevations

6.3.3 Cross-Frame Initial Geometry

As introduced in Chapter 4, generally there are four cross-frame detailing methods: No-Load-Fit (NLF), Steel Dead Load Fit (SDLF), Total Dead Load Fit (TDLF) and Twist Camber Fit (TCF). Since the girders of the Ford City Bridge are extremely stiff, it can be expected that the required forces for assembling the steel components would be quite large if the TDLF detailing method is used. Therefore, it is more realistic to adopt the SDLF detailing methods instead of using the TDLF detailing method. In addition, the NLF detailing method is also considered in this research for purposes of comparison.

6.3.4 Slab Geometry

The total tributary width is used as the width of longitudinal slab elements above each girder in the model of the girders in their composite condition as shown in Figure 6.20. Since the area of slab overhangs is not as large as the area of the tributary slab area on the inside of the facia girders, this means that the slab area over the facia girders is shifted away from the inside girders so that the corresponding beam elements representing the slab are centered over the facia girders. It should be noted that the resulting width-to-thickness ratios for the slab are 17.1 for the interior girders and 13.6 for the facia girders based on the interior slab thickness. The interior slab tributary width significantly exceeds the traditional AASHTO (2004) Article 4.6.2.6.1 effective flange width rule equal to one-half of the top flange width plus 12 times the thickness of the slab. Data from Chen et al. (2005) indicates that the full tributary slab width provides a better representation of the response than the traditional slab width equations for straight I-girder bridges. Logically, the participation of the slab with each individual girder in a curved bridge is quite similar to that in a straight bridge. Therefore, the full tributary widths are utilized in this study. Based on the analysis results in Section 5.4.2, the beam

grillage model 2 is slightly better than the beam grillage model 1. Therefore, for the Ford City Bridge, the transverse slab elements are created only on the top of each cross location and the width are taken as 0.3 girder spacing as in beam grillage model 2.

6.4 Study of The Staged Concrete Casting Sequence with The Considerations of Different Cross-Frame Details

6.4.1 Overview of Concrete Casting Sequence and Slab Modeling

The slab for the Ford City Bridge was placed in seven stages, one day for each stage. The planned concrete casting sequence is shown in the Figure 6.15. To reduce the potential for cracking in the concrete placed at earlier stages, the bridge segments subjected to positive bending moment under the total dead load were cast earlier than the segments subjected to negative bending.

Based on Topkaya et al. (2004), shear studs can transfer shear force as early as four hours and concrete can reach almost 90% of its 28-day its compression stiffness in this time in some cases. For the Ford City Bridge, it is assumed that the concrete casted at the previous stages is fully effective in this work. The concrete is assumed to be fully effective in tension as well as in compression.

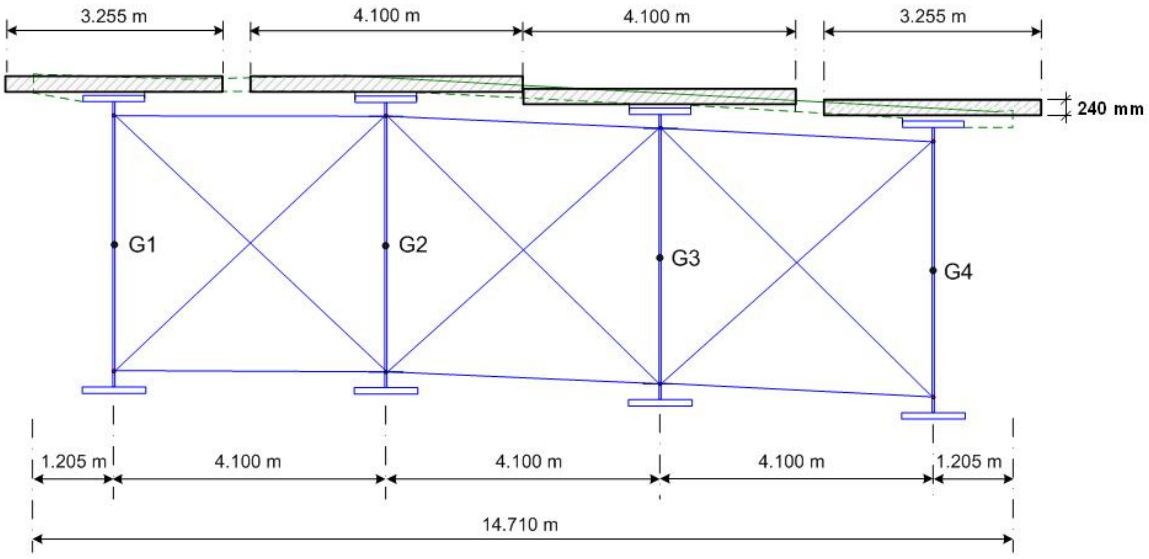

Figure 6.20 Effective width of the longitudinal slab element on the top of each girder

6.4.2 Case Studies

This Section focuses on two considerations: (1) the influence of steel detailing methods on the constructed geometry and (2) the influence of staged slab construction on the constructed geometry. The vertical support reactions and the tensile stresses in the concrete deck during the staged slab casting are also investigated. Four models are created in GT-SABRE for the purpose of this study. The girder cambers are based on the results of a NLF analysis without the consideration of staged slab casting in Model 1. Also, the cross-frames are detailed based on NLF method. The wet concrete load is applied to the bare girder system all at once. Model 2 is similar to Model 1 except that the effects of staged slab casting are considered in determining the girder cambers, and a staged slab casting analysis is performed to evaluate the overall bridge response. Models 3 and 4 are similar to the Models 1 and 2, respectively, except that the approach is changed from NLF to SDLF for both the girder camber design and cross-frame

detailing. All the analyses are elastic and geometric nonlinear. It should be noted that the lack-of-fit from the TDLF detailing method is larger than from the SDLF detailing method. For the Ford City Bridge, where the dimensions and stiffnesses of the girders and cross-frame members are large, this larger lack-of-fit can cause large required forces for the steel assembly resulting in significant construction difficulty. Therefore, use of the SDLF detailing method is more reasonable then use of the TDLF detailing method for the Ford City Bridge. This behavior is evaluated subsequently in the context of the results for the SDLF and NLF solutions.

With the aid of the uniqueness concept, the steel erection sequence is skipped for the calculation of the effects of the steel detailing method and the slab casting sequence on the final constructed geometry. The steel components are assembled together and then gravity is turned on. In other words, the steel structural model is the Instantaneously Instantiated Model or IIM discussed in Section 5.2. The bridge grade, superelevation, vertical curve and girder camber are considered in defining the initial girder geometry. For the NLF cross-frame detailing, the nodal coordinate of each of the cross-frame members is created based on the girder initial geometry. Therefore, all cross-frames are assumed to have different geometry as shown in Figure 4.2 (alternately, or in combination, the drop in the cross-frames relative to the top flange of the steel girders may be specified differently for the different connection plates). For the SDLF cross-frame detailing, the nodal coordinates of each of the cross-frame members is created based on the ideal girder steel dead load geometry, i.e., the geometry including the grade, superelevation, vertical curve and camber due to the total dead load minus the vertical steel dead load deflections for the girders. The procedures for detemining the induced stresses due to the lack-of-fit between the girders and the cross-frames in the analysis are discussed in Section 4.3.7.

6.4.2.1 Model 1 – Girder Cambers Based on NLF, Cross-Frame Details Based on NLF, Analysis without Staged Slab Casting

The NLF girder camber diagrams are determined for Model 1 as follows. First, a model of the complete non-composite bridge is constructed in the idealized geometry without inclusion of any camber and assuming perfect fit-up of the components. This is the geometry including the grade, superelevation and vertical curve. Then the gravity load is turned on such that the girders are deflected under the total dead load, e.g. steel dead load plus wet concrete load, without considering the casting sequence. The negative of the corresponding vertical deflections of each girder is taken as the NLF girder camber diagram. The resulting camber diagrams for girders G1 to G4 are shown along with those of the subsequent models in Figures 6.21 to 24.

Model 1 is then created based on the calculated camber diagrams. The girder webs are assumed to be plumb when they are fully-supported (i.e., blocked) in their no-load cambered geometry. The cross-frames are detailed such that they fit-up with the no-load cambered I-girders without inducing any deformations and internal stresses due to lack-of-fit. The staged slab casting simulation is not performed for this model.

6.4.2.2 Model 2 – Girder Cambers Based on NLF with Consideration of Staged Slab Casting, Cross-Frame Details Based on NLF, Analysis with Staged Slab Casting

The girder camber diagrams are determined for Model 2 as follows. First, a model of the complete non-composite bridge is constructed in the idealized geometry without inclusion of any camber and assuming perfect fit-up of the components. This is the geometry including the grade, superelevation and vertical curve. Then the steel dead load is applied to the bare girder system. Next, the wet concrete load is applied to the structure in the slab casting sequence shown in Figure 6.15. The models of the

corresponding concrete slab segments are created immediately after the load is applied for each stage. After the entire analysis of the concrete casting sequence is completed, the negative of the vertical deflections of each girder are taken as the girder camber diagrams. The resulting camber diagrams of girders G1 to G4 are shown in Figures 6.21 to 24. The cross-frames are detailed such that they fit-up with the no-load cambered I-girders without inducing any deformations and internal stresses due to lack-of-fit.

6.4.2.3 Model 3 – Girder Cambers Based on SDLF, Cross-Frame Details Based on SDLF, Analysis without Staged Slab Casting

The SDLF girder camber diagrams are determined for Model 3 as follows. First, a model of the complete non-composite bridge is constructed in the idealized geometry without inclusion of any camber and assuming perfect fit-up of the components. This is the geometry including the grade, superelevation and vertical curve. Then the steel dead load is applied to the girders. The negative of the corresponding vertical deflections of each girder are taken as the steel dead load camber diagrams. The concrete dead load is then applied to the girders. The negative of the vertical deflections of each girder due to concrete dead load are taken as the concrete dead load camber diagrams. Then a new model with the same initial geometry as the above model is created. In this new model, the girders are cambered based on the above temporary steel dead load cambers plus concrete dead load cambers but the cross-frames are detailed such that they fit-up with the girders as if they only have the concrete dead load cambers, i.e., the geometry including grade, superelevation, vertical curve and camber due to concrete dead load. Then the steel self-weight is applied to the girders. The induced stresses in the girders and cross-frames due to lack-of-fit are considered in analysis using the algorithm introduced in Section 4.3.7. The negative of the vertical deflections of each girder from this analysis are taken as the final steel dead load camber diagrams of the

Model 3. The staged slab casting simulation is not performed for this Model. The resulting camber designs are shown in Figures 6.21 to 6.24.

6.4.2.4 Model 4 – Girder Cambers Based on SDLF with Consideration of Staged Slab Casting, Cross-Frame Details Based on SDLF, Analysis with Staged Slab Casting

For this model, the process of obtaining the girder camber diagrams is the same as the one in Model 3. However, the concrete camber diagrams are obtained considering the staged slab casting as described in Section 6.4.2.1. The cross-frames are detailed such that they fit-up with the girders as if they only have the concrete dead load cambers, i.e., the geometry including grade, superelevation vertical curve and camber due to the concrete dead load. The staged slab casting simulation is performed for this model. The resulting camber designs are shown in Figures 6.21 to 6.24. It is noted that for the camber diagrams in Figures 6.21 to 6.24, the differences between Models 1 and 2 and Models 3 and 4 are due to the consideration of staged slab construction. The differences between Models 1 and 3 and Models 2 and 4 are due to the lack-of-fit due to the SDLF detailing.

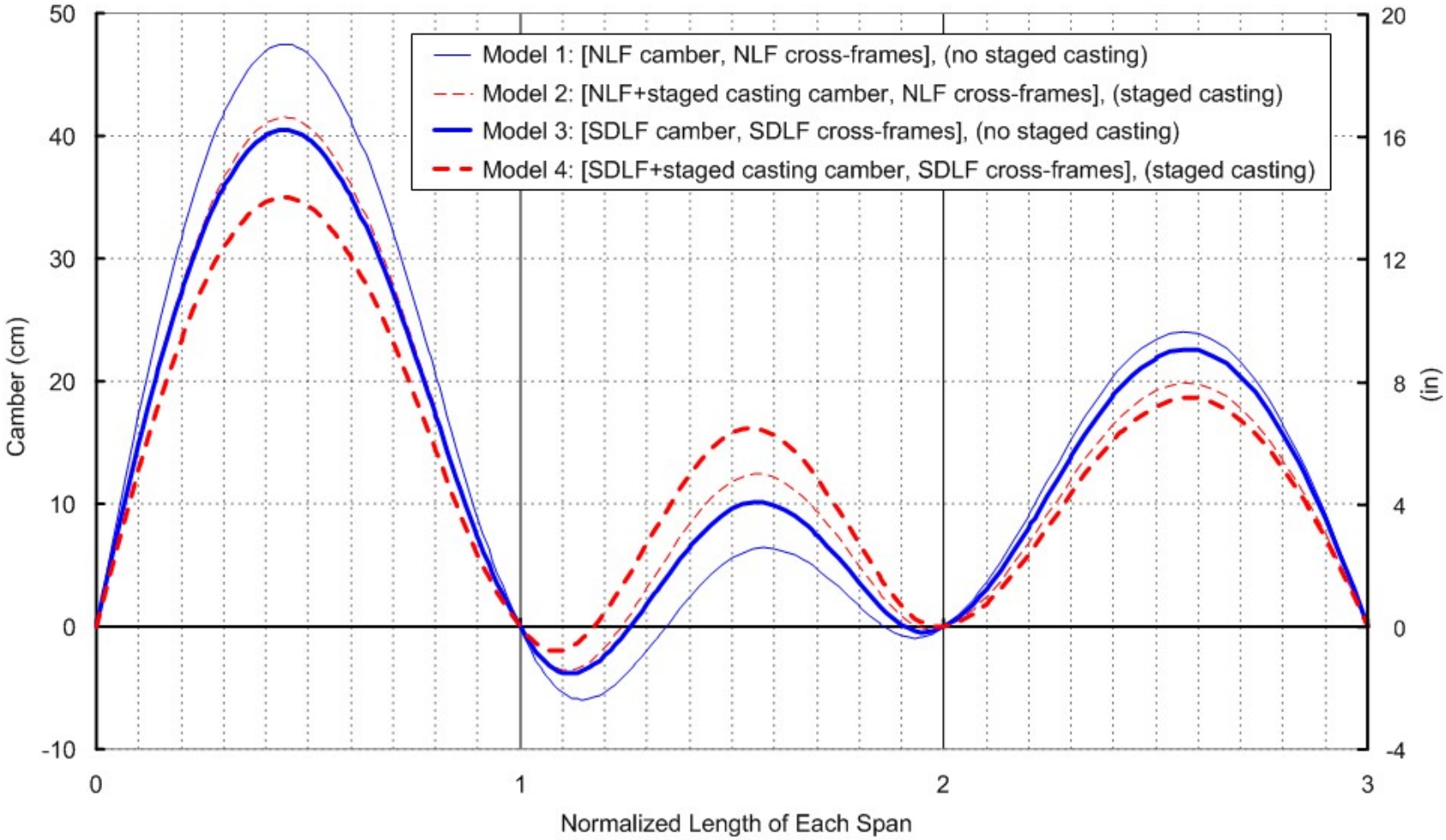

Figure 6.21 Girder G1 camber diagrams ([camber method, steel detailing method], (analysis type))

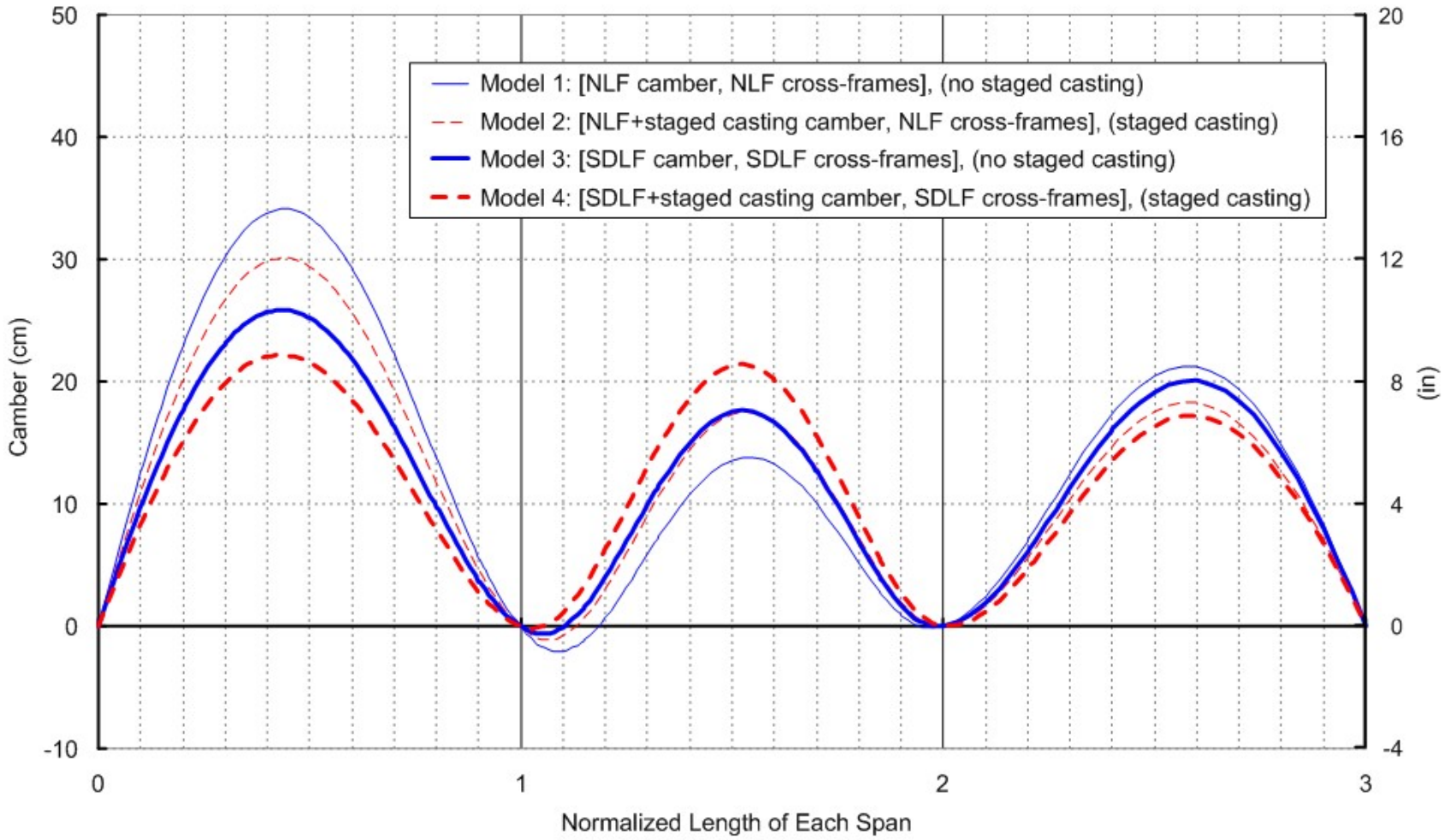

Figure 6.22 Girder G2 camber diagrams ([camber method, steel detailing method], (analysis type))

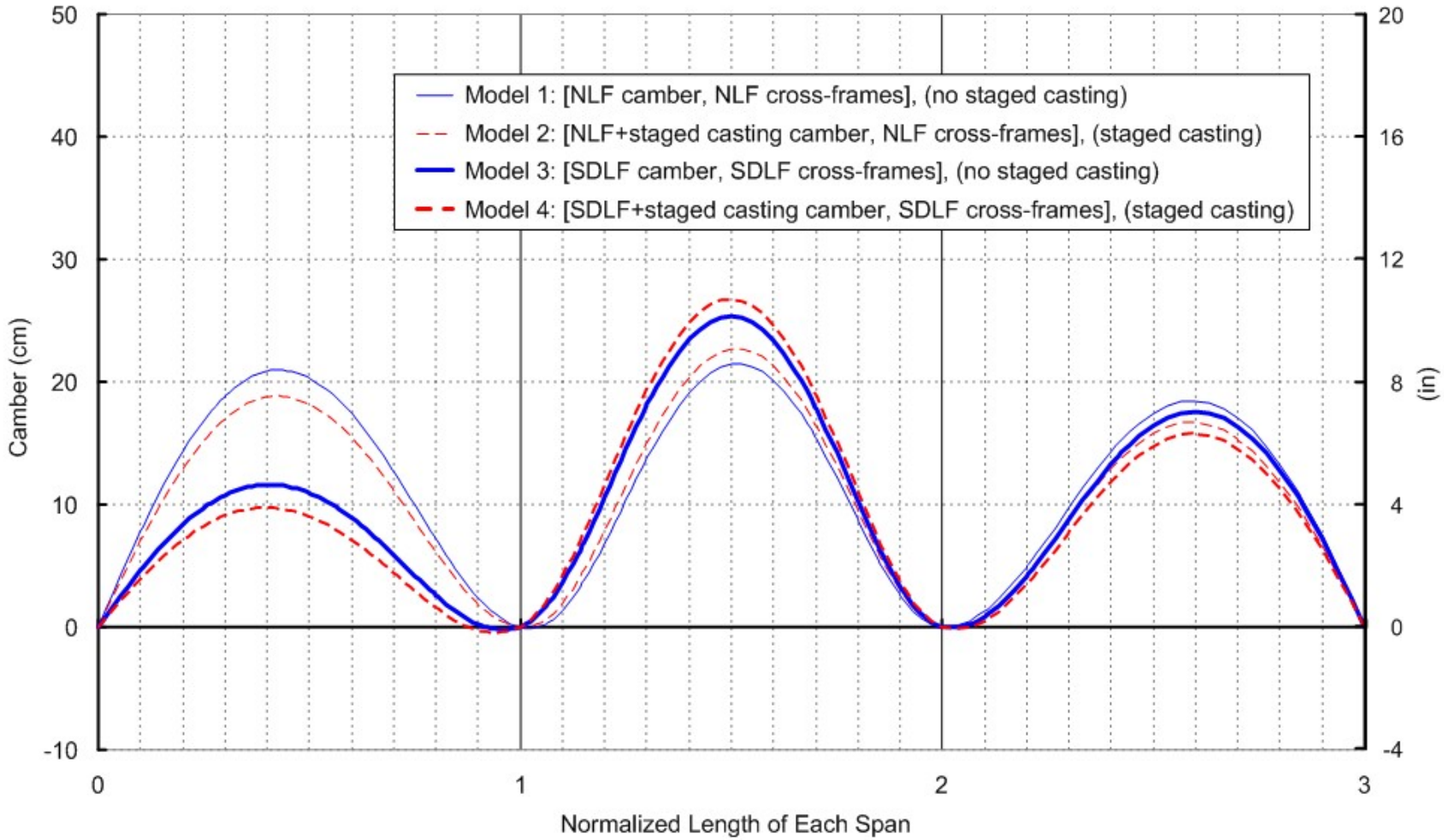

Figure 6.23 Girder G3 camber diagrams ([camber method, steel detailing method], (analysis type))

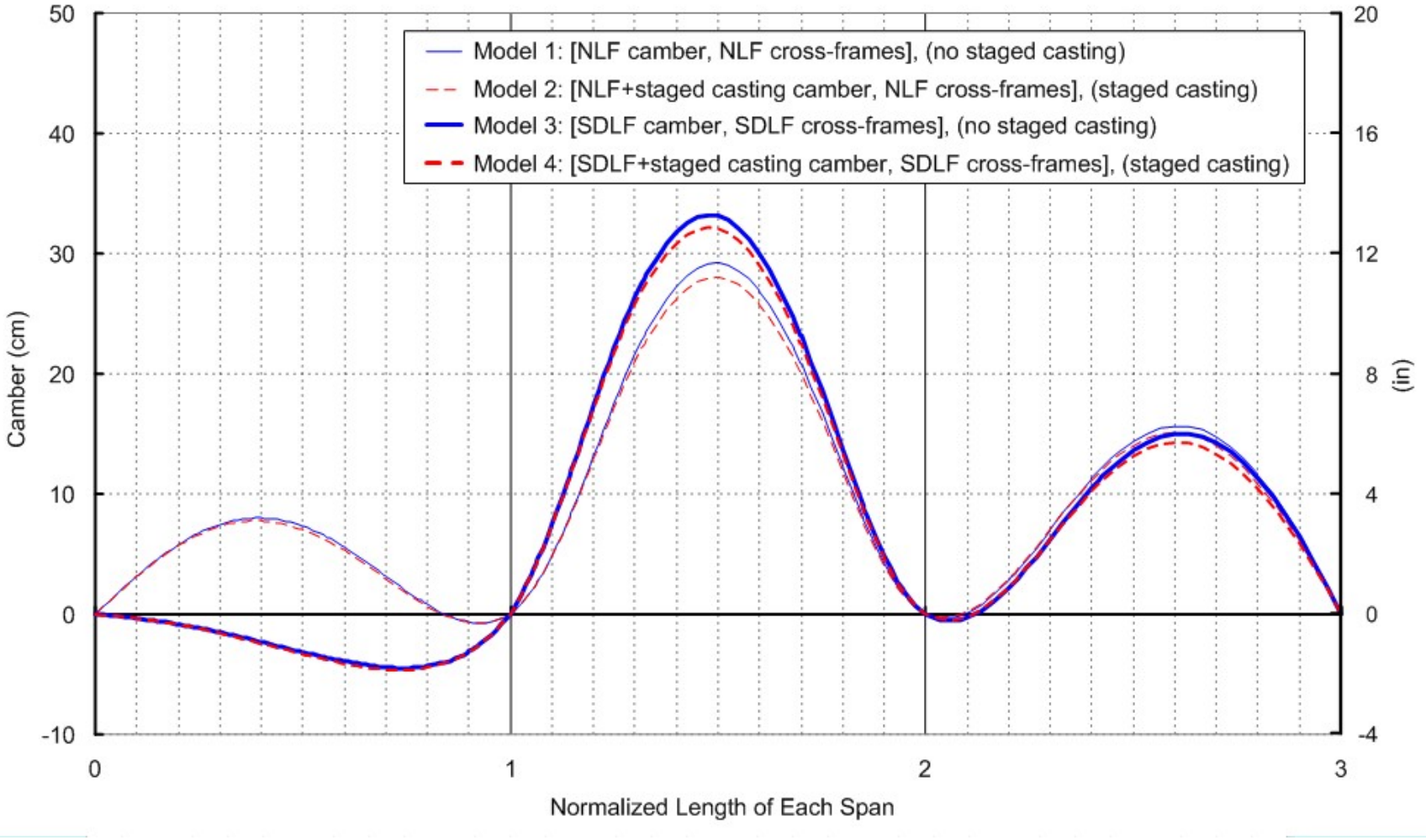

Figure 6.24 Girder G4 camber diagrams ([camber method, steel detailing method], (analysis type))

6.4.3 Analysis Results

Figure 6.25 shows the girder G1 final rotations about the global X-axis under the total dead load, which represents the component of girder web out-of-plumbness about the longitudinal axis of the straight portion of the bridge. Figure 6.26 shows the girder G1 final lateral (global Z-axis) displacements from the four different models. The girder web out-of-plumbness and lateral displacements for the other girders are close to those of girder G1 and are not shown here.

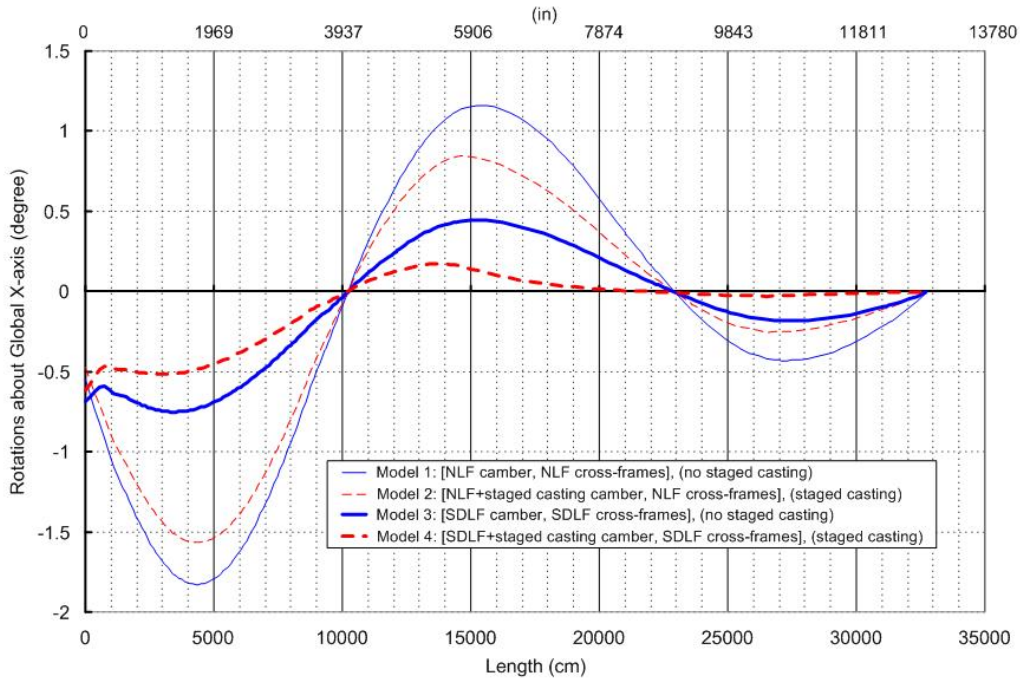

Figure 6.25 Girder G1 final rotations about the global X-axis

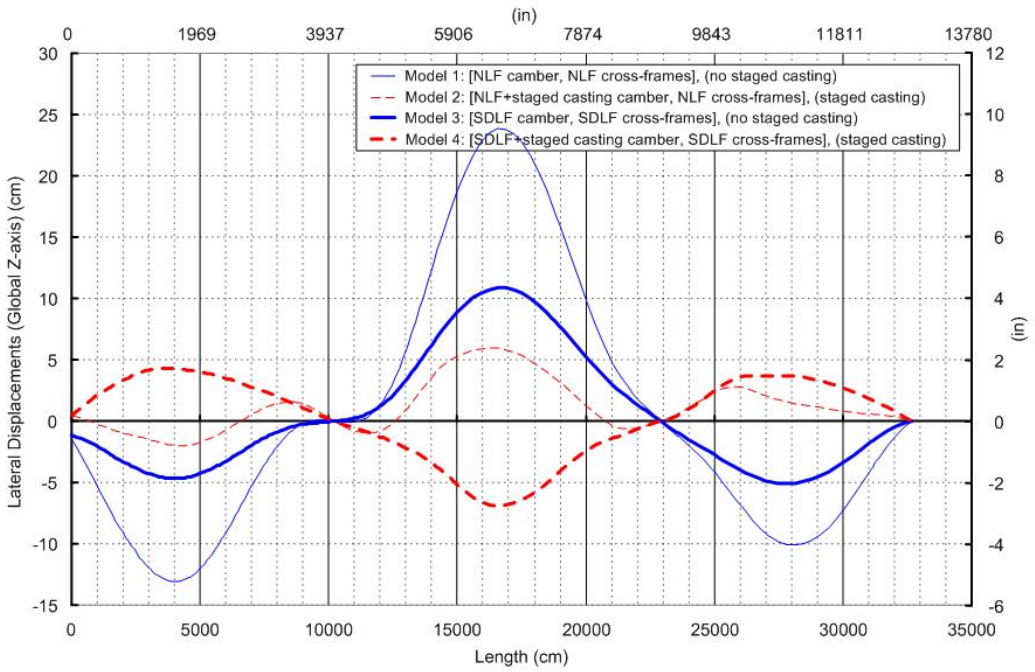

Figure 6.26 Girder G1 final lateral displacements in global Z-axis

The girder web out-of-plumbness is smaller in Model 4 than in Model 2, and it is smaller in Model 3 than in Model 1. This is because Models 2 and 1 do not account for the stiffness contribution from the previously cast stages of the slab. Also, using the SDLF steel detailing method as in Models 3 and 4 leads to a reduction in the web out-of-plumbness as expected. For Models 1 and 2, which use the NLF steel detailing method, no measures are taken to compensate for the torsional rotation of the bridge cross-section under dead load. This is consistent with the results in Section 5.2.2 and is because the induced stresses due to the lack-of-fit between the girders and the cross-frames cause the bridge cross-sections to twist in the opposite direction from the twist under the dead loads.

The girder lateral displacements in these four models have the same trend as the girder web out-of-plumbness. Based on these results, Model 4 (girder cambers based on

SDLF with consideration of staged slab casting, cross-frame details based on SDLF and analysis with staged slab casting simulation) is suggested for the design and analysis of the Ford City Bridge. The stage-by-stage bridge responses for Model 4 are discussed below.

Table 6.3 shows the stage-by-stage Model 4 vertical support reactions from the steel dead load condition to the completed casting and removal of the overhang brackets. Under the steel dead load, the girders G3 and G4 lift off of their bearings at abutment I so that the vertical support reactions at these locations are zero (the girders are assumed not to be tied down). The girder G3 vertical reaction at abutment I becomes nonzero after the casting stage 1. Girder G4 is still lifted off of its bearings at abutment I until the end of the casting stage 3 and it is lifted off of its bearings again after the casting stage 6. However, as shown in the following, the upward G4 displacements at abutment 1 are quite small at all the stages.

Figures 6.27 to 6.50 show the Girder G1 (outside) and G4 (inside) elevations relative to the designed final geometry and the corresponding model views in the GT-SABRE Viewer from the steel dead load condition to the last concrete casting stage 7 (the effect of the removal of the overhang brackets is small and is not shown here). In the casting stage 1, the wet concrete load is applied to the area 1 as shown in Figures 6.30 and 6.32. The deck elements in this region are created based on the deformed geometry of the bridge at the end of this stage. As shown in Figure 6.34, when the wet concrete load in area 2 is applied, girders G1 and G4 deflect downward (incrementally) in spans I and III but upward in span II. This results in tensile stresses in the prior cast concrete in area 1. Nevertheless, these stresses are relatively small compared to the modulus of rupture of the concrete. As mentioned before, the current study assumes that the concrete tensile stiffness is the same as its compression stiffness and that the previous cast concrete is fully effective at the beginning of the current stage. If the

concrete tensile strength were not large enough to resist the tension stresses, some cracking can be expected in area 1. The same situation happens for stage 3.

In the casting stage 4, the girders deflect downward (incrementally) in span III and upward (slightly) in span II near the Pier II as shown in Figure 6.40. The girder deflections in the other portions of the bridge are not significant. No significant additional concrete tensile stresses are developed at this stage.

In stage 5, under the wet concrete load within the areas 5a and 5b, the girders deflect downward (incrementally) in span I as shown in Figure 6.43. In span II, the inside girder G4 is deflected downward but the outside girder G1 is deflected upward. The girder deflections in span III in this stage are small. Therefore, the prior cast concrete in area 1 is subjected to additional tensile stresses between girder G2 and the outside edge of the deck.

The cast area of stage 6 covers the Pier I as shown in Figures 6.45 and 6.47. Under the wet concrete load within the area 6, the girders deflect downward (incrementally) in spans I and III but are deflected upward in span II as shown in Figure 6.46. Again, this results in additional tensile stresses on the concrete deck in span 2 that may cause some cracking in the previously cast concrete in areas 4a, 1 and 5a. The girder G4 vertical support reaction at abutment I becomes zero.

The cast area of the stage 7 covers the Pier II as shown in Figures 6.48 and 6.50. The trend of the girder deflections in stage 7 is similar to that in stage 6. Again, the previously cast concrete within span II may experience some cracking. Therefore, minimum negative concrete flexure deck reinforcement per AASHTO Article 6.10.1.7 should be placed in these regions such that the cracking is well distributed throughout the slab area.

Table 6.3 Stage-by-stage Model 4 vertical support reactions (KN) (1 kN = 0.225 kips)

Support	Girder	Steel DL	Stage 1	Stage 2	Stage 3	Stage 4	Stage 5	Stage 6	Stage 7	Bracket Removal
Abut I	G1	2,117.3	1,654.0	1,689.9	2,490.6	2,486.7	3,327.8	3,585.3	3,608.4	3,604.5
	G2	871.1	723.0	736.3	1,192.7	1,191.4	1,557.2	1,639.1	1,646.0	1,650.1
	G3	0.0	228.4	210.1	675.4	675.4	800.6	740.1	735.2	735.1
	G4	0.0	0.0	0.0	175.6	177.3	35.2	0.0	0.0	0.0
Pier I	G1	3,297.0	3,281.1	3,289.0	3,550.8	3,559.2	4,818.5	6,165.3	6,180.7	6,162.9
	G2	2,763.3	3,166.0	3,139.7	3,341.5	3,351.0	4,560.2	5,821.0	5,804.4	5,819.3
	G3	1,899.0	2,747.1	2,684.4	2,785.7	2,797.3	3,856.9	4,929.6	4,885.7	4,901.5
	G4	1,260.3	2,222.5	2,150.2	2,122.7	2,136.5	2,864.2	3,703.6	3,643.5	3,630.1
Pier II	G1	1,654.4	2,363.5	2,542.0	2,476.8	3,370.4	3,330.6	3,277.6	4,362.1	4,345.0
	G2	1,730.7	2,374.9	2,567.0	2,520.4	3,408.9	3,412.6	3,372.1	4,498.2	4,514.6
	G3	1,819.4	2,391.4	2,556.2	2,532.9	3,345.1	3,388.7	3,366.2	4,458.4	4,474.9
	G4	1,968.6	2,559.2	2,752.4	2,749.0	3,658.2	3,771.4	3,755.8	4,841.1	4,825.6
Abut II	G1	488.2	367.9	936.2	949.0	1,193.9	1,210.7	1,223.3	1,282.1	1,278.9
	G2	430.9	313.3	878.1	887.0	1,139.0	1,141.9	1,150.3	1,209.5	1,212.3
	G3	438.7	339.5	907.3	913.2	1,165.4	1,158.5	1,163.7	1,222.9	1,225.7
	G4	419.4	323.0	885.0	885.4	1,129.8	1,100.8	1,099.8	1,157.9	1,155.2
Stage Applied Load		21158.4	3896.5	2869.0	2324.7	4536.9	5549.9	4657.1	4543.1	0.0
Total Applied Load		21158.4	25054.9	27923.9	30248.7	34785.6	40335.5	44992.6	49535.7	49535.7

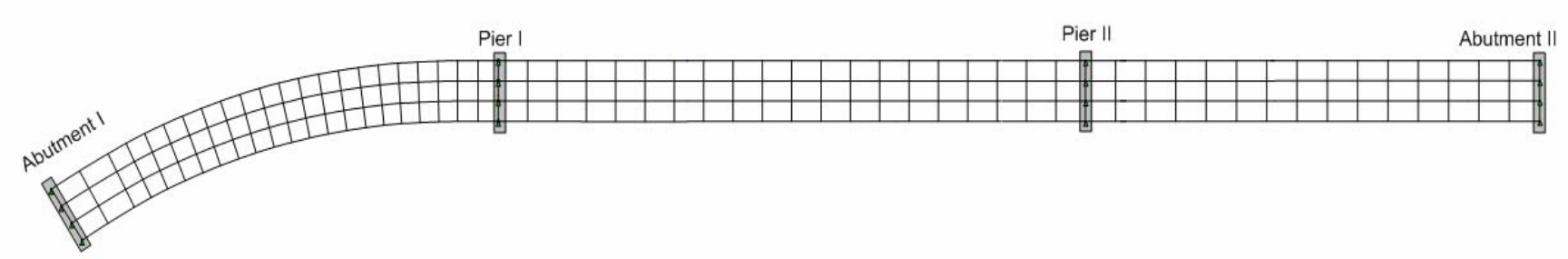

Figure 6.27 Illustration of the Ford City Bridge staged concrete casting – **steel dead load**

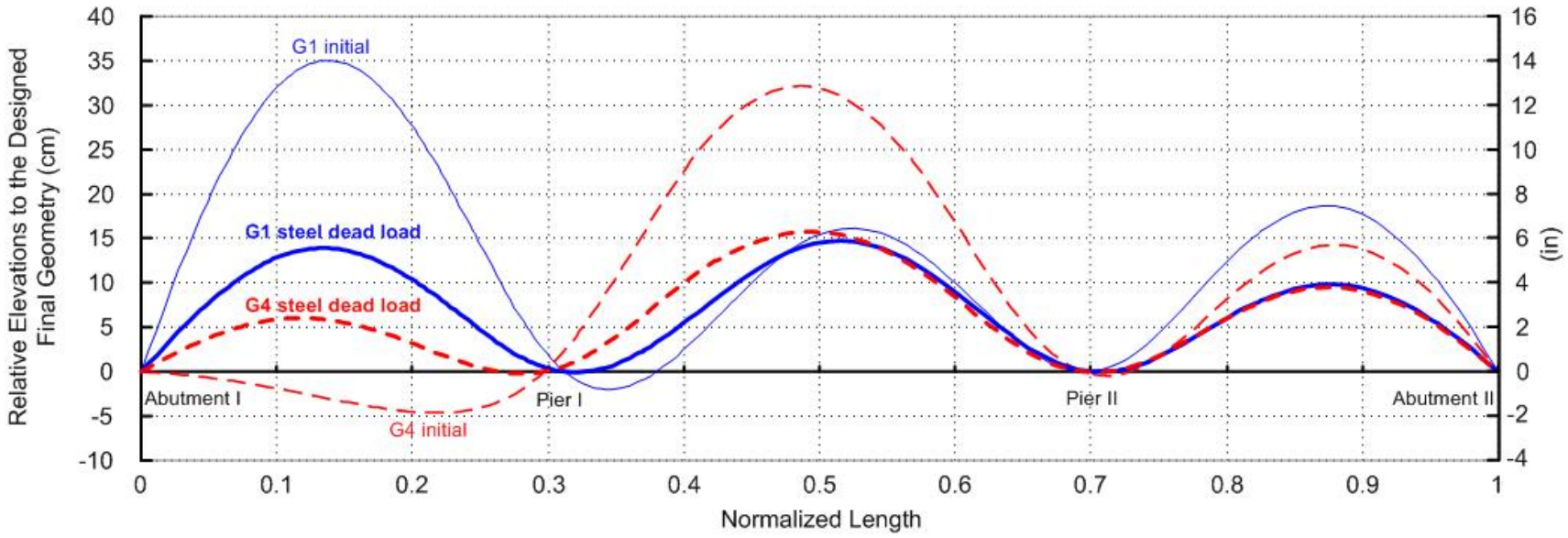

Figure 6.28 Girder G1(outside) and G4(inside) relative elevations to the designed final geometry under **steel dead load**

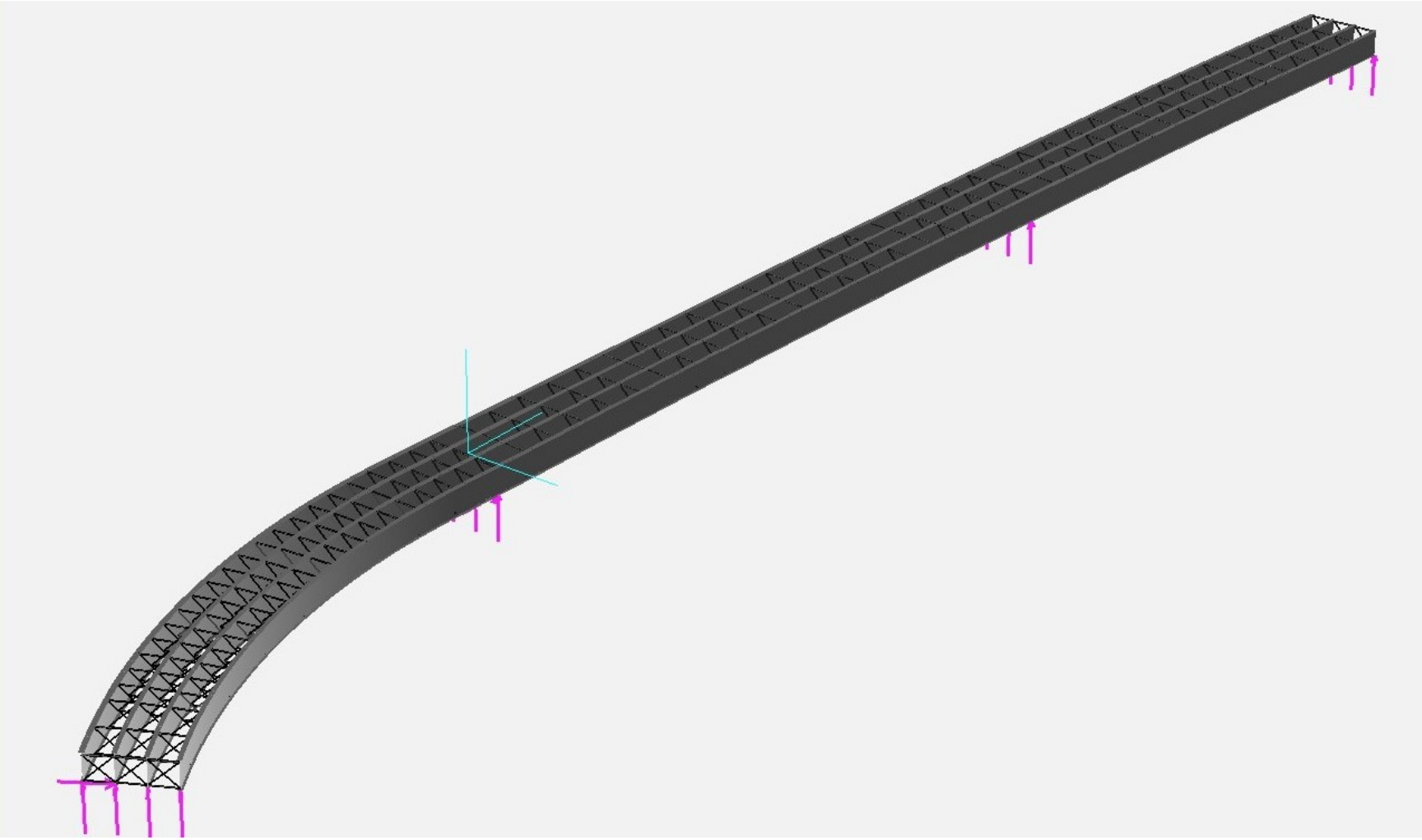

Figure 6.29 The Ford City Bridge model view under **steel dead load** in the GT-SABRE Viewer

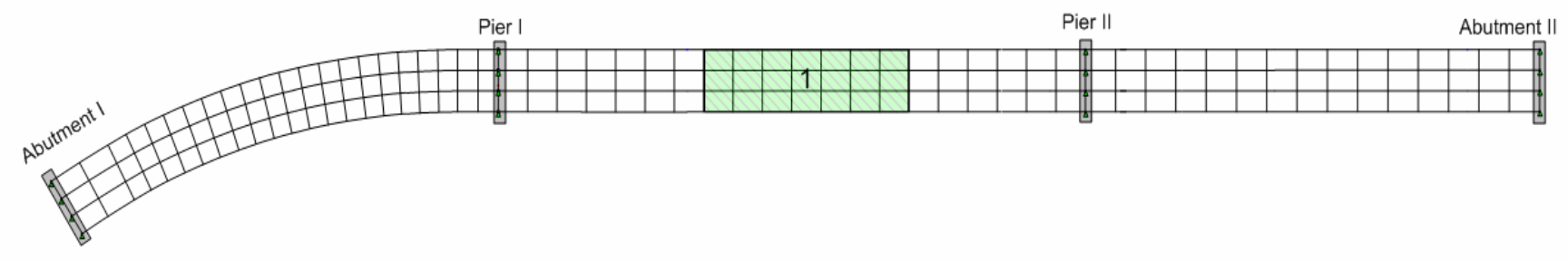

Figure 6.30 Illustration of the Ford City Bridge staged concrete casting – **casting stage 1**

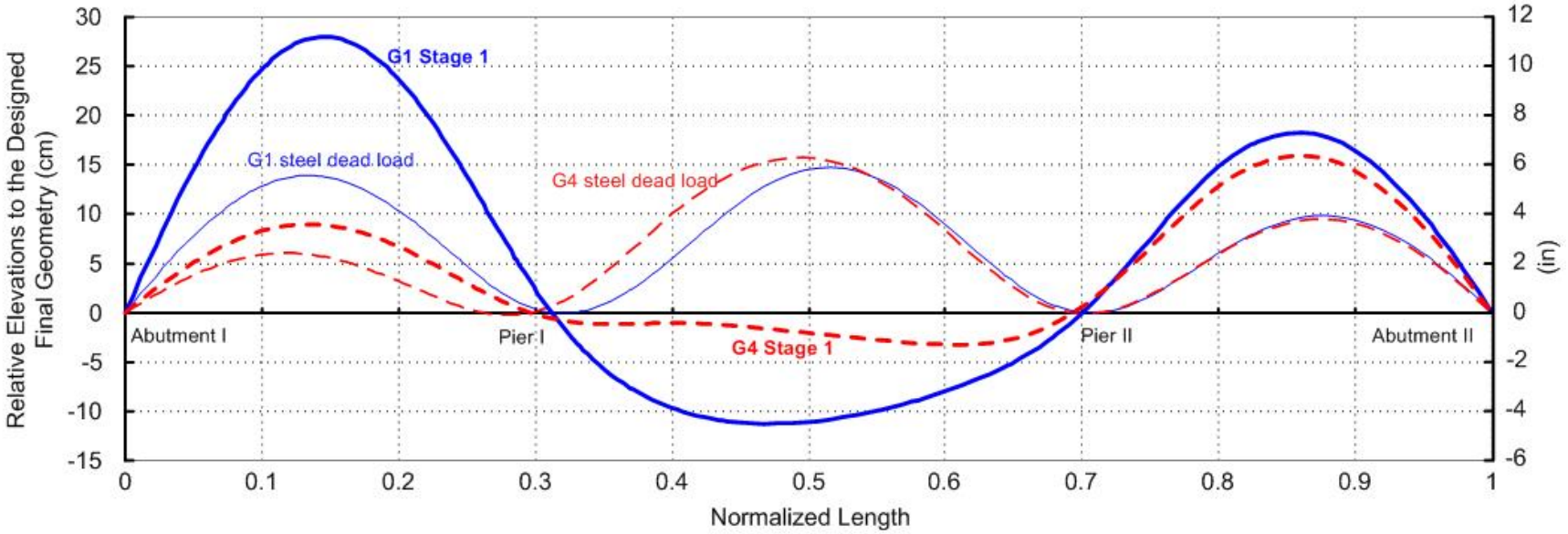

Figure 6.31 Girder G1(outside) and G4(inside) relative elevations to the designed final geometry in **casting stage 1**

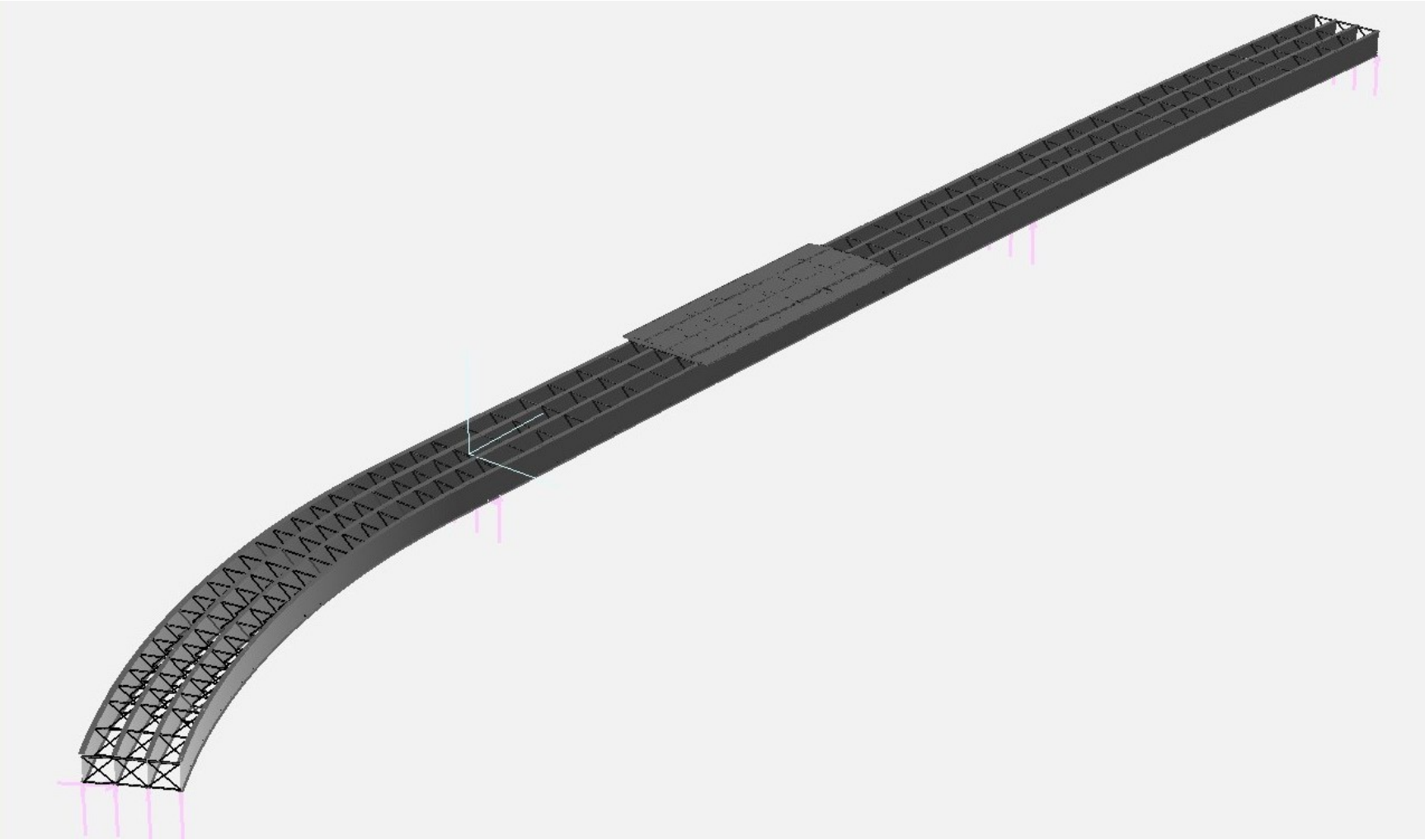

Figure 6.32 The Ford City Bridge model view in **casting stage 1** in the GT-SABRE Viewer

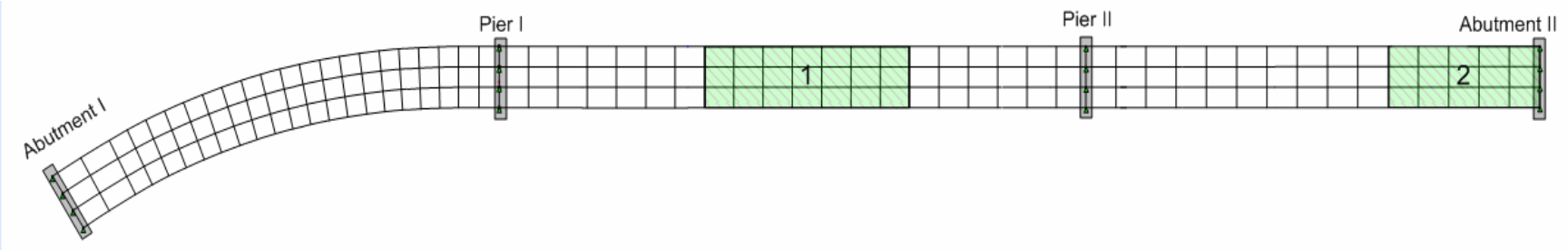

Figure 6.33 Illustration of the Ford City Bridge staged concrete casting – **casting stage 2**

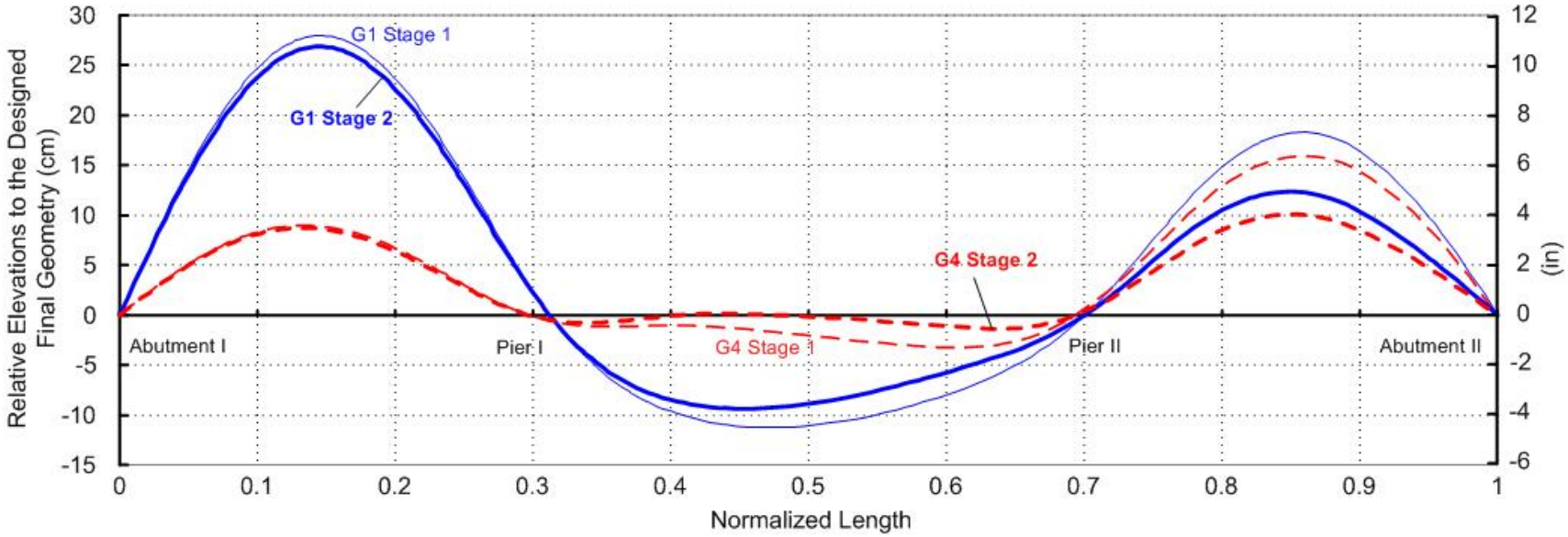

Figure 6.34 Girder G1(outside) and G4(inside) relative elevations to the designed final geometry in **casting stage 2**

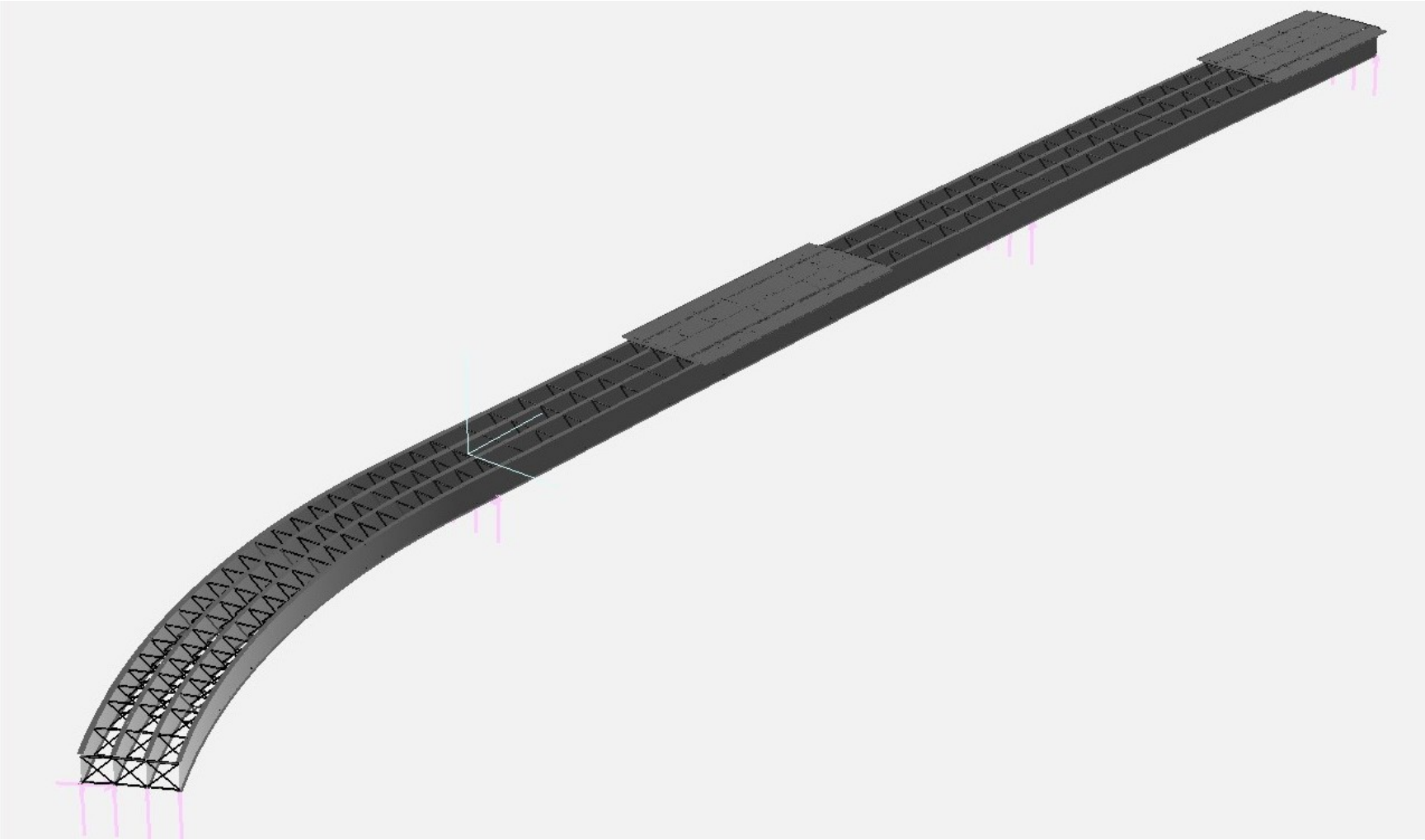

Figure 6.35 The Ford City Bridge model view in **casting stage 2** in the GT-SABRE Viewer

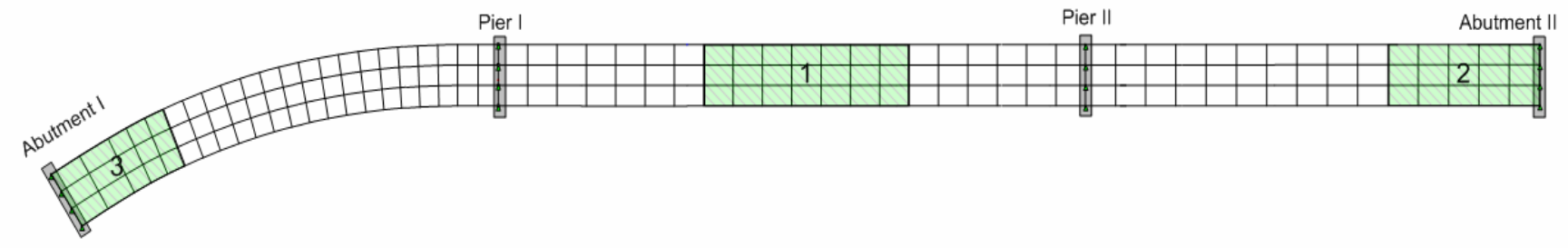

Figure 6.36 Illustration of the Ford City Bridge staged concrete casting – **casting stage 3**

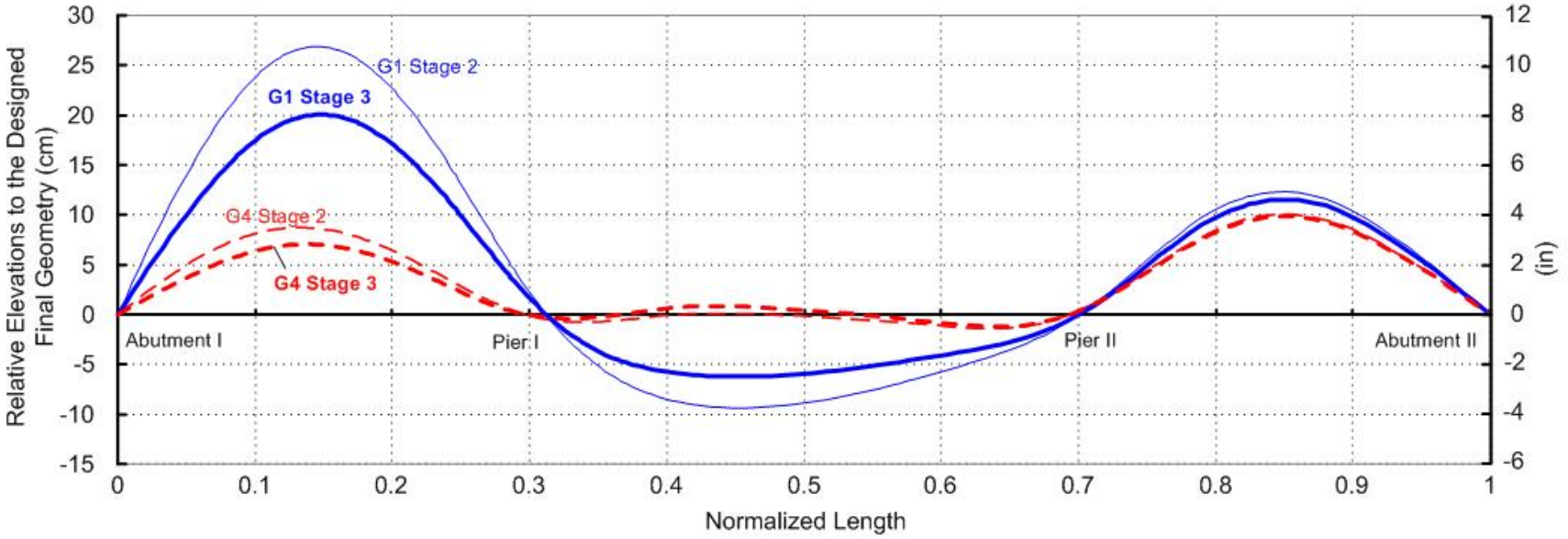

Figure 6.37 Girder G1(outside) and G4(inside) relative elevations to the designed final geometry in **casting stage 3**

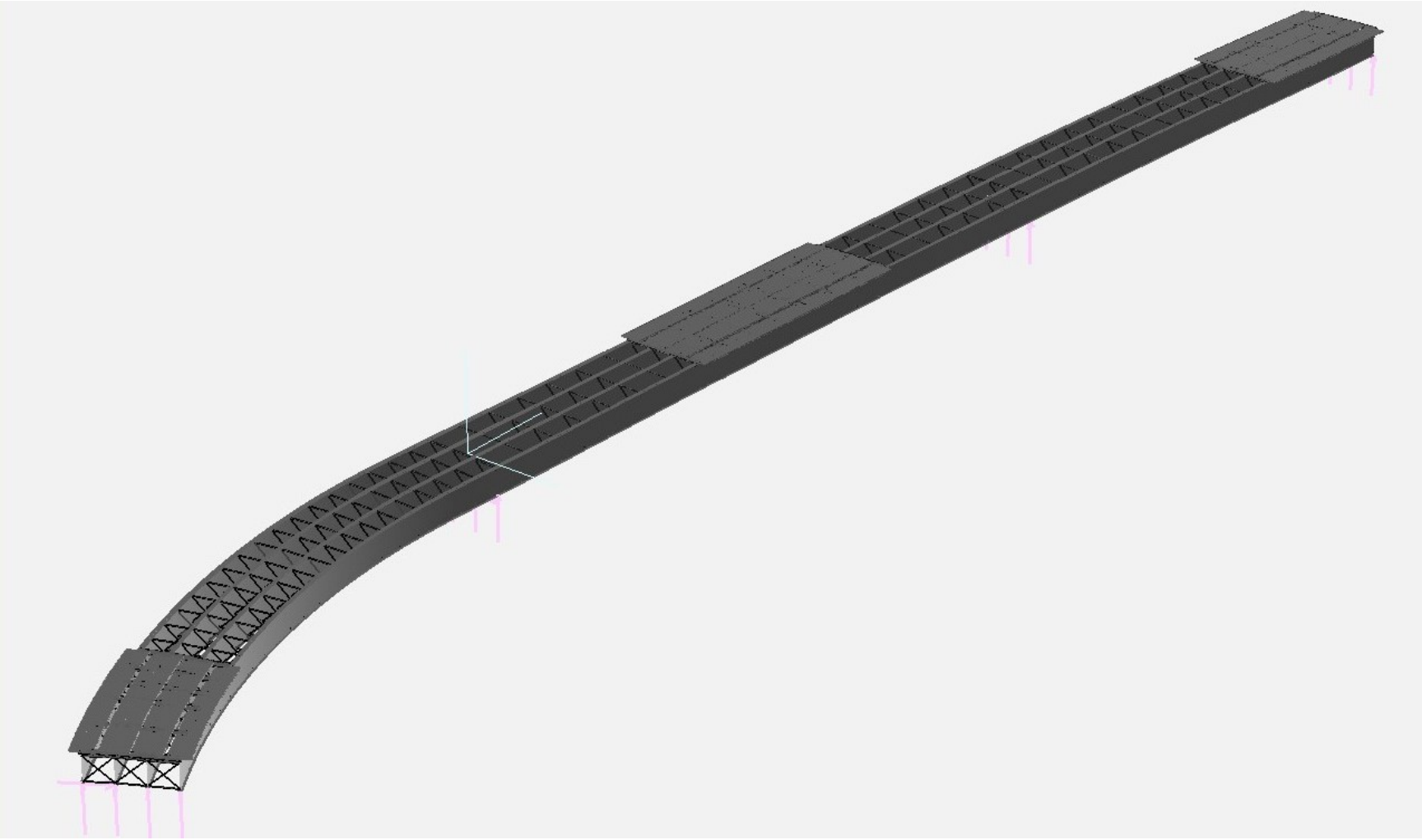

Figure 6.38 The Ford City Bridge model view in **casting stage 3** in the GT-SABRE Viewer

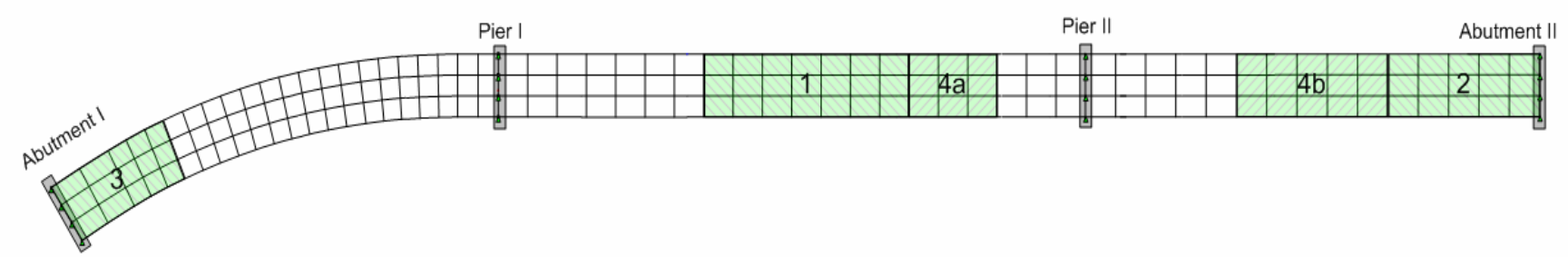

Figure 6.39 Illustration of the Ford City Bridge staged concrete casting – **casting stage 4**

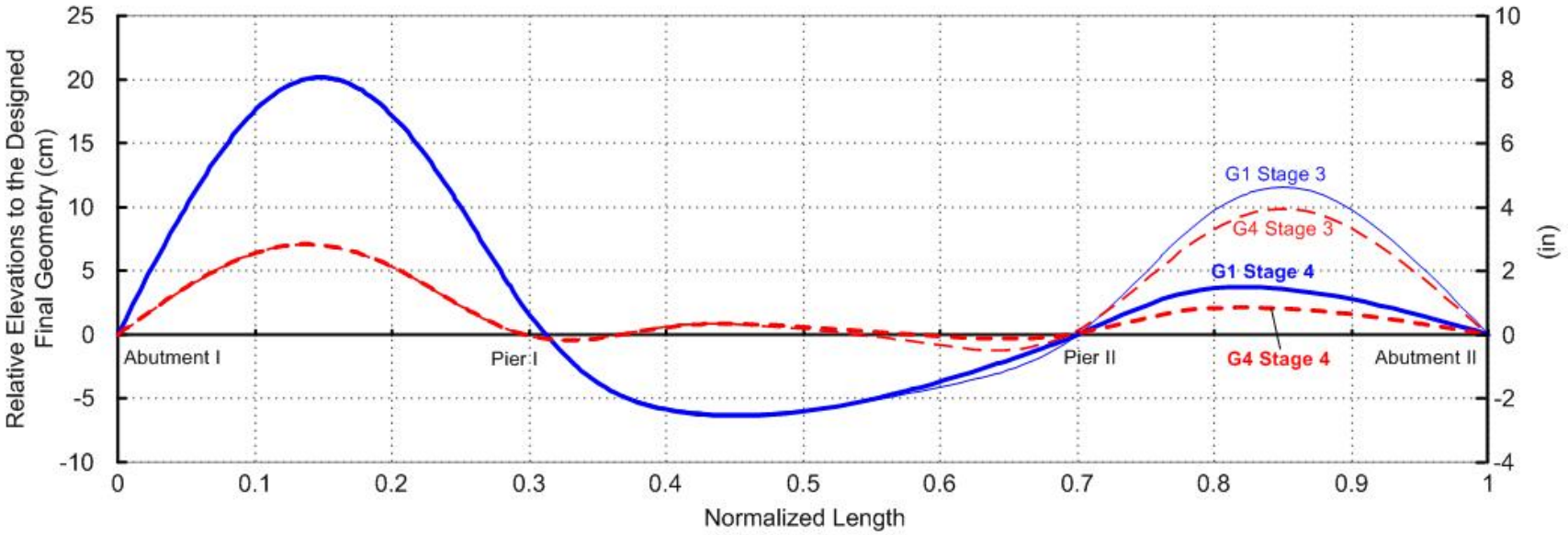

Figure 6.40 Girder G1(outside) and G4(inside) relative elevations to the designed final geometry in **casting stage 4**

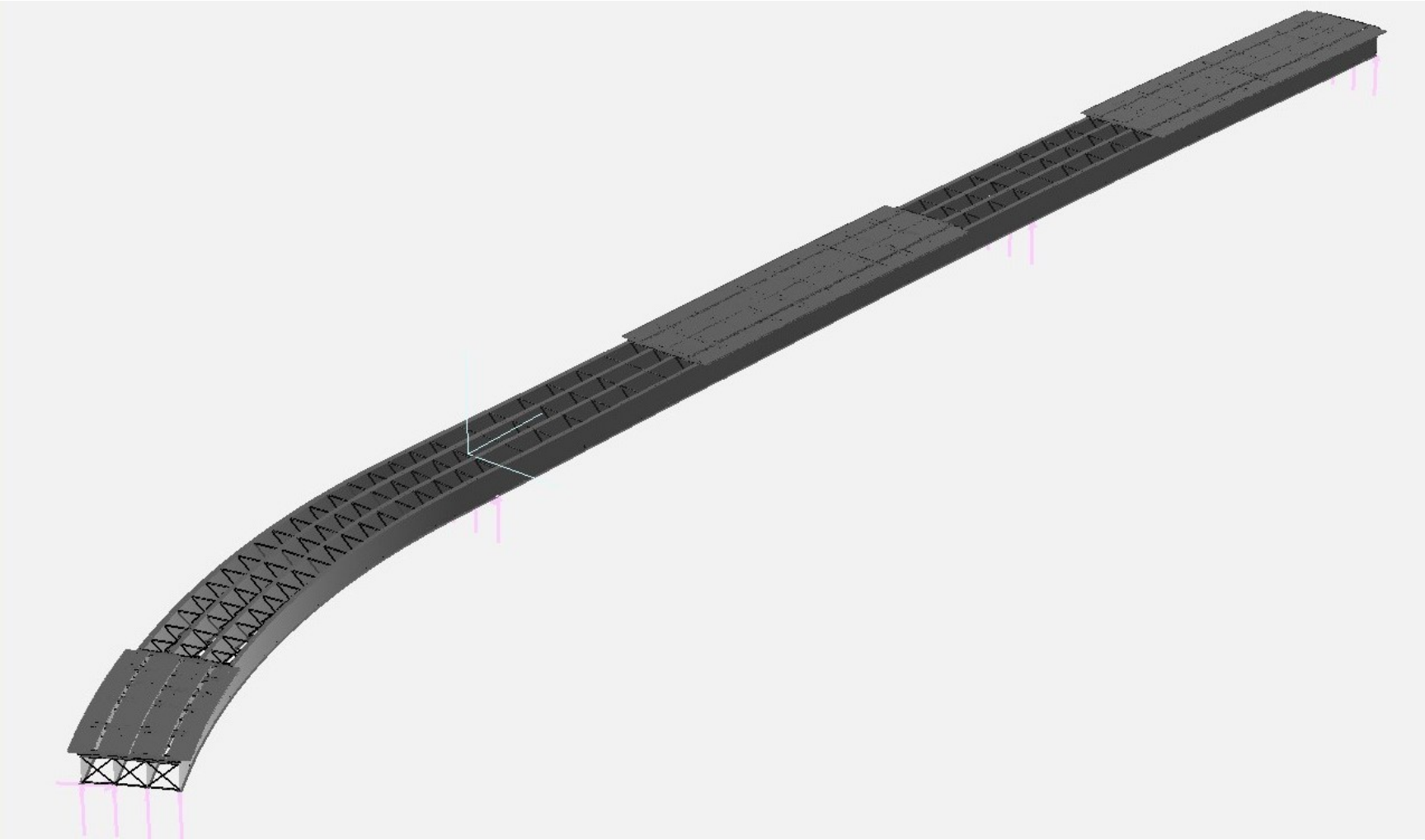

Figure 6.41 The Ford City Bridge model view in **casting stage 4** in the GT-SABRE Viewer

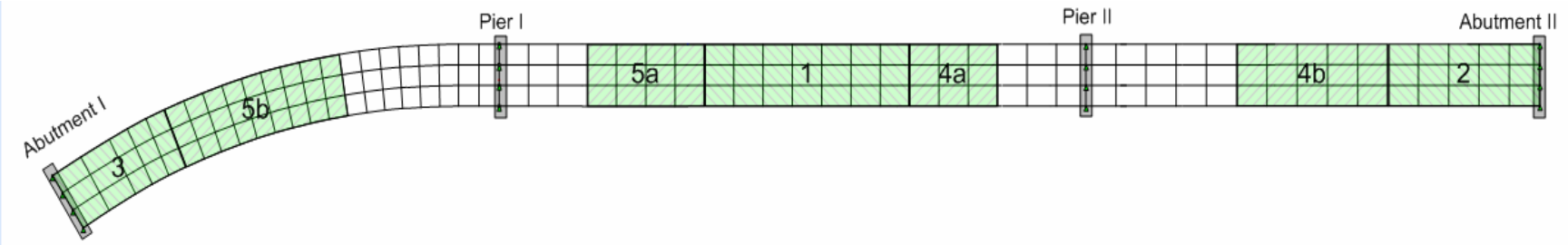

Figure 6.42 Illustration of the Ford City Bridge staged concrete casting – **casting stage 5**

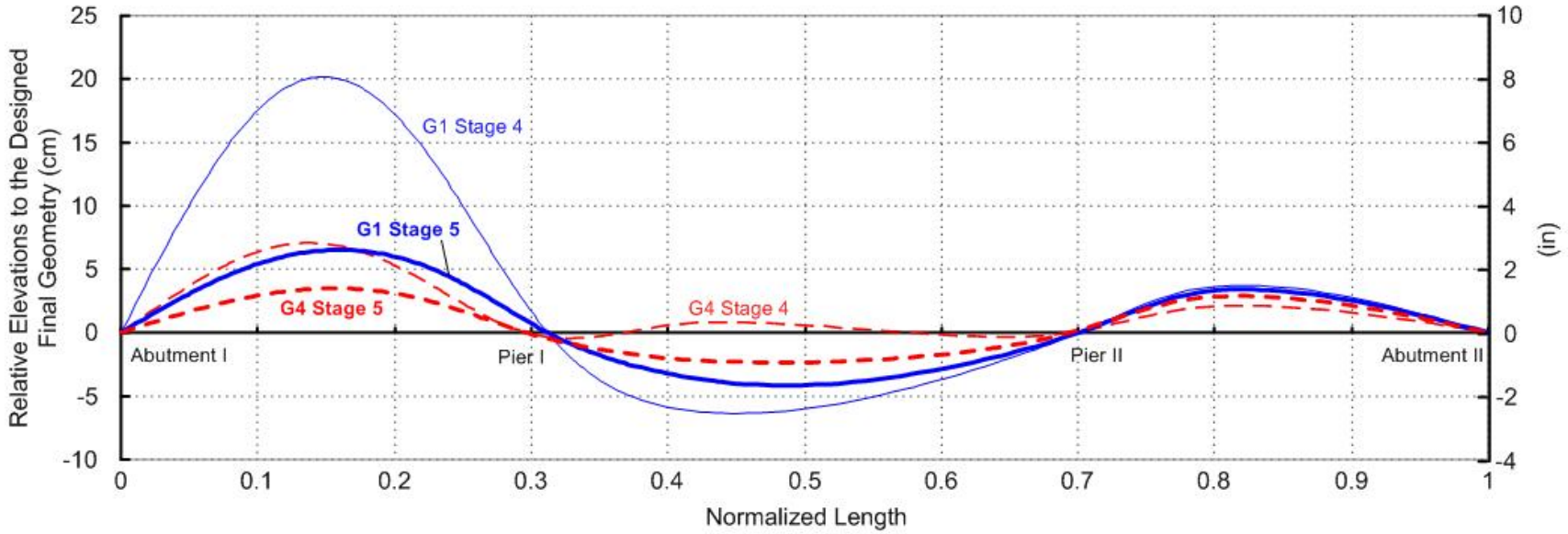

Figure 6.43 Girder G1(outside) and G4(inside) relative elevations to the designed final geometry in **casting stage 5**

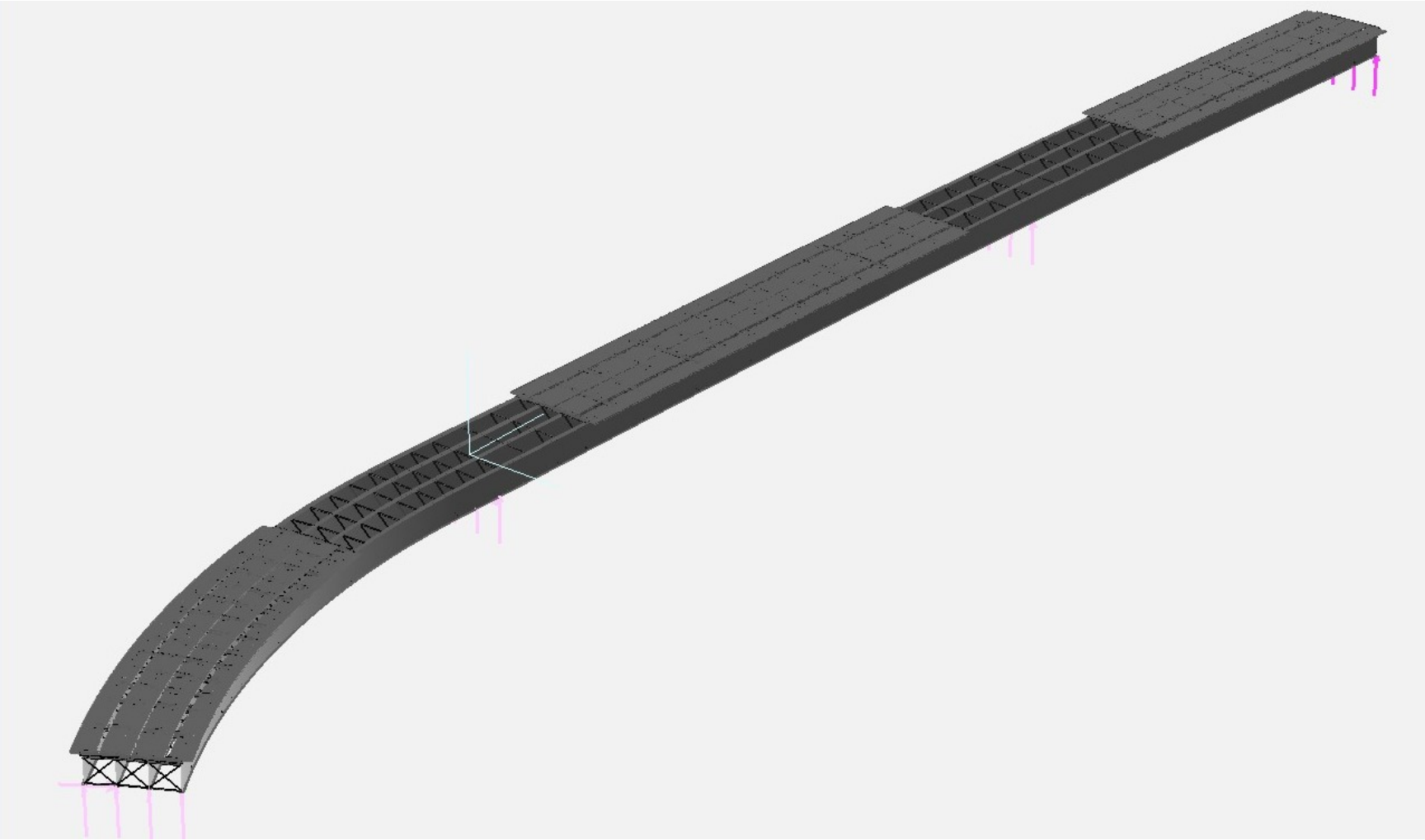

Figure 6.44 The Ford City Bridge model view in **casting stage 5** in the GT-SABRE Viewer

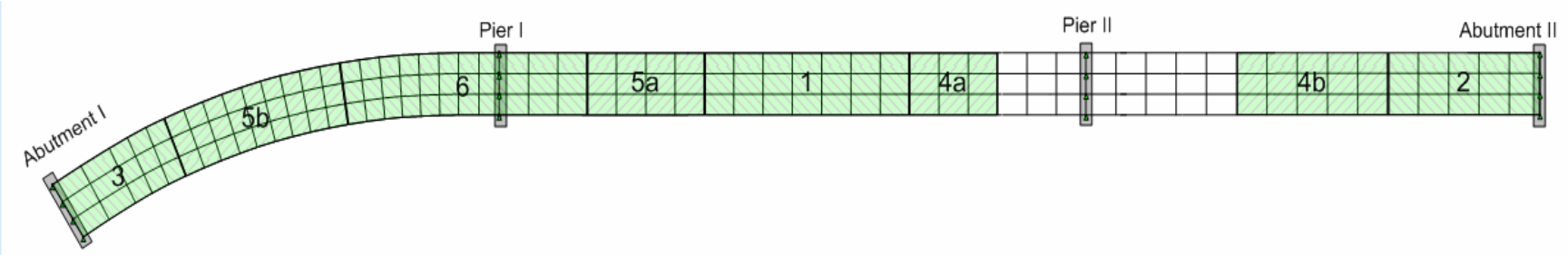

Figure 6.45 Illustration of the Ford City Bridge staged concrete casting – **casting stage 6**

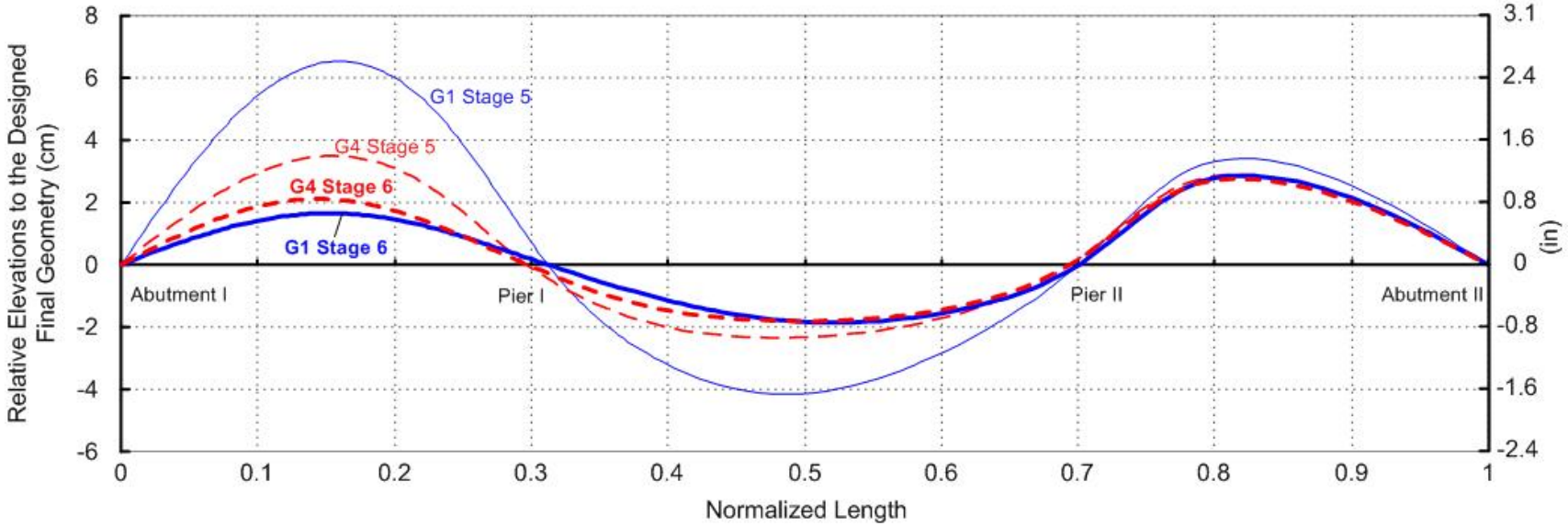

Figure 6.46 Girder G1(outside) and G4(inside) relative elevations to the designed final geometry in **casting stage 6**

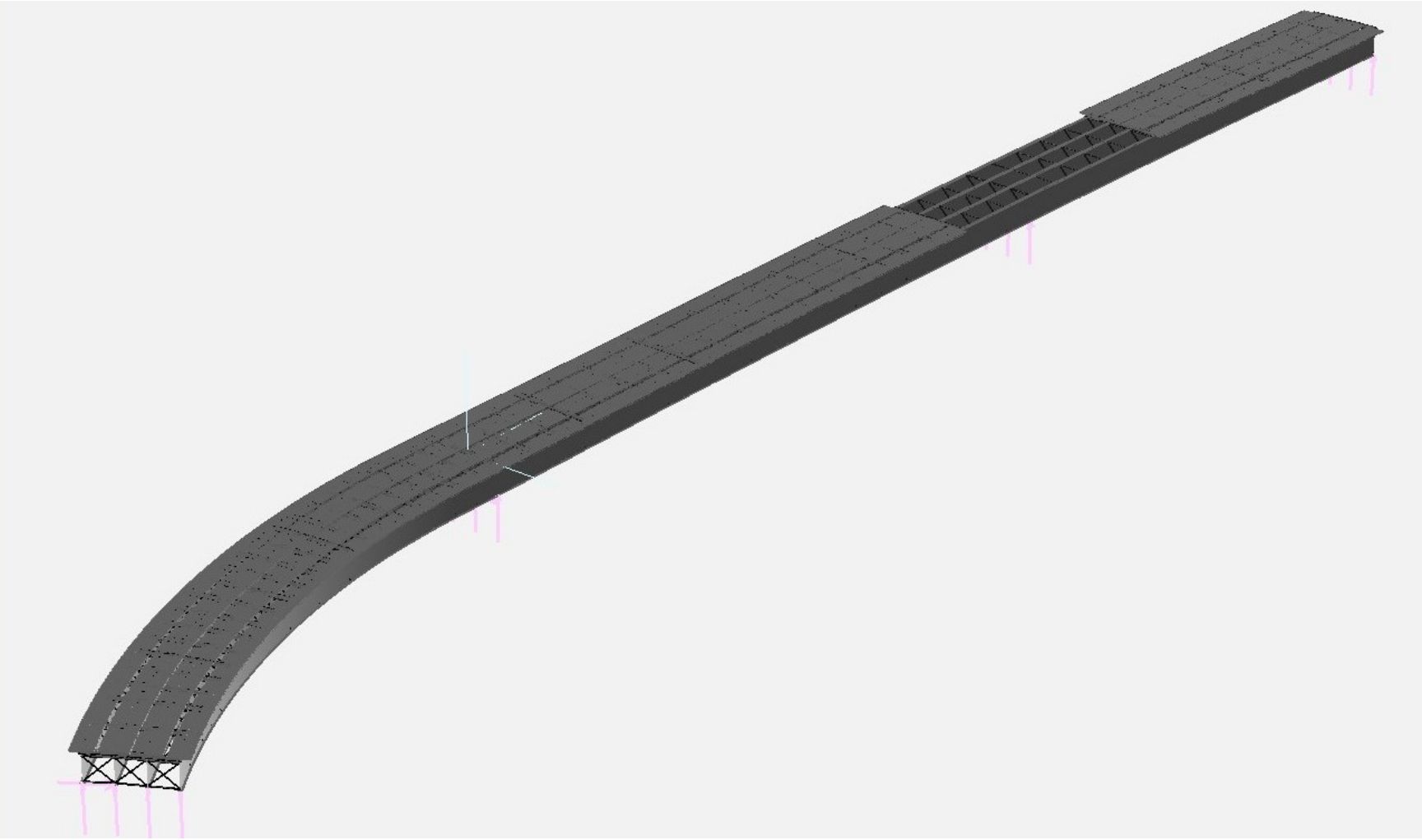

Figure 6.47 The Ford City Bridge model view in **casting stage 6** in the GT-SABRE Viewer

Figure 6.48 Illustration of the Ford City Bridge staged concrete casting – **casting stage 7**

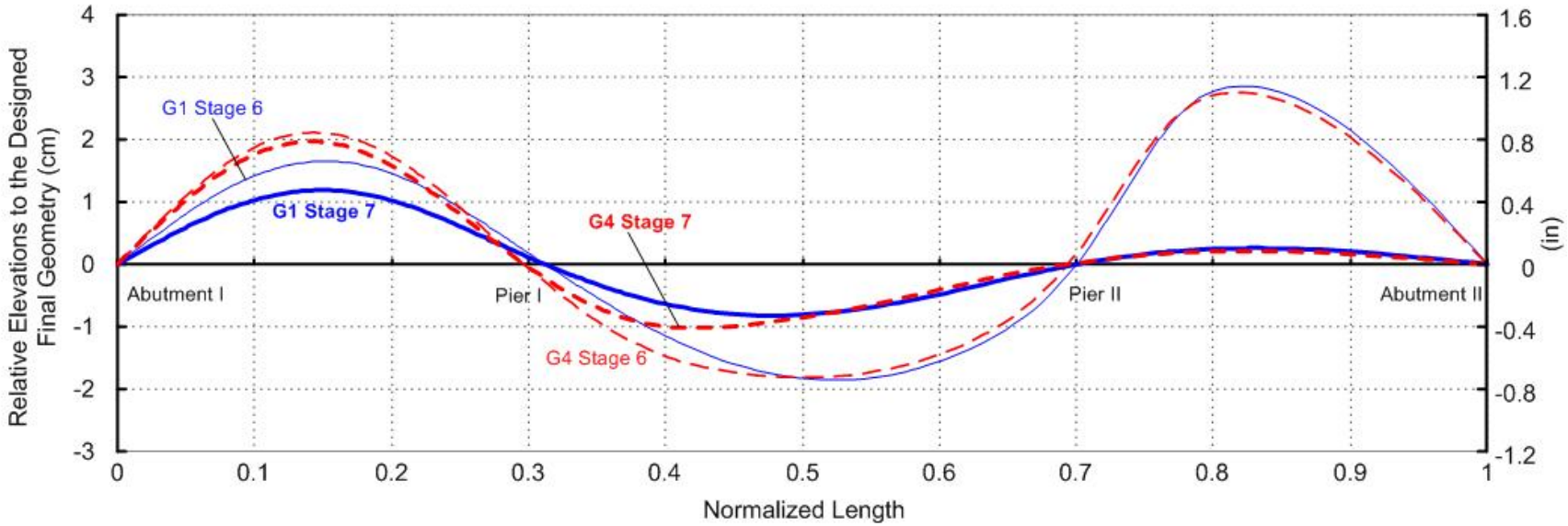

Figure 6.49 Girder G1(outside) and G4(inside) relative elevations to the designed final geometry in **casting stage 7**

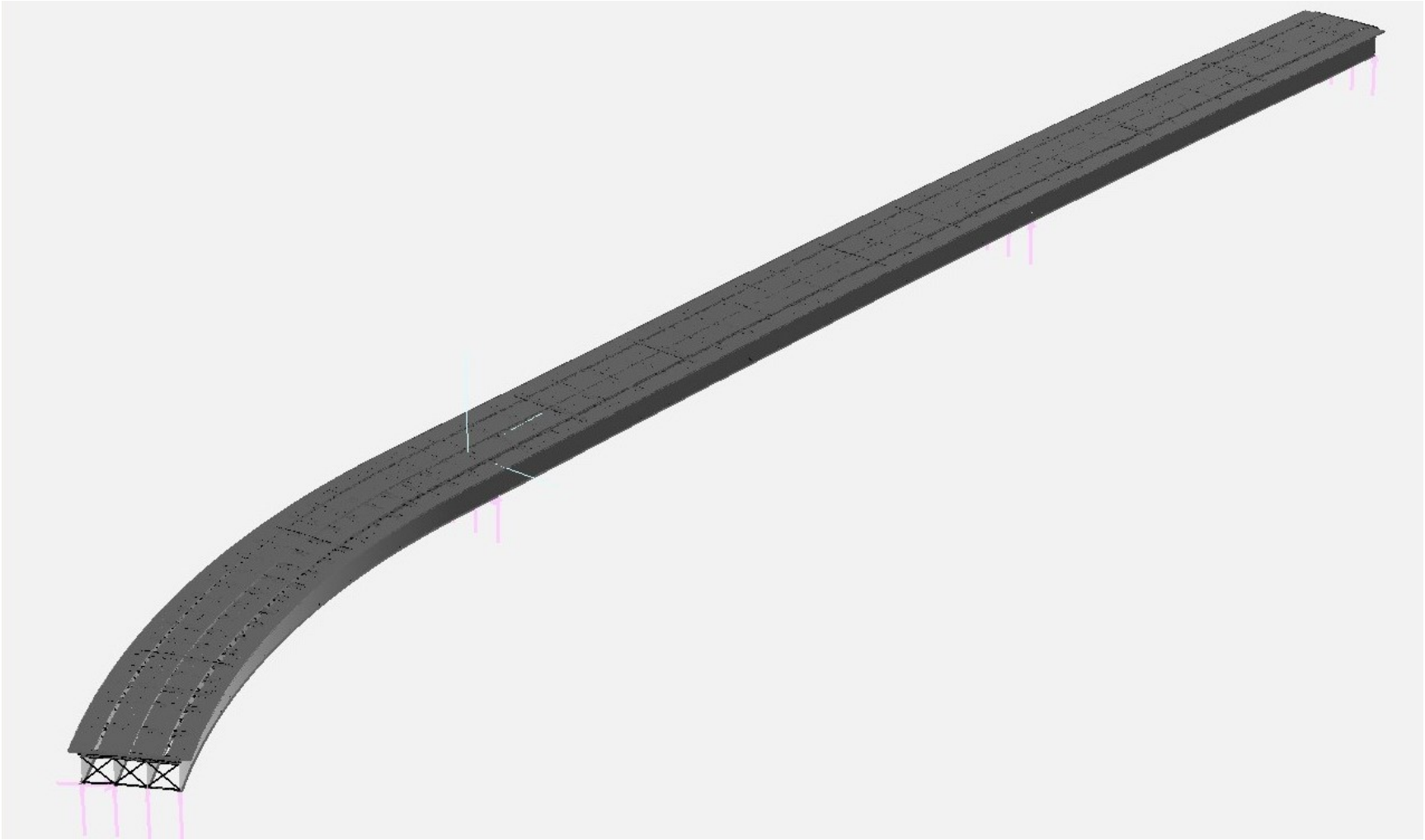

Figure 6.50 The Ford City Bridge model view in **casting stage 7** in the GT-SABRE Viewer

6.5 Study of the Steel Erection for the Curved Span

6.5.1 Model Description

The curved span of the Ford City Bridge includes field sections 1 through 4 and cross-frames 1A through 29C (see Figure 6.51). Section 4 becomes straight at 8.8 m (28.8 ft) from pier 1 and extends for 17.98 m (59 ft) into span II. The erection of these four field sections is considered in this section. The camber design in Model 4 in Section 6.4.2.4 is adopted. That is, the cross-frames are detailed based on the SDLF method and the girder camber is designed with the consideration of the staged concrete casting and the induced stresses due to lack-of-fit between the girders and cross-frames. The elevations of the temporary supports at the falsework 1, 2 and 2A, are set at the corresponding steel dead load elevations calculated in Model 4.

All the girder field sections are lifted and assembled individually as discussed in the next section. The lifting crane system described previously in Figure 4.6 is employed for this purpose.

6.5.2 Steel Erection Sequence in the Field and in Finite Element Modeling

The steel erection sequence in the current study closely follows field erection sequence described by Chavel and Earls (2001). This sequence is summarized in Tables 6.3 to 6.8. The erection sequence is subdivided into six stages. Stages 1 and 2 involve the erection of field sections 1 and 2 respectively. Stage 3 involves the installation of the interior girders G2 and G3 over pier 1. Stage 4 involves the splicing of girders G2 and G3 in field section 3 to field sections 2 and 4. Stage 5 involves the erection of the facia girders G1 and G4 in field section 4. Finally, stage 6 involves the splicing of girders G1 and G4 in field section 3 to field sections 2 and 4.

Initially, all the steel components of the Ford City Bridge curved span are created but are disassembled and placed on the ground before the erection simulation starts.

In the finite element model, four to five steps are employed for lifting the individual girders and placing them on their supports: (1) [Rigid Body Motion] for raising the girder; (2) [Geometric Nonlinear Analysis] for turning gravity on; (3) [Rigid Body Motion] for moving the girder to the support locations and (4) [Geometric Nonlinear Analysis] for setting the girder on its supports. The phrases within the brackets indicate the analysis type. Also, for some situations, it is advantageous to orient the girder so that its web is plumb at one of the supports to facilitate the connection of the cross-frames.

For each cross-frame installation, four steps are needed in the finite element model: (1) [Rigid Body Motion] for attaching the top and bottom chords of the cross-frame to a girder; (2) [Geometric Nonlinear Displacement Compatibility Analysis] for connecting the top (or bottom) chord of the cross-frame to the other girder; (3) [Geometric Nonlinear Displacement Compatibility Analysis] for connecting the bottom (or top) chord of the cross-frame to the same girder in (2); and (4) [Geometric Nonlinear Analysis] for applying the cross-frame self-weight to the connected girders. The forces applied in steps (2) and (3) can be either external forces applied at a desired location or internal equal-and-opposite forces applied at both the cross-frame node and the target connection point on the girder. Any external applied forces need to be released once the connection is made. For all cross-frame connections, the rotational degrees of freedom on the top chord, which is modeled using a 12-dof beam element, are released after the connection is made such that the top chord element behaves as a truss element. The connection tolerance is set as 0.01 cm (0.004 in) for all the cross-frame installations. The magnitude of the displacement gap between the two connection points is compared to the above tolerance to ascertain the convergence of the nonlinear iterations.

As mentioned in Section 4.3.5.2 and Figure 4.7, the girder splicing in the finite element model is made in four [Geometric Nonlinear Displacement Compatibility Analysis] steps: (1) translational continuity is enforced at the top (or bottom) flange of the I-girder elements; (2) translational continuity is enforced at the bottom (or top) flange of the I-girder elements; (3)

rotational continuity (compatibility of the girder section orientations) is established and (4) warping continuity is established. Once the translational continuity is made at the top flange, a new node is created at this connection point. The two girder nodes at the splice location are then constrained to this new node with rigid offsets. Three rotational degrees of freedom are released at this new node such that the to-be-spliced girders are effectively pinned together at this point. After the translational continuity is reached at the bottom flange of the two girders, the above rigid offset connections are removed and the two girders are linked together at their reference axis. The rotational degree of freedom about the element local Y axis is released at this instant. An external force is then applied to achieve the girder section orientation compatibility about the local Y axis. This is followed by applying a bi-moment to establish the warping continuity.

The tolerance for the translational compatibility is set as 0.001 cm (0.0004 in) and the tolerance for the rotational compatibility is set as 0.0001 rad. The tolerance for the warping continuity is set as 0.0001 / h_s, where h_s is taken as the larger distance between the cross-section shear center and the centroid of either flange. The norms of the above displacement and rotation gaps, and the absolute value of the discontinuity at the warping dof are compared against these tolerances.

Adjusting the girder elevation is useful when trying to make a girder splice or cross-frame connection. The girder elevation is adjusted by applying a vertical force to the elevation control spring on the lifting crane as discussed in Section 4.3.4.1 and Figure 4.6. In addition, the girder elevation adjustment is important when a temporary support is removed. If the temporary support has a large reaction before being removed, the analysis may have solution trouble if the temporary support is removed in one increment. To prevent this problem, the lifting crane needs to lift the girder to reduce the reaction on the temporary support. Then, the temporary support can be removed without any solution difficulty. Alternately, the elevation of the temporary support may be lowered incrementally until a gap is achieved between the girder and the

support. A similar problem happens when removing a lifting crane from a girder if the crane force is large. The crane lifting point needs to be lowered down to reduce the crane force.

In the finite element model, usually the cross-frame connection is completed by applying internal forces (equal magnitude and opposite direction) between the two connection points. When a girder is positioned on its supports and is held by a crane, the artificial springs on the crane are not removed until the lifted girder is connected by either top or bottom chord or the cross-frame that is already attached to the erected structure. This is because the lifted girder would swing easily under any lateral applied forces. Correspondingly, the finite element model would be unstable. Artificial springs are needed to stabilize the model. The required cross-frame connection forces are of course influenced by the artificial spring forces on the crane. Also, in some cases, solution difficulty is encountered even though the artificial springs are inserted to the model. For this case, external forces are applied to the erected structure to achieve the connection. This typically causes larger stresses in the bridge model that are non-physical and do not represent the actual field situation. Once the connection is made, the artificial springs are removed. Based on the uniqueness principle, the state of the structure at this instant is independent of the previous artificial devices that were required to numerically complete the connections.

In addition, in some cases, a lifted girder is seated on one support only prior to connecting it to the rest of the structure. For these cases, in addition to restraining three translational degrees of freedom at the support, artificial vertical and lateral restraints are placed at one free end of the girder for stability purposes. These artificial restraints influence the subsequent cross-frame installation forces until they are removed. They are removed once the girder is connected to the erected structure with two cross-frames (in the current work, the above cases occur when the lifted girder is being connected to the rest of the structure by cross-frames in one stage before making a splice connection in a subsequent stage).

Lastly, in the finite element model, a lifted girder is stabilized by artificial springs on the crane. When this girder is positioned to its desired location, the rigid body movement may include a rotation about the vertical axis. Since the orientations of the artificial springs on the crane are not rotated along with the girder and the crane, this rotation about the vertical axis may cause solution trouble for long field sections with a large weight. To avoid this problem, the girder self-weight is applied after the girder is spliced and seated on its supports.

Since the structural responses associated with the above cases do not represent a physical loading, these responses and the corresponding construction requirements are not presented in this study. However, based on the uniqueness concept introduced in Section 4.2, the subsequent analysis results are not influenced by these special cases, since the artificial spring constraints and/or loads are removed after the connection or connections are made. Also, since the above problems all relate to the assembly of partially constrained components into the structure, the corresponding stresses in the system and the construction force requirements are generally expected to be of a similar magnitude to the predicted values in adjacent steps where the predicted values are physical.

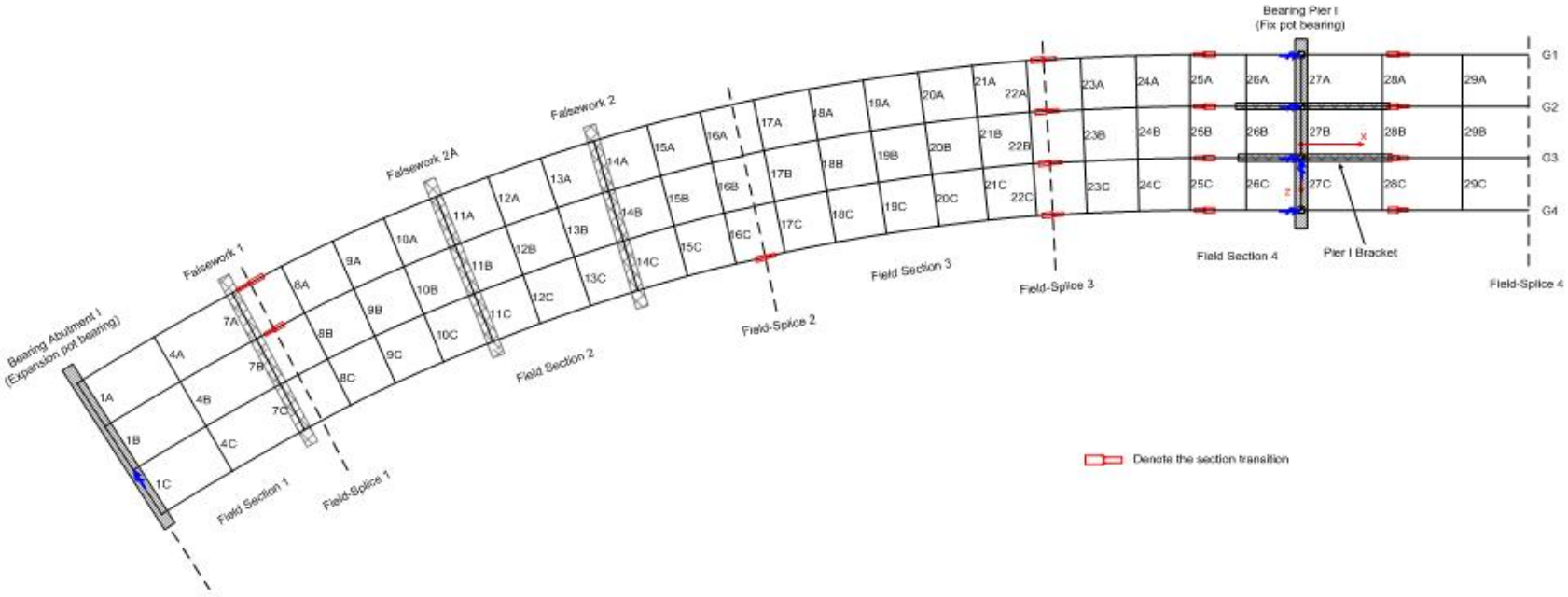

Figure 6.51 Ford City Bridge curved span plan view showing field section, falsework and cross-frame numbering

Table 6.4 Stage 1 of the Ford City Bridge steel erection sequence

Stage	Action
1A	Girder G3 field section 1 (G3-FS1) was lifted by lifting crane and then placed on the abutment 1 and falsework 1.
1B	Cross-frames at abutment 1 (1B and 1C) and at falsework 1 (7B and 7C) were attached to the girder G3-FS1.
1C	Cross-frames were blocked and tied down at abutment 1 and falsework 1. Also, the girder G3-FS1 was blocked laterally at the abutment.1 and falsework 1.
1D	The lifting crane released the girder G3-FS1.
1E	Girder G2 field section 1 (G2-FS1) was lifted by the lifting crane and then placed on the abutment 1 and falsework 1.
1F	Girder G2-FS1 was held by lifting crane and then was connected to girder G3-FS1 by previously installed cross-frame 1B and 7B.
1G	Cross-frame 4B was installed.
1H	The lifting crane released the girder G2 section 1.
1-I	Girder G4 field section 1 (G4-FS1) was lifted by the lifting crane and then placed on the bearing at abutment 1 and falsework 1.
1J	Girder G4-FS1 was held by lifting crane and then was connected to girder G3-FS1 by previously installed cross-frame 1C and 7C.
1K	Cross-frame 4C was installed.
1L	The lifting crane released the girder G4-FS1.
1M	Attached cross-frame 1A to the girder G2-FS1.
1N	Girder G1 field section 1 (G1-FS1) was lifted by the lifting crane and then placed on the abutment 1 and falsework 1.
1-O	Girder G1-FS1 was held by lifting crane and then was connected to girder G2-FS1 by previously installed cross-frame 1A.
1P	Cross-frame 4A was installed and was followed by the cross-frame 7A installation.
1Q	The lifting crane released the girder G1-FS1.

Table 6.5 Stage 2 of the Ford City Bridge steel erection sequence

Stage	Action
2A	Girder G3 field section 2 (G3-FS2) was lifted by lifting crane and was held in place on falsework 2A and 2, field splice 1 was completed.
2B	Attached cross-frames 11B, 11C, 14B and 14C to the girder G3-FS2. Then they were blocked and tied down. Girder G3-FS2 was blocked laterally at the bottom flange at falsework 2A and 2.
2C	Once positive contact had been verified at falsework 2A and a, the lifting crane released the girder G3-FS2.
2D	Girder G2 field section 2 (G2-FS2) was lifted by lifting crane and was held in place on falsework 2A and 2. Field splice 1 was completed. Then girder G2-FS2 was connected to the previously installed cross-frames 11B and 14B.
2E	Girder G2-FS2 was still held by lifting crane as the second crane lifted and installed the cross-frames in the order of 8B, 9B, 10B, 12B, 13B, 15B and 16B.
2F	The lifting crane released the girder G2-FS2.
2G	Girder G4 field section 2 (G4-FS2) was lifted by the lifting crane and was held in place on falsework 2A and 2. Field splice 1 was completed. Then girder G4-FS2 was connected to the previously installed cross-frames 11C and 14C.
2H	Girder G4-FS2 was still held by lifting crane as the second crane lifted and installed the cross-frames in the order of 8C, 9C, 10C, 12C, 13C, 15C and 16C.
2-I	The lifting crane released the girder G4-FS2.
2J	Girder G1 field section 2 (G1-FS2) was lifted by lifting crane and was held in place on falsework 2A and 2. Field splice 1 was completed.
2K	Cross-frames 11A and 14A were installed.
2L	Girder G1-FS2 was still held by lifting crane as the second crane lifted and installed the cross-frames in the order of 8A, 9A, 10A, 12A, 13A, 15A and 16A.
2M	The lifting crane released the girder G1-FS2.

Table 6.6 Stage 3 of the Ford City Bridge steel erection sequence

Stage	Action
3A	Pier 1 brackets for the girder G2 and G3 field section 4 (G2-FS4 and G3-FS4) were set and adjusted, also the pier 1 bearing were adjusted.
3B	Girder G3-FS4 was lifted by lifting crane and was placed on the pier brackets and bearing. It was held in place as the cross-frames 27 and 27C covered pier 1.
3C	Cross-frames at both ends of the pier 1 brackets 26B and 28B were attached to the girder G3-FS4.
3D	The lifting crane released the girder G3-FS4 once the attached cross-frames were blocked and tied down to the pier and pier brackets.
3E	Girder G2-FS4 was lifted by lifting crane and was placed on the pier 1 brackets and bearing. It was held in place as the previously installed cross-frames 27B and 26B and 28B connected to it.
3F	Girder G2-FS4 was still held by lifting crane as the second crane lifted and installed the cross-frames in the order of 25B, 24B, 23B and 29B. Note that once the cross-frame 25B was installed, the lifting crane released the girder G2-FS4.

Table 6.7 Stage 4 of the Ford City Bridge steel erection sequence

Stage	Action
4A	Girder G3 field section 3 (G3-FS3) was lifted by lifting crane. A cantilever “come-along” assembly was used to prevent the girder from rolling over.
4B	Place the drop-in girder G3-FS3 in between the girder G3-FS4 and G3-FS2. The field splice 3 was made first, then field splice 2. *Note:* There were some difficulties for the field splice 2. Also, a few alignment problems were noted.
4C	Girder G2 field section 3 (G2-FS3) was lifted by lifting crane. A cantilever “come-along” assembly was used to prevent the girder from rolling over.
4D	Place the drop-in girder G2-FS3 in between the girder G2-FS4 and G2-FS2. The field splice 3 was made first, then field splice 2. ***Note:*** **Extreme difficulties were encountered in trying to make the field splice 2**. Longitudinal jacking devises at abutment 1 were used to close the gap for field splice 2. In the field, the field splice 2 was not made until all cross-frames between G2-FS3 and G3-FS3 were installed.
4E	Cross-frames were installed in the order of 17B, 18B, 19B, 22B, 20B and 21B.
4F	Pier 1 brackets were fully removed.

Table 6.8 Stage 5 of the Ford City Bridge steel erection sequence

Stage	Action
5A	Girder G4 field section 4 (G4-FS4) was lifted by the lifting crane and was placed on the pier 1.
5B	Previously installed cross-frame 27C was connected to the girder G4-FS4.
5C	Girder G4-FS4 was held by lifting crane and the cross-frames 23C~28C were installed. The order is unknown and when the lifting crane was removed is unknown. It is assumed that the order is 28C, 29C, 26C, 25C, 24C and 23C. Also it is assumed that as before, the lifting crane was removed once the cross-frame 25C was installed.
5D	Girder G4-FS4 was lifted by the lifting crane and was placed on the pier 1.
5E	Cross-frames 27A and 28A were installed first, then 29A and 26A.
5F	The installation order of the cross-frames 23A, 24A and 25A is unknown. Also when the lifting crane released the girder G4-FS4 is unknown. But it is assumed the order is as before: 25A, 24A and 23A, and assumed the lifting crane was removed once the cross-frame 25A was installed

Table 6.9 Stage 6 of the Ford City Bridge steel erection sequence

Stage	Action
6A	Girder G4 field section 3 (G4-FS3) was lifted by the lifting crane. A cantilever "come-along" assembly was used to prevent the girder from rolling over.
6B	Place the drop-in girder G4-FS3 in between the girder G4-FS4 and G4-FS2. The field splice 3 was made first, then field splice 2. ***Note:*** **The field splice 2 was made with little or no alignment problem**.
6C	The girder G4-FS3 was held by lifting crane as the cross-frames 17C~22C were installed. The order is unknown. But it is assumed that the order is as before: 17C, 18C, 19C, 22C, 20C and 21C.
6D	The lifting crane released the girder G4-FS3.
6E	Girder G1 field section 3 (G1-FS3) was lifted by the lifting crane. A cantilever "come-along" assembly was used to prevent the girder from rolling over.
6F	Place the drop-in girder G1-FS3 in between the girder G1-FS4 and G1-FS2. The field splice 3 was made first, then field splice 2. ***Note:*** **Extreme difficulties were encountered in trying to make the field splice 2**. Longitudinal jacking devises at abutment 1 were used to close the gap for field splice 2. In the field, the field splice 2 was not made until all cross-frames between girder G1-FS3 and G2-FS3 were installed.
6G	The girder G1-FS3 was held by lifting crane as the cross-frames 17C~22C were installed. The order is unknown. But it is assumed that the order is as before: 17A, 18A, 19A, 22A, 20A and 21A.
6H	The lifting crane released the girder G1-FS3.
6-I	The falsework 2A was removed.
6J	The falsework 1 was removed.

6.5.3 Analysis Results

The focus of the following discussions is on the required forces for the steel assembly and the maximum girder and cross-frame member stresses during each cross-frame installation and girder splicing operation. For the cross-frame installation and girder splicing, the initial gap, i.e., the distance between the connection points, the resulting small residual relative displacement at the end of the solution, and the calculated required forces are listed in Appendix III. The peak stresses in the girders and cross-frames at each steel erection step are shown in the Figures 6.52 and 6.53 respectively. Table 6.10 explains the key analysis steps relating to the above structural responses. These step numbers are also labeled in Figures 6.52 and 6.53. The complete erection simulation is defined in 426 steps. A summary of each of these steps is provided at the beginning of Appendix III. In addition, the support reactions and any lifting of the girders off of their supports during the steel erection are monitored. The support vertical reactions at the end of each stage are shown in Table 6.11.

As indicated in Table 6.7 Stage 4D and Table 6.9 Stage 6F, the girder G2 and G1 field splice 2 encountered extreme difficulties in the field such that the steel erection sequence had to be changed to make the splice (Chavel and Earls 2001). All of the above analysis results correspond to the erection sequence implemented in the field. The *planned sequence* was also investigated in this research. In this study, GT-SABRE encountered a convergence problem in enforcing the bottom flange translational continuity at the girder G2 field splice 2 when analyzing for the planned sequence (see Figure 4.7(c) for an illustration of this step of the splicing). In the *field sequence*, the bottom flange translational continuity at the above locations is achieved after the three adjacent cross-frames are installed. The following discussions are based on the results from the *field sequence* simulation.

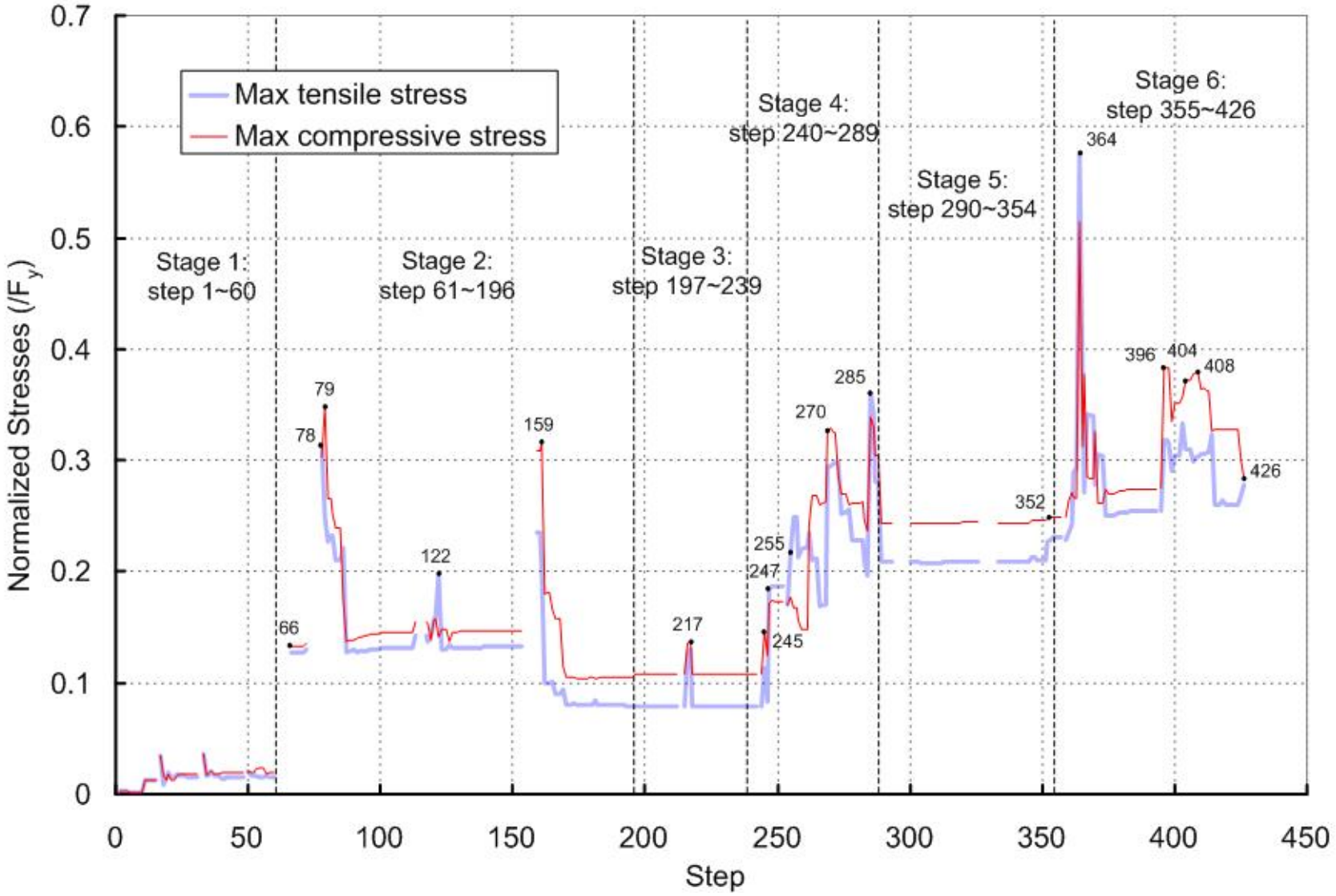

Figure 6.52 The maximum girder stress for each of the total 426 steps. The number on the curve is the step number and the corresponding action in the finite element model is shown in Table 6.10

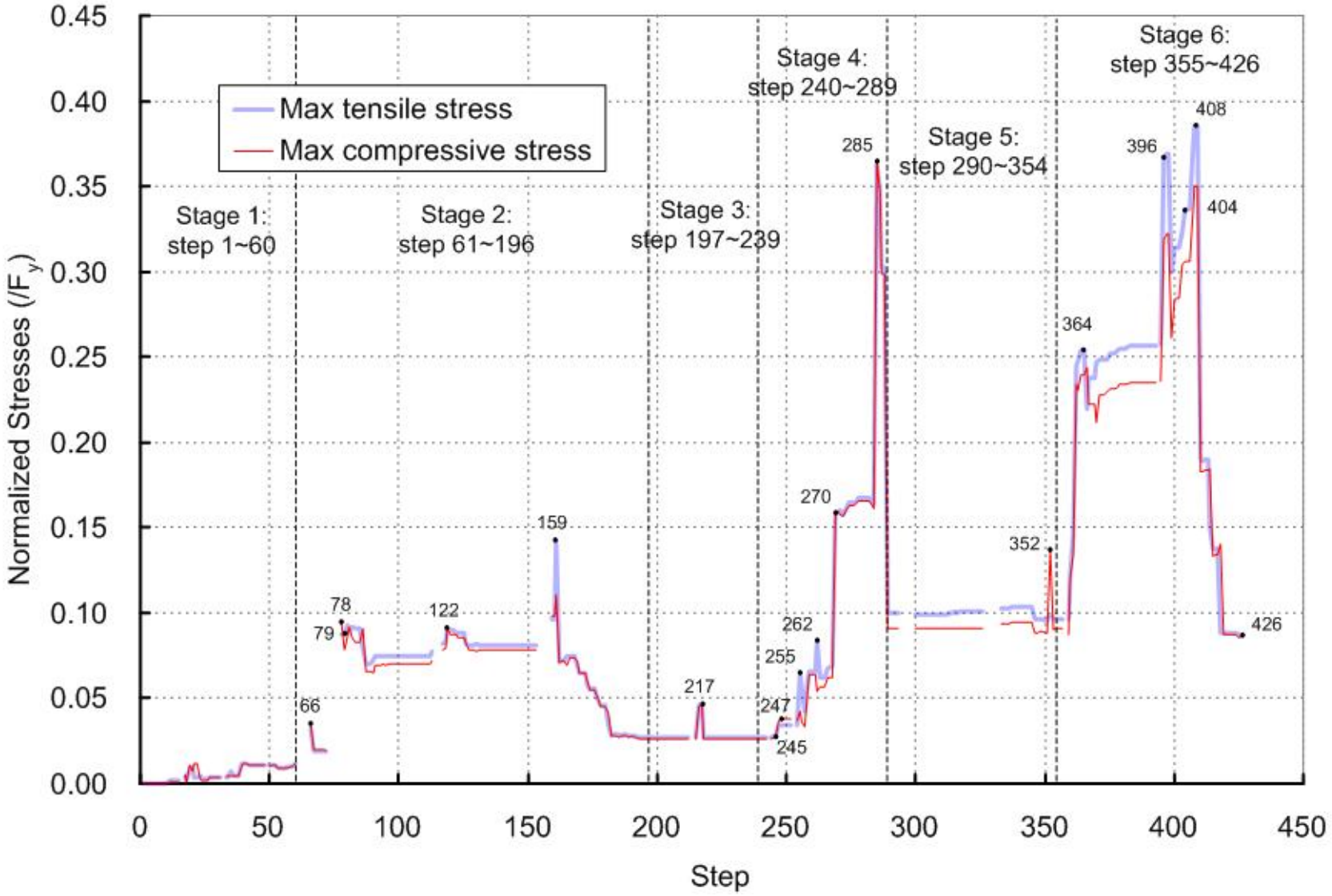

Figure 6.53 The maximum cross-frame member stress for each of the total 426 steps. The number on the curve is the step number and the corresponding action in the finite element model is shown in Table 6.10

Table 6.10 The description of the specific steps in Figures 6.52 and 6.53

Step	Action in the FEA model	Max. girder compr. Stress at	Max. girder tensile. Stress at	Max. CF member compr. Stress at	Max. CF member tensile. Stress at
66	Apply steel self-weight to the girder G3-FS2, which has been spliced to G3-FS1 and seated on the falsework 1	G3 top flange at falsework 1	G3 bottom flange at falsework 1	CF-7B diagonal	CF-7B diagonal
78	The girder G2-FS2 is seat on its supports under self-weight	G2 top flange at falsework 1	G2 bottom flange at falsework 1	CF-7B diagonal	CF-7B diagonal
79	Connect CF-11B (already attached to G3-FS2) bottom chord to girder G4-FS2	G2 top flange at falsework 1	G2 bottom flange at falsework 1	CF-7B bottom chord	CF-7B top chord
122	Connect CF-14C (already attached to G3-FS2) bottom chord to girder G4-FS2	G2 top flange at falsework 1	G4 bottom flange at falsework 2A	CF-7B bottom chord	CF-7B top chord
159	Apply steel self-weight to the girder G1-FS2, which has been spliced to G1-FS1 and seated on the falsework 1	G1 top flange at falsework 1	G1 top flange at falsework 1	CF-7A bottom chord	CF-7A top chord
217	Connect CF-26B (already attached to G3-FS4) bottom chord to the girder G2-FS4E	G3 bottom flange at pier I	G3 top flange at pier I	CF-28B diagonal	CF-28B bottom chord
245	Achieve the translational continuity between girders G3-FS2 and G3-FS3 top flange for the field splice 2	G3 bottom flange near the field splice 3	G3 bottom flange near the field splice 3	CF-11A diagonal	CF-11A diagonal
247	Achieve the translational continuity between girders G3-FS2 and G3-FS3 bottom flange for the field splice 2	G3 top flange at the CF-23B location	G3 top flange at CF-23B location	CF-12C diagonal	CF-16Cdiagonal
255	Achieve the translational continuity between girders G2-FS2 and G2-FS3 top flange for the field splice 2	G3 bottom flange at the CF-23B location	G3 bottom flange at the field splice 2	CF-11A diagonal	CF-11A diagonal
262	Connect CF-18B (already attached to G3-FS3) top chord to the girder G2-FS3	G3 top flange near the CF-17B	G3 bottom flange near the CF-18B	CF-16B diagonal	CF-18B diagonal
270	Achieve the rotational continuity between girders G2-FS2 and G2-FS3 for the field splice 2	G2 top flange at the CF-19B location	G2 top flange at the CF-19B location	CF-16A diagonal	CF-16A diagonal
285	Raise the lifting crane on the girder G2-FS3 for the pier bracket G2-BK1 and G2-BK2 removal	G2 top flange at CF-16A location	G3 top flange at the CF-16A location	CF-16B diagonal	CF-16A diagonal
352	Connect CF-23A (already attached to G2-FS4) top chord to the girder G1-FS4	G2 top flange near the CF-19B	G2 bottom flange near the CF-23A	CF-23A top chord	CF-23A diagonal
364	Achieve warping continuity between girders G4-FS2 and G4-FS3 for the field splice 2	G4 bottom flange near the field splice 2	G4 top flange near the field splice 2	CF-16B bottom chord	CF-16B top chord
396	Achieve the translational continuity between girders G1-FS2 and G1-FS3 top flange for the field splice 2	G2 top flange near the field splice 2	G2 bottom flange near the CF-17A	CF-16A diagonal	CF-16B top chord

Table 6.10 The description of the specific steps in Figures 6.52 and 6.53 (continued)

Step	Action in the FEA model	Max. girder compr. Stress at	Max. girder tensile. Stress at	Max. CF member compr. Stress at	Max. CF member tensile. Stress at
404	Connect CF-17A (already attached to G2-FS3) bottom chord to the girder G1-FS3	G2 top flange at field splice 2	G2 bottom flange near the CF-18A	CF-17A diagonal	CF-17B top chord
408	Connect CF-19A (already attached to G2-FS3) bottom chord to the girder G1-FS3	G2 top flange at field splice 2	G2 bottom flange at field splice 2	CF-17B bottom chord	CF-17B top chord
426	Complete the steel erection and release the moment resistance at the ends of all the cross-frame bottom chord	G1 top flange near the CF-7A location	G1 bottom flange near the CF-23A	CF-18A bottom chord	CF-18A top chord

Table 6.11 The support vertical reactions at the end of each stage (kN) (1 kN = 0.225 kips)

Support	Girder	Stage 1 1 ~ 60	Stage 2 61 ~ 196	Stage 3 197 ~ 239	Stage 4 240 ~ 289	Stage 5 290 ~ 354	Stage 6 355 ~ 426	IIM of curved span at end of Stage 6)	% diff
Abut I	G1	143.33	684.90	684.90	953.92	942.90	1,766.94	1,760.39	0.37
	G2	159.91	340.47	340.47	403.32	400.59	801.15	808.32	-0.89
	G3	91.25	113.24	113.24	79.39	79.07	115.56	110.35	4.72
	G4	98.78	35.55	35.55	0.00	0.00	0.00	0.00	0.00
FW I	G1	171.54	0.00	0.00	0.00	0.00	------	------	------
	G2	178.86	0.00	0.00	0.00	0.00	------	------	------
	G3	100.75	0.00	0.00	0.00	0.00	------	------	------
	G4	116.04	87.04	87.04	425.70	425.16	------	------	------
FW 2A	G1	------	0.00	0.00	0.00	0.00	------	------	------
	G2	------	0.00	0.00	0.00	0.00	------	------	------
	G3	------	0.00	0.00	0.00	0.00	------	------	------
	G4	------	926.88	926.88	675.51	679.71	------	------	------
FW 2	G1	------	1,182.69	1,182.69	1,997.54	2,007.67	1,598.96	1,597.68	0.08
	G2	------	705.63	705.63	20.41	61.86	0.00	0.00	0.00
	G3	------	237.47	237.47	0.00	0.00	0.00	0.00	0.00
	G4	------	0.00	0.00	0.00	0.00	319.48	328.77	-2.83
BK	G2	------	------	187.71	------	0.00	------	------	------
	G3	------	------	265.63	------	0.00	------	------	------
Pier I	G1	------	------	------	------	792.60	2,217.68	2,231.30	-0.61
	G2	------	------	630.06	1,797.37	1,829.46	1,506.07	1,481.11	1.69
	G3	------	------	516.63	486.93	562.21	712.10	713.69	-0.22
	G4	------	------	------	------	674.83	498.28	504.63	-1.26
Stage Applied Load		1,060.45	3,253.43	1,600.03	926.19	1,615.94	1,080.19		
Total Applied Load		1,060.45	4,313.88	5,913.91	6,840.10	8,456.04	9,536.22	9,536.24	0.00

6.5.3.1 Steel Erection Stage 1

Sixty steps are employed to simulate the steel erection stage 1 in GT-SABRE. There is no difficulty for the simulation of this stage. Figure 6.54 shows that G3-FS1 (Girder 3 – Field Section 1) is lifted under its self-weight in the finite element model. The rest of the structural components remain on the ground at this stage. In addition to temporary radial restraints at abutment 1 and falsework 1, a temporary longitudinal restraint is applied to the girder bottom flange at abutment 1 for structural stability when G3-FS1 is placed on its supports. Also, G3-FS1 is still held by the crane after it is placed on its supports. Before attaching the cross-frames 1B, 7B, 1C and 7C to G3-FS1, the girder web is adjusted so that it is plumb at abutment 1. This facilitates the cross-frame connections in a subsequent step. The cross-frames 1C and 7C are tied-down and then the lifting crane is removed. Figure 6.55 shows G3-FS1 with the cross-frames installed after the lifting crane removal.

Next, when G2-FS1 is placed on the supports while being held by the crane, the same types of temporary restraints used for G3-FS1 are applied. For the connection of the girder G2-FS1 to cross-frame 1B, it is easier to connect the bottom chord first. The artificial crane-system springs are needed during the first cross-frame connection in this stage, i.e., the connection of the cross-frame 1B bottom chord to G2-FS1. Once the G2-FS1 is connected to the cross-frame 1B bottom chord, the artificial springs are removed. Then the connection of the top chord of cross-frame 1B to G2-FS1 is completed. This is followed by the connections of the cross-frame 7B to G2-FS1. Next, cross-frame 4B (see Figure 6.51) is installed between G3-FS1 and G2-FS1. A similar installation process is used for the G4-FS1 and G1-FS1 placement and the corresponding cross-frame installations.

As shown in Table A3.8, the required forces for the cross-frame connections in stage 1 are relatively small (compared to the subsequent stages). The largest required force in this stage happens when connecting the bottom chord of the cross-frame 7B, which is already attached to G3-FS1, to the girder G2-FS1. The required force is 21.3 kN (4.8 kips). As shown in

Figures 6.52 and 6.53, the girder stresses and cross-frame member stresses throughout stage 1 are small and well below the yield stress F_y (344.73 MPa or 50 ksi). Some of the girders are lifted off of their supports during the cross-frame installation. However, at the end of the stage, all of the girders are seated on their supports and the largest vertical support reaction is 178.86 kN (40.24 kips) at G2 falsework 1 as shown in Table 6.11. Figure 6.56 shows the finite element model of field section 1 at the end of the stage 1.

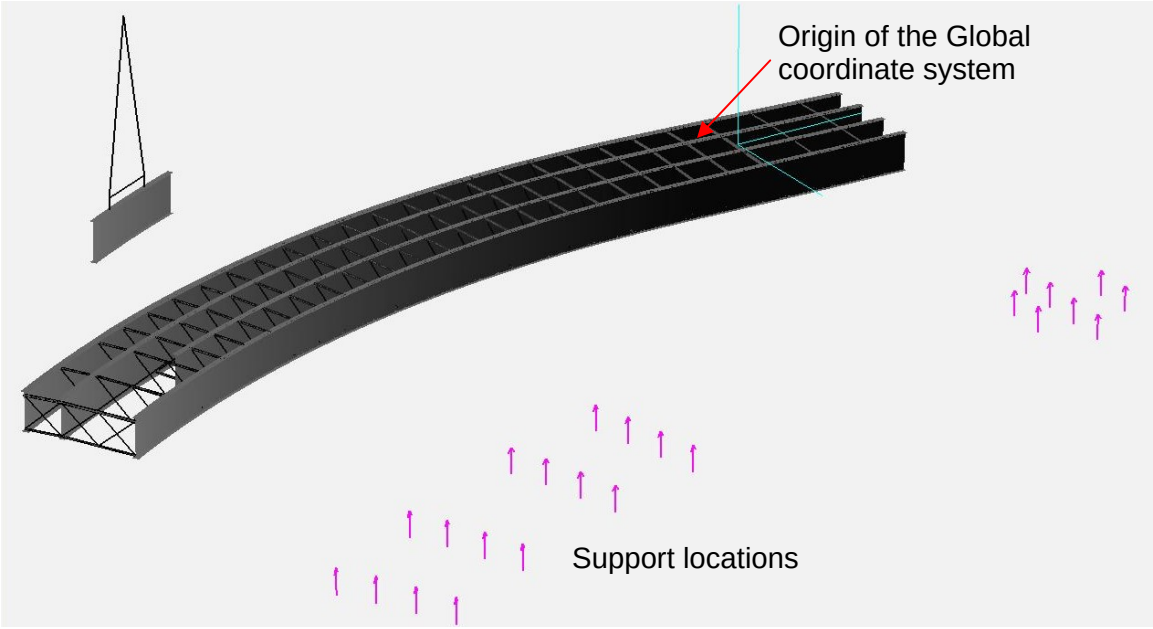

Figure 6.54 Girder G3-FS1 is lifted under self-weight. The rest of the structural components remain “on the ground” in the FEA model

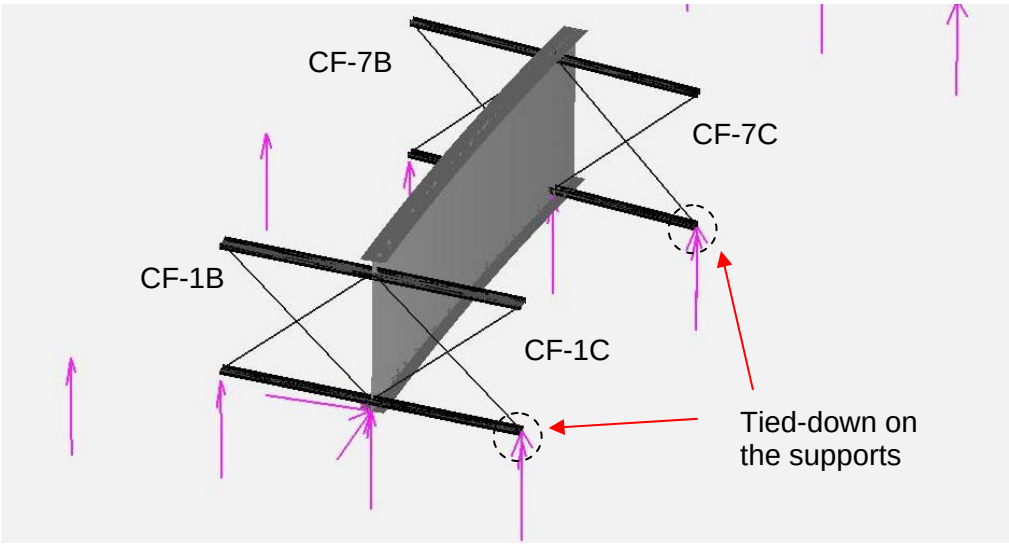

Figure 6.55 Girder G3-FS1 is stabilized by the tied-down cross-frame CF-1C and CF-7C in the FEA model

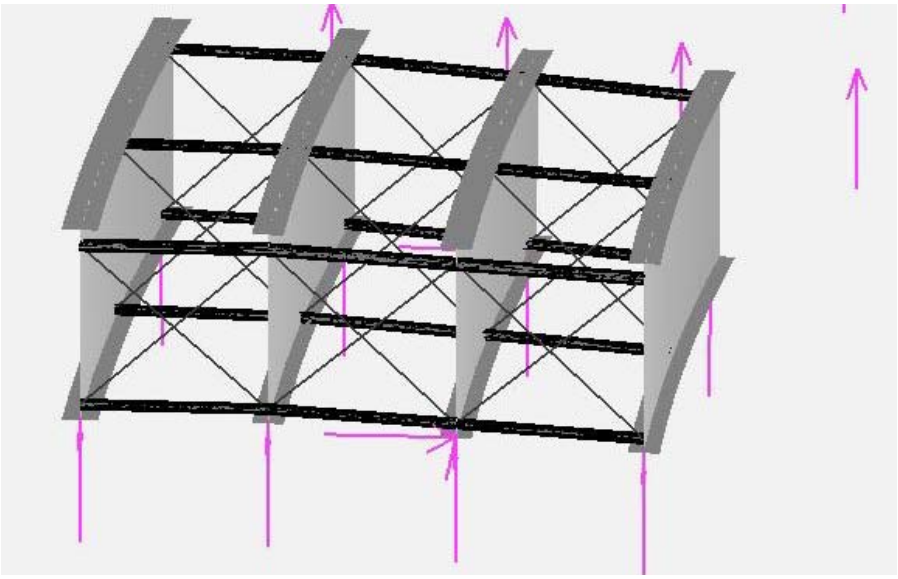

Figure 6.56 The steel erection status at the end of the stage 1 in the FEA model

6.5.3.2 Steel Erection Stage 2

The simulation of the steel erection stage 2 requires 136 steps (steps 61 to 196). The girders and cross-frames in field section 2 are erected in this stage. Unlike the girder lifting sequence in other stages, the individual girder self-weights are applied after each of the girders is spliced to the corresponding girder in field section 1 and seated on the temporary supports. First, translational and rotational continuity is achieved at the four splice points within the specified tolerances solely due to the rigid body movement of the individual girders. Also, no bi-moment is needed to make the splice because the warping incompatibility at the splice point is less than the tolerance. The lifted girder elevations are then adjusted to position the girders on their supports at the falseworks 2A and 2. Interestingly, girders G3-FS2 and G2-FS2 never come into contact with the support at falsework 2A. With this method, the girders are stable under their self-weight without the use of artificial springs on the lifting crane. As noted previously, the solution results are not reported for steps where artificial measures are employed to accomplish the assembly operations (since the results are affected by the artificial forces or constraints). Thus, for example, the results for steps 61 through 65 are not shown in Figures 6.52 and 6.53 since the weight of the girders has not yet been applied to the structural model during these stages.

Figure 6.57 shows the girder G3-FS2 after it is spliced to G3-FS1 and seated on falsework 2. At this point, the cross-frames 11B, 14B, 11C and 14C are attached to G3-FS2 to stabilize the girder before the lifting crane removal. The cross-frames 11C and 14C (see Figure 6.51) are tied-down on falseworks 2A and 2 to stabilize the girder. It is found that later after girder G2-FS2 is spliced to G2-FS1 and set on falsework 2A and 2, girders G1, G2 and G3 are lifted off of falsework 1. G3-FS2 is also lifted off the falsework 2A at this time. Throughout stage 2, falsework 2A is never touched by girders G2 and G3 (note that the supports at falsework 2a are set at the steel dead load elevations calculated in the analysis of the full bridge using Model 4 as discussed in Sections 6.4.2 and 6.4.3). Also falsework 1 is seldom contacted by the girders

during stage 2. At the end of this stage, the abutment 1 and falsework 2 below the girder G1 and the falsework 2A under girder G4 support the largest dead load as shown in Table 6.11.

As shown in Figure 6.52, the girder stresses are increased near the field splice location after the girder sections are spliced and seated on the falseworks under their self-weight, especially for G2-FS2 (steps 78 and 79) and G1-FS2 (step 159). For G2-FS2, the girder maximum stress increased from 46.50 MPa (6.74 ksi) in compression at the top flange, before making the splice to G2-FS1, to 108.08 MPa (15.67 ksi) at the bottom flange near the G2-FS2 field splice 1 after making the splice. For the girder G1-FS2 splicing, the girder maximum stress increased from 50.68 MPa (7.35 ksi) to 106.53 MPa (15.45 ksi) at the bottom flange near the G1-FS2 field splice 1. However, the maximum stress reduces to less than 40.00 MPa (5.80 ksi) after the cross-frames are installed. The maximum cross-frame member stress for each step in this stage, shown in Figure 6.53, has the same trend as in Figure 6.52. The largest stress is 49.04 MPa (7.11 ksi) in one of the diagonal members of cross-frame 11A.

The required forces for the cross-frame connections are usually larger near the splice locations and above the supports. As shown in Tables A3.9, A3.10 and A3.11, the required jacking/come-along force is about 167.53 kN (37.66 kips) for connecting the cross-frame 11B top chord to the girder G2-FS2 in step 80, 82.98 kN (18.65 kips) for connecting the cross-frame 11C top chord to the girder G4-FS2 in step 119 and 252.60 kN (56.79 kips) for connecting the cross-frame 11A bottom chord to the girder G1-FS2 in step 161. Figures 6.58 and 6.59 illustrate the cross-frame 14B top chord connection process in the finite element model.

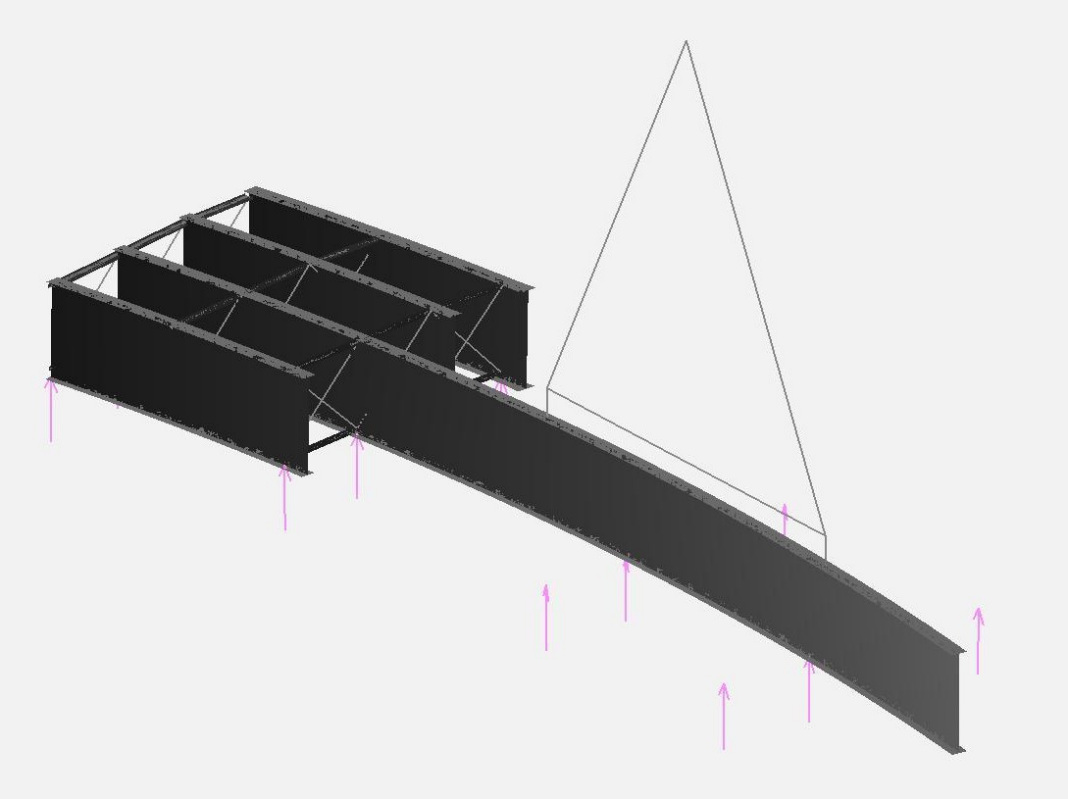

Figure 6.57 Girder G3-FS2 is spliced to the girder G3-FS1 and seated on the falsework 2A and 2.

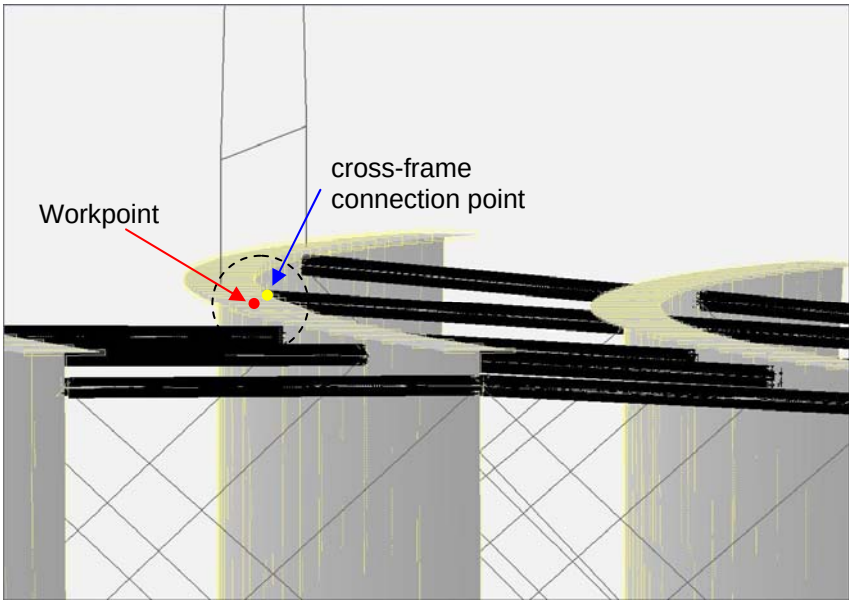

Figure 6.58 Illustration of the cross-frame connection 1: the gap between the connection point of the cross-frame 14B top chord and the workpoints on the girder G2-FS2 before the connection

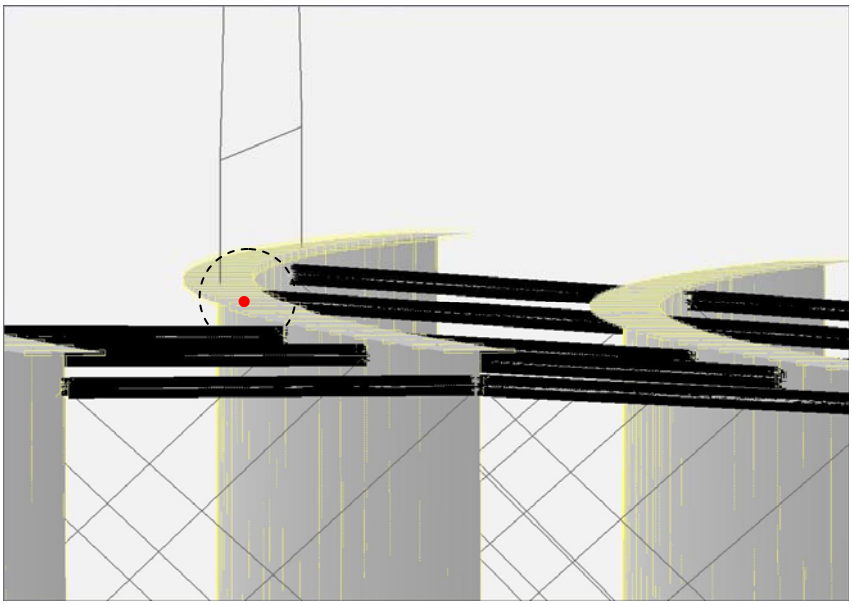

Figure 6.59 Illustration of the cross-frame connection 2: the connection point of the cross-frame 14B top chord and the workpoints on the girder G2-FS2 are connected

6.5.3.3 Steel Erection Stage 3

Forty-three steps (steps 197 to 239) are used for the simulation of the steel erection stage 3. Pier brackets are set on the both sides of pier 1 to stabilize the girders G2-FS4 and G3-FS4. The pier bracket on the side of the curved span is denoted BK1, and the pier bracket on the side of the center span is referred to as BK2 in the following. The elevations of the pier brackets are set based on the steel dead load elevation of the girders obtained from the Model 4 analysis in Section 6.4.2.4. The pier brackets BK2 are never contacted by the girders during the erection of the curved span. Figure 6.60 shows that G3-FS4 is stabilized initially by tying the attached cross-frames 26B and 28B to the pier brackets. Then G2-FS4 is positioned on its bearing at pier 1 (see Figure 6.61).

As shown in Table A3.12, Figure 6.52 and 6.53, the required cross-frame connection forces and the girder and cross-frame member stresses are relatively small in this stage. The maximum girder stress in the erected structure at the end of this stage is at the top flange of G1-FS2 near the field splice 1 with the magnitude of 27.34 MPa (3.97 ksi) (i.e., the peak stress is not located in field section 4). Figure 6.62 shows the erected structure at the end of the stage 3.

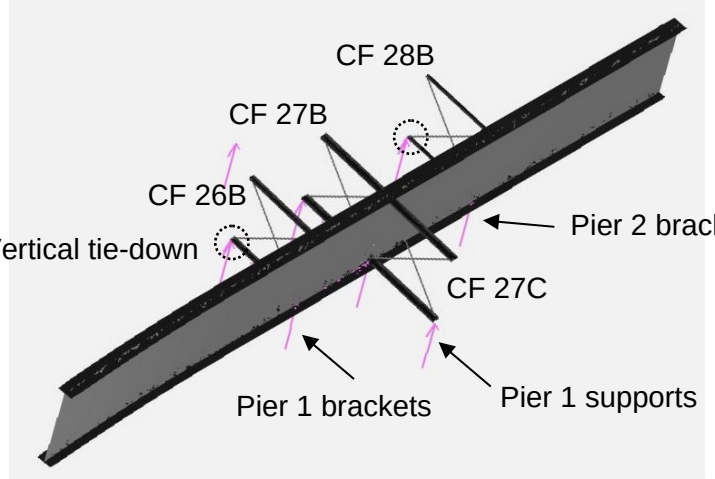

Figure 6.60 Girder G3-FS4 is stabilized by the attached cross-frames 26B and 28B on the pier brackets 1 and 2 in the FEA model

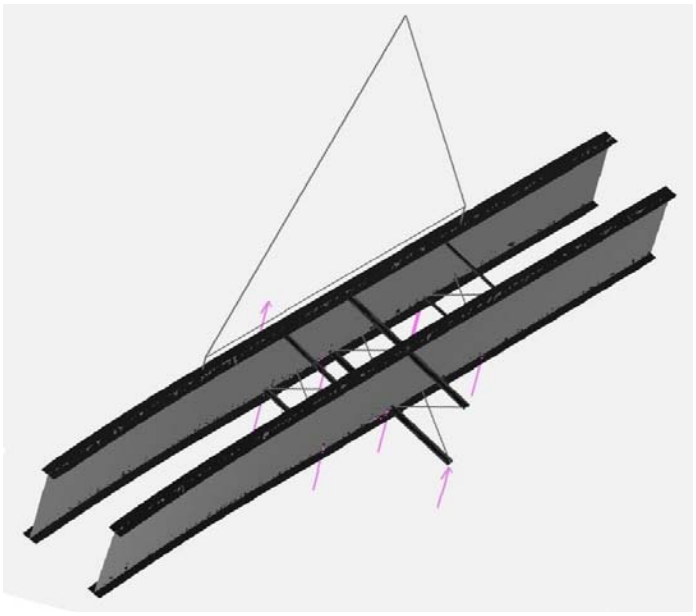

Figure 6.61 Girder G2-FS4 is held by lifting crane and set on the Pier 1 and pier brackets before connecting to the stabilized girder G3-FS4 set in the FEA model

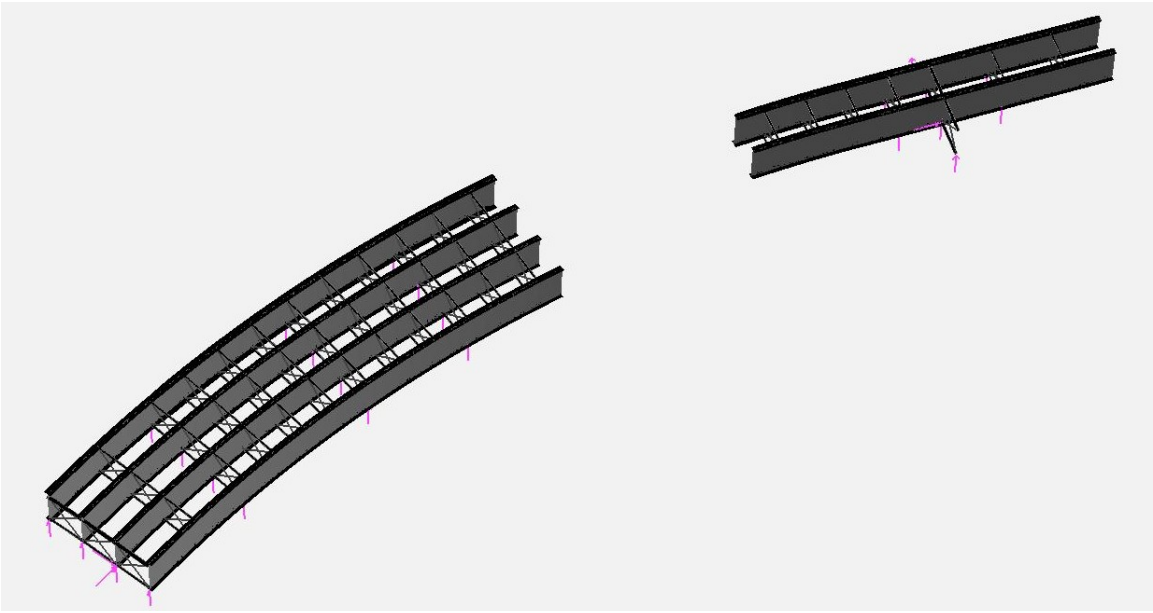

Figure 6.62 The erected structures at the end of the stage 3, including all girders and cross-frames in field section 1 and 2, and the girder G3-FS4 and G2-FS4 with cross-frames in between as well as CF-27C in the FEA model

6.5.3.4 Steel Erection Stage 4

Fifty steps (steps 240 to 289) are employed for the simulation of the steel erection stage 4. This stage includes the splicing of the drop-in girders G3-FS3 and G2-FS3 to field sections 2 and 4 as well as the installation of the cross-frames between these drop-in girders. There is no difficulty for the G3-FS3 and G2-FS3 installation when following the *field sequence*, i.e., when the cross-frames 17B, 18B and 19B are installed between girders G2-FS3 and G3-FS3 before making the field splice 2. Tables A3.13 and A3.14 show the required forces for the field splice of G3-FS2 and G3-FS3, and G2-FS2 and G2-FS3. Figures 6.63 to 6.66 illustrate the girder G3 connection to field section 2 at field splice 2 in the FEA model.

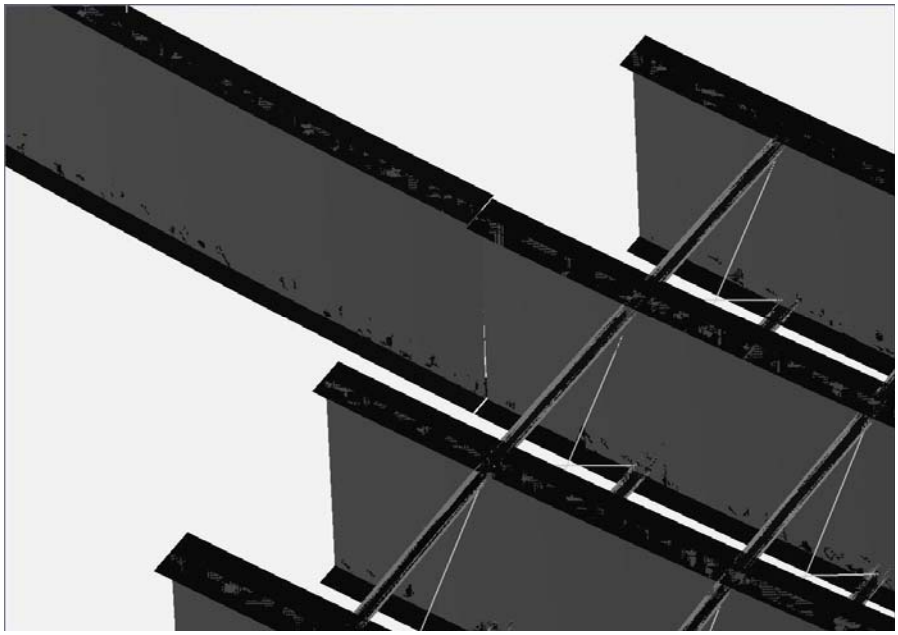

Figure 6.63 Illustration of the girder G3-FS3 connection to field section 2 at field splice 2 in the FEA model – 1: before splicing

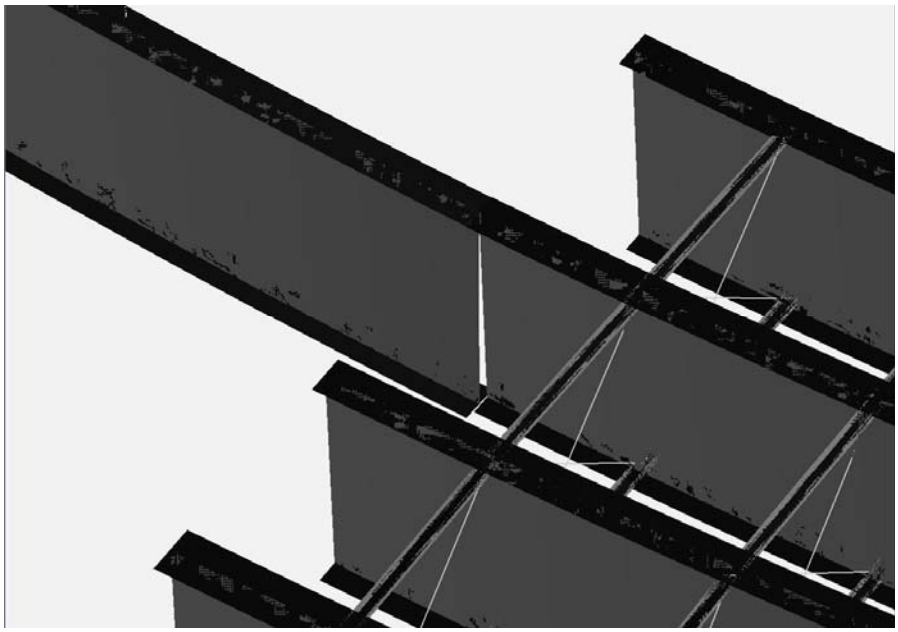

Figure 6.64 Illustration of the girder G3-FS3 connection to field section 2 at field splice 2 in the FEA model – 2: Top-Flange translational continuity

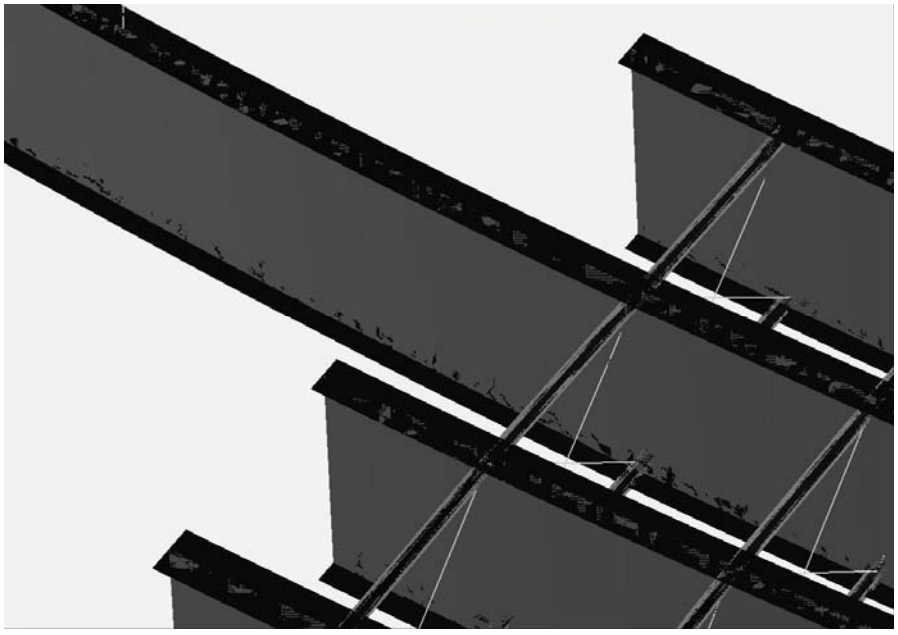

Figure 6.65 Illustration of the girder G3-FS3 connection to field section 2 at field splice 2 in the FEA model – 3: Bottom-Flange translational continuity

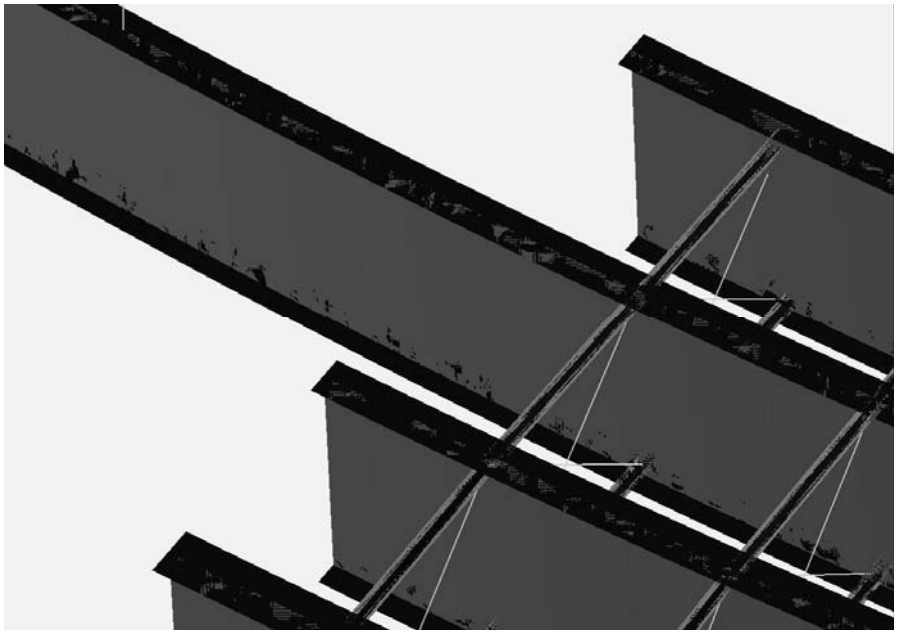

Figure 6.66 Illustration of the girder G3-FS3 connection to field section 2 at field splice 2 in the FEA model – 4: completed splicing

For the field splice 2 of girder G2-FS3 and G2-FS2, the top flanges of G2-FS3 and G2-FS2 are pinned together first. This requires a come-along force of 304.83 kN (68.59 kips) at step 253 as shown in Table A3.14. The continuity at the G2-FS3 and G2-FS2 bottom flanges is made after the cross-frames 17B, 18B and 19B are installed (following the *field sequence* for the Ford City Bridge). However, the required force to make this connection is quite large (5,323 kN or 1,198 kips, shown for step 269 in Table A3.14). Figure 6.67 shows the erected structure after the second girder, G2-FS3, is spliced to G2-FS2. Figures 6.68 and 6.69 show the progressions of the girder G2 warping and top flange lateral bending stresses during the installation of its splice based on the *field sequence*.

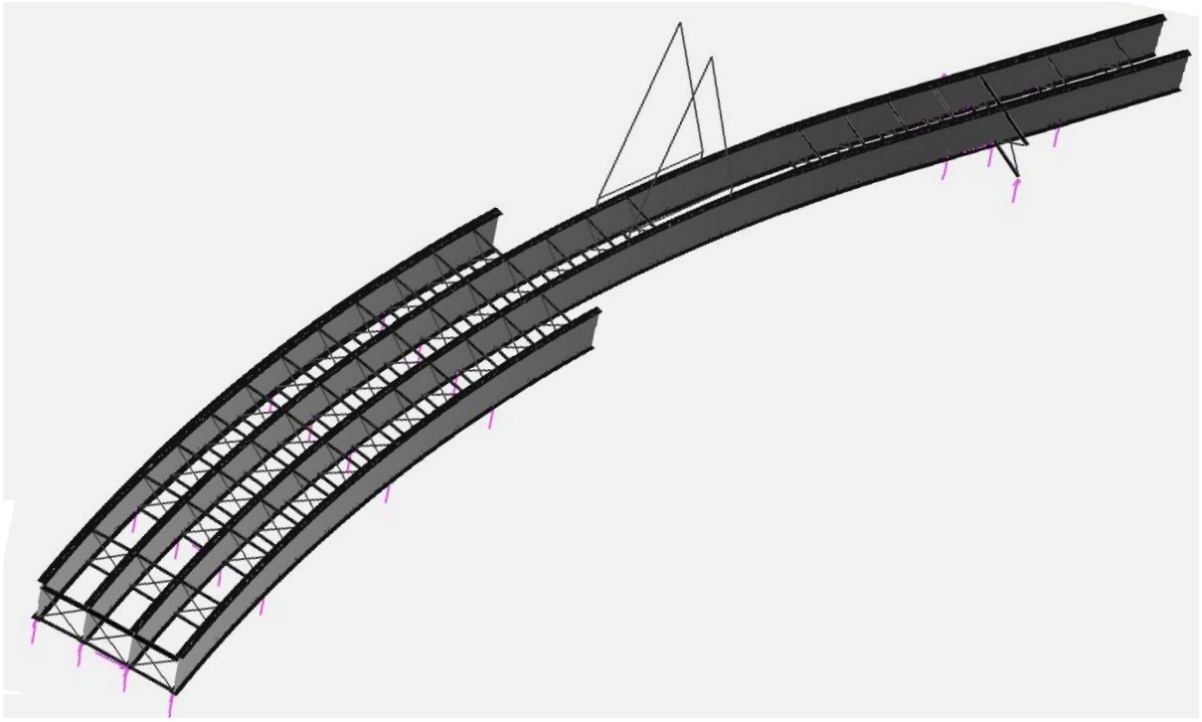

Figure 6.67 The erected structure when the girders G2-FS2 and G2-FS3 are spliced in the stage 4.

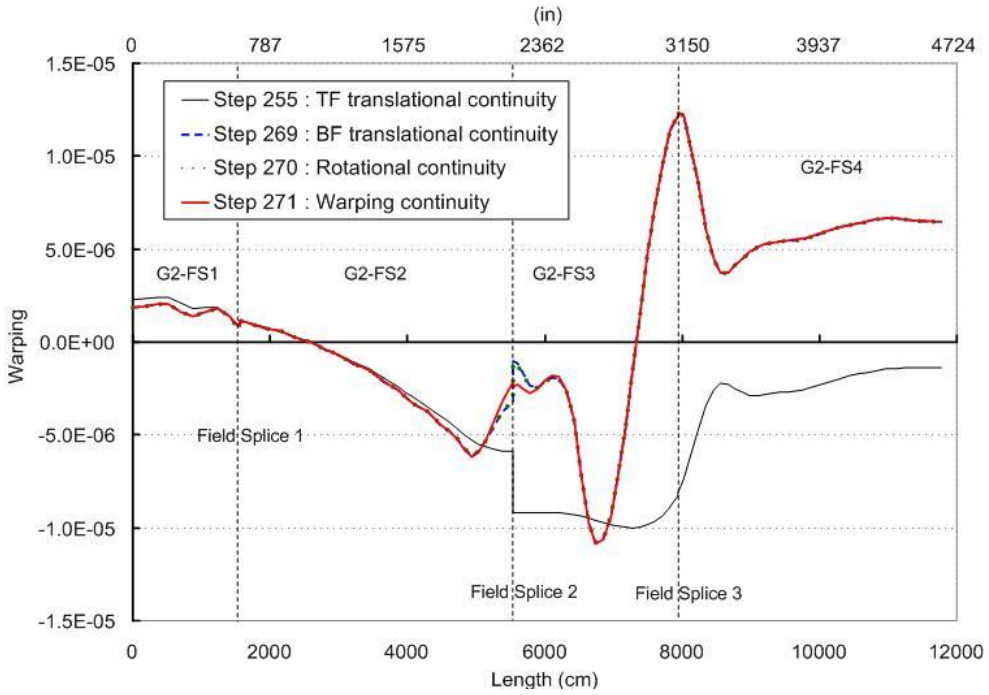

Figure 6.68 The progression of the girder G2 warping displacements along the curved span during the field splice 2 based on the *field sequence*

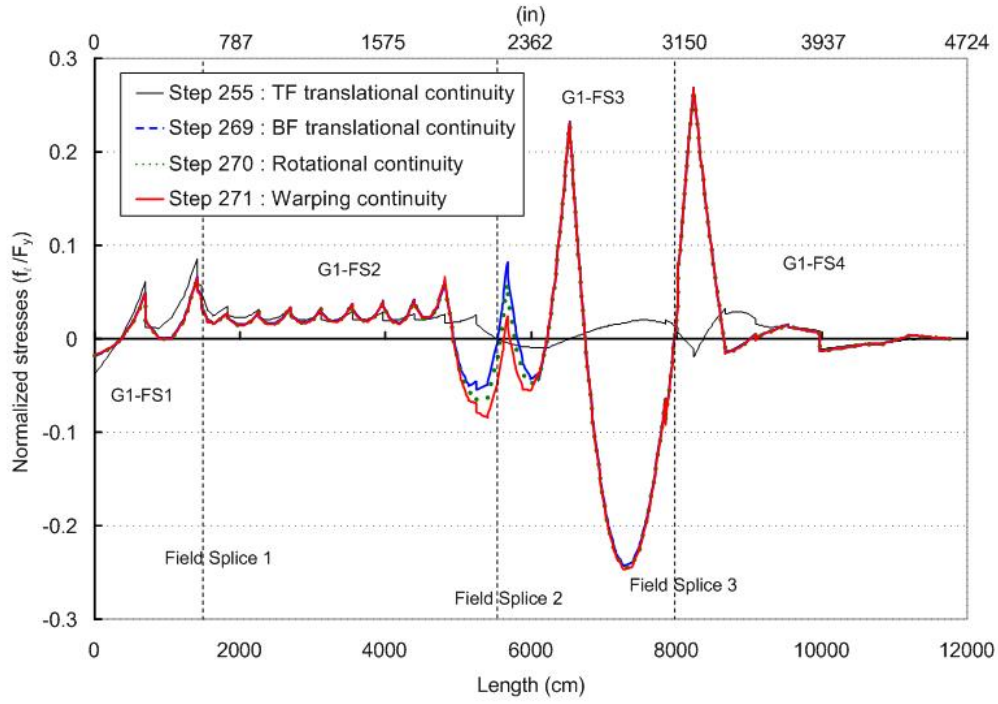

Figure 6.69 The progression of the girder G2 top flange lateral bending stresses along the curved span during the field splice 2 based on the *field sequence*

Once the two drop-in girders G3-FS3 and G2-FS3 are installed, field sections one through four of each of the girders G2 and G3 are completely connected. After all the cross-frames between girders G2-FS3 and G3-FS3 are installed, both girders are lifted off of pier I and all the falseworks. In other words, only abutment 1 and the pier bracket 1 (BK1) have non-zero reactions under girders G2 and G3. The reactions are 1,683.64 kN (378.82 kips) at G2-BK1 and 518.83 kN (116.74 kips) at G3-BK1 (not shown). The lifting cranes still hold G3-FS3 and G2-FS3 until the pier brackets are removed. In order to remove the pier brackets, G3-FS3 is raised to reduce the reaction at G3-BK1. After removing G3-BK1 and BK2, the lifting crane lowers the G3-FS3 to reduce the force in the crane cables so that the lifting crane can be removed without any solution difficulty. The same process is used to remove the pier brackets G2-BK1 and BK2 and the G2-FS3 lifting crane. During the process of the lifting crane removal, the maximum girder stress reaches 124.70 MPa (18.09 ksi) at the girder G3-FS2 near field splice 2 as shown in Figure 6.52 step 285. The maximum cross-frame stress also reaches 124.98 MPa (18.26 ksi) at CF-16B bottom chord as shown in Figure 6.53 at this step. The support reactions at the end of this stage are shown in Table 6.11. The required forces for the cross-frame installation during this stage are shown in Table A3.15.

6.5.3.5 Steel Erection Stage 5

Sixty-five steps (steps 290 to 354) are used for the simulation of the steel erection stage 5. Girders G4-FS4 and G1-FS4 are placed on pier 1 and connected to the erected girders G3-FS4 and G2-FS4 respectively during this stage.

The required cross-frame connection forces in this stage are shown in Table A3.16 and A3.17. The girder and cross-frame member stresses are relatively small in this stage. As shown in Figures 6.52 and 6.53, the maximum girder and cross-frame member stresses are essentially unchanged during this stage. The erected structure at end of this stage is shown in Figure 6.70.

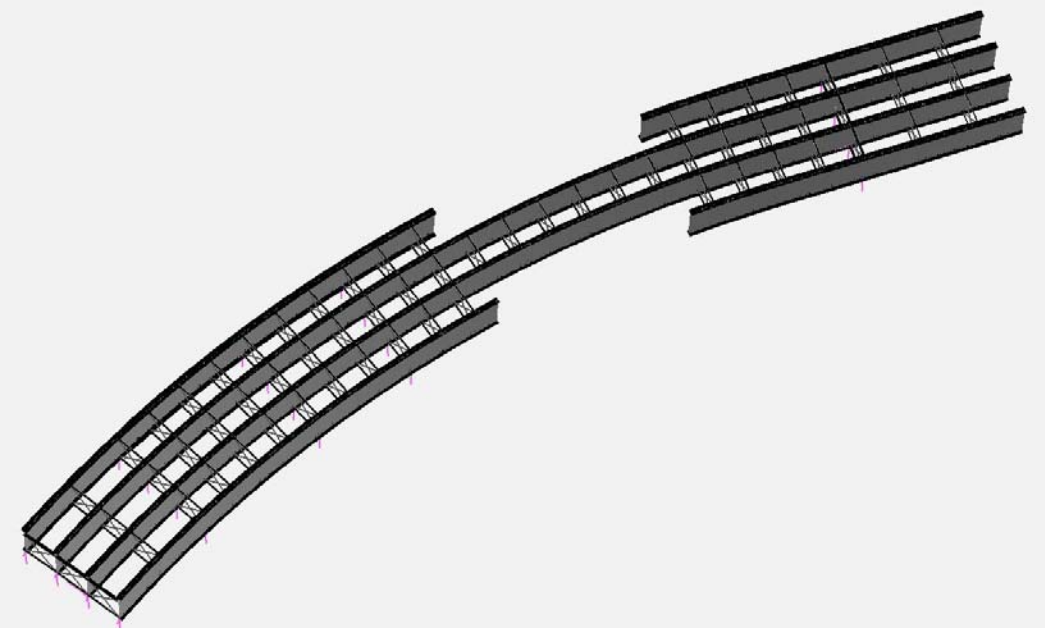

Figure 6.70 The erected structure at end of the stage 5 in the FEA model

6.5.3.6 Steel Erection Stage 6

Seventy-two steps (steps 355 to 426) are employed for the simulation of the steel erection stage 6. Two drop-in girders, G4-FS3 and G1-FS3, as well as cross-frames between these girders and G1-FS3 and G2-FS3 are installed to finish the steel erection simulation of the Ford City Bridge curved span in this stage. In the finite element model, there is no difficulty in inserting the girder G4-FS3 and installing the cross-frames between this girder and G3-FS3. The required forces for the girder splice 2 are shown in Table A3.18. The maximum girder stress is increased from 86.04 MPa (12.48 ksi) to 198.24 MPa (28.75 ksi) during the splice of G4-FS3 and G4-FS2 at step 364. This magnitude is the largest girder stress during the entire steel erection simulation as shown in Figure 6.52 and explained in Table 6.10. The maximum cross-frame member stress is increased from 33.26 MPa (4.82 ksi) to 87.62 MPa (12.71 ksi) during the field splice 2 of the girders G4-FS2 and G4-FS3 as shown in Figure 6.53 (at step 364). The required forces for the cross-frame installations between girders G4-FS3 and G3-FS3 are listed in Table A3.19. The installation of the cross-frame 17C, which is near the field splice 2,

requires the largest force of 237.91 kN (53.53 kips) in this stage. The corresponding erected structure is shown in Figure 6.71.

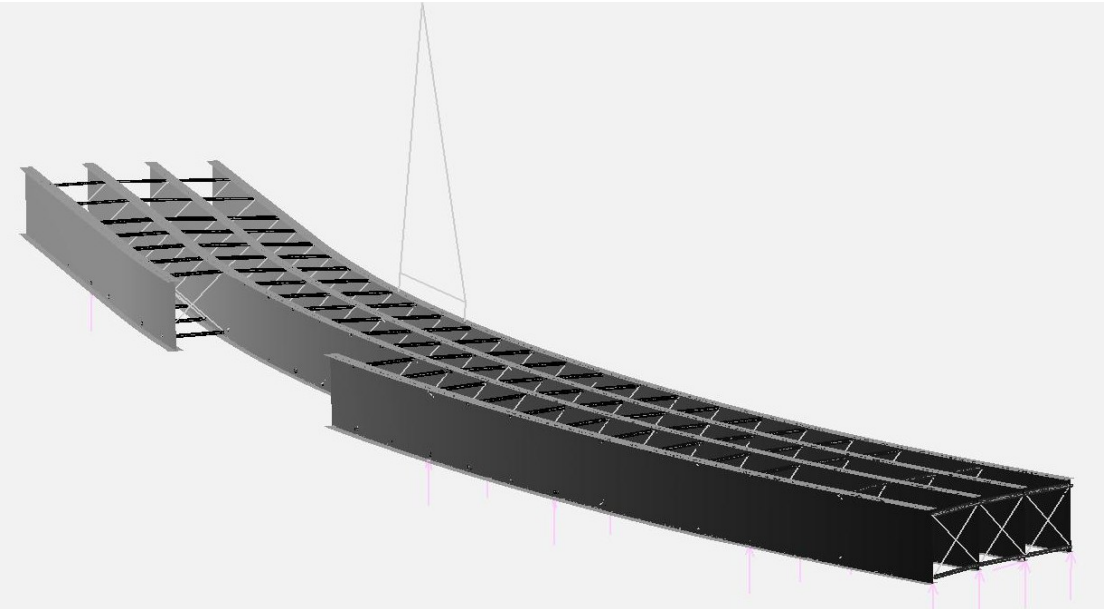

Figure 6.71 The erected structure before inserting the girder G1-FS3 in the FEA model

As mentioned in Table 6.9, there are difficulties at stage 6F in splicing the girders G1-FS3 and G1-FS2 at field splice 2 based on the *planned sequence*. In the finite element model, this field splice can not be achieved based on the *planned sequence* either. After the girders G1-FS3 and G1-FS2 are pinned together at their top flanges, the cross-frames 17A, 18A and 19A need to be installed before making the connection of the G1-FS3 and G1-FS2 bottom flanges. Similar to the girder G2 field splice 2, the required force for the girder bottom flange translational continuity is quite large as shown in Table A3.20 step 410 (sufficiently large such that additional measures may be required during the construction to complete the splice). This is followed by achieving the section orientation compatibility and the warping continuity. The progressions of the warping displacements and top flange lateral bending stresses in girder G1 along the length are shown in Figures 6.72 to 6.75.

For the temporary supports, the falsework 1 and 2A are seldom contacted by girders within stage 6. At the end of this stage, only the falsework 2 supports at G1 and G4 still support any self-weight. Therefore, the falsework 1 and 2A can be directly removed. The abutment 1, falsework 2 and pier 1 under the girder G1 support most of the structure's self-weight at the end of the steel erection simulation as shown in Table 6.11.

The forces required during installation of the cross-frames between girders G1-FS3 and G2-FS3 are listed in Table A3.21.

The completed FEA model of the Ford City Bridge curved span is shown in Figures 6.76 and 6.77. It is informative to compare the final responses of the curved span based on the field erection sequence, which is referred to as the SAM (Sequentially Assembled Model) in Section 5.2.2.1, to the results from the IIM (Instantaneously Instantiated Model) of the curved span. The vertical deflections, warping displacements, and flange major-axis bending stresses between these two models match closely. The vertical support reactions for the two models are shown in Table 6.11. The flange major-axis and lateral bending stresses are shown in Figures 6.78 and 6.79 respectively.

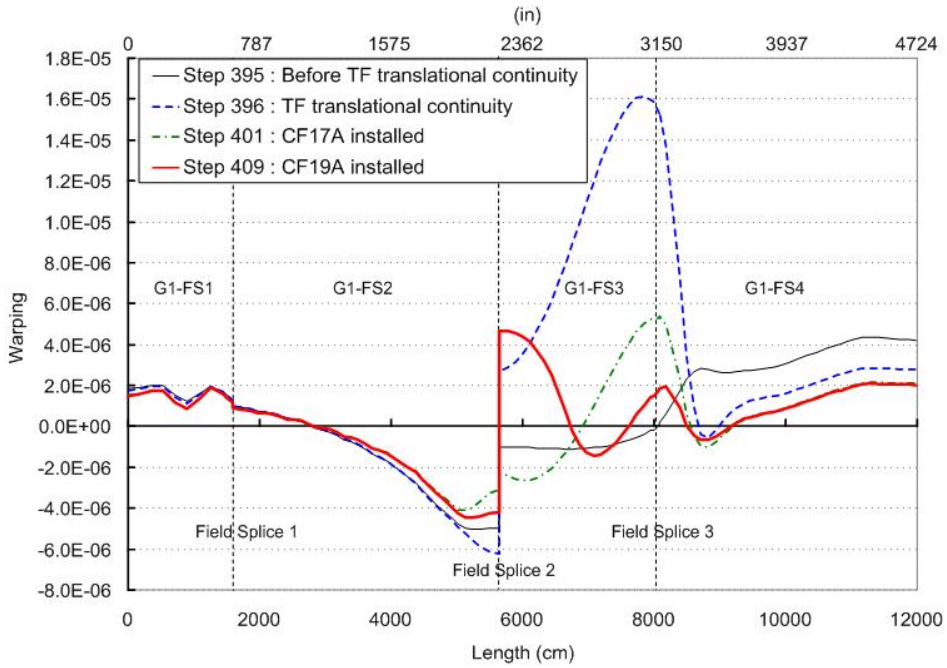

Figure 6.72 The progression of the girder G1 warping displacements along the curved span during the field splice 2 based on the *field sequence* (up to the time where CF19A is installed)

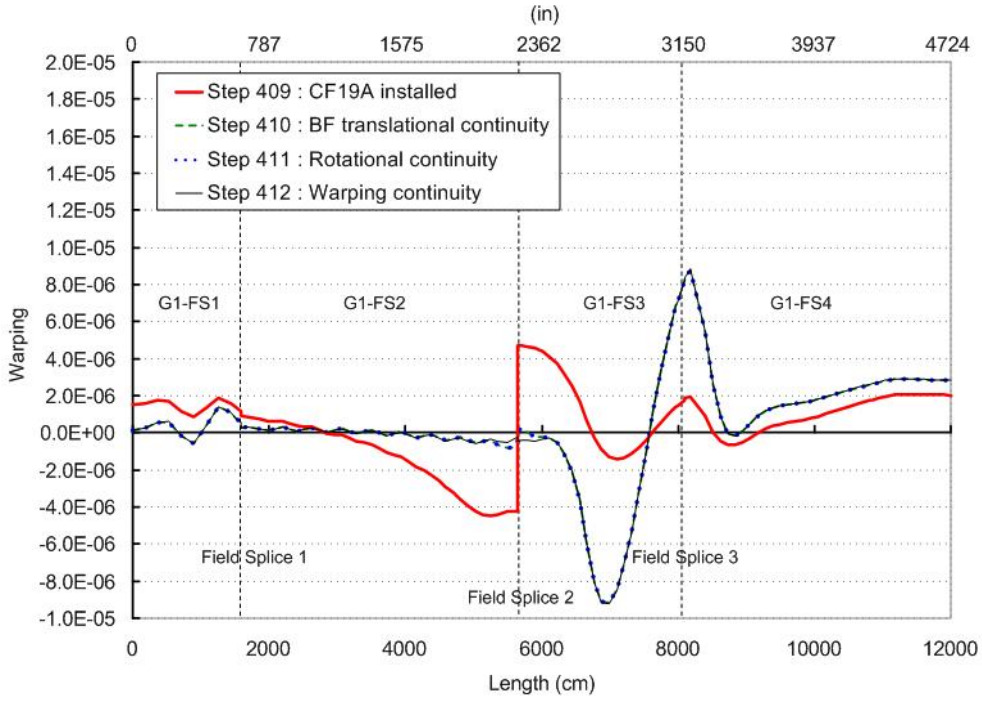

Figure 6.73 The progression of the girder G1 warping displacements along the curved span during the field splice 2 based on the *field sequence* (from the time CF19A is installed to the completion of the splice)

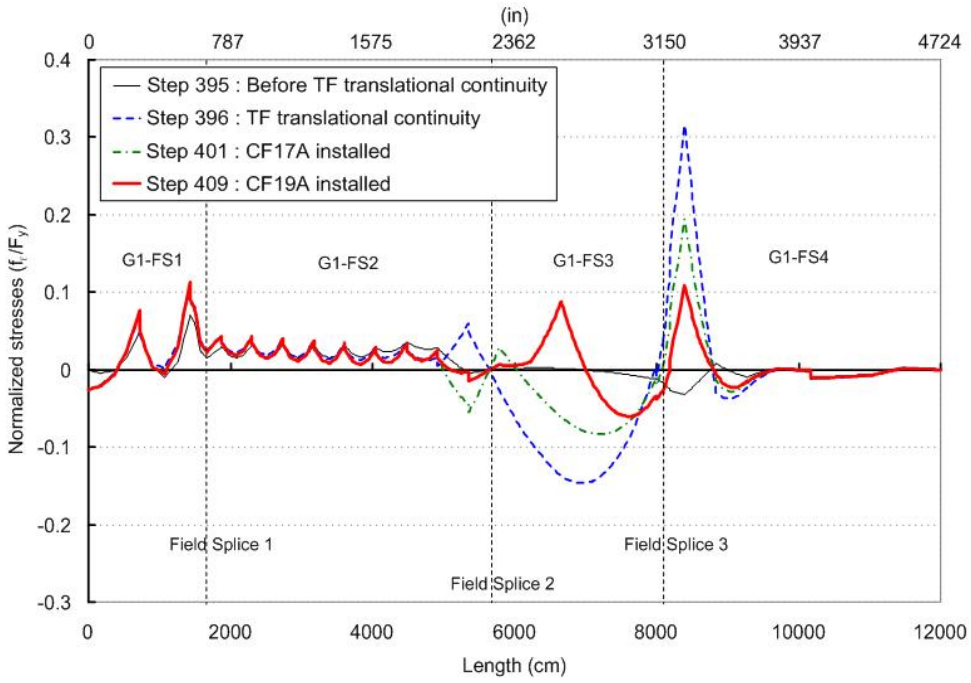

Figure 6.74 The progression of the girder G1 top flange lateral bending stresses along the curved span during the field splice 2 based on the *field sequence* (up to the time where CF19A is installed)

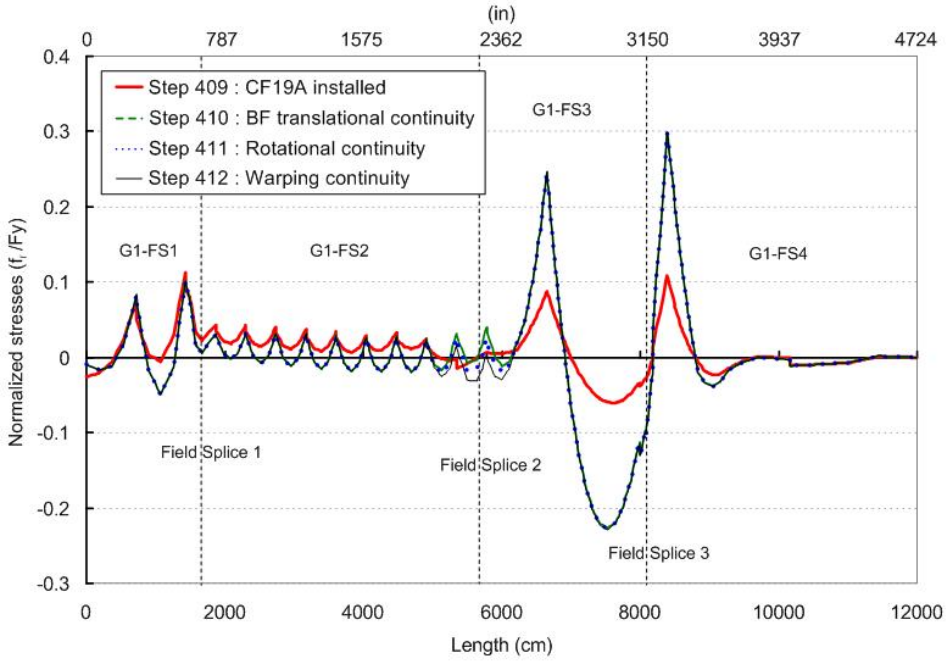

Figure 6.75 The progression of the girder G1 top flange lateral bending stresses along the curved span during the field splice 2 based on the *field sequence* (from the time CF19A is installed to the completion of the splice)

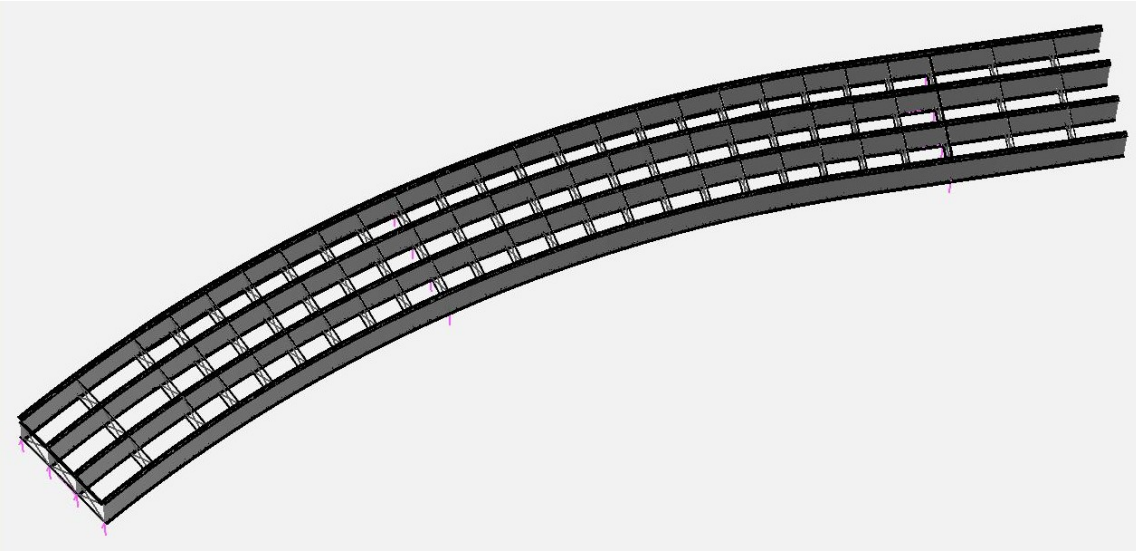

Figure 6.76 The complete structure of the Ford City Bridge curved span after the steel erection simulation is completed (view 1)

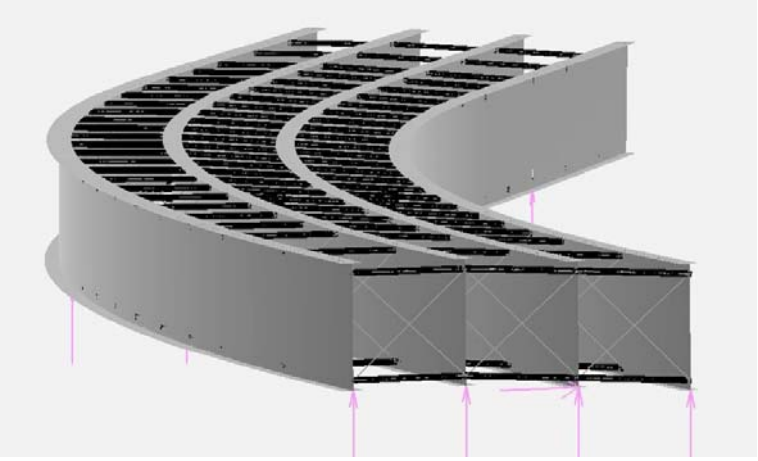

Figure 6.77 The complete structure of the Ford City Bridge curved span after the steel erection simulation is completed (view 2)

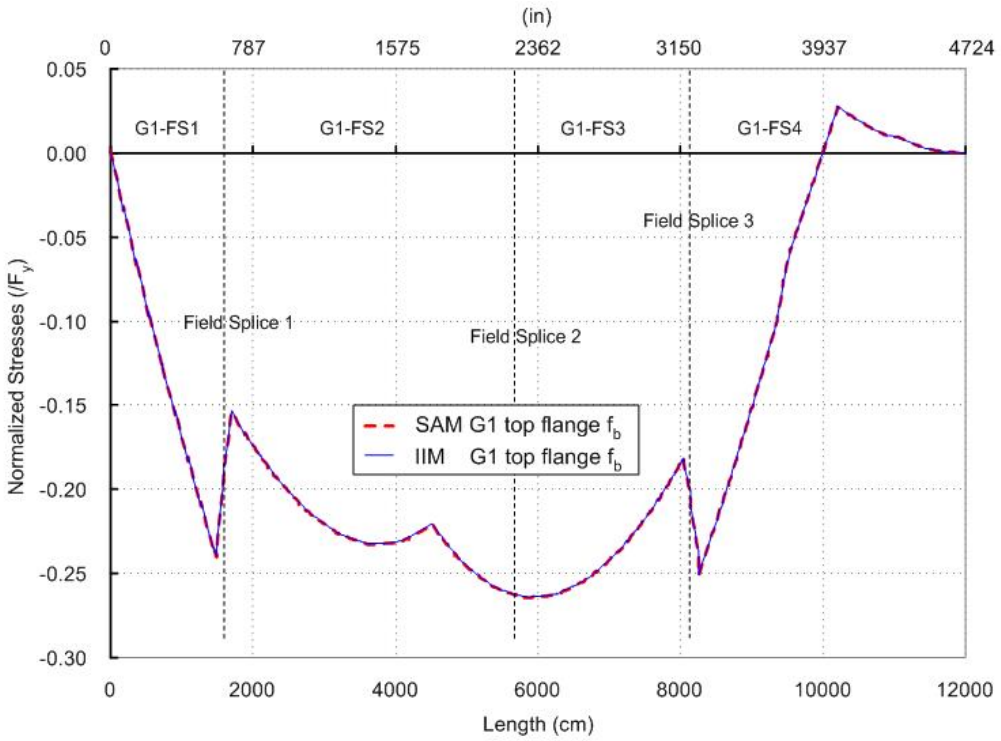

Figure 6.78 Comparison of the girder G1 top flange major-axis bending stresses between the SAM model and IIM model at the end of the final stage

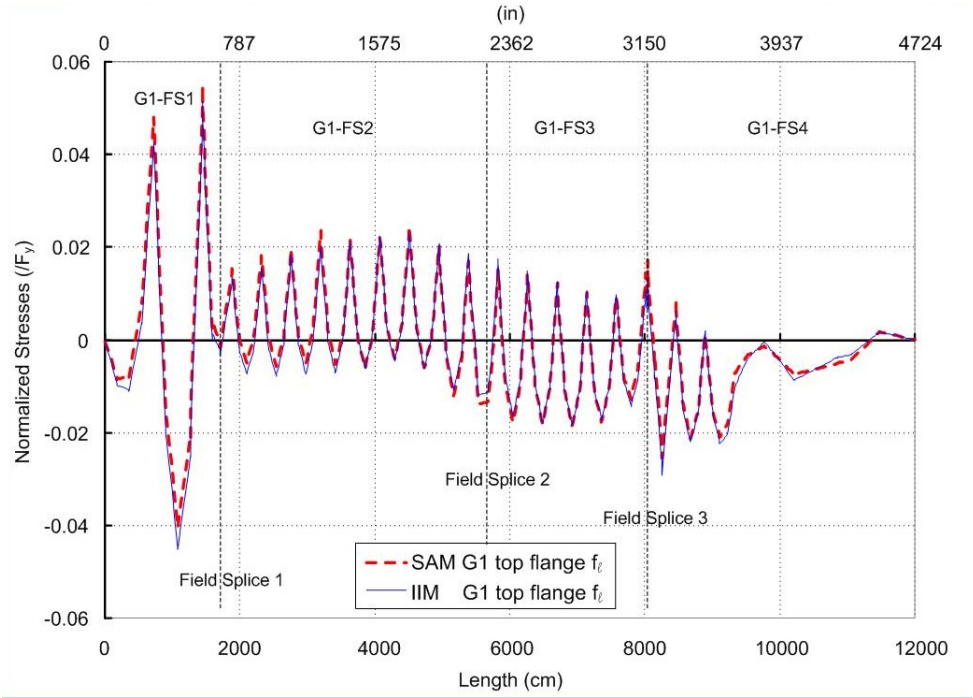

Figure 6.79 Comparison of the girder G1 top flange lateral bending stresses between the SAM model and IIM model at the end of the final stage

6.5.4 Concluding Remarks

The field splice 2 of the two outside girders G1 and G2, can not be achieved for the *planned steel erection sequence* in the GT-SABRE analysis. This prediction matches the field situation as indicated in Tables 6.6 and 6.8. The forces required to make this connection using the planned steel erection sequence are quite large. By installing the cross-frames CF-17, CF-18 and CF-19 before completing the splice, the geometric nonlinearity associated with closing the splice and the incompatibility at the splice are reduced. As a result, it can be concluded that changing the erection sequence by inserting cross-frames in advance of making the splice solves the construction difficulties.

Tables A3.8 through A3.21 show the initial gaps between the cross-frame and girder connection points and the required forces for the cross-frame connections. Interestingly, the required force for the cross-frame connections is not proportional to the size of the gap. For example, in Table A3.9, the initial gap between the cross-frame 8B bottom chord and the girder G2-FS2 workpoint is 1.18 cm (0.46 in) and the required force for the connection is 150.29 kN (33.81 kips). However, for the cross-frame 14B top chord, the initial gap is 15.14 cm (5.96 in) but the required force for the connection is only 18.8 kN (4.23 kips). As a result, the constructibility can not be judged simply based on measuring the gap between the two connection points. Also, the constructibility can not be judged simply based on measuring the lack-of-fit between girders and cross-frames in the no load condition.

As mentioned in Chapter 5, some of the structural responses such as the vertical support reactions may be sensitive to the connection tolerance. Through the steel erection study of the Ford City Bridge curved section, it is found that the girder flange lateral bending stresses and the subsequent required cross-frame installation forces are sensitive to the tolerance for the warping continuity. The selected tolerance for the warping continuity of $0.0001 / h_s$ explained in Section 6.5.2 leads to results that match to within four significant digits between the IIM and SAM solutions. It should be noted that the IIM solution imposes the compatibility exactly since

the model is assembled all at once. Since the cross-frames in the Ford City Bridge are X-type, the lack-of-fit due to the SDLF detailing is h4andled directly by initial stresses in the cross-frame members. This is in contrast to the IIM-TDLF solution for the composite test bridge discussed in Section 5.2.

Based on the analysis results, the girder and cross-frame stresses are usually increased significantly during the field splicing and girder elevation adjustment for temporary support removal. These high stresses are reduced after the subsequent cross-frames are installed. Also, the cross-frame connection near the field splice locations and above the supports usually requires larger forces. From the comparisons between the model considering the erection simulation (SAM) and the model that assembles all steel components and applied gravity load (IIM), the uniqueness of the analysis results stated in Section 4.2 is verified again and the steel erection sequence of the Ford City Bridge curved section is successfully accomplished using the GT-SABRE software system.

CHAPTER 7

SUMMARY AND CONCLUSIONS

7.1 Summary

Prototype capabilities for calculation of the construction requirements, structural responses during construction, and the final dead load state (stresses, deflections, forces and reactions) in general curved steel I-girder bridges are addressed in this study. A three-dimensional beam element based on open-section thin-walled beam theory is developed for modeling of bridge I-girders. The proposed prototype capabilities for construction simulation as well as the derived beam element are implemented in the GT-SABRE software system (acronym for Georgia Tech – Structural Analysis and BRidge Evaluation) (Chang 2006). Modeling techniques are investigated and recommended to achieve accuracy of analysis results using the above beam element in a 3D grid approach.

In Chapter 2, a displacement-based beam finite element formulation based on Vlasov kinematics is derived for modeling of curved I-girders. The element is formulated using a Total Lagrangian–Corotational (TL-CR) approach. Finite 3D rotation updates are handled based on the exponential mapping. The transformation of the stiffness matrix between corotational and global systems follows Rankin and Nour-Omid's (1988) projector concept. Different from Rankin and Nour-Omid's (1988) formulation, the corotational frame is defined based on the average rotation of the two end nodes. The transverse displacements are interpolated using cubic Hermitian shape functions and the element twist and warping are interpolated using the analytical equations from the geometric linear solution for the torsion of a straight member. The horizontal curvature effects are handled by imposing initial rotations at the ends of the beam element relative

to its straight reference configuration. Cross-section monosymmetry and tapered geometry are considered. Instead of considering the variation of the total web depth, the variation of the distances between the cross-section shear center and the top and bottom flange junctures are defined along the element length. Using the Gauss-Lobatto integration points along the length, the provided method is able to account for the fact that the shear center line of a tapered singly symmetric I-section member is not straight.

In Chapter 3, composite bridge modeling considerations, which include girder web distortion, cross-frames, support and load height, and displacement compatibility between the girders and slab, are addressed. Web distortion effects are investigated and approximate approaches for capture of these effects using open-section thin-walled beam elements for the steel I-girder are recommended. A number of analysis approaches including line girder analysis, the V-load method, grid methods and general finite element methods for analysis of curved I-girder bridge structural systems are discussed. The qualities and limitations of these modeling strategies for design analysis of curved I-girder bridge structural systems are investigated.

In Chapter 4, the procedure of steel I-girder bridge construction including the steel detailing, steel erection and concrete casting sequence in current practice, and the conditions for the uniqueness of the analysis results are introduced. The four common cross-frame detailing methods – No-Load Fit (NLF), Total Dead Load Fit (TDLF), Steal Dead Load Fit (SDLF) and Twist Camber Fit (TCF) are discussed in detail. The cross-frame detailing has an important influence on construction requirements, the definition of and achievement of a targeted geometry for the completed structure, as well as the performance of curve I-girder bridges. The application of the uniqueness concept is discussed. That is, if the connections between girders and cross-frames are made ideally with zero tolerance, the structure is maintained in an elastic condition during the construction operations and no unintended restraint is introduced from the supports, the

analysis solution at final construction stage is unique and independent of the construction sequence for different detailing methods. By using this concept, if engineers are not interested in the girder responses before a certain steel erection stage, and if none of the erection processes before this stage lead to a non-uniqueness, a model of the bridge can be created containing all the components at this stage and the structure self-weight can be applied to the model all at once to determine the corresponding responses.

The finite element modeling methodologies for steel I-girder bridge construction simulation are provided in this Chapter. The girder no-load geometry, including the consideration of the girder vertical curve due to the grade and superelevation, and girder camber, is modeled precisely using a specific curve fitting method. Geometric nonlinearity needs to be considered in general during construction because of the flexibility of the I-girders in torsion and lateral bending. The steel components are assembled through the positioning and assembly. The algorithm and finite element modeling techniques for simulating the positioning and assembly are provided. Cross-frame connections are made by enforcing translational continuity between the workpoints of the cross-frame member and the girder. Girder splicing is achieved in four steps: (1) translational continuity at the girder top flange; (1) translational continuity at the girder bottom flange; (3) nodal rotational and (4) warping continuity. Girder section transitions are modeled by tapering the section dimensions within a transition length from one size to the other at girder splice and steps locations. Furthermore, for many bridges, concrete casting can not be finished in one stage due to the large volume of concrete. The concrete poured in the earlier stage may gain strength and provide stiffness.

In Chapter 5, the FHWA composite curved test bridge is utilized for validation and demonstration of the proposed finite element methodologies for bridge construction

simulation. The uniqueness concept is validated by assembling all the steel components of the test bridge with different sequences. The influence of different cross-frame detailing methods (NLF and TDLF) on the girder camber design and on the girder responses at the end of steel erection are investigated. The methodologies for positioning and assembly of steel components are validated and demonstrated. The modeling techniques for composite bridges using the open-section thin-walled beam element for the girders and beam grillage model for the slab is validated by comparing the results to the results from a refined shell finite element model and from experimental data.

In Chapter 6, a long-span curved I-girder bridge – the Ford City Bridge – is utilized for further demonstration of the proposed methodologies for bridge construction simulation. The influence of different cross-frame detailing methods (NLF and SDLF) and staged slab construction on the girder camber design and the bridge responses at the end of construction are investigated. The precise initial geometry of the girders is modeled considering the girder vertical curve including grade and superelevation, and girder camber specified in the engineering drawings. The analysis begins with the instantaneously instantiated bare girder model under steel self-weight. Then the concrete load and deck elements are added stage-by-stage to the deformed geometry of the bridge model. The concrete is assumed to be fully effective at the beginning of the next casting stage. The curved span of the Ford City Bridge is utilized for the steel erection simulation. The cross-frames are detailed based on the SDLF method and the girder camber is designed considering the staged slab construction and the effects of lack-of-fit between the girders and cross-frames. All the steel components of the Ford City Bridge curved span are created but are disassembled and placed on the ground before the erection simulation.

7.2 Conclusions

The accomplishments of this research are as follows:

- The derived beam element is shown to accurately account for the effects of horizontal curvature, cross-section monosymmetry, tapered section geometry and geometric nonlinearity.
- Suggested approximate approaches for capture of composite I-girder web-distortion effects using 3D grid methods are investigated and proposed: (1) when using an open-section thin-walled beam element for the bridge I girder and either shell elements or a beam-grid system for the slab, a rotational release is needed between the slab and the top flange of the I-girders in order to compensate the web distortion effects; (2) when using an open-section thin-walled beam element for the combined slab and steel I-girder via an equivalent composite I-girder cross-section model, the contribution from the slab to the St. Venant torsional constant J is suggested to be neglected for the same reason. Lack of the consideration of the web distortion effects results in a significant underestimation of the girder bottom flange lateral bending stresses.
- Based on the uniqueness concept, if engineers are not interested in the girder responses before a certain steel erection stage, and if none of the erection processes before this stage lead to a non-uniqueness, they can simply define all the steel components together in the analysis model and “turn on” the gravity load.
- The influence of the different cross-frame detailing methods is clarified. For NLF detailing, there is no control on the web-plumbness and girder radial deflections. TDLF and SDLF detailing results in lack-of-fit between girders and cross-frames, and induces locked-in stresses in steel components. The

required forces for the cross-frame installation are larger in the case with TDLF or SDLF detailing than in the case that the cross-frame are detailed with NLF. However, the resulting locked-in stresses reduce the girder web out-of-plumbness and radial deflections as well as the vertical deflections under the total dead load. As a consequence, the detailing method has an important impact on the required girder cambers, the construction procedures for simulation of staged slab construction requirements, and the final constructed geometry.

- The influence of staged slab casting on the final bridge responses is investigated for a representative long span curved I-girder bridge. With the consideration of the staged slab construction, the girder final vertical and lateral displacements and girder web out-of-plumbness is reduced. As a result, the required girder cambers can be reduced.
- The girder and cross-frame stresses are usually increased significantly during the process of field splicing and the temporary support removal. The steel stresses of steel components can reach up to 0.58 F_y. These high stresses are reduced gradually after the cross-frames are installed.
- The constructability of curved steel I-girder bridges can be affected by the sequence of steel erection. It can not be judged simply based on measuring the gap between the two connection points. Also, it can not be judged simply based on measuring the lack-of-fit between girders and cross-frames in the no load condition. As an example, the reported solutions for the Ford City Bridge show that the forces required for cross-frame installation are not proportional to the magnitude of the lack-of-fit. The construction force requirements are related to many variables including the

weight of the structure and the structure's broad stiffness characteristics for a given current configuration.

- The proposed prototype capabilities for construction simulation and the derived beam element for modeling of curved I-girders are successfully implemented in the GT-SABRE software system. This prototype software system is able to simulate the complete construction processes (steel erection and staged slab construction sequence) to predict construction requirements (i.e., required temporary supports, crane capacities and tie-down, jacking or come-along forces as well as the steel detailing methods), and intermediate and final states (displacements, stresses, forces and reactions). The accuracy and applicability of these capabilities are validated and demonstrated.

7.3 Future Work

Based on the current study, the following future work is suggested:

- The proposed beam finite element is based on the Vlasov kinematics. That is, the shear deformations due to beam shear and due to nonuniform or warping torsion are neglected. In some cases, the beam shear deformations can be important in thin-web I-girders. The transverse displacements are interpolated using the cubic Hermitian functions. If the concrete deck is modeled with four-node shell elements, the girder element with the same linear interpolation functions matches the displacement field of the four-node shell element. In this regard, a beam element based on the Reissner's kinematics, which includes beam shear deformation and general

warping deformations, would be valuable for the bridge modeling and analysis.

- Currently the concrete deck is modeled with a beam-grillage system. For a longer, multiple-span bridge such as the Ford City Bridge, the concrete deck is not cast at once. The beam grillage model may not be able to capture the creep and shrinkage accurately. In this regard, the shell finite element with the capabilities of modeling the concrete time-dependent creep and shrinkage will be a great addition.
- In this study, the girder lifting points are selected without calculation. However, it is found that the spring constants of the fictitious springs on the lifting crane are associated with the selection of the lifting points. Currently the spring constants are determined based on a trial-and-error method. It will be beneficial to the Engineers if an algorithm can be developed to determine the appropriate spring constants for these fictitious springs.
- The steel erection simulation for the curved span of the Ford City Bridge includes more than 400 steps in the finite element modeling. The total number of lines of the input file is more than 10,000. It is easily to have mistakes during the model creation. In addition, for some situations, one may need to change the construction sequence or make fine adjustments for the intermediate step(s) if the program encounters a convergence problem or the analysis results are suspect. Therefore, enhancements to the graphical user interface (GUI) are beneficial to make the scripting of the various erection scenarios easier to perform and modify. In addition to the large size of the input file, the amount of the output data is even larger. Use of a more sophisticated database management system is needed to speed up the access to the output data.

APPENDIX I

PROJECTION OPERATOR AND EXTERNAL GEOMETRIC STIFFNESS MATRIX

In Section 2.4, the transformation matrix $\mathbf{G}$ is used to transform the structural responses from the global coordinates to the element local coordinate system. The projection operator (or projector) $\mathbf{P}$ maps the absolute element displacement and rotation increments to the corresponding "deformational" increments, expressed in element corotational (CR) coordinates. In this appendix, a detailed derivation of the projector and the element external stiffness matrix associated with the variation of the projector and transformation matrix is provided.

A1.1 Fundamental Kinematic Relationships

Since the warping degree of freedom does not need to be operated on during the local-to-global transformation, it is omitted to simplify the presentation in the following derivation. It is simply appended into the final matrix equations. In other words, the total global degrees of freedom of an element are reduced to 12, and the total degrees of freedom in the corotational frame (CR frame, or natural frame) are reduced to 7 in the following developments. Therefore, Figure 2.2 simplifies to Figure A1.1.

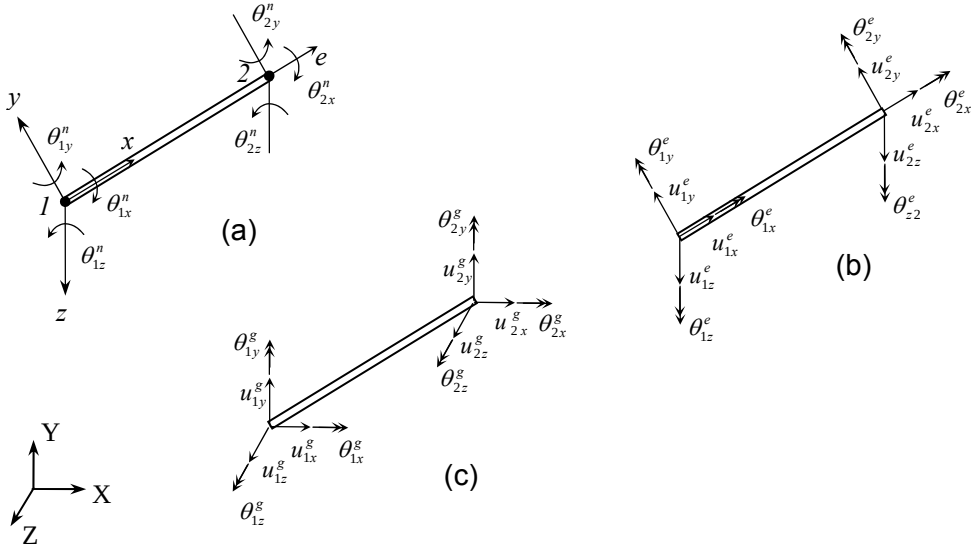

Figure A1.1 The element degrees of freedom in (a) the CR frame, (b) the element frame, and (c) the global frame

Also, Eqs. (2.6) simplify to

$$\begin{aligned}\mathbf{q}_n{}^T &= \left\{ 0 \quad 0 \quad 0 \quad \theta_{1x}^n \quad \theta_{1y}^n \quad \theta_{1z}^n \quad e \quad 0 \quad 0 \quad \theta_{2x}^n \quad \theta_{2y}^n \quad \theta_{2z}^n \right\} \\ &= \left\{ \mathbf{u}_1^n \quad \boldsymbol{\theta}_1^n \quad \mathbf{u}_2^n \quad \boldsymbol{\theta}_2^n \right\}\end{aligned} \tag{A1.1}$$

$$\begin{aligned}\mathbf{q}_e{}^T &= \left\{ u_{1x}^e \quad u_{1y}^e \quad u_{1z}^e \quad \theta_{1x}^e \quad \theta_{1y}^e \quad \theta_{1z}^e \quad u_{2x}^e \quad u_{2y}^e \quad u_{2z}^e \quad \theta_{2x}^e \quad \theta_{2y}^e \quad \theta_{2z}^e \right\} \\ &= \left\{ \mathbf{u}_1^e \quad \boldsymbol{\theta}_1^e \quad \mathbf{u}_2^e \quad \boldsymbol{\theta}_2^e \right\}\end{aligned} \tag{A1.2}$$

$$\begin{aligned}\mathbf{q}_g{}^T &= \left\{ u_{1x}^g \quad u_{1y}^g \quad u_{1z}^g \quad \theta_{1x}^g \quad \theta_{1y}^g \quad \theta_{1z}^g \quad u_{2x}^g \quad u_{2y}^g \quad u_{2z}^g \quad \theta_{2x}^g \quad \theta_{2y}^g \quad \theta_{2z}^g \right\} \\ &= \left\{ \mathbf{u}_1^g \quad \boldsymbol{\theta}_1^g \quad \mathbf{u}_2^g \quad \boldsymbol{\theta}_2^g \right\}\end{aligned} \tag{A1.3}$$

The subscripts 'x', 'y' and 'z' represent the displacements in the $\mathbf{e}_1$, $\mathbf{e}_2$ and $\mathbf{e}_3$ directions (defined in Section 2.3). For a two-node 3D frame element, $\mathbf{q}_g$ contains all the absolute element nodal displacements and rotations in global coordinates (Figure A1.1(c)), $\mathbf{q}_e$ contains all the absolute element nodal displacements and rotations in

element local coordinates (Figure A1.1(b)), and $\mathbf{q}_n$ contains the corresponding element deformational displacements and rotations in element CR coordinates (Figure A1.1(a)).

The relationship between the nodal positions in the global coordinate system and the displacements in the CR frame can be expressed as

$$\mathbf{u}_a^n = \mathbf{E}^T(\mathbf{X}_a^g + \mathbf{u}_a^g - \mathbf{X}_o^g - \mathbf{u}_o^g) = \mathbf{E}^T(\mathbf{x}_a^g - \mathbf{x}_o^g) \tag{A1.4}$$

in which

$\mathbf{u}_a^n$ Translation (or "deformational" translation) of node a relative to the origin of the CR frame, expressed in element CR coordinates at node a (a = 1, 2)

$\mathbf{E}$ Orthonormal basis of the element CR frame in the current state, expressed in global coordinates, [$\mathbf{e}_1$ $\mathbf{e}_2$ $\mathbf{e}_3$]. The basis vector $\mathbf{e}_1$ is defined as a unit vector directed from node 1 to node 2 (see Figure 2.3). Also, the basis vectors $\mathbf{e}_2$ and $\mathbf{e}_3$ are established at the beginning of the analysis based on the initial cross-section orientation, and they are updated based on an approximate average twist rotation of the two element ends. All the rigid body translations and rotations of points in the element relative to the CR frame, defined in this way, tend to be small (at least in the limit that a large number of elements are utilized in the finite element discretization, if the actual deformations are large), while still maintaining simplicity. Specific definitions of these basis vectors are provided subsequently. The origin of the element CR frame is located at node 1.

$\mathbf{X}_a^g$ Position of node a in the initial configuration, expressed in global coordinates

$\mathbf{u}_a^g$ Current displacement of node a, expressed in global coordinates

$\mathbf{x}_a^g$ Current position of node a, equal to $\mathbf{X}_a^g + \mathbf{u}_a^g$, expressed in global coordinates

$\mathbf{X}_o^g$ Position of the CR frame origin in the initial configuration, equal to $\mathbf{X}_1^g$ for the element developed in this work, expressed in global coordinates

$\mathbf{u}_o^g$ Current displacement of the CR frame origin, equal to $\mathbf{u}_1^g$ in this development, expressed in global coordinates

$\mathbf{x}_{\mathrm{o}}^{\mathrm{g}}$ Current position of the CR frame origin, equal to $\mathbf{x}_1^g$ in this development, expressed in global coordinates

The orthogonal transformation (rotation matrix) between the global coordinates and the element CR coordinate frame can be expressed as

$$\mathbf{T}_a^n = \mathbf{E}^T\left[(\mathbf{S}_a\mathbf{E}_o)\mathbf{E}^T\right]\mathbf{E} = \mathbf{E}^T\mathbf{S}_a\mathbf{E}_o \tag{A1.5}$$

in which

$\mathbf{T}_a^n$ Orthogonal transformation matrix associated with the orientation of the triad at node a relative to the current element CR frame $\mathbf{E}$, expressed in element CR coordinates

$\mathbf{S}_a$ Orthogonal transformation matrix associated with the total rotation at node a from the initial to the current configuration, expressed in global coordinates ($\mathbf{S}_a = \mathbf{I}$ in the initial configuration)

$\mathbf{E}_{\mathrm{o}}$ Orthonormal basis of the element CR frame in the initial configuration, expressed in global coordinates

$\mathbf{S}_a\mathbf{E}_o$ Orthogonal transformation that gives the current orientation of the triad at node a, expressed in global coordinates

$(\mathbf{S}_a\mathbf{E}_o)\ \mathbf{E}$ Orthogonal transformation that represents the rotation from the element CR frame $\mathbf{E}$ to the current triad at node a ($\mathbf{S}_a\mathbf{E}_o$), expressed in global coordinates

The variations of Eqs.(A1.4) and (A1.5) are:

$$\delta\mathbf{u}_a^n = \delta\mathbf{E}^T(\mathbf{x}_a^g - \mathbf{x}_o^g) + \mathbf{E}^T(\delta\mathbf{u}_a^g - \delta\mathbf{u}_o^g) \tag{A1.6}$$

$$\delta\mathbf{T}_a^n = \delta\mathbf{E}^T\mathbf{S}_a\mathbf{E}_o + \mathbf{E}^T\delta\mathbf{S}_a\mathbf{E}_o \tag{A1.7}$$

It should be noted that $\mathbf{X}^g$ are constant initial positions and that all the variations in Eqs. (A1.6) and (A1.7) are solely functions of the global displacements. Both Eqs.(A1.6) and (A1.7) require the variation of an orthogonal matrix.

As introduced in Section 2.2, the rotation from the vector $\mathbf{r}_o$ to $\mathbf{r}_n$ due to the finite rotation increment $\Delta\boldsymbol{\omega}$ (about the axis directed along the unit vector $\mathbf{e}$ in Figure 2.1(a)) involves an orthogonal transformation (exponential mapping) and can be expressed as

$$\mathbf{r}_n = \mathbf{R}\cdot\mathbf{r}_o \tag{2.1}$$

where

$$\mathbf{R} = \mathbf{R}(\Delta\boldsymbol{\omega}) = \exp(\boldsymbol{\Theta}(\Delta\boldsymbol{\omega})) \tag{2.3}$$

and

$$\boldsymbol{\Theta}(\Delta\boldsymbol{\omega}) = Spin(\Delta\boldsymbol{\omega}) = \Delta\boldsymbol{\omega}\otimes = \begin{bmatrix} 0 & -\Delta\omega_3 & \Delta\omega_2 \\ \Delta\omega_3 & 0 & -\Delta\omega_1 \\ -\Delta\omega_2 & \Delta\omega_1 & 0 \end{bmatrix} \tag{2.4}$$

This equation is based on the correspondence between the cross-product operation and the product with a skew-symmetric tensor, specifically

$$Spin(\boldsymbol{\omega})\,\mathbf{r} = \boldsymbol{\omega}\times\mathbf{r} = -\mathbf{r}\times\boldsymbol{\omega} = -Spin(\mathbf{r})\,\boldsymbol{\omega} \tag{A1.8}$$

for any pair of vectors $\mathbf{r}$ and $\boldsymbol{\omega}$.

Consider the effect of two successive rotations, $\boldsymbol{\theta}_{0-1}$ followed by $\boldsymbol{\theta}_{1-2}$. The first rotation maps a vector $\mathbf{r}_0$ to

$$\mathbf{r}_1 = exp(Spin(\boldsymbol{\theta}_{0-1}))\,\mathbf{r}_0 = \mathbf{R}(\boldsymbol{\theta}_{0-1})\,\mathbf{r}_0 = \mathbf{R}_{0-1}\,\mathbf{r}_0 \tag{A1.9}$$

and the second rotation produces

$$\mathbf{r}_2 = \mathbf{R}(\boldsymbol{\theta}_{1-2})\,\mathbf{r}_1 = \mathbf{R}_{1-2}\,(\mathbf{R}_{0-1}\,\mathbf{r}_0) = \mathbf{R}_{0-2}\,\mathbf{r}_0 \tag{A1.10}$$

where

$$\mathbf{R}_{0-2} = exp(\boldsymbol{\Theta}_{1-2})\,\mathbf{R}_{0-1} \tag{A1.11}$$

More generally, if the effect of all prior rotations is represented by $\mathbf{R}$ (and by a corresponding rotation vector $\boldsymbol{\theta}_R$), and if a rotation from the current configuration is represented by the axial vector $\varepsilon\,\delta\boldsymbol{\omega}_R$, with the corresponding skew-symmetric matrix $\varepsilon\,\delta\boldsymbol{\Omega}_R$, we can write the new rotational transformation matrix resulting from these rotations as

$$\mathbf{R}_\varepsilon = exp(\varepsilon\,\delta\boldsymbol{\Omega}_R)\,\mathbf{R} \tag{A1.12}$$

That is, $\mathbf{R}_\varepsilon$ is the rotation matrix resulting from a rotation $\varepsilon\,\delta\boldsymbol{\omega}_R$ being applied to a configuration that has already been rotated by $\boldsymbol{\theta}_R = \theta_R\mathbf{e}$, with the effect of $\boldsymbol{\theta}_R$ being represented by $\mathbf{R}$. The quantity $\varepsilon\,\delta\boldsymbol{\omega}_R$ is an incremental rotation superposed on the existing rotation $\boldsymbol{\theta}_R$.

Consider the change in $\mathbf{R}$ caused by the rotation $\varepsilon\,\delta\boldsymbol{\omega}_R$ in the limit that ε approaches zero, i.e., the variation in $\mathbf{R}$:

$$\delta\mathbf{R} = \frac{d}{d\varepsilon}\mathbf{R}_{\varepsilon}\,|_{\varepsilon=0} = \frac{d}{d\varepsilon}\left[exp(\varepsilon\,\delta\boldsymbol{\Omega}_R)\,\mathbf{R}\right]\Big|_{\varepsilon=0}$$

$$= \frac{d}{d\varepsilon}\left[\mathbf{I} + \varepsilon\,\delta\boldsymbol{\Omega}_R + \frac{1}{2!}\varepsilon^2\,\delta\boldsymbol{\Omega}_R\,\delta\boldsymbol{\Omega}_R + ...\right]\mathbf{R}\,\Big|_{\varepsilon=0}$$

$$= \left[\delta\boldsymbol{\Omega}_R + 2\varepsilon\,\delta\boldsymbol{\Omega}_R\,\delta\boldsymbol{\Omega}_R + ...\right]\mathbf{R}\,|_{\varepsilon=0} = \delta\boldsymbol{\Omega}_R\mathbf{R}$$

$$= Spin(\delta\boldsymbol{\omega}_R)\,\mathbf{R} \tag{A1.13}$$

By post-multiplying both sides of this equation by $\mathbf{R}^{\mathrm{T}}$, we obtain

$$\delta\boldsymbol{\Omega}_{\mathrm{R}} = Spin(\delta\boldsymbol{\omega}_{\mathrm{R}}) = \delta\mathbf{R}\,\mathbf{R}^{\mathrm{T}} \tag{A1.14}$$

in which $\delta\boldsymbol{\omega}_{\mathrm{R}}$ is an infinitesimal rotation superposed on the existing finite rotation $\boldsymbol{\theta}_{\mathrm{R}}$ represented by $\mathbf{R}$. Since $\delta\boldsymbol{\omega}_{\mathrm{R}}$ is applied to the *current configuration*, it is by definition a *spatial object*. The quantity $\delta\boldsymbol{\omega}_{\mathrm{R}}$ is referred to as the non-additive incremental rotation vector (Alemdar 2001). It is important to note that $\mathbf{R}_{\mathrm{n}} \neq exp(Spin(\boldsymbol{\theta}_{\mathrm{R}} + \delta\boldsymbol{\omega}_{\mathrm{R}}))$. The variation $\delta\boldsymbol{\omega}_{\mathrm{R}}$ is converted to the additive incremental rotation vector $\delta\boldsymbol{\theta}_R$ with the use of Eq.(2.4) such that $\mathbf{R}_n = exp(Spin(\boldsymbol{\theta}_R + \delta\boldsymbol{\theta}_R))$ is correct.

With the aid of Eq. (A1.13), Eq. (A1.6) can be rewritten as

$$\delta\mathbf{u}_a^n = \mathbf{E}^T\left[-Spin(\delta\boldsymbol{\omega}_E^g)\,(\mathbf{x}_a^g - \mathbf{x}_o^g) + (\delta\mathbf{u}_a^g - \delta\mathbf{u}_o^g)\right] \tag{A1.15}$$

in which the property of a skew-symmetric matrix $\boldsymbol{\Omega}^T\,(= -\boldsymbol{\Omega} = -Spin(\delta\boldsymbol{\omega}_E^g))$ is utilized to obtain the final form of this expression, and $\delta\boldsymbol{\omega}_{\mathrm{E}}^{\mathrm{g}}$ is the incremental spatial rotation of the element CR frame relative to its current orientation. It should be noted that the quantity within the square brackets of Eq. (A1.15) is simply the deformational part of the nodal displacement increments in global coordinates. Similarly, Eq. (A1.7) can be written as

$$\delta\boldsymbol{\Gamma}_a^n = \mathbf{E}^T\left[-Spin(\delta\boldsymbol{\omega}_E^g) + Spin(\delta\boldsymbol{\omega}_a^g)\right]\mathbf{S}_a\mathbf{E}_o \tag{A1.16}$$

in which $\delta\boldsymbol{\omega}_a^g$ is the incremental spin of the nodal triad $\mathbf{S}_a$ relative to its current orientation, expressed in global coordinates.

The expressions in Eqs. (A1.15) and (A1.16) may be further simplified by using the fact that $\mathbf{E}$ is the transformation matrix from the global coordinate system to the element local coordinates. That is,

$$\mathbf{x}^e = \mathbf{E}^T \mathbf{x}^g \tag{A1.17}$$

and

$$Spin(\delta\boldsymbol{\omega}_{\mathrm{E}}^{\mathrm{e}}) = \mathbf{E}^{\mathrm{T}}\ Spin(\delta\boldsymbol{\omega}_{\mathrm{E}}^{\mathrm{g}})\ \mathbf{E} \tag{A1.18}$$

Therefore, Eqs. (A1.15) can be simplified as:

$$\begin{aligned}\delta\mathbf{u}_a^n &= \mathbf{E}^T\left[-Spin(\delta\boldsymbol{\omega}_E^g)\ \mathbf{E}\ \mathbf{E}^T(\mathbf{x}_a^g - \mathbf{x}_o^g) + (\delta\mathbf{u}_a^g - \delta\mathbf{u}_o^g)\right] \\ &= -\left(\mathbf{E}^T Spin(\delta\boldsymbol{\omega}_E^g)\ \mathbf{E}\right)\mathbf{E}^T(\mathbf{x}_a^g - \mathbf{x}_o^g) + \mathbf{E}^T(\delta\mathbf{u}_a^g - \delta\mathbf{u}_o^g) \\ &= -Spin(\delta\boldsymbol{\omega}_E^e)\ (\mathbf{x}_a^e - \mathbf{x}_o^e) + (\delta\mathbf{u}_a^e - \delta\mathbf{u}_o^e)\end{aligned} \tag{A1.19}$$

Finally, by using Eq. (A1.8) and recognizing that $\mathbf{x}_o^e = \mathbf{0}$, Eq. (A1.19) may be written as

$$\delta\mathbf{u}_a^n = Spin(\mathbf{x}_a^e)\ \delta\boldsymbol{\omega}_E^e + \delta\mathbf{u}_a^e - \delta\mathbf{u}_o^e \tag{A1.20}$$

in which $Spin(\mathbf{x}_a^e)$ is a skew-symmetric matrix constructed from the components of $\mathbf{x}_a^e$ according to Eq. (2.4) (i.e., it is the matrix representation of the moment-arm tensor), $\delta\boldsymbol{\omega}_E^e$ is the incremental spatial rotation of the moving element CR frame, $\delta\mathbf{u}_a^e$ is the increment in the displacement at node a, and $\delta\mathbf{u}_o^e$ is the increment in the displacement at the origin of the element CR frame. All of the quantities in Eq. (A1.20) are expressed in the current element CR coordinates.

By following a similar procedure to that employed in Eq. (A1.19), Eq. (A1.16) may be written as

$$\delta\boldsymbol{\Gamma}_a^n = \left[-Spin(\delta\boldsymbol{\omega}_E^e) + Spin(\delta\boldsymbol{\omega}_a^e)\right]\mathbf{E}^T\mathbf{S}_a\mathbf{E}_o \tag{A1.21}$$

which, after substituting Eq. (A1.5), becomes

$$\delta\mathbf{\Gamma}_a^n = \left[-Spin(\delta\boldsymbol{\omega}_E^e) + Spin(\delta\boldsymbol{\omega}_a^e)\right]\mathbf{T}_a^n \tag{A1.22}$$

Note that $\delta\mathbf{\Gamma}_a^n$ is the orthogonal transformation matrix that represents the effect of the rotation from the current element CR frame $\mathbf{E}$ to the current nodal triad at node a, $\mathbf{S}_a$. The term $\delta\boldsymbol{\omega}_a^e$ is the incremental spatial rotation at node a. Similar to Eq. (A1.20), all of the quantities in Eq. (A1.22) are expressed in the current element CR coordinates.

The second part of Eq. (A1.2) gives $\delta\mathbf{\Gamma}_a^n$ in the absence of any incremental rotation of the element CR frame, whereas the first part of this equation gives the change in $\mathbf{T}_a^n$ due to the incremental rotation of the CR frame. By comparing these terms to Eq. (A1.13), it is clear that we can write

$$\delta\boldsymbol{\omega}_a^n = \delta\boldsymbol{\omega}_a^e - \delta\boldsymbol{\omega}_E^e \tag{A1.23}$$

in which $\delta\boldsymbol{\omega}_a^n$ is the "deformational" spatial rotation increment at node a within the moving element CR frame, expressed in terms of the current element CR coordinates. That is, $\delta\boldsymbol{\omega}_a^n$ is the rotation of node a relative to the moving element CR frame, associated with the incremental motion from the current geometry, expressed in terms of the current element CR coordinates.

A1.2 Selection of Element Corotational Frame Basis Vectors to Minimize Rigid-Body Rotations Relative to the CR Frame

The element CR basis defined by Nour-Omid and Rankin (1991) ensures that the natural rotations about the element chord are of the same order as those which produce torsion. However, the CR frame as defined by Nour-Omid and Rankin (1991) is not

influenced at all by the rotations at node 2. Therefore, if the twisting of the element about its $\mathbf{e}_1$ axis is large, the cross-section at node 2 may undergo significant rigid body rotation relative to the CR frame. Crisfield (1990) bases his corotational formation on an approximate average rotation of the two end nodes. However, since Crisfield conducts his formulation directly in global coordinates, rather than transforming the element quantities to CR coordinates, his formulation is significantly more complex. An alternative definition of the element CR frame, which tends to minimize the natural rigid body rotations and is similar in form and simplicity to Nour-Omid and Rankin's (1991) approach is developed below.

The basis vector $\mathbf{e}_1^g$ is defined as

$$\mathbf{e}_1^g = \frac{\mathbf{x}_2 - \mathbf{x}_1}{\left|\mathbf{x}_2 - \mathbf{x}_1\right|} = \frac{\mathbf{x}_2 - \mathbf{x}_1}{\ell} \tag{A1.24}$$

in which $\mathbf{x}_2$ is equal to $\mathbf{X}_a^g + \mathbf{u}_a^g$, and

$$\ell = \sqrt{(\mathbf{x}_2 - \mathbf{x}_1)^T (\mathbf{x}_2 - \mathbf{x}_1)} \tag{A1.25}$$

is the current length between the element end nodes.

As mentioned in Section 2.3, the direction of the vector $\mathbf{e}_2$ is taken as the average of the basis vectors $\mathbf{t}_2$ and $\mathbf{u}_2$ of the nodal triads $\mathbf{T}$ and $\mathbf{U}$ at the element end nodes in Figure 2.3. That is,

$$\hat{\mathbf{y}}_{avg} = (\hat{\mathbf{y}}_1 + \hat{\mathbf{y}}_2)/2 \tag{A1.26}$$

in which $\hat{\mathbf{y}}_1 = \mathbf{t}_2$ and $\hat{\mathbf{y}}_2 = \mathbf{u}_2$. Based on this definition, the basis vectors $\mathbf{e}_2$ and $\mathbf{e}_3$ can be obtained as

$$\mathbf{e}_3 = \frac{\mathbf{e}_1 \times \hat{\mathbf{y}}_{avg}}{\left|\mathbf{e}_1 \times \hat{\mathbf{y}}_{avg}\right|} \tag{A1.27}$$

$$\mathbf{e}_2 = -\mathbf{e}_1 \times \mathbf{e}_3 \tag{A1.28}$$

To derive the projection operator $\mathbf{P}$, the variation of the incremental spatial rotation of the moving element CR frame $\delta\boldsymbol{\omega}_E^e$ must be determined. With the aid of Eqs. (A1.14) and (A1.18), we have

$$\mathbf{E}^{eT}\delta\mathbf{E}^e = Spin(\delta\boldsymbol{\omega}_E^e) \tag{A1.29}$$

or

$$\begin{bmatrix}\mathbf{e}_1^{eT}\\ \mathbf{e}_2^{eT}\\ \mathbf{e}_3^{eT}\end{bmatrix}\begin{bmatrix}\delta\mathbf{e}_1^e & \delta\mathbf{e}_2^e & \delta\mathbf{e}_3^e\end{bmatrix}=\begin{bmatrix}\mathbf{e}_1^{eT}\delta\mathbf{e}_1^e & \mathbf{e}_1^{eT}\delta\mathbf{e}_2^e & \mathbf{e}_1^{eT}\delta\mathbf{e}_3^e\\ \mathbf{e}_2^{eT}\delta\mathbf{e}_1^e & \mathbf{e}_2^{eT}\delta\mathbf{e}_2^e & \mathbf{e}_2^{eT}\delta\mathbf{e}_3^e\\ \mathbf{e}_3^{eT}\delta\mathbf{e}_1^e & \mathbf{e}_3^{eT}\delta\mathbf{e}_2^e & \mathbf{e}_3^{eT}\delta\mathbf{e}_3^e\end{bmatrix}=\begin{bmatrix}0 & -\delta\omega_{E3}^e & \delta\omega_{E2}^e\\ \delta\omega_{E3}^e & 0 & -\delta\omega_{E1}^e\\ -\delta\omega_{E2}^e & \delta\omega_{E1}^e & 0\end{bmatrix} \tag{A1.30}$$

That is,

$$\mathbf{e}_1^{eT}\delta\mathbf{e}_1^e = \mathbf{e}_2^{eT}\delta\mathbf{e}_2^e = \mathbf{e}_3^{eT}\delta\mathbf{e}_3^e = 0 \tag{A1.31}$$

$$\delta\omega_{E1}^e = \mathbf{e}_3^{eT}\delta\mathbf{e}_2^e = -\mathbf{e}_2^{eT}\delta\mathbf{e}_3^e \tag{A1.32}$$

$$\delta\omega_{E2}^e = \mathbf{e}_1^{eT}\delta\mathbf{e}_3^e = -\mathbf{e}_3^{eT}\delta\mathbf{e}_1^e \tag{A1.33}$$

$$\delta\omega_{E3}^e = \mathbf{e}_2^{eT}\delta\mathbf{e}_1^e = -\mathbf{e}_1^{eT}\delta\mathbf{e}_2^e \tag{A1.34}$$

The variation of $\mathbf{e}_1^g$ in Eq. (A1.24) is

$$\begin{aligned}\delta\mathbf{e}_1 &= \frac{\delta\mathbf{u}_2-\delta\mathbf{u}_1}{\ell}-\frac{(\mathbf{x}_2-\mathbf{x}_1)}{\ell^2}\delta\ell = \frac{\delta\mathbf{u}_2-\delta\mathbf{u}_1}{\ell}-\frac{1}{\ell}\mathbf{e}_1\left(\frac{1}{\ell}(\mathbf{x}_2-\mathbf{x}_1)^T(\delta\mathbf{u}_2-\delta\mathbf{u}_1)\right)\\ &= \frac{1}{\ell}\left[\mathbf{I}-\mathbf{e}_1\mathbf{e}_1^T\right](\delta\mathbf{u}_2-\delta\mathbf{u}_1)\\ &= \frac{1}{\ell}\begin{Bmatrix}0\\ \delta u_{2y}^e-\delta u_{1y}^e\\ \delta u_{2z}^e-\delta u_{1z}^e\end{Bmatrix}\end{aligned} \tag{A1.35}$$

in which, for example, δu_{1y}^e is the component in the $\mathbf{e}_2$ direction of the variation in the displacement at node 1. Also,

$$\delta\mathbf{e}_3 = \frac{1}{\left|\mathbf{e}_1\times\hat{\mathbf{y}}_{avg}\right|}\left[\delta\mathbf{e}_1\times\hat{\mathbf{y}}_{avg}+\mathbf{e}_1\times\delta\hat{\mathbf{y}}_{avg}\right]+\frac{1}{\left|\mathbf{e}_1\times\hat{\mathbf{y}}_{avg}\right|^2}\delta\left(\left|\mathbf{e}_1\times\hat{\mathbf{y}}_{avg}\right|\right)(\mathbf{e}_1\times\hat{\mathbf{y}}_{avg}) \tag{A1.36}$$

where

$$\left|\mathbf{e}_1 \times \hat{\mathbf{y}}_{avg}\right| = \hat{y}^e_{avg_y} \tag{A1.37}$$

$$\mathbf{e}_1 \times \hat{\mathbf{y}}_{avg} = \hat{y}^e_{avg_y}\, \mathbf{e}_3 \tag{A1.38}$$

The variation of $\mathbf{e}_3$ can be further arranged as:

$$\begin{aligned}
\delta\mathbf{e}_3 &= \frac{1}{\hat{y}^e_{avg_y}}\left[-Spin(\hat{\mathbf{y}}_{avg})\frac{1}{\ell}\left[\mathbf{I} - \mathbf{e}_1\mathbf{e}_1^T\right](\delta\mathbf{u}_2 - \delta\mathbf{u}_1) + Spin(\mathbf{e}_1)\delta\hat{\mathbf{y}}_{avg} \right] + \frac{1}{\hat{y}^{e\ 2}_{avg_y}}\delta\hat{y}^e_{avg_y}\hat{y}^e_{avg_y}\,\mathbf{e}_3 \\
&= \frac{1}{\ell\,\hat{y}^e_{avg_y}}\left(-\begin{bmatrix} 0 & -\hat{y}^e_{avg_z} & \hat{y}^e_{avg_y} \\ \hat{y}^e_{avg_z} & 0 & -\hat{y}^e_{avg_x} \\ -\hat{y}^e_{avg_y} & \hat{y}^e_{avg_x} & 0 \end{bmatrix}\begin{bmatrix} 0 & 0 & 0 \\ 0 & 1 & 0 \\ 0 & 0 & 1 \end{bmatrix}(\delta\mathbf{u}_2^e - \delta\mathbf{u}_1^e) + \ell\begin{bmatrix} 0 & 0 & 0 \\ 0 & 0 & -1 \\ 0 & 1 & 0 \end{bmatrix}\begin{Bmatrix} \delta\hat{y}^e_{avg_x} \\ \delta\hat{y}^e_{avg_y} \\ \delta\hat{y}^e_{avg_z} \end{Bmatrix}\right) + \frac{\delta\hat{y}^e_{avg_y}}{\hat{y}^e_{avg_y}}\mathbf{e}_3 \\
&= \frac{1}{\ell\,\hat{y}^e_{avg_y}}\begin{bmatrix} \hat{y}^e_{avg_z}\left(\delta u^e_{2y} - \delta u^e_{1y}\right) - \hat{y}^e_{avg_y}\left(\delta u^e_{2z} - \delta u^e_{1z}\right) \\ \hat{y}^e_{avg_x}\left(\delta u^e_{2z} - \delta u^e_{1z}\right) - \ell\,\delta\hat{y}^e_{avg_z} \\ -\hat{y}^e_{avg_x}\left(\delta u^e_{2y} - \delta u^e_{1y}\right) + \ell\,\delta\hat{y}^e_{avg_y} + \ell\,\delta\hat{y}^e_{avg_y}/\hat{y}^e_{avg_y} \end{bmatrix}
\end{aligned}$$

(A1.39)

Therefore, with the use of Eqs.(A1.24) to (A1.39), the incremental spatial rotation of the element CR frame $\delta\boldsymbol{\omega}^e_E$ can be expressed as

$$\delta\boldsymbol{\omega}^e_E = \begin{Bmatrix} \delta\omega^e_{E1} \\ \delta\omega^e_{E2} \\ \delta\omega^e_{E3} \end{Bmatrix} = \begin{Bmatrix} -\mathbf{e}_2^{eT}\delta\mathbf{e}^e_3 \\ -\mathbf{e}_3^{eT}\delta\mathbf{e}^e_1 \\ \mathbf{e}_2^{eT}\delta\mathbf{e}^e_1 \end{Bmatrix}\begin{Bmatrix} \dfrac{1}{\ell\,\hat{y}^e_{avg_y}}\left[\ell\,\delta\hat{y}^e_{avg_z} - \hat{y}^e_{avg_x}\left(\delta u^e_{2z} - \delta u^e_{1z}\right)\right] \\ -\dfrac{1}{\ell}\left[\delta u^e_{2z} - \delta u^e_{1z}\right] \\ \dfrac{1}{\ell}\left[\delta u^e_{2y} - \delta u^e_{1y}\right] \end{Bmatrix} \tag{A1.40}$$

In above equation, $\delta\hat{\mathbf{y}}_{avg} = (\delta\hat{\mathbf{y}}_1 + \delta\hat{\mathbf{y}}_2)/2$, and

$$\delta\hat{\mathbf{y}}^e_a = \mathrm{Spin}(\delta\boldsymbol{\omega}^e_a)\hat{\mathbf{y}}^e_a = \begin{Bmatrix} -\delta\omega^e_{az}\hat{y}^e_{ay} + \delta\omega^e_{ay}\hat{y}^e_{az} \\ \delta\omega^e_{az}\hat{y}^e_{ax} - \delta\omega^e_{ax}\hat{y}^e_{az} \\ -\delta\omega^e_{ay}\hat{y}^e_{ax} + \delta\omega^e_{ax}\hat{y}^e_{ay} \end{Bmatrix} \tag{A1.41}$$

Therefore, Eq.(A1.40) can be rewritten as

$$\delta\boldsymbol{\omega}_E^e = \begin{Bmatrix} -\frac{1}{2}\left[\delta\omega_{1\,y}^e\xi_1 + \delta\omega_{2\,y}^e\xi_2\right] + \frac{1}{2}\left[\delta\omega_{1\,x}^e\eta_1 + \delta\omega_{2\,x}^e\eta_2\right] - \frac{\xi_{avg}}{\ell}\left[\delta u_{2\,z}^e - \delta u_{1\,z}^e\right] \\ -\frac{1}{\ell}\left[\delta u_{2\,z}^e - \delta u_{1\,z}^e\right] \\ \frac{1}{\ell}\left[\delta u_{2\,y}^e - \delta u_{1\,y}^e\right] \end{Bmatrix} \tag{A1.42}$$

in which

$$\xi_{avg} = \frac{\hat{y}_{avg\,x}^e}{\hat{y}_{avg\,y}^e} \tag{A1.43}$$

$$\xi_a = \frac{\hat{y}_{a\,x}^e}{\hat{y}_{avg\,y}^e},\ a = 1,\ 2 \tag{A1.44}$$

$$\eta_a = \frac{\hat{y}_{a\,y}^e}{\hat{y}_{avg\,y}^e},\ a = 1,\ 2 \tag{A1.45}$$

A1.3 Projection Operator $\mathbf{P}$

In Eq. (2.15)

$$\delta\mathbf{q}_n = \left(\frac{\partial\mathbf{q}_n}{\partial\mathbf{q}_e}\right)\delta\mathbf{q}_e = \mathbf{P}\delta\mathbf{q}_e = \mathbf{P}\mathbf{G}^T\delta\mathbf{q}_g$$

in which $\mathbf{P}$ is referred to as the projection operator (or the projector)(Rankin and Nour-Omid 1991) and $\mathbf{G}$ is the coordinate transformation matrix between the element frame and the global frame. The projection operator $\mathbf{P}$ can be expressed as

$$\mathbf{P} = \frac{\partial \mathbf{q}_n}{\partial \mathbf{q}_e} = \left[\begin{array}{cc:cc} \frac{\partial \mathbf{u}_1^n}{\partial \mathbf{u}_1^e} & \frac{\partial \mathbf{u}_1^n}{\partial \boldsymbol{\omega}_1^e} & \frac{\partial \mathbf{u}_1^n}{\partial \mathbf{u}_2^e} & \frac{\partial \mathbf{u}_1^n}{\partial \boldsymbol{\omega}_2^e} \\ \frac{\partial \boldsymbol{\omega}_1^n}{\partial \mathbf{u}_1^e} & \frac{\partial \boldsymbol{\omega}_1^n}{\partial \boldsymbol{\omega}_1^e} & \frac{\partial \boldsymbol{\omega}_1^n}{\partial \mathbf{u}_2^e} & \frac{\partial \boldsymbol{\omega}_1^n}{\partial \boldsymbol{\omega}_2^e} \\ \hdashline \frac{\partial \mathbf{u}_2^n}{\partial \mathbf{u}_1^e} & \frac{\partial \mathbf{u}_2^n}{\partial \boldsymbol{\omega}_1^e} & \frac{\partial \mathbf{u}_2^n}{\partial \mathbf{u}_2^e} & \frac{\partial \mathbf{u}_2^n}{\partial \boldsymbol{\omega}_2^e} \\ \frac{\partial \boldsymbol{\omega}_2^n}{\partial \mathbf{u}_1^e} & \frac{\partial \boldsymbol{\omega}_2^n}{\partial \boldsymbol{\omega}_1^e} & \frac{\partial \boldsymbol{\omega}_2^n}{\partial \mathbf{u}_2^e} & \frac{\partial \boldsymbol{\omega}_2^n}{\partial \boldsymbol{\omega}_2^e} \end{array}\right] = \begin{bmatrix} [\mathbf{P}_{11}] & [\mathbf{P}_{12}] \\ [\mathbf{P}_{21}] & [\mathbf{P}_{22}] \end{bmatrix} \tag{A1.46}$$

and the coordinate transformation matrix is expressed as

$$\mathbf{G}^T = \frac{\partial \mathbf{q}_e}{\partial \mathbf{q}_q} = \begin{bmatrix} \mathbf{E}^T & \mathbf{0} & \mathbf{0} & \mathbf{0} \\ \mathbf{0} & \mathbf{E}^T & \mathbf{0} & \mathbf{0} \\ \mathbf{0} & \mathbf{0} & \mathbf{E}^T & \mathbf{0} \\ \mathbf{0} & \mathbf{0} & \mathbf{0} & \mathbf{E}^T \end{bmatrix} \tag{A1.47}$$

Based on Eqs. (A1.20) and (A1.23), the components in Eq. (A1.46) can be written as

$$\frac{\partial \mathbf{u}_c^n}{\partial \mathbf{u}_b^e} = \frac{\partial \mathbf{u}_c^e}{\partial \mathbf{u}_b^e} + Spin(\mathbf{x}_c^e)\frac{\partial \boldsymbol{\omega}_E^e}{\partial \mathbf{u}_b^e} - \frac{\partial \mathbf{u}_o^e}{\partial \mathbf{u}_b^e} \tag{A1.48}$$

$$\frac{\partial \mathbf{u}_c^n}{\partial \boldsymbol{\omega}_b^e} = \frac{\partial \mathbf{u}_c^e}{\partial \boldsymbol{\omega}_b^e} + Spin(\mathbf{x}_c^e)\frac{\partial \boldsymbol{\omega}_E^e}{\partial \boldsymbol{\omega}_b^e} - \frac{\partial \mathbf{u}_o^e}{\partial \boldsymbol{\omega}_b^e} = Spin(\mathbf{x}_c^e)\frac{\partial \boldsymbol{\omega}_E^e}{\partial \boldsymbol{\omega}_b^e} \tag{A1.49}$$

$$\frac{\partial \boldsymbol{\omega}_c^n}{\partial \mathbf{u}_b^e} = \frac{\partial \boldsymbol{\omega}_c^e}{\partial \mathbf{u}_b^e} - \frac{\partial \boldsymbol{\omega}_E^e}{\partial \mathbf{u}_b^e} = -\frac{\partial \boldsymbol{\omega}_E^e}{\partial \mathbf{u}_b^e} \tag{A1.50}$$

$$\frac{\partial \boldsymbol{\omega}_c^n}{\partial \boldsymbol{\omega}_b^e} = \frac{\partial \boldsymbol{\omega}_c^e}{\partial \boldsymbol{\omega}_b^e} - \frac{\partial \boldsymbol{\omega}_E^e}{\partial \boldsymbol{\omega}_b^e} \tag{A1.51}$$

in which the terms $\frac{\partial \mathbf{u}_c^e}{\partial \boldsymbol{\omega}_b^e}$, $\frac{\partial \mathbf{u}_o^e}{\partial \boldsymbol{\omega}_b^e}$ and $\frac{\partial \boldsymbol{\omega}_c^e}{\partial \mathbf{u}_b^e}$ in Eqs. (A1.49) and (A1.50) are zero since the nodal displacements and nodal rotations are independent variables. Therefore, $[\mathbf{P}_{cb}]$ can be expressed as

$$\left[\mathbf{P}_{cb}\right]=\begin{bmatrix} \dfrac{\partial \mathbf{u}_c^e}{\partial \mathbf{u}_b^e}+Spin(\mathbf{x}_c^e)\dfrac{\partial \boldsymbol{\omega}_E^e}{\partial \mathbf{u}_b^e}-\dfrac{\partial \mathbf{u}_o^e}{\partial \mathbf{u}_b^e} & Spin(\mathbf{x}_c^e)\dfrac{\partial \boldsymbol{\omega}_E^e}{\partial \boldsymbol{\omega}_b^e} \\ -\dfrac{\partial \boldsymbol{\omega}_E^e}{\partial \mathbf{u}_b^e} & \dfrac{\partial \boldsymbol{\omega}_c^e}{\partial \boldsymbol{\omega}_b^e}-\dfrac{\partial \boldsymbol{\omega}_E^e}{\partial \boldsymbol{\omega}_b^e} \end{bmatrix} \tag{A1.52}$$

Note that $[\mathbf{P}_{cb}]$ maps the absolute variations in the nodal displacements and nodal spatial rotations to the corresponding element deformational quantities, where all the quantities are expressed in element CR coordinates.

With the aid of Eqs. (A1.42) to (A1.45), the projection operator $\mathbf{P}$ in Eq.(A1.52) can be expressed in the following closed form:

$$\mathbf{P}=\begin{bmatrix}[\mathbf{P}_{11}] & [\mathbf{P}_{12}] \\ [\mathbf{P}_{21}] & [\mathbf{P}_{22}]\end{bmatrix}$$

$$=\left[\begin{array}{ccc:ccc:ccc:ccc}
\multicolumn{3}{c:}{\mathbf{0}_3} & \multicolumn{3}{c:}{\mathbf{0}_3} & \multicolumn{3}{c:}{\mathbf{0}_3} & \multicolumn{3}{c}{\mathbf{0}_3} \\ \hdashline
0 & 0 & -\xi_{avg}/\ell & 1-\eta_1/2 & \xi_1/2 & 0 & 0 & 0 & \xi_{avg}/\ell & -\eta_2/2 & \xi_2/2 & 0 \\
0 & 0 & -1/\ell & 0 & 1 & 0 & 0 & 0 & 1/\ell & 0 & 0 & 0 \\
0 & 1/\ell & 0 & 0 & 0 & 1 & 0 & -1/\ell & 0 & 0 & 0 & 0 \\ \hdashline
-1 & 0 & 0 & \multicolumn{3}{c:}{} & 1 & 0 & 0 & \multicolumn{3}{c}{} \\
0 & 0 & 0 & \multicolumn{3}{c:}{\mathbf{0}_3} & 0 & 0 & 0 & \multicolumn{3}{c}{\mathbf{0}_3} \\
0 & 0 & 0 & \multicolumn{3}{c:}{} & 0 & 0 & 0 & \multicolumn{3}{c}{} \\ \hdashline
0 & 0 & -\xi_{avg}/\ell & -\eta_1/2 & \xi_1/2 & 0 & 0 & 0 & \xi_{avg}/\ell & 1-\eta_2/2 & \xi_2/2 & 0 \\
0 & 0 & -1/\ell & 0 & 0 & 0 & 0 & 0 & 1/\ell & 0 & 1 & 0 \\
0 & 1/\ell & 0 & 0 & 0 & 0 & 0 & -1/\ell & 0 & 0 & 0 & 1
\end{array}\right] \tag{A1.53}$$

From Eqs. (A1.53) and (2.15), which is $\delta\mathbf{q}_n=\mathbf{P}\delta\mathbf{q}_e$, it can be observed that:

1. $\mathbf{P}$ maps $\delta\mathbf{q}_e$ to $\delta\mathbf{u}_1^n=\mathbf{0}$.
2. $\mathbf{P}$ maps $\delta\mathbf{q}_e$ to $\delta u_{2y}^n=\delta u_{2z}^n=0$.
3. $\mathbf{P}$ maps $\delta\mathbf{q}_e$ to $\delta u_{2x}^n=\delta u_{2x}^e-\delta u_{1x}^e$.

Based on the above observations, rows 1 through 3, 8 and 9 of $\mathbf{P}$ can be automatically dropped in the numerical implementation of the corotational mapping, and only the degrees of freedom 4 through 7 and 10 through 12 need to be handled in the calculations within the element CR frame.

Also, from Eq. (2.16), $\mathbf{Q}_e = \mathbf{P}^T \mathbf{Q}_n$, one can observe that $\mathbf{P}$ maps the element forces $\mathbf{Q}_n$ to

$$\{\mathbf{Q}_e\} = \{\mathbf{Q}_n\} = \lfloor -P \quad -V_y \quad -V_z \quad -T \quad m_{1y} \quad m_{1z} \quad P \quad V_y \quad V_z \quad T \quad m_{2y} \quad m_{2z} \rfloor^T \tag{A1.54}$$

assuming that the forces in $\mathbf{Q}_n$ are in equilibrium, and neglecting the effect of any element internal loadings. The individual force terms in this equation are illustrated in Figure A1.2

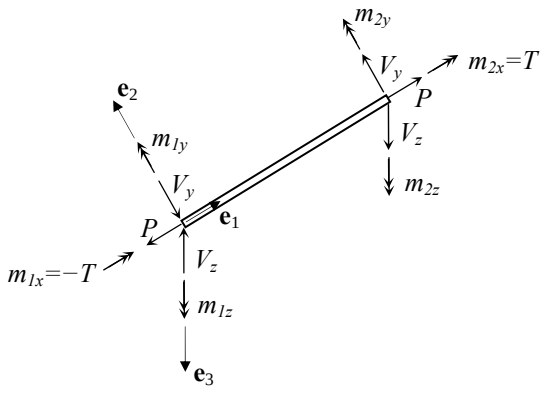

Figure A1.2 The element nodal forces in the CR frame

and

$$V_y = \frac{-(m_{1z} + m_{2z})}{\ell} \tag{A1.55}$$

$$V_z = \frac{(m_{1y} + m_{2y})}{\ell} \tag{A1.56}$$

based on equilibrium. For the elements considered in this work, the nodal forces obtained from the element state determination calculations always satisfy equilibrium in the current deformed configuration. Similarly, for the first term in the parentheses of Eq. (2.21), $\mathbf{K}_e = \mathbf{P}^T\mathbf{K}_n\mathbf{P} = \mathbf{K}_e$ if rows 1-3, 8 and 9 are retained in $\mathbf{P}$. However, when rows 1-3, 8 and 9 are discarded in $\mathbf{P}$, the projector $\mathbf{P}$ maps the 7x7 element natural stiffness $\mathbf{K}_n$ to the contribution to the 12x12 element global stiffness $\mathbf{K}_g$ associated with $\delta\mathbf{Q}_n$.

A1.4 Element External Geometric Stiffness Matrix – Contribution from δP

Given Eq. (A1.53), $\delta\mathbf{P}$ can be determined as

$$\delta\mathbf{P} = \left[\begin{array}{cccccc|cccccc} \multicolumn{3}{c}{\mathbf{0}_3} & \multicolumn{3}{c|}{\mathbf{0}_3} & \multicolumn{3}{c}{\mathbf{0}_3} & \multicolumn{3}{c}{\mathbf{0}_3} \\ \hline 0 & 0 & A & D_1 & C_1 & 0 & 0 & 0 & -A & D_2 & C_2 & 0 \\ 0 & 0 & B & 0 & 0 & 0 & 0 & 0 & -B & 0 & 0 & 0 \\ 0 & -B & 0 & 0 & 0 & 0 & 0 & B & 0 & 0 & 0 & 0 \\ \hline \multicolumn{3}{c}{\mathbf{0}_3} & \multicolumn{3}{c|}{\mathbf{0}_3} & \multicolumn{3}{c}{\mathbf{0}_3} & \multicolumn{3}{c}{\mathbf{0}_3} \\ \hline 0 & 0 & A & D_1 & C_1 & 0 & 0 & 0 & -A & D_2 & C_2 & 0 \\ 0 & 0 & B & 0 & 0 & 0 & 0 & 0 & -B & 0 & 0 & 0 \\ 0 & -B & 0 & 0 & 0 & 0 & 0 & B & 0 & 0 & 0 & 0 \end{array}\right] \tag{A1.57}$$

in which

$$A = -\delta\left(\frac{\xi_{avg}}{\ell}\right) = -\frac{1}{\ell}\delta\xi_{avg} + \frac{\xi_{avg}}{\ell^2}\delta\ell \tag{A1.58}$$

$$B = -\delta\left(\frac{1}{\ell}\right) = \frac{\delta\ell}{\ell^2} = \frac{1}{\ell^2}\left[\delta u^e_{2x} - \delta u^e_{1x}\right] \tag{A1.59}$$

$$C_1 = \frac{\delta\xi_1}{2} \tag{A1.60}$$

$$C_2 = \frac{\delta\xi_2}{2} \tag{A1.61}$$

$$D_1 = -\frac{\delta\eta_1}{2} \tag{A1.62}$$

$$D_2 = -\frac{\delta\eta_2}{2} \tag{A1.63}$$

If we recognize that $(m_{1x}+m_{2x}) = (-T+T) = 0$, then the term $\delta\mathbf{P}^T\mathbf{Q}_n$ in Eq. (2.19) reduces to

$$\delta\mathbf{P}^T\mathbf{Q}_n = \begin{bmatrix} 0 & -B(m_{1z}+m_{2z}) & B(m_{1y}+m_{2y}) & 0 & 0 & 0 & 0 & B(m_{1z}+m_{2z}) & -B(m_{1y}+m_{2y}) & 0 & 0 & 0 \end{bmatrix}^T \tag{A1.64}$$

which can be rewritten (using Eqs. (A1.55), (A1.56) and (A1.59)) as

$$\delta\mathbf{P}^T\mathbf{Q}_n = \mathbf{K}^e_{ext1}\delta\mathbf{q}_e$$

$$= \left[\begin{array}{ccc:c:ccc:c} 0 & 0 & 0 & & 0 & 0 & 0 & \\ -V_y/\ell & 0 & 0 & \mathbf{0}_3 & V_y/\ell & 0 & 0 & \mathbf{0}_3 \\ -V_z/\ell & 0 & 0 & & V_z/\ell & 0 & 0 & \\ \hdashline & & & & & & & \\ & \mathbf{0}_3 & & \mathbf{0}_3 & & \mathbf{0}_3 & & \mathbf{0}_3 \\ & & & & & & & \\ \hdashline 0 & 0 & 0 & & 0 & 0 & 0 & \\ V_y/\ell & 0 & 0 & \mathbf{0}_3 & -V_y/\ell & 0 & 0 & \mathbf{0}_3 \\ V_z/\ell & 0 & 0 & & -V_z/\ell & 0 & 0 & \\ \hdashline & & & & & & & \\ & \mathbf{0}_3 & & \mathbf{0}_3 & & \mathbf{0}_3 & & \mathbf{0}_3 \\ & & & & & & & \end{array}\right] \left\{\begin{array}{c} \delta u^e_{1x} \\ \delta u^e_{1y} \\ \delta u^e_{1z} \\ \delta\omega^e_{1x} \\ \delta\omega^e_{1y} \\ \delta\omega^e_{1z} \\ \delta u^e_{2x} \\ \delta u^e_{2y} \\ \delta u^e_{2z} \\ \delta\omega^e_{2x} \\ \delta\omega^e_{2y} \\ \delta\omega^e_{2z} \end{array}\right\} \tag{A1.65}$$

A1.5 Element External Geometric Stiffness Matrices – Contribution from δG

Consider the third contribution to the element consistent tangent stiffness in Eqs. (2.17) and (2.20). With the aid of Eq. (A1.14), this term may be rewritten as

$$\begin{aligned}\delta\mathbf{G}\mathbf{P}^T\mathbf{Q}_n &= \begin{bmatrix}\delta\mathbf{E} & \mathbf{0} & \mathbf{0} & \mathbf{0}\\ \mathbf{0} & \delta\mathbf{E} & \mathbf{0} & \mathbf{0}\\ \mathbf{0} & \mathbf{0} & \delta\mathbf{E} & \mathbf{0}\\ \mathbf{0} & \mathbf{0} & \mathbf{0} & \delta\mathbf{E}\end{bmatrix}\mathbf{P}^T\mathbf{Q}_n\\ &= \text{diag}[\text{Spin}(\delta\boldsymbol{\omega}_E^g)\mathbf{E}]\,\mathbf{P}^T\mathbf{Q}_n = \text{diag}[\text{Spin}(\delta\boldsymbol{\omega}_E^g)]\mathbf{G}\mathbf{P}^T\mathbf{Q}_n\\ &= \mathbf{G}\Big(\mathbf{G}^T\text{diag}[\text{Spin}(\delta\boldsymbol{\omega}_E^g)]\mathbf{G}\Big)\mathbf{Q}_e = \mathbf{G}\,\text{diag}[\text{Spin}(\delta\boldsymbol{\omega}_E^e)]\begin{Bmatrix}\mathbf{f}_1^e\\ \mathbf{m}_1^e\\ \mathbf{f}_2^e\\ \mathbf{m}_2^e\end{Bmatrix}\\ &= -\mathbf{G}\begin{Bmatrix}\text{Spin}(\mathbf{f}_1^e)\\ \text{Spin}(\mathbf{m}_1^e)\\ \text{Spin}(\mathbf{f}_2^e)\\ \text{Spin}(\mathbf{m}_2^e)\end{Bmatrix}\delta\boldsymbol{\omega}_E^e = -\mathbf{G}\,\overline{\mathbf{F}}\,\delta\boldsymbol{\omega}_E^e\end{aligned} \tag{A1.66}$$

Furthermore, $\delta\boldsymbol{\omega}_E^e$ may be expressed as

$$\delta\boldsymbol{\omega}_E^e = \boldsymbol{\Gamma}^T\delta\mathbf{q}_e = \boldsymbol{\Gamma}^T\mathbf{G}^T\delta\mathbf{q}_g \tag{A1.67}$$

With the aid of Eqs. (A1.50) and (A1.51), $\boldsymbol{\Gamma}^T$ can be written as

$$\begin{aligned}\boldsymbol{\Gamma}^T &= \begin{bmatrix}\dfrac{\partial\boldsymbol{\omega}_E^e}{\partial\mathbf{u}_1^e} & \dfrac{\partial\boldsymbol{\omega}_E^e}{\partial\boldsymbol{\omega}_1^e} & \dfrac{\partial\boldsymbol{\omega}_E^e}{\partial\mathbf{u}_2^e} & \dfrac{\partial\boldsymbol{\omega}_E^e}{\partial\boldsymbol{\omega}_2^e}\end{bmatrix}^T\\ &= \left[\begin{array}{ccc:ccc:ccc:ccc}0 & 0 & \xi_{avg}/\ell & \eta_1/2 & -\xi_1/2 & 0 & 0 & 0 & -\xi_{avg}/\ell & \eta_2/2 & -\xi_2/2 & 0\\ 0 & 0 & 1/\ell & 0 & 0 & 0 & 0 & 0 & -1/\ell & 0 & 0 & 0\\ 0 & -1 & 0 & 0 & 0 & 0 & 0 & 1/\ell & 0 & 0 & 0 & 0\end{array}\right]\end{aligned} \tag{A1.68}$$

Therefore, the Eq. (A1.66) can be written as

$$\delta\mathbf{G}\mathbf{P}^T\mathbf{Q}_n = -\mathbf{G}\,\overline{\mathbf{F}}\,\boldsymbol{\Gamma}^T\mathbf{G}^T\delta\mathbf{q}_g = \mathbf{G}\mathbf{K}_{ext2}^e\mathbf{G}^T\delta\mathbf{q}_g \tag{A1.69}$$

in which

$$\mathbf{K}^{e}_{ext2} = -\bar{\mathbf{F}}\,\boldsymbol{\Gamma}^{T}$$

$$= \left[\begin{array}{ccc:ccc:ccc:ccc} 0 & -V_y/\ell & -V_z/\ell & 0 & 0 & 0 & 0 & V_y/\ell & V_z/\ell & 0 & 0 & 0 \\ 0 & P/\ell & V_z\xi_{avg}/\ell & V_z\eta_1/2 & -V_z\xi_1/2 & 0 & 0 & -P/\ell & -V_z\xi_{avg}/\ell & V_z\eta_2/2 & -V_z\xi_2/2 & 0 \\ 0 & 0 & (-V_y\xi_{avg}+P)/\ell & -V_y\eta_1/2 & V_y\xi_1/2 & 0 & 0 & 0 & (V_y\xi_{avg}-P)/\ell & -V_y\eta_2/2 & V_y\xi_2/2 & 0 \\ \hdashline 0 & m_{1y}/\ell & m_{1z}/\ell & 0 & 0 & 0 & 0 & -m_{1y}/\ell & -m_{1z}/\ell & 0 & 0 & 0 \\ 0 & T/\ell & -m_{1z}\xi_{avg}/\ell & -m_{1z}\eta_1/2 & m_{1z}\xi_1/2 & 0 & 0 & -T/\ell & m_{1z}\xi_{avg}/\ell & -m_{1z}\eta_2/2 & m_{1z}\xi_2/2 & 0 \\ 0 & 0 & (m_{1y}\xi_{avg}+T)/\ell & m_{1y}\eta_1/2 & -m_{1y}\xi_1/2 & 0 & 0 & 0 & (-m_{1y}\xi_{avg}-T)/\ell & m_{1y}\eta_2/2 & -m_{1y}\xi_2/2 & 0 \\ \hdashline 0 & V_y/\ell & V_z/\ell & 0 & 0 & 0 & 0 & -V_y/\ell & -V_z/\ell & 0 & 0 & 0 \\ 0 & -P/\ell & -V_z\xi_{avg}/\ell & -V_z\eta_1/2 & V_z\xi_1/2 & 0 & 0 & P/\ell & V_z\xi_{avg}/\ell & -V_z\eta_2/2 & V_z\xi_2/2 & 0 \\ 0 & 0 & (V_y\xi_{avg}-P)/\ell & V_y\eta_1/2 & -V_y\xi_1/2 & 0 & 0 & 0 & (-V_y\xi_{avg}+P)/\ell & V_y\eta_2/2 & -V_y\xi_1/2 & 0 \\ \hdashline 0 & m_{2y}/\ell & m_{2z}/\ell & 0 & 0 & 0 & 0 & -m_{2y}/\ell & -m_{2z}/\ell & 0 & 0 & 0 \\ 0 & -T/\ell & -m_{2z}\xi_{avg}/\ell & -m_{2z}\eta_1/2 & m_{2z}\xi_1/2 & 0 & 0 & T/\ell & m_{2z}\xi_{avg}/\ell & -m_{2z}\eta_2/2 & m_{2z}\xi_2/2 & 0 \\ 0 & 0 & (m_{2y}\xi_{avg}-T)/\ell & m_{2y}\eta_1/2 & -m_{2y}\xi_1/2 & 0 & 0 & 0 & (-m_{2y}\xi_{avg}+T)/\ell & m_{2y}\eta_2/2 & -m_{2y}\xi_2/2 & 0 \end{array}\right] \tag{A1.70}$$

A1.6 Implementation

The order of the rotational variables in the CR frame in Eq. (A1.1) is different from the order in Eq. (2.9). Also, the degrees of freedom of an element in the CR frame are different in both equations. Therefore, a mapping matrix $\mathbf{M}$ is needed. If both equations include the warping degree of freedom, then the relationship between two equations can be written as

$$\mathbf{q}_{n,Eq.(A1.1a)\text{ with warping }dof} = \mathbf{M}^{T}\mathbf{q}_{n,Eq.(2.6a)} \tag{A1.71}$$

or

$$\begin{Bmatrix} 0 \\ 0 \\ 0 \\ \hdashline \theta_{1x}^n \\ \theta_{1y}^n \\ \theta_{1z}^n \\ \hdashline \phi_1' \\ \hdashline e \\ 0 \\ 0 \\ \hdashline \theta_{2x}^n \\ \theta_{2y}^n \\ \theta_{2z}^n \\ \hdashline \phi_2' \end{Bmatrix}_{14\,x1} = \left[\begin{array}{cccc:c:cccc:c} 0 & & & & 0 & & & & 0 \\ 0 & & \mathbf{0}_3 & & 0 & & \mathbf{0}_3 & & 0 \\ 0 & & & & 0 & & & & 0 \\ \hdashline 0 & 1 & 0 & 0 & 0 & & & & 0 \\ 0 & 0 & 0 & 1 & 0 & & \mathbf{0}_3 & & 0 \\ 0 & 0 & 1 & 0 & 0 & & & & 0 \\ \hdashline 0 & 0 & 0 & 0 & 1 & 0 & 0 & 0 & 0 \\ \hdashline 1 & & & & 0 & & & & 0 \\ 0 & & \mathbf{0}_3 & & 0 & & \mathbf{0}_3 & & 0 \\ 0 & & & & 0 & & & & 0 \\ \hdashline 0 & & & & 0 & 1 & 0 & 0 & 0 \\ 0 & & \mathbf{0}_3 & & 0 & 0 & 0 & 1 & 0 \\ 0 & & & & 0 & 0 & 1 & 0 & 0 \\ \hdashline 0 & 0 & 0 & 0 & 0 & 0 & 0 & 0 & 1 \end{array}\right]_{14\,x9} \begin{Bmatrix} e \\ \hdashline \theta_{1x}^n \\ \theta_{1z}^n \\ \theta_{1y}^n \\ \hdashline \phi_1' \\ \hdashline \theta_{2x}^n \\ \theta_{2z}^n \\ \theta_{2y}^n \\ \hdashline \phi_2' \end{Bmatrix}_{9x1} \tag{A1.72}$$

Therefore, the element tangent stiffness matrix $\mathbf{K}_n$ with dimension 9x9 defined in Section 2.4.2 needs to be mapped to a 14x14 matrix for the projection algorithm. That is,

$$\mathbf{K}_{n,14x14} = (\mathbf{M}^T)_{14x9}\mathbf{K}_{n,9x9}\mathbf{M}_{9x14} \tag{A1.73}$$

As a result, the first term in Eq. (2.23) can be rearranged as

$$\begin{aligned} \mathbf{G}_{14x14}\mathbf{P}_{14x14}^T\mathbf{K}_{n,14x14}\mathbf{P}_{14x14}\mathbf{G}_{14x14}^T &= \mathbf{G}\mathbf{P}^T[(\mathbf{M}^T)_{14x9}\mathbf{K}_{n,9x9}\mathbf{M}_{9x14}]\mathbf{P}\mathbf{G}^T \\ &= \mathbf{G}(\mathbf{M}\mathbf{P})^T\mathbf{K}_{n,9x9}(\mathbf{M}\mathbf{P})\mathbf{G}^T \\ &= \mathbf{G}(\overline{\mathbf{P}}^T)_{14x9}\mathbf{K}_{n,9x9}\overline{\mathbf{P}}_{9x14}\mathbf{G}^T \end{aligned} \tag{A1.74}$$

in which

$$\mathbf{G}_{14x14} = \left[\begin{array}{ccc:ccc} \mathbf{E} & \mathbf{0}_3 & 0 & \mathbf{0}_3 & \mathbf{0}_3 & 0 \\ \mathbf{0}_3 & \mathbf{E} & 0 & \mathbf{0}_3 & \mathbf{0}_3 & 0 \\ \hdashline 0 & 0 & 1 & 0 & 0 & 0 \\ \hdashline \mathbf{0}_3 & \mathbf{0}_3 & 0 & \mathbf{E} & \mathbf{0} & 0 \\ \mathbf{0}_3 & \mathbf{0}_3 & 0 & \mathbf{0}_3 & \mathbf{E} & 0 \\ \hdashline 0 & 0 & 0 & 0 & 0 & 1 \end{array}\right] \tag{A1.75}$$

and

$$\overline{\mathbf{P}}_{9x14} = \begin{bmatrix} -1 & 0 & 0 & 0 & 0 & 0 & 0 & 1 & 0 & 0 & 0 & 0 & 0 & 0 \\ 0 & 0 & -\xi_{avg}/\ell & 1-\eta_1/2 & \xi_1/2 & 0 & 0 & 0 & 0 & \xi_{avg}/\ell & -\eta_2/2 & \xi_2/2 & 0 & 0 \\ 0 & 1/\ell & 0 & 0 & 0 & 1 & 0 & 0 & -1/\ell & 0 & 0 & 0 & 0 & 0 \\ 0 & 0 & -1/\ell & 0 & 1 & 0 & 0 & 0 & 0 & 1/\ell & 0 & 0 & 0 & 0 \\ 0 & 0 & 0 & 0 & 0 & 0 & 1 & 0 & 0 & 0 & 0 & 0 & 0 & 0 \\ 0 & 0 & -\xi_{avg}/\ell & -\eta_1/2 & \xi_1/2 & 0 & 0 & 1 & 0 & \xi_{avg}/\ell & 1-\eta_2/2 & \xi_2/2 & 0 & 0 \\ 0 & 1/\ell & 0 & 0 & 0 & 0 & 0 & 0 & -1/\ell & 0 & 0 & 0 & 1 & 0 \\ 0 & 0 & -1/\ell & 0 & 0 & 0 & 0 & 0 & 0 & 1/\ell & 0 & 1 & 0 & 0 \\ 0 & 0 & 0 & 0 & 0 & 0 & 0 & 0 & 0 & 0 & 0 & 0 & 0 & 1 \end{bmatrix}_{9x14}$$

(A1.76)

APPENDIX II

CROSS-SECTION TANGENT STIFFNESS MATRIX

The formulation of the open-section thin-walled beam element is provided in Chapter 2. The resulting tangent stiffness matrix for a general singly-symmetric I-section element with the consideration of the effects of nonprismatic geometry is shown in Eqs. (2.77) and (2.78). The integration of each component in the section tangent stiffness matrix is summarized in this Appendix.

Equation (2.78) is:

$$\mathbf{S}^{\mathrm{T}}\mathbf{C}\mathbf{S} = E \cdot \begin{bmatrix} 1 & & & & & \\ -y & y^2 & & & Sym. & \\ z & -yz & z^2 & & & \\ y^2+z^2 & -y(y^2+z^2) & z(y^2+z^2) & (y^2+z^2)^2 & & \\ \varpi & -y\varpi & z\varpi & (y^2+z^2)\varpi & \varpi^2 & \\ \psi & -y\psi & z\psi & (y^2+z^2)\psi & \varpi\psi & \psi^2+4G\hat{r}^2/E \end{bmatrix}$$

in which y and z are measured from the cross-section reference coordinate axis, and $\hat{y}$ and $\hat{z}$ are measured from the shear center of the cross-section. The function $\varpi(\hat{x},\hat{y},\hat{z})$ is expressed with respect to the shear center of the cross section.

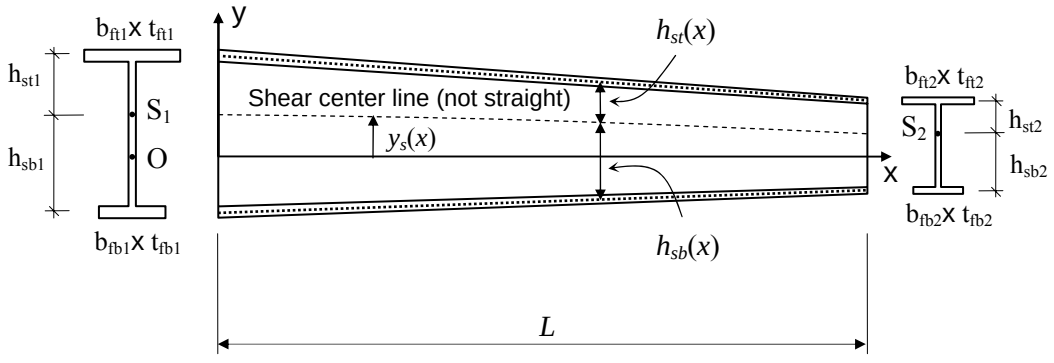

Figure A2.1 Beam element with a singly-symmetric cross-section and a general linear taper in all of its cross-section dimensions

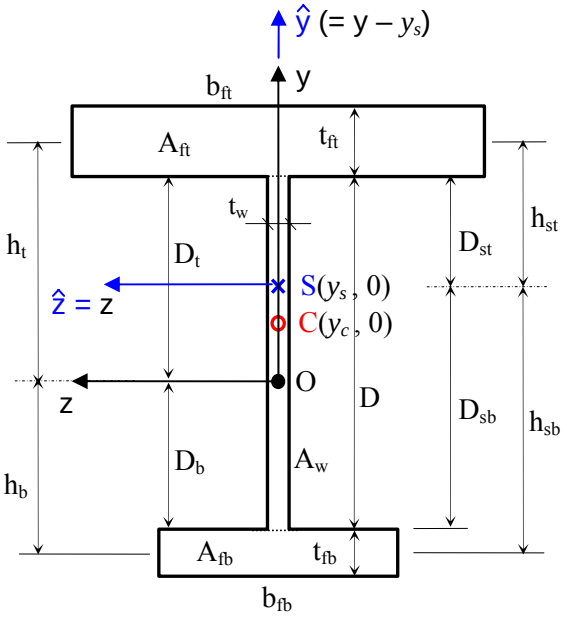

Figure A2.2 Cross Section dimensions at a general location *x*

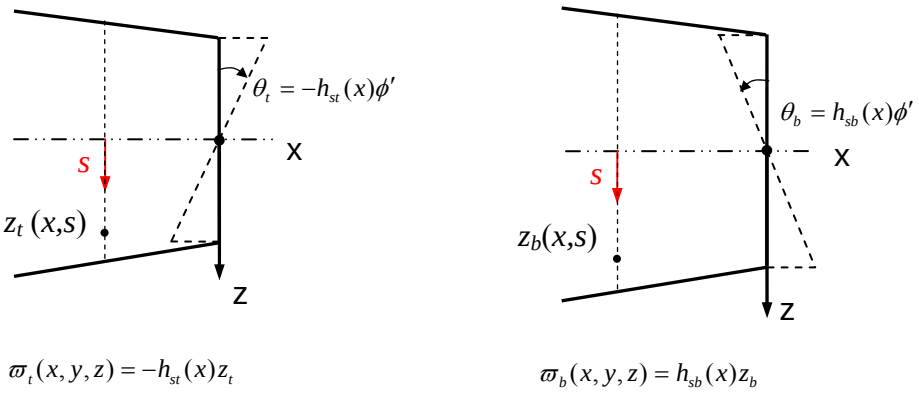

(a) Top flange

(b) Bottom flange

Figure A2.3 Warping functions in top and bottom flanges

The integration of each component in the above matrix is shown below:

(1) $k_{11} = \int_{A_o} dA = A_o$: Cross section area

(2) $k_{21} = -\int_{A_o} ydA = -\int_{A_o} (y - y_c + y_c)dA = -\int_{A_o} (y - y_c)dA - \int_{A_o} y_c dA = 0 - y_c A_o$

$= -y_c A_o$: First moment of area about the reference z axis

(3) $k_{31} = \int_{A_o} zdA = 0$

(4) $k_{22} = \int_{A_o} y^2 dA = I_{oz}$: Moment of inertia about the reference z axis

(5) $k_{33} = \int_{A_o} z^2 dA = I_{oy}$: Moment of inertia about the reference y axis

(6) $k_{32} = -\int_{A_o} yzdA = -\int_{A_o} (y - y_c + y_c)zdA = -\int_{A_o} (y - y_c)zdA - y_c \int_{A_o} zdA = 0$: Product of inertia about the reference axis

(7) $k_{41} = \int_{A_o} (y^2 + z^2)dA = I_{oy} + I_{oz}$: polar moment of inertia about the shear center

(8) $k_{42} = -\int_{A_o} y(y^2 + z^2)dA$

$= -\int_{A_o} y^3 dA$ (8a)

$-\int_{A_o} yz^2 dA$ (8b)

(8a) $-\int_{A_o} y^3 dA$

$= -\int_{A_{ft}} y^3 dzdy - \int_{A_{fb}} y^3 dzdy - \int_{A_w} y^3 dzdy$

$= -\int_{D_t}^{D_t + t_{ft}} \int_{-\frac{1}{2}b_{ft}}^{\frac{1}{2}b_{ft}} y^3 dzdy - \int_{-D_b - t_{fb}}^{-D_b} \int_{-\frac{1}{2}b_{fb}}^{\frac{1}{2}b_{fb}} y^3 dzdy - \int_{-D_b}^{D_t} \int_{-\frac{1}{2}t_w}^{\frac{1}{2}t_w} y^3 dzdy$

$= -\frac{b_{ft}}{4}\left[(D_t + t_{ft})^4 - D_t^4\right] - \frac{b_{fb}}{4}\left[D_b^4 - (D_b + t_{fb})^4\right] - \frac{t_w}{4}(D_t^4 - D_b^4)$

$$= -\frac{b_{ft}}{4}\left[(D_t + t_{ft})^2 + D_t^{\,2}\right]\left[(D_t + t_{ft}) + D_t\right]\left[(D_t + t_{ft}) - D_t\right]$$
$$+ \frac{b_{fb}}{4}\left[D_b^{\,2} + (D_b + t_{fb})^2\right]\left[D_b + (D_b + t_{fb})\right]\left[D_b - (D_b + t_{fb})\right]$$
$$- \frac{t_w}{4}\left[D_t^{\,2} + D_b^{\,2}\right]\left[D_t + D_b\right]\left[D_t - D_b\right]$$

(8b) $-\int_{A_o} yz^2 dA$

$$= -\int_{A_{ft}} yz^2 dzdy - \int_{A_{fb}} yz^2 dzdy - \int_{A_w} yz^2 dzdy$$
$$= -\int_{D_t}^{D_t + t_{ft}} \int_{-\frac{1}{2}b_{ft}}^{\frac{1}{2}b_{ft}} yz^2 dzdy - \int_{-D_b - t_{fb}}^{-D_b} \int_{-\frac{1}{2}b_{fb}}^{\frac{1}{2}b_{fb}} yz^2 dzdy - \int_{-D_b}^{D_t} \int_{-\frac{1}{2}t_w}^{\frac{1}{2}t_w} yz^2 dzdy$$
$$= -\frac{1}{3}\left(\frac{b_{ft}^{\,3}}{8} + \frac{b_{ft}^{\,3}}{8}\right)\frac{1}{2}\left[(D_t + t_{ft})^2 - D_t^{\,2}\right] - \frac{1}{3}\left(\frac{b_{fb}^{\,3}}{8} + \frac{b_{fb}^{\,3}}{8}\right)\frac{1}{2}\left[D_b^{\,2} - (D_b + t_{fb})^2\right]$$
$$- \frac{1}{3}\left(\frac{t_w^{\,3}}{8} + \frac{t_w^{\,3}}{8}\right)\frac{1}{2}\left(D_t^{\,2} - D_b^{\,2}\right)$$
$$= -\frac{t_{ft} b_{ft}^{\,3}}{24}(2D_t + t_{ft}) + \frac{t_{fb} b_{fb}^{\,3}}{24}(2D_b + t_{fb}) - \frac{D t_w^{\,3}}{24}(D_t - D_b)$$

$$k_{42} = -\left[A_{ft}\left(D_t^{\,2} + D_t t_{ft} + \frac{t_{ft}^{\,2}}{2}\right)\left(D_t + \frac{t_{ft}}{2}\right) - A_{fb}\left(D_b^{\,2} + D_b t_{fb} + \frac{t_{fb}^{\,2}}{2}\right)\left(D_b + \frac{t_{fb}}{2}\right)\right.$$
$$\left. + A_w\left(\frac{D_t^{\,2} + D_b^{\,2}}{2}\right)\left(\frac{D_t - D_b}{2}\right) + I_{ft}\left(D_t + \frac{t_{ft}}{2}\right) - I_{fb}\left(D_b + \frac{t_{fb}}{2}\right) + I_{w,y}\left(\frac{D_t - D_b}{2}\right)\right]$$

(9) $k_{43} = \int_{A_o} z(y^2 + z^2) dA = \int_{A_o} zy^2 dA + \int_{A_o} z^3 dA = 0$

(10) $k_{44} = \int_{A_o} (y^2 + z^2)^2 dA = \int_{A_{ft}} (y^2 + z^2)^2 dA + \int_{A_{fb}} (y^2 + z^2)^2 dA + \int_{A_w} (y^2 + z^2)^2 dA$

$$= \int_{D_t}^{D_t + t_{ft}} \int_{-\frac{1}{2}b_{ft}}^{\frac{1}{2}b_{ft}} (y^4 + 2y^2 z^2 + z^4) dzdy \qquad \text{(10a)}$$

$$+ \int_{-D_b - t_{fb}}^{-D_b} \int_{-\frac{1}{2}b_{fb}}^{\frac{1}{2}b_{fb}} (y^4 + 2y^2 z^2 + z^4) dzdy \qquad \text{(10b)}$$

$$+\int_{-D_b}^{D_t}\int_{-\frac{1}{2}t_w}^{\frac{1}{2}t_w}(y^4+2y^2z^2+z^4)dzdy \qquad (10c)$$

(10a) $\int_{D_t}^{D_t+t_{ft}}\int_{-\frac{1}{2}b_{ft}}^{\frac{1}{2}b_{ft}}(y^4+2y^2z^2+z^4)dzdy=\int_{D_t}^{D_t+t_{ft}}\int_{-\frac{1}{2}b_{ft}}^{\frac{1}{2}b_{ft}}y^4dzdy+2\int_{D_t}^{D_t+t_{ft}}\int_{-\frac{1}{2}b_{ft}}^{\frac{1}{2}b_{ft}}y^2z^2dzdy+\int_{D_t}^{D_t+t_{ft}}\int_{-\frac{1}{2}b_{ft}}^{\frac{1}{2}b_{ft}}z^4dzdy$

$$=\frac{b_{ft}}{5}\left[(D_t+t_{ft})^5-D_t^5\right]+\frac{2}{3}\left(\frac{b_{ft}^3}{8}+\frac{b_{ft}^3}{8}\right)\frac{1}{3}\left[(D_t+t_{ft})^3-D_t^3\right]+\frac{1}{5}\left(\frac{b_{ft}^5}{32}+\frac{b_{ft}^5}{32}\right)\left[(D_t+t_{ft})-D_t\right]$$

$$=\frac{b_{ft}}{5}\left[(D_t+t_{ft})^5-D_t^5\right]+\frac{b_{ft}^3}{18}\left[(D_t+t_{ft})^3-D_t^3\right]+\frac{b_{ft}^5t_{ft}}{80}$$

(10b) $\int_{-D_b-t_{fb}}^{-D_b}\int_{-\frac{1}{2}b_{fb}}^{\frac{1}{2}b_{fb}}(y^4+2y^2z^2+z^4)dzdy=\int_{-D_b-t_{fb}}^{-D_b}\int_{-\frac{1}{2}b_{fb}}^{\frac{1}{2}b_{fb}}y^4dzdy+2\int_{-D_b-t_{fb}}^{-D_b}\int_{-\frac{1}{2}b_{fb}}^{\frac{1}{2}b_{fb}}y^2z^2dzdy+\int_{-D_b-t_{fb}}^{-D_b}\int_{-\frac{1}{2}b_{fb}}^{\frac{1}{2}b_{fb}}z^4dzdy$

$$=\frac{b_{fb}}{5}\left[(D_b+t_{fb})^5-D_b^5\right]+\frac{2}{3}\left(\frac{b_{fb}^3}{8}+\frac{b_{fb}^3}{8}\right)\frac{1}{3}\left[(D_b+t_{fb})^3-D_b^3\right]+\frac{1}{5}\left(\frac{b_{fb}^5}{32}+\frac{b_{fb}^5}{32}\right)\left[(D_b+t_{fb})-D_b\right]$$

$$=\frac{b_{fb}}{5}\left[(D_b+t_{fb})^5-D_b^5\right]+\frac{b_{fb}^3}{18}\left[(D_b+t_{fb})^3-D_b^3\right]+\frac{b_{fb}^5t_{fb}}{80}$$

(10c) $\int_{-D_b}^{D_t}\int_{-\frac{1}{2}t_w}^{\frac{1}{2}t_w}(y^4+2y^2z^2+z^4)dzdy=\int_{-D_b}^{D_t}\int_{-\frac{1}{2}t_w}^{\frac{1}{2}t_w}y^4dzdy+2\int_{-D_b}^{D_t}\int_{-\frac{1}{2}t_w}^{\frac{1}{2}t_w}y^2z^2dzdy+\int_{-D_b}^{D_t}\int_{-\frac{1}{2}t_w}^{\frac{1}{2}t_w}z^4dzdy$

$$=\frac{t_w}{5}\left(D_t^5+D_b^5\right)+\frac{2}{3}\left(\frac{t_w^3}{8}+\frac{t_w^3}{8}\right)\frac{1}{3}\left(D_t^3+D_b^3\right)+\frac{1}{5}\left(\frac{t_w^5}{32}+\frac{t_w^5}{32}\right)\left(D_t+D_b\right)$$

$$=\frac{t_w}{5}\left(D_t^5+D_b^5\right)+\frac{t_w^3}{18}\left(D_t^3+D_b^3\right)+\frac{t_w^5D}{80}$$

Based on $\varpi_t=-h_{st}(x)\hat{z}=-h_{st}z$ and $\varpi_b=h_{sb}(x)\hat{z}=h_{sb}z$

(11) $k_{51}=\int_{A_o}\varpi dA=\int_{A_{ft}}\varpi_t dA+\int_{A_{fb}}\varpi_b dA=0$

(12) $k_{52}=-\int_{A_o}y\varpi dA=-\int_{A_{ft}}y\varpi_t dA-\int_{A_{fb}}y\varpi_b dA$

$$=-\int_{D_{st}}^{D_{st}+t_{ft}}\int_{-\frac{b_{ft}}{2}}^{\frac{b_{ft}}{2}}(\hat{y}+y_s)(-h_{st}z)dzd\hat{y}-\int_{-D_{sb}-t_{fb}}^{-D_{sb}}\int_{-\frac{b_{fb}}{2}}^{\frac{b_{fb}}{2}}(\hat{y}+y_s)(h_{sb}z)dzd\hat{y}=0$$

(13) $k_{53}=\int_{A_o}z\varpi dA=\int_{A_{ft}}z\varpi_t dA+\int_{A_{fb}}z\varpi_b dA$

$$= \int_{D_{st}}^{D_{st}+t_{ft}} \int_{-\frac{b_{ft}}{2}}^{\frac{b_{ft}}{2}} (-h_{st} z) z dz d\hat{y} + \int_{-D_{sb}-t_{fb}}^{-D_{sb}} \int_{-\frac{b_{fb}}{2}}^{\frac{b_{fb}}{2}} (h_{sb} z) z dz d\hat{y}$$

$$= -h_{st} I_{ft} + h_{sb} I_{fb} = 0$$

(14) $$k_{54} = \int_{A_o} (y^2 + z^2) \varpi dA = \int_{A_{ft}} (y^2 + z^2) \varpi_t dA + \int_{A_{fb}} (y^2 + z^2) \varpi_b dA$$

$$= \int_{A_{ft}} (y^2 + z^2)(-h_{st} z) dA + \int_{A_{fb}} (y^2 + z^2)(h_{sb} z) dA = 0$$

(15) $$k_{55} = \int_{A_o} \varpi^2 dA = \int_{A_{ft}} (-h_{st} z)^2 dA + \int_{A_{fb}} (h_{sb} z)^2 dA$$

$$= h_{st}{}^2 \int_{D_{st}}^{D_{st}+t_{ft}} \int_{-\frac{b_{ft}}{2}}^{\frac{b_{ft}}{2}} (-z)^2 dz dy + h_{sb}{}^2 \int_{-D_{sb}-t_{fb}}^{-D_{sb}} \int_{-\frac{b_{fb}}{2}}^{\frac{b_{fb}}{2}} z^2 dz dy$$

$$= h_{st}{}^2 I_{ft} + h_{sb}{}^2 I_{fb} = C_w$$

The ψ function at the top flange is:

$$\begin{aligned} \psi_t(x, y, z) &= \varpi_t'(x, \hat{y}, z) - y'z + z'y \\ &= (-h_{st} z)' - (h_{st}' + y_s')z + (h_{st} + y_s)z' \\ &= -h_{st}' z - h_{st} z' - h_{st}' z - y_s' z + h_{st} z' + y_s z' \\ &= (-2h_{st}' - y_s')z + y_s z' \end{aligned}$$

The ψ function at the bottom flange is:

$$\begin{aligned} \psi_b(x, y, z) &= \varpi_b'(x, \hat{y}, z) - y'z + z'y \\ &= (h_{sb} z_b)' - (-h_{sb}' + y_s')z + (-h_{sb} + y_s)z' \\ &= h_{sb}' z + h_{sb} z' + h_{sb}' z - y_s' z - h_{sb} z' + y_s z' \\ &= (2h_{sb}' - y_s')z + y_s z' \end{aligned}$$

For a tapered flange,

$$z(x, s) = b_f(x) \cdot s = \left(\frac{b_{f,2} - b_{f,1}}{2L} x \right) \cdot s = \frac{b_f'}{2} xs$$

and

$$z' = \frac{b_f'}{2} s = \frac{b_f'}{2} \cdot \left(\frac{2z}{b_{f,i}} \right) = \frac{b_f'}{b_{f,i}} z$$

in which $b_{f,2}$ is the flange width at $x = L$ (L is the element length) and $b_{f,1}$ is the flange width at $x = 0$, $b_{f,i}$ is the flange with at $x = x_i$, ($0 \le x \le L$) and b'_f is the rate of the width change of the flange along the length. Therefore, the ψ functions can be written as

$$\psi_t(x, y, z) = R_t z$$

and

$$\psi_b(x, y, z) = R_b z$$

in which

$$R_t = R_t(x) = -2h'_{st}(x) - y'_s(x) + y_s(x)\frac{b'_{ft}}{b_{ft}(x)}$$

and

$$R_b = R_b(x) = 2h'_{sb}(x) - y'_s(x) + y_s(x)\frac{b'_{fb}}{b_{fb}(x)}$$

$$(16)\ k_{61} = \int_{A_o} \psi dA = \int_{A_{ft}} \psi_t dA + \int_{A_{fb}} \psi_b dA$$

$$= \int_{A_{ft}} R_t z dA + \int_{A_{fb}} R_b z dA$$

$$= 0$$

$$(17)\ k_{62} = \int_{A_o} -y\psi dA = -\int_{A_{ft}} y\psi_t dA - \int_{A_{fb}} y\psi_b dA$$

$$= -\int_{A_{ft}} yR_t z dA - \int_{A_{fb}} yR_b z dA$$

$$= -R_t \int_{A_{ft}} yz dA - R_b \int_{A_{fb}} yz dA$$

$$= 0$$

$$(18)\ k_{63} = \int_{A_o} z\psi dA = \int_{A_{ft}} z\psi_t dA + \int_{A_{fb}} z\psi_b dA$$

$$= \int_{A_{ft}} zR_t z dA + \int_{A_{fb}} zR_b z dA$$

$$= R_t \int_{A_{ft}} z^2 dA + R_b \int_{A_{fb}} z^2 dA$$

$$= R_t I_{ft} + RI_{fb}$$

(19) $k_{64} = \int_{A_o} (y^2 + z^2)\psi dA = \int_{A_{ft}} (y^2 + z^2)\psi_t dA + \int_{A_{fb}} (y^2 + z^2)\psi_b dA$

$$= \int_{A_{ft}} (y^2 + z^2) R_t z dA + \int_{A_{fb}} (y^2 + z^2) R_b z dA$$
$$= 0$$

(20) $k_{65} = \int_{A_o} \varpi\psi \, dA = \int_{A_{ft}} \varpi_t \psi_t dA + \int_{A_{fb}} \varpi_b \psi_b dA$

$$= \int_{A_{ft}} (-h_{st} z) R_t z dA + \int_{A_{fb}} (h_{sb} z) R_b z dA$$
$$= -h_{st} R_t \int_{A_{ft}} z^2 dA + h_{sb} R_b \int_{A_{fb}} z^2 dA$$
$$= -h_{st} R_t I_{ft} + h_{sb} R_b I_{fb}$$

(21) $k_{66} = \int_{A_o} \psi^2 dA + \frac{1}{E} \int_{A_o} 4G\hat{r}^2 dA = \int_{A_{ft}} {\psi_t}^2 dA + \int_{A_{fb}} {\psi_b}^2 dA + \frac{GJ}{E}$

$$= \int_{A_{ft}} (R_t z)^2 dA + \int_{A_{fb}} (R_b z)^2 dA + \frac{GJ}{E}$$
$$= {R_t}^2 I_{ft} + {R_b}^2 I_{fb} + \frac{GJ}{E}$$

Based on the above calculation, the section tangent stiffness matrix is summarized as:

$$\mathbf{k} = \begin{bmatrix} EA_o & & \ddots & & & \\ -EA_o y_c & EI_{oz} & & Sym & & \\ 0 & 0 & EI_{oy} & & \ddots & \\ E(I_{oy} + I_{oz}) & k_{42} & 0 & k_{44} & & \\ 0 & 0 & 0 & 0 & EC_w & \\ 0 & 0 & R_t EI_{ft} + R_b EI_{fb} & 0 & -R_t h_{st} EI_{ft} + R_b h_{sb} EI_{fb} & {R_t}^2 EI_{ft} + {R_b}^2 EI_{fb} + GJ \end{bmatrix}$$

APPENDIX III

THE FORD CITY BRIDGE STEEL ERECTION SIMULATION – DETAIL SUMMARY AND ANALYSIS RESULTS

Table A3.1 Description of steps in the steel erection stage 1

Step	Description
1	Raise G3-FS1 using lifting crane CRANE13
2	Apply G3-FS1 selfweight
3	Position G3-FS1 and CRANE13 on its supports, abutment 1 (ABUT-1) and falsework 1 (FW-1)
4	Seat G3-FS1 on ABUT-1 and FW-1
5	Replace vertifcal restraints at G3 ABUT-1 and FW-1 by gap elements Set G3-FS1 web plumb at ABUT-1
6	Attach CF-1C to G3-FS1
7	Attach CF-7B to G3-FS1
8	Attach CF-7C to G3-FS1
9	Attach CF-7C to G3-FS1
10	Tie down CF-1C and CF1-7C Remove CRANE13
11	Apply 1/2 CF-1B, CF-1C and CF-7B, CF-7C weight to G3-FS1
12	Raise G2-FS1 using lifting crane CRANE12
13	Apply G2-FS1 selfweight
14	Position G2-FS1 and CRANE12 on its supports ABUT-1 and FW-1
15	Seat G2-FS1 on ABUT-1 and FW-1
16	Replace vertifcal restraints at G2 ABUT-1 and FW-1 by gap elements *Connect CF-1B bottom chord to G2-FS1*
17	**Remove artificial springs on CRANE12** Connect CF-1B top chord to G2-FS1
18	Apply 1/2 CF-1B weight to G2-FS1
19	Connect CF-7B Bottom chord to G2-FS1
20	Connect CF-7B top chord to G2-FS1
21	Remove Tie down at CF-1C and CF1-7C Apply 1/2 CF-7B weight to G2-FS1
22	Attach CF-4B to G3-FS1

Table A3.1 Description of steps in the steel erection stage 1 (continued)

Step	Description
23	Connect CF-4B top chord to G2-FS1
24	Connect CF-4B bottom chord to G2-FS1
25	Lower G2-FS1 for contacting the FW-1
26	Remove CRANE12
27	Apply CF-4B weight to G2-FS1 and G3-FS1
28	Raise G4-FS1 using lifting crane CRANE14
29	Apply G4-FS1 selfweight
30	Position G4-FS1 and CRANE14 on its supports ABUT-1 and FW-1
31	Seat G4-FS1 on ABUT-1 and FW-1
32	Replace vertical restraints at G4 ABUT-1 and FW-1 by gap elements *Connect CF-1C bottom chord to G4-FS1*
33	**Remove artificial springs on CRANE14** Connect CF-1C top chord to G4-FS1
34	Apply 1/2 CF-1C weight to G4
35	Connect CF-7C bottom chord to G4-FS1
36	Connect CF-7C top chord to G4-FS1
37	Apply 1/2 CF-1C weight to G4-FS1 Remove restraints at G4 ABUT-1 (longitudinal and radial) and FW1 (radial)
38	Attach CF-4C to G3
39	Connect CF-4C top chord to G4-FS1
40	Connect CF-4C bottom chord to G4-FS1
41	Remove CRANE14
42	Apply 1/2 CF-7B weight to G3-FS1 and G4-FS1
43	Attach CF-1A to G2-FS2
44	Apply 1/2 CF-1A weight to G2
45	Raise G1-FS1 using lifting crane CRANE11
46	Apply G1-FS1 selfweight
47	Position G1-FS1 and CRANE11 on its supports ABUT-1 and FW-1
48	Seat G1-FS1 on ABUT-1 and FW-1
49	Replace vertical restraints at G1 ABUT-1 and FW-1 by gap elements *Connect CF-1A bottom chord to G1-FS1*
50	**Remove artificial springs on CRANE11** Connect CF-1A top chord to G1-FS1

Table A3.1 Description of steps in the steel erection stage 1 (continued)

Step	Description
51	Apply 1/2 CF-1A weight to G1-FS1
52	Attach CF-4A to G2-FS1
53	Connect CF-4A top chord to G1-FS1
54	Connect CF-4A bottom chord to G1-FS1
55	Apply 1/2 CF-4A weight to G1-FS1 and G2-FS1
56	Attach CF1-7A to G2-FS1
57	Connect CF-7A top chord to G1-FS1
58	Connect CF-7A bottom chord to G1-FS1
59	Remove CRANE11
60	Apply 1/2 CF-7A weight to G1-FS1 and G2-FS1

Table A3.2 Description of steps in the steel erection stage 2

Step	Description
61	*Raise G3-FS2 using lifting crane CRANE23 (no artificial spring)*
62	*Position G3-FS2 and CRANE23 such that the translational and rotational continuity between G3-FS2 and G3-FS1 is achieved at field splice 1*
63	*Apply bi-moment for warping continuity at G3 field splice 1*
64	*Seat G3-FS2 on FW-2* *Replace vertical restraint at G3 FW2 a gap element*
65	*Seat G3-FS2 on FW-2A* *Replace vertical restraint at G3 FW2A a gap element*
66	Apply G3-FS2 selfweight
67	Attach CF-11B to G3-FS2
68	Attach CF-14B to G3-FS2
69	Attach CF-11C to G3-FS2
70	Attach CF-14C to G3-FS2
71	Tie down CF-11C and CF1-14C Remove CRANE23
72	Apply 1/2 CF-11B, CF-11C and CF-14B, CF-14C weight to G3-FS2
73	*Raise G2-FS2 using lifting crane CRANE22 (no artificial spring)*
74	*Position G2-FS2 and CRANE22 such that the translational and rotational continuity between G2-FS2 and G2-FS1 is achieved at field splice 1*
75	*Apply bi-moment for warping continuity at G2 field splice 1*
76	*Seat G2-FS2 on FW-2* *Replace vertical restraint at G2 FW2 a gap element*
77	*Seat G2-FS2 on FW-2A* *Replace vertical restraint at G2 FW2A a gap element*
78	Apply G2-FS2 selfweight
79	Remove tie down at CF-11C Connect CF-11B bottom chord to G2-FS2
80	Connect CF-11B top chord to G2-FS2
81	Remove tie down at CF-14C Apply 1/2 CF-11B weight to G2-FS2
82	Connect CF-14B top chord to G2-FS2
83	Connect CF-14B bottom chord to G2-FS2
84	Apply 1/2 CF-14B weight to G2-FS2
85	Attach CF-8B to G3-FS2
86	Connect CF-8B top chord to G2-FS2

Table A3.2 Description of steps in the steel erection stage 2 (continued)

Step	Description
87	Connect CF-8B bottom chord to G2-FS2
88	Apply 1/2 CF-8B weight to G2-FS2 and G3-FS2
89	Attach CF-9B to G3-FS2
90	Connect CF-9B top chord to G2-FS2
91	Connect CF-9B bottom chord to G2-FS2
92	Apply 1/2 CF-9B weight to G2-FS2 and G3-FS2
93	Attach CF-10B to G3-FS2
94	Connect CF-10B top chord to G2-FS2
95	Connect CF-10B bottom chord to G2-FS2
96	Apply 1/2 CF-10B weight to G2-FS2 and G3-FS2
97	Attach CF-12B to G3-FS2
98	Connect CF-12B top chord to G2-FS2
99	Connect CF-12B bottom chord to G2-FS2
100	Apply 1/2 CF-12B weight to G2-FS2 and G3-FS2
101	Attach CF-13B to G3-FS2
102	Connect CF-13B top chord to G2-FS2
103	Connect CF-13B bottom chord to G2-FS2
104	Apply 1/2 CF-13B weight to G2-FS2 and G3-FS2
105	Attach CF-15B to G3-FS2
106	Connect CF-15B top chord to G2-FS2
107	Connect CF-15B bottom chord to G2-FS2
108	Apply 1/2 CF-15B weight to G2-FS2 and G3-FS2
109	Attach CF-16B to G3-FS2
110	Connect CF-16B top chord to G2-FS2
111	Connect CF-16B bottom chord to G2-FS2
112	Remove CRANE22
113	Apply 1/2 CF-16B weight to G2-FS2 and G3-FS2
114	*Raise G4-FS2 using lifting crane CRANE24 (no artificial spring)*
115	*Position G4-FS2 and CRANE24 such that the translational and rotational continuity between G4-FS2 and G4-FS1 is achieved at field splice 1*
116	*Apply bi-moment for warping continuity at G4 field splice 1*
117	Add a gap element between G4-FS2 and FW2 Add a gap element between G4-FS2 and FW2A Apply G4-FS2 selfweight

Table A3.2 Description of steps in the steel erection stage 2 (continued)

Step	Description
118	Seat G4-FS2 on FW-2A (No effect on seating G4-FS2 on FW-2, so, skip)
119	Connect CF-11C top chord to G4-FS2
120	Connect CF-11C bottom chord to G4-FS2
121	Apply 1/2 CF-11C weight to G4-FS2
122	Connect CF-14C top chord to G4-FS2
123	Connect CF-14C bottom chord to G4-FS2
124	Apply 1/2 CF-14C weight to G4-FS2
125	Attach CF-8C to G3-FS2
126	Connect CF-8C top chord to G4-FS2
127	Connect CF-8C bottom chord to G4-FS2
128	Apply 1/2 CF-8C weight to G3-FS2 and G4-FS2
129	Attach CF-9C to G3-FS2
130	Connect CF-9C top chord to G4-FS2
131	Connect CF-9C bottom chord to G4-FS2
132	Apply 1/2 CF-9C weight to G4-FS2 and G3-FS2
133	Attach CF-10C to G3-FS2
134	Connect CF-10C top chord to G4-FS2
135	Connect CF-10C bottom chord to G4-FS2
136	Apply 1/2 CF-10C weight to G4-FS2 and G3-FS2
137	Attach CF-12C to G3-FS2
138	Connect CF-12C top chord to G4-FS2
139	Connect CF-12C bottom chord to G4-FS2
140	Apply 1/2 CF-12C weight to G4-FS2 and G3-FS2
141	Attach CF-13C to G3-FS2
142	Connect CF-13C top chord to G4-FS2
143	Connect CF-13C bottom chord to G4-FS2
144	Apply 1/2 CF-13C weight to G4-FS2 and G3-FS2
145	Attach CF-15C to G3-FS2
146	Connect CF-15C top chord to G4-FS2
147	Connect CF-15C bottom chord to G4-FS2
148	Apply 1/2 CF-15C weight to G4-FS2 and G3-FS2
149	Attach CF-16C to G3-FS2
150	Connect CF-16C top chord to G4-FS2

Table A3.2 Description of steps in the steel erection stage 2 (continued)

Step	Description
151	Connect CF-16C bottom chord to G4-FS2
152	Remove CRANE24
153	Apply 1/2 CF-16C weight to G3-FS2 and G4-FS2
154	*Raise G1-FS2 using lifting crane CRANE21 (no artificial spring)*
155	*Position G1-FS2 and CRANE21 such that the translational and rotational continuity between G1-FS2 and G1-FS1 is achieved at field splice 1*
156	*Apply bi-moment for warping continuity at G2 field splice 1*
157	*Seat G1-FS2 on FW-2* *Replace vertical restraint at G1 FW2 a gap element*
158	*Seat G1-FS2 on FW-2A* *Replace vertical restraint at G1 FW2A a gap element*
159	Apply G1-FS2 selfweight
160	Attach CF-11A to G2-FS2
161	Connect CF-11A bottom chord to G1-FS2
162	Connect CF-11A top chord to G1-FS2
163	Apply 1/2 CF-11A weight to G1-FS2 and G2-FS2
164	Attach CF-14A to G2-FS2
165	Connect CF-14A top chord to G1-FS2
166	Connect CF-14A bottom chord to G1-FS2
167	Apply 1/2 CF-14A weight to G1-FS2 and G2-FS2
168	Attach CF-8A to G2-FS2
169	Connect CF-8A top chord to G1-FS2
170	Connect CF-8A bottom chord to G1-FS2
171	Apply 1/2 CF-8A weight to G1-FS2 and G2-FS2
172	Attach CF-9A to G2-FS2
173	Connect CF-9A top chord to G1-FS2
174	Connect CF-9A bottom chord to G1-FS2
175	Apply 1/2 CF-9A weight to G1-FS2 and G2-FS2
176	Attach CF-10A to G2-FS2
177	Connect CF-10A top chord to G1-FS2
178	Connect CF-10A bottom chord to G1-FS2
179	Apply 1/2 CF-10A weight to G1-FS2 and G2-FS2
180	Attach CF-12A to G2-FS2
181	Connect CF-12A top chord to G1-FS2

Table A3.2 Description of steps in the steel erection stage 2 (continued)

Step	Description
182	Connect CF-12A bottom chord to G1-FS2
183	Apply 1/2 CF-12A weight to G1-FS2 and G2-FS2
184	Attach CF-13A to G2-FS2
185	Connect CF-13A top chord to G1-FS2
186	Connect CF-13A bottom chord to G1-FS2
187	Apply 1/2 CF-13A weight to G1-FS2 and G2-FS2
188	Attach CF-15A to G2-FS2
189	Connect CF-15A top chord to G1-FS2
190	Connect CF-15A bottom chord to G1-FS2
191	Apply 1/2 CF-15A weight to G1-FS2 and G2-FS2
192	Attach CF-16A to G2-FS2
193	Connect CF-16A top chord to G1-FS2
194	Connect CF-16A bottom chord to G1-FS2
195	Remove CRANE21
196	Apply 1/2 CF-16A weight to G1-FS2 and G2-FS2

Table A3.3 Description of steps in the steel erection stage 3

Step	Description
197	Raise G3-FS4 using lifting crane CRANE43
198	Apply G3-FS4 selfweight
199	Position G3-FS4 and CRANE43 on its supports, Pier 1 and Pier bracket 1 (BK-1)
200	Seat G3-FS4 on Pier 1 and BK-1
201	Release translational artificial springs on CRANE43 Replace vertical restraints at G3 Pier-1 and BK-1 by gap elements
202	Attach CF-27B to G3-FS4
203	Attach CF-27C to G3-FS4
204	Attach CF-26B to G3-FS4
205	Attach CF-28B to G3-FS4
206	Tie down CF-26B and CF1-28B Remove CRANE43
207	Apply 1/2 CF-26B, CF-27B and CF-28B, CF-27C weight to G3-FS4
208	Raise G2-FS4 using lifting crane CRANE42
209	Apply G2-FS4 selfweight
210	Position G2-FS4 and CRANE42 on its supports, Pier 1 and BK-1
211	Seat G2-FS4 on Pier 1 and BK-1
212	Release translational artificial springs on CRANE42
213	*Connect CF-27B bottom chord to G2-FS4*
214	*Connect CF-27B top chord to G2-FS4*
215	Remove tie down at CF-26B **Remove artificial springs on CRANE42** Apply 1/2 CF-27B weight to G2-FS4
216	Connect CF-26B top chord to G2-FS4
217	Connect CF-26B bottom chord to G2-FS4
218	Remove tie down at CF-28B Apply 1/2 CF-28B weight to G2-FS4
219	Connect CF-28B top chord to G2-FS4
220	Connect CF-28B bottom chord to G2-FS4
221	Replace vertical restraints at G2 Pier-1 and BK-1 by gap elements Apply 1/2 CF-28B weight to G2-FS4
222	Attach CF-25B to G3-FS4
223	Connect CF-25B top chord to G2-FS4

Table A3.3 Description of steps in the steel erection stage 3 (continued)

Step	Description
224	Connect CF-25B bottom chord to G2-FS4
225	Lower G2-FS4 for contacting the BK-1
226	Remove CRANE42
227	Apply 1/2 CF-25B weight to G2-FS4 and G3-FS4
228	Attach CF-24B to G3-FS4
229	Connect CF-24B top chord to G2-FS4
230	Connect CF-24B bottom chord to G2-FS4
231	Apply 1/2 CF-24B weight to G2-FS4 and G3-FS4
232	Attach CF-23B to G3-FS4
233	Connect CF-23B top chord to G2-FS4
234	Connect CF-23B bottom chord to G2-FS4
235	Apply 1/2 CF-23B weight to G2-FS4 and G3-FS4
236	Attach CF-29B to G3-FS4
237	Connect CF-29B top chord to G2-FS4
238	Connect CF-29B bottom chord to G2-FS4
239	Apply 1/2 CF-29B weight to G2-FS4 and G3-FS4

Table A3.4 Description of steps in the steel erection stage 4

Step	Description
240	Raise G3-FS3 using lifting crane CRANE33
241	Apply G3-FS3 selfweight
242	Position G3-FS3 and CRANE33 such that the translational and rotational continuity between G3-FS3 and G3-FS4 is achieved at field splice 3
243	*Apply bi-moment for warping continuity at G3 field splice 3*
244	**Release artificial springs on CRANE33**
245	Achieve translational continuity (pinned connection at G3-FS2 and G3-FS3 top flange (field splice 2)
246	Adjust G3-FS3 elevation for achieving bottom flange translational continuity at field splice 2
247	Achieve G3 bottom flange translational continuity at field splice 2
248	Achieve G3 rotational continuity at field splice 2
249	Achieve G3 warping continuity at field splice 2
250	Raise G2-FS3 using lifting crane CRANE32
251	Apply G2-FS3 selfweight
252	Position G2-FS3 and CRANE32 such that the translational and rotational continuity between G2-FS3 and G2-FS4 is achieved at field splice 3
253	*Apply bi-moment for warping continuity at G2 field splice 3*
254	**Release artificial springs on CRANE32**
255	Achieve translational continuity (pinned connection at G2-FS2 and G2-FS3 top flange (field splice 2)
256	Adjust G2-FS3 elevation for achieving bottom flange translational continuity at field splice 2
257	Attach CF-17B to G3-FS3
258	Connect CF-17B top chord to G2-FS3
259	Connect CF-17B bottom chord to G2-FS3
260	Apply 1/2 CF-17B weight to G2-FS3 and G3-FS3
261	Attach CF-18B to G3-FS3
262	Connect CF-18B top chord to G2-FS3
263	Connect CF-18B bottom chord to G2-FS3
264	Apply 1/2 CF-18B weight to G2-FS3 and G3-FS3
265	Attach CF-19B to G3-FS3
266	Connect CF-19B top chord to G2-FS3
267	Connect CF-19B bottom chord to G2-FS3
268	Apply 1/2 CF-19B weight to G2-FS3 and G3-FS3

Table A3.4 Description of steps in the steel erection stage 4 (continued)

Step	Description
269	Achieve G2 bottom flange translational continuity at field splice 2
270	Achieve G2 rotational continuity at field splice 2
271	Achieve G2 warping continuity at field splice 2
272	Attach CF-22B to G3-FS3
273	Connect CF-22B top chord to G2-FS3
274	Connect CF-22B bottom chord to G2-FS3
275	Apply 1/2 CF-22B weight to G2-FS3 and G3-FS3
276	Attach CF-20B to G3-FS3
277	Connect CF-20B top chord to G2-FS3
278	Connect CF-20B bottom chord to G2-FS3
279	Apply 1/2 CF-20B weight to G2-FS3 and G3-FS3
280	Attach CF-21B to G3-FS3
281	Connect CF-21B top chord to G2-FS3
282	Connect CF-21B bottom chord to G2-FS3
283	Raise G3-FS3 for G3 BK-1 removal
284	Remove G3 BK-1 Lower G3-GS3
285	Raise G2-GS3 for G2 BK-1 removal
286	Remove G2 BK-1 Lower G2-GS3
287	Remove CRANE33
288	Remove CRANE32
289	Apply 1/2 CF-21B weight to G2-FS3 and G3-FS3

Table A3.5 Description of steps in the steel erection stage 5

Step	Description
290	Raise G4-FS4 using lifting crane CRANE44
291	Apply G4-FS4 selfweight
292	Position G4-FS4 and CRANE44 on its support, Pier 1
293	Add temporary lateral restraint at G4-FS4 bottom flange at CF-28C location Adjust G4-FS4 elevation for CF-27C bottom chord connectoin
294	Add temporary vertical restraint at G4-FS4 bottom flange at CF-28C location *Connect CF-27C bottom chord to G4-FS4*
295	*Connect CF-27C top chord to G4-FS4*
296	*Apply 1/2 CF-27C weight to G4-FS4*
297	Attach CF-28C to G3-FS4
298	*Connect CF-28C top chord to G4-FS4*
299	*Connect CF-28C bottom chord to G4-FS4*
300	Remove temporary vertical and lateral restraints at G4-FS4 bottom flange at CF-28C location **Remove artificial springs on CRANE44** Replace vertical restraints at G4 Pier-1 by gap elements Apply 1/2 CF-28C weight to G3-FS4 and G4-FS4
301	Attach CF-29C to G3-FS4
302	Connect CF-29C top chord to G4-FS4
303	Connect CF-29C bottom chord to G4-FS4
304	Apply 1/2 CF-29C weight to G3-FS4 and G4-FS4
305	Attach CF-26C to G3-FS4
306	Connect CF-26C top chord to G4-FS4
307	Connect CF-26C bottom chord to G4-FS4
308	Apply 1/2 CF-26C weight to G3-FS4 and G4-FS4
309	Attach CF-25C to G3-FS4
310	Connect CF-25C top chord to G4-FS4
311	Connect CF-25C bottom chord to G4-FS4
312	Remove CRANE44
313	Apply 1/2 CF-25C weight to G3-FS4 and G4-FS4
314	Attach CF-24C to G3-FS4
315	Connect CF-24C top chord to G4-FS4
316	Connect CF-24C bottom chord to G4-FS4
317	Apply 1/2 CF-24C weight to G3-FS4 and G4-FS4

Table A3.5 Description of steps in the steel erection stage 5 (continued)

Step	Description
318	Attach CF-23C to G3-FS4
319	Connect CF-23C top chord to G4-FS4
320	Connect CF-23C bottom chord to G4-FS4
321	Apply 1/2 CF-23C weight to G3-FS4 and G4-FS4
322	Raise G1-FS4 using lifting crane CRANE41
323	Apply G1-FS4 selfweight
324	Position G1-FS4 and CRANE42 on its support, Pier 1 Add temporary lateral restraint at G4-FS4 bottom flange at CF-28C location
325	Attach CF-27A to G2-FS4
326	Adjust G1-FS4 elevation for CF-27A bottom chord connectoin
327	Add temporary vertical restraint at G1-FS4 bottom flange at CF-28A location *Connect CF-27A bottom chord to G1-FS4*
328	*Connect CF-27A top chord to G1-FS4*
329	Remove temporary vertical restraints at G1-FS4 bottom flange at CF-28A location *Apply 1/2 CF-27A weight to G1-FS4 and G2-FS4*
330	*Attach CF-28A to G2-FS4*
331	*Connect CF-28A top chord to G1-FS4*
332	*Connect CF-28A bottom chord to G1-FS4*
333	Remove temporary lateral restraints at G1-FS4 bottom flange at CF-28A location **Remove artificial springs on CRANE41** Replace vertical restraints at G1 Pier-1 by gap elements Apply 1/2 CF-28A weight to G1-FS4 and G2-FS4
334	Attach CF-29A to G2-FS4
335	Connect CF-29A top chord to G1-FS4
336	Connect CF-29A bottom chord to G1-FS4
337	Apply 1/2 CF-29A weight to G1-FS4 and G2-FS4
338	Attach CF-26A to G2-FS4
339	Connect CF-26A top chord to G1-FS4
340	Connect CF-26A bottom chord to G1-FS4
341	Apply 1/2 CF-26A weight to G1-FS4 and G2-FS4
342	Attach CF-25A to G2-FS4
343	Connect CF-25A top chord to G1-FS4
344	Connect CF-25A bottom chord to G1-FS4
345	Remove CRANE41

Table A3.5 Description of steps in the steel erection stage 5 (continued)

Step	Description
346	Apply 1/2 CF-25A weight to G1-FS4 and G2-FS4
347	Attach CF-24A to G2-FS4
348	Connect CF-24A top chord to G1-FS4
349	Connect CF-24A bottom chord to G1-FS4
350	Apply 1/2 CF-24A weight to G1-FS4 and G2-FS4
351	Attach CF-23A to G2-FS4
352	Connect CF-23A top chord to G1-FS4
353	Connect CF-23A bottom chord to G1-FS4
354	Apply 1/2 CF-23A weight to G1-FS4 and G2-FS4

Table A3.6 Description of steps in the steel erection stage 6

Step	Description
355	Raise G4-FS3 using lifting crane CRANE34
356	Apply G4-FS3 selfweight
357	Position G4-FS3 and CRANE34 such that the translational and rotational continuity between G4-FS3 and G4-FS4 is achieved at field splice 3
358	*Apply bi-moment for warping continuity at G4 field splice 3*
359	**Remove artificial springs on CRANE34**
360	Achieve translational continuity (pinned connection at G4-FS2 and G4-FS3 top flange (field splice 2)
361	Adjust G4-FS3 elevation for achieving bottom flange translational continuity at field splice 2
362	Achieve G4 bottom flange translational continuity at field splice 2
363	Achieve G4 rotational continuity at field splice 2
364	Achieve G4 warping continuity at field splice 2
365	Attach CF-17C to G3-FS3
366	Connect CF-17C top chord to G4-FS3
367	Connect CF-17C bottom chord to G4-FS3
368	Apply 1/2 CF-17C weight to G3-FS3 and G4-FS3
369	Attach CF-18C to G3-FS3
370	Connect CF-18C top chord to G4-FS3
371	Connect CF-18C bottom chord to G4-FS3
372	Apply 1/2 CF-18C weight to G3-FS3 and G4-FS3
373	Attach CF-19C to G3-FS3
374	Connect CF-19C top chord to G4-FS3
375	Connect CF-19C bottom chord to G4-FS3
376	Apply 1/2 CF-19C weight to G3-FS3 and G4-FS3
377	Attach CF-22C to G3-FS3
378	Connect CF-22C top chord to G4-FS3
379	Connect CF-22C bottom chord to G4-FS3
380	Apply 1/2 CF-22C weight to G3-FS3 and G4-FS3
381	Attach CF-20C to G3-FS3
382	Connect CF-20C top chord to G4-FS3
383	Connect CF-20C bottom chord to G4-FS3
384	Apply 1/2 CF-20C weight to G3-FS3 and G4-FS3
385	Attach CF-21C to G3-FS3

Table A3.6 Description of steps in the steel erection stage 6 (continued)

Step	Description
386	Connect CF-21C top chord to G4-FS3
387	Connect CF-21C bottom chord to G4-FS3
388	Lower G4-GS3 for CRANE 34 removal
389	Remove CRANE34
390	Apply 1/2 CF-21C weight to G3-FS3 and G4-FS3
391	Raise G1-FS3 using lifting crane CRANE31
392	Apply G1-FS3 selfweight
393	Position G1-FS3 and CRANE31 such that the translational and rotational continuity between G1-FS3 and G1-FS4 is achieved at field splice 3
394	*Apply bi-moment for warping continuity at G1 field splice 3*
395	**Remove artificial springs on CRANE31**
396	Achieve translational continuity (pinned connection at G1-FS2 and G1-FS3 top flange (field splice 2)
397	Adjust G1-FS3 elevation for achieving bottom flange translational continuity at field splice 2
398	Attach CF-17A to G2-FS3
399	Connect CF-17A top chord to G1-FS3
400	Connect CF-17A bottom chord to G1-FS3
401	Apply 1/2 CF-17A weight to G1-FS3 and G2-FS3
402	Attach CF-18A to G2-FS3
403	Connect CF-18A top chord to G1-FS3
404	Connect CF-18A bottom chord to G1-FS3
405	Apply 1/2 CF-18A weight to G1-FS3 and G2-FS3
406	Attach CF-19A to G2-FS3
407	Connect CF-19A top chord to G1-FS3
408	Connect CF-19A bottom chord to G1-FS3
409	Apply 1/2 CF-19A weight to G1-FS3 and G2-FS3
410	Achieve G1 bottom flange translational continuity at field splice 2
411	Achieve G1 rotational continuity at field splice 2
412	Achieve G1 warping continuity at field splice 2
413	Attach CF-22A to G2-FS3
414	Connect CF-22A top chord to G1-FS3
415	Connect CF-22A bottom chord to G1-FS3
416	Apply 1/2 CF-22A weight to G1-FS3 and G2-FS3

Table A3.6 Description of steps in the steel erection stage 6 (continued)

Step	Description
417	Attach CF-20A to G2-FS3
418	Connect CF-20A top chord to G1-FS3
419	Connect CF-20A bottom chord to G1-FS3
420	Apply 1/2 CF-20A weight to G1-FS3 and G2-FS3
421	Attach CF-21A to G2-FS3
422	Connect CF-21A top chord to G1-FS3
423	Connect CF-21A bottom chord to G1-FS3
424	Remove FW1 and FW2A Remove CRANE31
425	Apply 1/2 CF-21A weight to G1-FS3 and G2-FS3
426	Release bottom chord moment resistent for all cross-frames

Table A3.7 Self-weight of each girder section

Girder Section	Weight, kN (kips)	Girder Section	Weight, kN (kips)
G1-FS1	310.42 (69.85)	G1-FS3	639.30 (143.84)
G2-FS1	234.76 (52.82)	G2-FS3	505.15 (113.66)
G3-FS1	226.18 (50.89)	G3-FS3	346.18 (77.89)
G4-FS1	178.41 (40.14)	G4-FS3	290.99 (65.47)
G1-FS2	1,060.83 (238.69)	G1-FS4	783.49 (176.29)
G2-FS2	833.90 (187.63)	G2-FS4	788.43 (177.40)
G3-FS2	569.22 (128.07)	G3-FS4	717.09 (161.35)
G4-FS2	452.36 (101.78)	G4-FS4	668.49 (150.41)

Table A3.8 The initial gaps[(1)], residual relative displacements and required resultant forces for the cross-frame connections in the steel erection stage 1

Step	Cross-frame Member	Connect to Girder	Initial Gap cm (in)	Residual relative displ. cm (in)	Required Forces kN (kips)
16	1B - Bottom chord	G2_FS1	0.913 (0.359)	NA	NA
17	1B - Top chord	G2_FS1	0.982 (0.387)	2.6E-04 (1.0E-04)	16.92 (3.81)
19	7B - Bottom chord	G2_FS1	1.222 (0.481)	7.3E-03 (2.9E-03)	21.32 (4.80)
20	7B - Top chord	G2_FS1	0.949 (0.374)	9.1E-05 (3.6E-05)	8.08 (1.82)
23	4B - Top chord	G2_FS1	1.070 (0.421)	2.1E-03 (8.4E-04)	8.12 (1.83)
24	4B - Bottom chord	G2_FS1	0.712 (0.280)	2.1E-03 (8.4E-04)	5.43 (1.22)
32	1C - Bottom chord	G4_FS1	0.912 (0.359)	NA	NA
33	1C - Top chord	G4_FS1	0.916 (0.361)	6.5E-04 (2.6E-04)	17.63 (3.97)
35	7C - Bottom chord	G4_FS1	1.153 (0.454)	5.0E-03 (1.9E-03)	7.01 (1.58)
36	7C - Top chord	G4_FS1	0.957 (0.377)	2.0E-03 (8.0E-04)	7.01 (1.58)
39	4C - Top chord	G4_FS1	1.044 (0.411)	8.5E-03 (3.4E-03)	21.07 (4.74)
40	4C - Bottom chord	G4_FS1	0.721 (0.284)	6.5E-04 (2.5E-04)	15.39 (3.46)
49	1A - Bottom chord	G1_FS1	0.635 (0.250)	NA	NA
50	1A - Top chord	G1_FS1	0.661 (0.260)	2.4E-04 (9.5E-05)	11.07 (2.49)
53	4A - Top chord	G1_FS1	0.676 (0.266)	3.7E-03 (1.4E-03)	5.86 (1.32)
54	4A - Bottom chord	G1_FS1	0.499 (0.196)	7.6E-06 (3.0E-06)	6.08 (1.37)
57	7A - Bottom chord	G1_FS1	0.415 (0.163)	3.5E-05 (1.4E-05)	8.26 (1.86)
58	7A - Top chord	G1_FS1	0.423 (0.167)	4.9E-04 (1.9E-04)	6.36 (1.43)

(1) The distance between two connection points

Table A3.9 The initial gaps[(1)], residual relative displacements and required resultant forces for the cross-frame connections between girder G2-FS2 and G3-FS2 in the steel erection stage 2

Step	Cross-frame Member	Connect to Girder	Initial Gap cm (in)	Residual relative displ. cm (in)	Required Forces kN (kips)
79	11B – Bottom chord	G2-FS2	5.193 (2.044)	2.7E-04 (1.1E-04)	30.32 (6.82)
80	11B – Top chord	G2-FS2	8.954 (3.525)	8.6E-03 (3.4E-03)	167.53 (37.69)
82	14B – Top chord	G2-FS2	15.140 (5.961)	8.1E-03 (3.2E-03)	18.80 (4.23)
83	14B – Bottom chord	G2-FS2	3.890 (1.532)	9.1E-03 (3.6E-03)	26.49 (5.96)
86	8B – Top chord	G2-FS2	1.345 (0.530)	5.8E-06 (2.3E-06)	79.98 (18.00)
87	8B – Bottom chord	G2-FS2	1.175 (0.463)	1.5E-05 (5.8E-06)	150.29 (33.81)
90	9B – Top chord	G2-FS2	1.060 (0.417)	4.1E-03 (1.6E-03)	36.50 (8.21)
91	9B – Bottom chord	G2-FS2	0.866 (0.341)	3.4E-05 (1.3E-05)	75.46 (16.98)
94	10B – Top chord	G2-FS2	0.918 (0.362)	1.6E-03 (6.3E-04)	18.59 (4.18)
95	10B – Bottom chord	G2-FS2	0.840 (0.331)	1.4E-05 (5.5E-06)	36.26 (8.16)
98	12B – Top chord	G2-FS2	0.675 (0.266)	2.4E-03 (9.6E-04)	29.90 (6.73)
99	12B – Bottom chord	G2-FS2	0.767 (0.302)	1.3E-05 (5.2E-06)	60.19 (13.54)
102	13B – Top chord	G2-FS2	0.467 (0.184)	3.5E-03 (1.4E-03)	22.08 (4.97)
103	13B – Bottom chord	G2-FS2	0.755 (0.297)	5.9E-06 (2.3E-06)	34.91 (7.85)
106	14B – Top chord	G2-FS2	0.351 (0.138)	6.8E-03 (2.7E-03)	16.83 (3.79)
107	14B – Bottom chord	G2-FS2	0.876 (0.345)	8.4E-06 (3.3E-06)	21.34 (4.80)
110	15B – Top chord	G2-FS2	0.222 (0.087)	5.8E-03 (2.3E-03)	10.89 (2.45)
111	15B – Bottom chord	G2-FS2	0.814 (0.321)	3.9E-03 (1.5E-03)	15.87 (3.57)

[(1)] The distance between two connection points

Table A3.10 The initial gaps[(1)], residual relative displacements and required resultant forces for the cross-frame connections between girder G3-FS2 and G4-FS2 in the steel erection stage 2

Step	Cross-frame Member	Connect to Girder	Initial Gap cm (in)	Residual relative displ. cm (in)	Required Forces kN (kips)
119	11C – Top chord	G4-FS2	3.939 (1.551)	1.5E-03 (6.0E-04)	82.98 (18.67)
120	11C – Bottom chord	G4-FS2	4.997 (1.967)	2.0E-03 (7.7E-04)	76.86 (17.29)
122	14C – Bototm chord	G4-FS2	3.595 (1.415)	3.1E-03 (1.2E-03)	54.48 (12.26)
123	14C – Top chord	G4-FS2	6.135 (2.415)	1.8E-03 (7.0E-04)	67.49 (15.19)
126	8C – Top chord	G4-FS2	0.898 (0.354)	1.2E-05 (4.6E-06)	41.73 (9.39)
127	8C – Bottom chord	G4-FS2	0.808 (0.318)	1.1E-05 (4.3E-06)	38.03 (8.56)
130	9C – Top chord	G4-FS2	0.757 (0.298)	8.9E-03 (3.5E-03)	22.97 (5.17)
131	9C – Bottom chord	G4-FS2	0.692 (0.272)	3.7E-06 (1.5E-06)	26.55 (5.97)
134	10C – Top chord	G4-FS2	0.650 (0.256)	1.6E-03 (6.4E-04)	15.60 (3.51)
135	10C – Bottom chord	G4-FS2	0.644 (0.254)	2.4E-06 (9.6E-07)	12.31 (2.77)
138	12C – Top chord	G4-FS2	0.516 (0.203)	7.5E-03 (3.0E-03)	41.55 (9.35)
139	12C – Bottom chord	G4-FS2	0.705 (0.278)	1.2E-06 (4.9E-07)	37.65 (8.47)
142	13C – Top chord	G4-FS2	0.387 (0.152)	6.5E-03 (2.6E-03)	32.51 (7.32)
143	13C – Bottom chord	G4-FS2	0.702 (0.276)	1.3E-06 (5.2E-07)	23.50 (5.29)
146	14C – Top chord	G4-FS2	0.215 (0.085)	1.2E-03 (4.8E-04)	34.14 (7.68)
147	14C – Bottom chord	G4-FS2	0.812 (0.320)	7.4E-03 (2.9E-03)	20.29 (4.57)
150	15C – Top chord	G4-FS2	0.105 (0.041)	3.4E-04 (1.3E-04)	14.52 (3.27)
151	15C – Bottom chord	G4-FS2	0.804 (0.316)	4.1E-03 (1.6E-03)	10.06 (2.26)

(1) The distance between two connection points

Table A3.11 The initial gaps[(1)], residual relative displacements and required resultant forces for the cross-frame connections between girder G1-FS2 and G2-FS2 in the steel erection stage 2

Step	Cross-frame Member	Connect to Girder	Initial Gap cm (in)		Residual relative displ. cm (in)		Required Forces kN (kips)	
161	11A – Bottom chord	G1-FS2	5.404	(2.128)	3.2E-03	(1.3E-03)	252.60	(56.83)
162	11A – Top chord	G1-FS2	7.183	(2.828)	3.2E-03	(1.3E-03)	198.97	(44.77)
165	14A – Bottom chord	G1-FS2	2.536	(0.998)	3.8E-03	(1.5E-03)	19.73	(4.44)
166	14A – Top chord	G1-FS2	1.999	(0.787)	1.4E-03	(5.6E-04)	29.24	(6.58)
169	8A – Top chord	G1-FS2	0.356	(0.140)	6.0E-04	(2.4E-04)	104.25	(23.46)
170	8A – Bottom chord	G1-FS2	0.282	(0.111)	7.8E-03	(3.1E-03)	135.99	(30.60)
173	9A – Top chord	G1-FS2	0.118	(0.046)	7.2E-03	(2.8E-03)	75.92	(17.08)
174	9A – Bottom chord	G1-FS2	0.128	(0.051)	2.2E-03	(8.5E-04)	99.76	(22.45)
177	10A – Top chord	G1-FS2	0.119	(0.047)	2.7E-06	(1.1E-06)	49.40	(11.11)
178	10A – Bottom chord	G1-FS2	0.068	(0.027)	3.6E-03	(1.4E-03)	62.01	(13.95)
181	12A – Top chord	G1-FS2	0.378	(0.149)	1.1E-05	(4.4E-06)	69.67	(15.68)
182	12A – Bottom chord	G1-FS2	0.135	(0.053)	2.7E-06	(1.1E-06)	86.41	(19.44)
185	13A – Top chord	G1-FS2	0.505	(0.199)	1.2E-05	(4.6E-06)	44.58	(10.03)
186	13A – Bottom chord	G1-FS2	0.070	(0.028)	1.8E-06	(7.2E-07)	55.32	(12.45)
190	14A – Top chord	G1-FS2	0.906	(0.357)	2.0E-05	(7.7E-06)	39.00	(8.77)
191	14A – Bottom chord	G1-FS2	0.168	(0.066)	2.3E-05	(9.0E-06)	42.12	(9.48)
193	15A – Top chord	G1-FS2	1.056	(0.416)	2.9E-05	(1.1E-05)	38.56	(8.67)
194	15A – Bottom chord	G1-FS2	0.133	(0.052)	3.6E-05	(1.4E-05)	35.70	(8.03)

[(1)] The distance between two connection points

Table A3.12 The initial gaps[(1)], residual relative displacements and required forces for the cross-frame connections between girder G2-FS4 and G3-FS4 in the steel erection stage 3

Step	Cross-frame Member	Connect to Girder	Initial Gap cm (in)	Residual relative displ. cm (in)	Required Forces kN (kips)
213	27B – Bottom chord	G2-FS4	3.546 (1.396)	NA	NA
214	27B – Top chord	G2-FS4	2.819 (1.110)	NA	NA
216	26B – Top chord	G2-FS4	2.794 (1.100)	2.9E-03 (1.1E-03)	45.79 (0.30)
217	26B – Bottom chord	G2-FS4	0.227 (0.090)	1.3E-03 (5.1E-04)	42.30 (9.52)
219	28B – Top chord	G2-FS4	0.439 (0.173)	6.0E-03 (2.4E-03)	10.81 (2.43)
220	28B – Bottom chord	G2-FS4	0.619 (0.244)	4.4E-05 (1.7E-05)	10.96 (2.47)
223	25B – Top chord	G2-FS4	0.129 (0.051)	1.4E-03 (5.7E-04)	9.07 (2.04)
224	25B – Bottom chord	G2-FS4	0.253 (0.099)	6.5E-04 (2.6E-04)	13.08 (2.94)
229	24B – Top chord	G2-FS4	0.561 (0.221)	1.6E-03 (6.3E-04)	3.85 (0.87)
230	24B – Bottom chord	G2-FS4	0.590 (0.232)	1.4E-05 (5.5E-06)	5.15 (1.16)
233	23B – Top chord	G2-FS4	0.662 (0.261)	1.4E-03 (5.4E-04)	5.06 (1.14)
234	23B – Bottom chord	G2-FS4	0.685 (0.270)	2.4E-05 (9.5E-06)	3.74 (0.84)
237	29B – Top chord	G2-FS4	0.722 (0.284)	5.9E-03 (2.3E-03)	3.23 (0.73)
238	29B – Bottom chord	G2-FS4	0.955 (0.376)	2.9E-03 (1.1E-03)	3.00 (0.68)

(1) The distance between two connection points

Table A3.13 Required resultant forces and moments for the field splice 2 of the girder G3-FS3 in the steel erection stage 4

Step	Drop-in Girder	Connect to Girder	Initial Gap cm (in)	Residual relative displ. cm (in)	Required Forces kN (kips)
245	G3_FS3 - TF Trans.	G3-FS2	6.210 (2.445)	2.0E-04 (7.9E-05)	75.17 (16.91)
247	G3_FS3 - BF Trans.		1.103 (0.434)	7.2E-04 (2.8E-04)	703.69 (158.33)
Step	**Drop-in Girder**	**Connect to Girder**	**Initial angle (rad)**	**Result angle (rad)**	**Required Force kN (kips)**
248	G3_FS3 - Section Orientation	G3-FS2	0.0020	2.8E-05	8.45 (0.06)
Step	**Drop-in Girder**	**Connect to Girder**	**Initial angle (rad)**	**Result angle (rad)**	**Required Moment kN-cm (kip-ft)[(1)]**
249	G3-FS3 – TF Orientation(warping)	G3-FS2	-0.0007	6.4E-05	-1,263.03 (-9.32)

(1) Resultant moment, for the flange, the moment is obtained by dividing the bi-moment by the distance between the centers of top and bottom flanges

Table A3.14 Required resultant forces and moments for the field splice 2 and 3 of the girder G2-FS3 in the steel erection stage 4

Step	Drop-in Girder	Connect to Girder	Initial angle (rad)	Result angle (rad)	Required Moment kN-cm (kip-ft)[1]
253	G2_FS3 - TF Orientation(warping)	G2-FS4	0.0009	NA	NA
Step	**Drop-in Girder**	**Connect to Girder**	**Initial Gap cm (in)**	**Result cm (in)**	**Required Forces kN (kips)**
255	G2_FS3 - TF Trans.	G2-FS2	6.408 (2.523)	1.0E-04 (3.9E-05)	304.83 (68.59)
269	G2_FS3 - BF Trans.		2.542 (1.001)	8.8E-04 (3.5E-04)	5,323.26 (1,198)
Step	**Drop-in Girder**	**Connect to Girder**	**Initial angle (rad)**	**Result angle (rad)**	**Required Force kN (kips)**
270	G2_FS3 - Section Orientation	G2-FS2	0.0008	2.2E-06	5.95 (0.04)
Step	**Drop-in Girder**	**Connect to Girder**	**Initial angle (rad)**	**Result angle (rad)**	**Required Moment kN-cm (kip-ft)[1]**
271	G2-FS3 – TF Orientation(warping)	G2-FS2	0.0005	-6.9E-05	4000.27 (29.53)

[1] The resultant moment is for the flange and is obtained by dividing the bi-moment by the distance between the centers of top and bottom flanges

Table A3.15 The initial gaps[1], residual relative displacements and required resultant forces for the cross-frame connections between girder G2-FS3 and G3-FS3 in the steel erection stage 4

Step	Cross-frame Member	Connect to Girder	Initial Gap cm (in)	Residual relative displ. cm (in)	Required Forces kN (kip)
258	17B - Top chord	G2_FS3	2.280 (0.898)	5.0E-03 (2.0E-03)	109.26 (24.58)
259	17B - Bottom chord	G2_FS3	2.660 (1.047)	7.6E-03 (3.0E-03)	53.87 (12.12)
262	18B - Top chord	G2_FS3	3.034 (1.194)	3.1E-04 (1.2E-04)	148.50 (33.41)
263	18B - Bottom chord	G2_FS3	1.104 (0.435)	5.4E-05 (2.1E-05)	111.50 (25.09)
266	19B - Top chord	G2_FS3	1.924 (0.757)	4.9E-05 (1.9E-05)	89.18 (20.07)
267	19B - Bottom chord	G2_FS3	0.959 (0.378)	8.7E-05 (3.4E-05)	44.81 (10.08)
273	22B - Top chord	G2_FS3	2.312 (0.910)	6.0E-05 (2.4E-05)	172.78 (38.87)
274	22B - Bottom chord	G2_FS3	2.006 (0.790)	2.2E-04 (8.8E-05)	280.27 (63.06)
277	20B - Top chord	G2_FS3	1.737 (0.684)	3.6E-05 (1.4E-05)	111.30 (25.04)
278	20B - Bottom chord	G2_FS3	1.439 (0.566)	9.7E-05 (3.8E-05)	223.70 (50.33)
281	21B - Top chord	G2_FS3	1.681 (0.662)	2.2E-05 (8.5E-06)	67.28 (15.14)
282	21B - Bottom chord	G2_FS3	1.400 (0.551)	1.3E-05 (5.0E-06)	116.89 (26.30)

[1] The distance between two connection points

Table A3.16 The initial gaps[(1)], residual relative displacements and required resultant forces for the cross-frame connections between girder G3-FS4 and G4-FS4 in the steel erection stage 5

Step	Cross-frame Member	Connect to Girder	Initial Gap cm (in)	Residual relative displ. cm (in)	Required Forces kN (kips)
294	27C - Bottom chord	G4_FS4	0.993 (0.391)	NA	NA
295	27C - Top chord	G4_FS4	13.356 (5.258)	NA	NA
298	28C - Top chord	G4_FS4	21.911 (8.626)	NA	NA
299	28C - Bottom chord	G4_FS4	0.844 (0.332)	NA	NA
302	29C - Top chord	G4_FS4	0.916 (0.361)	1.1E-05 (4.3E-06)	16.11 (3.62)
303	29C - Bottom chord	G4_FS4	0.376 (0.148)	3.0E-06 (1.2E-06)	9.52 (2.14)
306	26C - Top chord	G4_FS4	1.759 (0.693)	3.8E-05 (1.5E-05)	54.10 (12.17)
307	26C - Bottom chord	G4_FS4	0.658 (0.259)	4.3E-05 (1.7E-05)	43.99 (9.90)
310	25C - Top chord	G4_FS4	1.771 (0.697)	1.6E-05 (6.1E-06)	62.94 (14.16)
311	25C - Bottom chord	G4_FS4	0.683 (0.269)	3.4E-05 (1.4E-05)	37.37 (8.41)
315	24C - Top chord	G4_FS4	1.854 (0.730)	4.1E-06 (1.6E-06)	33.34 (7.50)
316	24C - Bottom chord	G4_FS4	0.917 (0.361)	2.1E-05 (8.1E-06)	18.28 (4.11)
319	23C - Top chord	G4_FS4	1.904 (0.750)	1.7E-05 (6.9E-06)	86.38 (19.44)
329	23C - Bottom chord	G4_FS4	0.992 (0.390)	1.9E-05 (7.6E-06)	48.04 (10.81)

(1) The distance between two connection points

Table A3.17 The initial gaps[(1)], residual relative displacements and required resultant forces for the cross-frame connections between girder G1-FS4 and G2-FS4 in the steel erection stage 5

Step	Cross-frame Member	Connect to Girder	Initial Gap cm (in)	Residual relative displ. cm (in)	Required Forces kN (kips)
327	27A - Bottom chord	G1_FS4	0.229 (0.090)	NA	NA
328	27A - Top chord	G1_FS4	1.224 (0.482)	NA	NA
331	28A - Top chord	G1_FS4	3.457 (1.361)	NA	NA
332	28A - Bottom chord	G1_FS4	0.642 (0.253)	NA	NA
335	29A - Top chord	G1_FS4	0.800 (0.315)	2.5E-05 (9.7E-06)	20.26 (4.56)
336	29A - Bottom chord	G1_FS4	0.294 (0.116)	3.1E-06 (1.2E-06)	10.99 (2.47)
339	26A - Top chord	G1_FS4	0.970 (0.382)	2.3E-05 (9.0E-06)	76.70 (17.26)
340	26A - Bottom chord	G1_FS4	0.221 (0.087)	2.2E-01 (8.7E-02)	46.15 (10.38)
343	25A - Top chord	G1_FS4	1.059 (0.417)	1.4E-05 (5.7E-06)	39.16 (8.81)
344	25A - Bottom chord	G1_FS4	0.218 (0.086)	2.9E-05 (1.1E-05)	24.84 (5.59)
348	24A - Top chord	G1_FS4	1.424 (0.560)	6.9E-06 (2.7E-06)	127.12 (28.60)
349	24A - Bottom chord	G1_FS4	0.283 (0.111)	3.5E-06 (1.4E-06)	80.51 (18.11)
352	23A - Top chord	G1_FS4	1.648 (0.649)	8.3E-03 (3.3E-03)	241.17 (54.26)
353	23A - Bottom chord	G1_FS4	0.367 (0.144)	7.8E-03 (3.1E-03)	149.15 (33.56)

(1) The distance between two connection points

Table A3.18 Required resultant forces and moments for the field splice 2 and 3 of the girder G4-FS3 in the steel erection stage 6

Step	Drop-in Girder	Connect to Girder	Initial angle (rad)	Result angle (rad)	Required Moment kN-cm (kip-ft)[(1)]
358	G4_FS3 - TF Orientation(warping)	G4-FS4	-0.0020	NA	NA
Step	**Drop-in Girder**	**Connect to Girder**	**Initial Gap cm (in)**	**Result cm (in)**	**Required Forces kN (kips)**
360	G4_FS3 - TF Trans.	G4-FS2	9.428 (3.712)	2.2E-05 (8.8E-06)	299.19 (67.32)
362	G4_FS3 - BF Trans.		2.489 (0.980)	1.5E-04 (5.9E-05)	983.31 (221.25)
Step	**Drop-in Girder**	**Connect to Girder**	**Initial angle (rad)**	**Result angle (rad)**	**Required Force kN (kips)**
363	G4_FS3 - Section Orientation	G4-FS2	0.014	1.5E-06	10.64 (0.08)
Step	**Drop-in Girder**	**Connect to Girder**	**Initial angle (rad)**	**Result angle (rad)**	**Required Moment kN-cm (kip-ft)[(1)]**
364	G4-FS3 – TF Orientation(warping)	G4-FS2	0.0046	-9.4E-05	8,215.82 (60.65)

(1) The resultant moment is for the flange and is obtained by dividing the bi-moment by the distance between the centers of top and bottom flanges

Table A3.19 The initial gaps[(1)], residual relative displacements and required resultant forces for the cross-frame connections between girder G3-FS3 and G4-FS3 in the steel erection stage 6

Step	Cross-frame Member	Connect to Girder	Initial Gap cm (in)	Residual relative displ. cm (in)	Required Forces kN (kips)
366	17C - Top chord	G4_FS3	1.863 (0.733)	5.0E-05 (2.0E-05)	237.91 (53.53)
367	17C - Bottom chord	G4_FS3	2.466 (0.971)	7.4E-05 (2.9E-05)	220.56 (49.63)
370	18C - Top chord	G4_FS3	1.707 (0.672)	5.2E-05 (2.0E-05)	198.88 (44.75)
371	18C - Bottom chord	G4_FS3	2.216 (0.872)	4.1E-05 (1.6E-05)	189.12 (42.55)
374	19C - Top chord	G4_FS3	1.549 (0.610)	4.2E-05 (1.6E-05)	159.49 (35.89)
375	19C - Bottom chord	G4_FS3	1.879 (0.740)	5.4E-06 (2.1E-06)	145.65 (32.77)
378	22C - Top chord	G4_FS3	1.696 (0.668)	8.2E-05 (3.2E-05)	116.84 (26.29)
379	22C - Bottom chord	G4_FS3	1.484 (0.584)	1.6E-05 (6.3E-06)	99.83 (22.46)
382	20C - Top chord	G4_FS3	1.393 (0.548)	3.3E-05 (1.3E-05)	92.28 (20.76)
383	20C - Bottom chord	G4_FS3	1.480 (0.583)	3.4E-07 (1.4E-07)	75.88 (17.07)
386	21C - Top chord	G4_FS3	1.469 (0.578)	3.2E-05 (1.3E-05)	58.69 (13.21)
387	21C - Bottom chord	G4_FS3	1.421 (0.560)	4.7E-06 (1.8E-06)	46.27 (10.41)

(1) The distance between two connection points

Table A3.20 Required resultant forces and moments for the field splice 2 and 3 of the girder G1-FS3 in the steel erection stage 6

Step	Drop-in Girder	Connect to Girder	Initial angle (rad)	Result angle (rad)	Required Moment KN-cm (kip-ft)[(1)]
394	G1-FS3 - TF Orientation(warping)	G1-FS4	-0.0007	NA	NA
Step	**Drop-in Girder**	**Connect to Girder**	**Initial Gap cm (in)**	**Result cm (in)**	**Required Forces kN (kips)**
386	G1-FS3 - TF Trans.	G1-FS2	12.046 (4.742)	1.6E-04 (6.3E-05)	598.18 (134.59)
410	G1-FS3 - BF Trans.		3.197 (1.259)	7.1E-04 (2.8E-04)	9,407.53 (2,117)
Step	**Drop-in Girder**	**Connect to Girder**	**Initial angle (rad)**	**Result angle (rad)**	**Required Force kN (kips)**
411	G1-FS3 - Section Orientation	G1-FS2	0.0004	2.0E-06	9.50 (0.07)
Step	**Drop-in Girder**	**Connect to Girder**	**Initial angle (rad)**	**Result angle (rad)**	**Required Moment KN-cm (kip-ft)[(1)]**
412	G1-FS3 – TF Orientation(warping)	G1-FS2	0.0003	-6.0E-05	4,011.79 (29.61)

(1) The resultant moment is for the flange and is obtained by dividing the bi-moment by the distance between the centers of top and bottom flanges

Table A3.21 The initial gaps[(1)], residual relative displacements and required resultant forces for the cross-frame connections between girder G1-FS3 and G2-FS3 in the steel erection stage 6

Step	Cross-frame Member	Connect to Girder	Initial Gap cm (in)		Residual relative displ. cm (in)		Required Forces kN (kips)	
399	17A - Top chord	G1_FS3	2.059	(0.811)	2.5E-04	(9.7E-05)	641.94	(144.44)
400	17A - Bottom chord	G1_FS3	1.969	(0.775)	2.0E-03	(8.0E-04)	430.59	(96.88)
403	18A - Top chord	G1_FS3	1.082	(0.426)	1.9E-05	(7.5E-06)	269.24	(60.58)
404	18A - Bottom chord	G1_FS3	0.859	(0.338)	8.0E-05	(3.2E-05)	302.43	(68.05)
407	19A - Top chord	G1_FS3	1.256	(0.495)	3.1E-05	(1.2E-05)	516.32	(116.17)
408	19A - Bottom chord	G1_FS3	0.580	(0.228)	3.5E-03	(1.4E-03)	389.86	(87.72)
414	22A - Top chord	G1_FS3	1.160	(0.457)	6.3E-06	(2.5E-06)	341.24	(76.78)
415	22A - Bottom chord	G1_FS3	1.098	(0.432)	9.9E-05	(3.9E-05)	455.97	(102.59)
418	20A - Top chord	G1_FS3	0.638	(0.251)	5.7E-06	(2.3E-06)	245.47	(55.23)
419	20A - Bottom chord	G1_FS3	0.609	(0.240)	5.8E-06	(2.3E-06)	356.92	(80.31)
422	21A - Top chord	G1_FS3	0.427	(0.168)	3.0E-06	(1.2E-06)	145.31	(32.70)
423	21A - Bottom chord	G1_FS3	0.479	(0.189)	5.4E-06	(2.1E-06)	206.61	(46.49)

(1) The distance between two connection points

REFERENCES

AASHTO Guide Specifications for Horizontally Curved Steel Girder Highway Bridges (2003) – With Design Examples for I-Girder and Box-Girder Bridges. American Association of State and Highway Transportation Officials, Washington D.C.

AASHTO LRFD Bridge Design Specifications with Interim 2005, 3rd Edition. (2004). American Association of State and Highway Transportation Officials, Washington D.C.

AASHTO/NSBA (2003). "Guidelines for Design for Constructibility." AASHTO/NSBA Steel Bridge Collaboration, G 12.1-2003.

AASHTO/NSBA (2006). "Guidelines for Design Details," AASHTO/NSBA Steel Bridge Collaboration, G 1.4 – 2006.

ABAQUS (2005) Hibbitt, Karlsson and Sorenson, Inc. "ABAQUS Standard Manual Version 6.4-1."

AISC (2005). *Steel Construction Manual*, 13th Edition, American Institute of Steel Construction, Chicago, IL.

AISC (1994). "Steel Erection for Highway, Railroad and Other Bridge Structures." Highway Structures Design Handbook, Vol. I, Chapter 14, AISC Marketing, Inc.

Watt, Alan (2000). "3D Computer Graphics." 3rd Edition, Addison-Wesley.

Andrade, A. and Camotim, D. (2005). "Lateral-Torsional Buckling of Singly Symmetric Tapered Beams: Theory and Applications." Journal of Engineering Mechanics, ASCE, 131:6, 586-597.

Alemdar, B. N. (2001). "Distributed Plasticity Analysis of Steel Building Structural System." Doctoral dissertation, Georgia Institute of Technology, Atlanta, GA.

Argyris, J. (1982). "An Excursion into Large Rotation." Computer Methods in Applied Mechanics And Engineering, 32, pp. 85-155.

Barker, R.M. and Puckett, J.A. (1997). Design of Highway Bridges, Wiley.

Boissonnade, N. and Maquoi, R. (2005). "A Geometrically and Materially Non-linear 3-D Beam Finite Element for the Analysis of Tapered Steel Members," Steel Structures, 5, 413-419.

Bradford, M.A. and Gao, Z. (1992). "Distortional Buckling Solutions for Continuous Composite Beams," Journal of Structural Engineering, ASCE, 118(1), 73-89.

Bradford, M. A. and Pi, Y.-L. (2001). "Behavior of unpropped composite girders curved in plan under construction loading." Engineering Structures, 23, 779-789.

BSDI. "BSDI 3D System - Computer Software for the Three-Dimensional Finite-Element Analysis of Bridge Superstructures." Bridge Software Development International, Ltd., P.O. Box 287, Coopersburg, PA.

Chang, C.-J. (2006). “GT-SABRE Manual.” Structural Engineering, Mechanics and Materials, School of Civil and Environmental Engineering, Georgia Institute of Technology, Atlanta, GA.

Chen, S.S., Aref, A.J., Ahn, I.-S., Chiewanichakorn, M., Carpenter, J.A., Nottis, A. and Kalpakidis, I. (2005). “Effective Slab Width for Composite Steel Bridge Members,” NCHRP Report 543, National Cooperative Highway Research Program, Transportation Research Board, Washington, D.C.

Chiewanichakorn, M. (2005). “Intrinsic Method of Effective Flange Width Evaluation for Steel-Concrete Composite Bridges,” Ph.D disserataion, SUNY, Buffalo, NY.

Chavel, B. W. and Earls, C. J. (2001). “Evaluation of Erection Procedures of The Horizontally Curved Steel I-Girder Ford City Bridge.” Research Report - University of Pittsburgh, Department of Civil and Environmental Engineering No. CE/ST 18.

Chavel, B. W. and Earls, C. J. (2006a). “Construction of a Horizontally Curved Steel I-Girder Bridge. Part I: Erection Sequence.” Journal of Bridge Engineering, Vol 11(1), pp. 81-90.

Chavel, B. W. and Earls, C. J. (2006b). “Construction of a Horizontally Curved Steel I-Girder Bridge. Part II: Inconsistent Detailing.” Journal of Bridge Engineering, Vol 11(1), pp. 91-98.

Crisfield, M. A. (1990). “A Consistent Co-Rotational Formulation For Non-Linear, Three-Dimensional, Beam-Elements.” Computer Methods in Applied Mechanics And Engineering, 81, pp. 131-150.

Crisfield, M. A. (1991). “Nonlinear Finite Element Analysis of Solids and Structures, Vol. 1.” John Wiley & Sons .

Crisfield, M. A. (1997). “Nonlinear Finite Element Analysis of Solids and Structures, Vol. 2: Advanced Topics.” John Wiley & Sons .

Davidson, J. S. (1996). “Nominal Bending and Shear Strength of Horizontally Curved Steel I-Girder Bridges.” Ph.D. Dissertation, Auburn University, Auburn, Alabama.

Descus I & II (2004), The Bridge Engineering Software & Technology Center of the University of Maryland.

Fukumoto, Y. and Nishida, S. (1981). “Ultimate load behavior of curved I-beams.” Journal of Engineering Mechanics Division, ASCE, 107(EM2), 367-385.

Galambos, T. V., Hajjar, J. F, Leon, R. T., Huang, W., Pulver, B. E. and Rudie, B. J. (1996), “Stresses in Steel Curver Girder Bridges.” Minnesota Dept. of Trans. Report No. MN/RC-96/28, August.

Galambos, T. V., Hajjar, J. F, Huang, W., Pulver, B. E., Leon, R. T and Rudie, B. J. (2000), "Comparison of measured and computed stresses in a steel curved girder bridge." Journal of Bridge Engineering, Vol. 5, No. 3, 191-199.

Gaylord, Jr., E. H., Gaylord, C. N., and Stallmeyer, J. E. (1997), "Structural Engineering HandBook," 4th Ed, McGraw-Hill.

Grubb, M. A., (1984). "Horizontally Curved I-Girder Bridge Analysis: V-Load Method." Transportation Research Record 982, Transportation Research Board, National Research Council, Washington, D. C. pp 26-35.

Hall, D. H., Brubb, M. A. and Yoo, C. H. (1999). "Improved Design Specifications for Horizontally Curved Steel Girder Highway Bridges." Report No. 424, NCHRP Project 12-38 Final Report, transportation Research Board, NRC, Washington, D. C.

Heins, C.P. and Kuo, J.T.C., (1972). "Torsional Properties of Composite Girders." AISC Engineering Journal, April.

Ibrahimbegovic, A., Frey, F. and Kozar, I. (1995). "Computational Aspects of Vector-Like Parametrization of Three-Dimensional Finite Rotations." International J. for Numerical Methods in Engineering, 38, pp. 3653-3673.

Izzuddin, B.A., and Smith, D.L, (1996). "Large-Displacement Analysis of Elasto-plastic Thin-Walled Frames. I: Formulation and Implementation." Journal of Structural Engineering, 122(8), pp. 905-914.

Izzuddin, B.A., (2003). "Integration of Beam-Column and Shell Elements in Large Displacement Structural Analysis." Proceedings of the International Symposium on New Perspectives for Shell and Spatial Structures, IASS-APCS 2003, Taipei, Taiwan, 22-25 October 2003.

Jung, S.-K., White, D.W., Bashah, F. and Wright, W. (2005). "Ultimate Strength of Horizontally-Curved I-Girder Bridge Structural Systems," Proc. Annual Technical Session, SSRC, Univ. of Missouri, Rolla, MO, April.

Kerensky, O. A., Flint, A. R. and Brown, W. C., (1956). "The Basis for Design of Beams and Plate Girders in the Revised British Standard 153." Proceeding, I.C.E., Part III, Vol. 5, August 1956, p. 396.

Kitipornchai, S. and Trahair, N.S. (1972). "Elastic Stability of Tapered I-Beams." Journal of Structural Division, ASCE, 98(ST3), pp. 713-728.

Kitipornchai, S. and Trahair, N.S. (1975). "Elastic Behavior of Tapered Monosymmetric I-Beams." Journal of Structural Division, ASCE, 101(ST8), pp. 1661-1678.

Kitipornchai, S. and Trahair, N.S. (1980). "Buckling Properties of Monosymmetric I-Beams." Journal of Structural Division, ASCE, 106(ST5), pp. 941-957.

Kitipornchai, S., Wang, C.M. and Trahair, N.S. (1986). "Buckling of Monosymmetric I-Beams under Moment Gradient." Journal of Structural Engineering, 112(4), pp. 781-799.

Huang, W.-H. (1996). “Curved I-Girder Systems.” PhD dissertation, Department of Civil and Environmental Engineering, University of Minnesota, Minneapolis, MN.

Linzell, D. G. (1999). “Studies of a full-scale horizontally curved steel I-girder bridge system under self-weight. “Ph.D. thesis, School of Civil and Environmental Engineering, Georgia Institute of Technology, Atlanta, GA.

Love, A. E. H. (1944). “A treatise on the mathematical theory of elasticity.” 4th Ed., Dover, New York.

MDX (2004). MDX Software Inc. “MDX User Manual, version 6.”

Mozer, J., and Culver, C. G. (1970). “Horizontally Curved Highway Bridges, Stability of Curved Plate Girders-P1.” FHWA, Contract No. FH-11-7389, Washington, D. C., pp. 1-95.

Nour-Omit, B. and Rankin, C. C. (1991). “Finite Rotation Analysis and Consistent Linearization Using Projectors.” Computer Methods in Applied Mechanics and Engineering 93, pp 353-384.

NSBA (1996). “V-Load Analysis, An Approximate Procedure, Simplified and Extended, for Determining Moments and Shears in Designing Horizontally-Curved Open-Framed Highway Bridges.” Highway Structures Design Handbook, Vol. I, Chapter 12, National Steel Bridge Alliance.

Nukala, P. K. (1997). “Three dimensional Second-Order Inelastic Analysis of Steel Frames.” Doctoral Dissertation, Purdue University, 221 pp.

Nukala, P. K. and White, D. W. (2004). “A Mixed Finite Element for Three-Dimensional Nonlinear Analysis of Steel Frames.” Structural Engineering, Mechanics and Materials Research Report, School of Civil and Environmental Engineering, Georgia Institute of Technology.

Pi, Y.-L. and Trahair, N. S. (1996). “Nonlinear Elastic Behavior of I-Beams Curved in Plan.” Research Report - University of Sydney, Department of Civil Engineering No. R734, 1-45.

Pi, Y.-L., Bradford, M. A. and Trahair, N. S. (2000). “Inelastic Analysis and Behavior of Steel I-Beams Curved in Plan.” Journal of Structural Engineering, ASCE, 126(7), 772-779.

Rankin, C. C. and Nour-Omid, B. (1988). “The use of projectors to improve finite element performance.” Computers & Structures Vol. 30 No. ½, pp. 257-267.

Ronagh, H. R., Bradford, M. A. and Attard, M. M. (2000a). “Nonlinear Analysis of Thin-Walled Members of Variable Cross-Sectoin. Part I: Theory.” Computers & Structures Vol. 77, pp. 257-299.

Ronagh, H. R., Bradford, M. A. and Attard, M. M. (2000b). “Nonlinear Analysis of Thin-Walled Members of Variable Cross-Sectoin. Part II: Application.” Computers & Structures Vol. 77, pp. 257-299.

Simo, J. C. and Vu-Quoc, L. (1991). “A Geometrically-Exact Rod Model Incorporating Shear and Torsion-Warping Deformation.” International Journal of Solids Structures, Vol. 27, No. 3, 371-393.

SSRC (1991). “A Look to The Future.” Report of Work Shop (14-15 Apr. 1991) on Horizontally Curved Girders, Structural Stability Research Council, Task Group 14.

Teh, L. H. and Clarke, M. J. (1998). “Co-rotational and Lagrangian formulations for elastic three-dimensional beam finite elements.” J. of Constructional Steel Research 48, pp. 123-144.

Topkaya, C. and Williamson, E. B. (2003). “Development of computational software for analysis of curved girders under construction loads.” Computer and Structures, 81, 2087-2098.

Topkaya, C., Yura, J. A. and Williamson, E. B. (2004). “Composite Shear Stud Strength at Early Concrete Ages.” Journal of Structural Engineering, 130 (6), 952-960.

White, D.W., Jung, S.K. and Chang, C.-J. (2002). “Design of Curved Composite Test Bridge,” Report to Professional Services Industries and Federal Highway Administration, December, 99 pp. .

White, D.W. and Jung, S.K. (2003). “Simplified Lateral-Torsional Buckling Equations for Singly-Symmetric I-Shaped Members,” Structural Engineering, Mechanics and Materials Report No. 24b, School of Civil and Environmental Engineering, Georgia Institute of Technology, Atlanta, GA.

Wekezer, J. W. (1985). “Instability of Thin Walled Bars” Journal of Engineering Mechanics, 111(7), 923-935.

Yang, Y.-B. and Yau, J.-D. (1988). “Stability of Beams with Tapered I-Sections” Journal of Engineering Mechanics, 113(9), 1337-1357.

Yoshida, H. and Maegawa, K. (1983). “Ultimate strength analysis of curved I-beams.” Journal of Engineering Mechanics Division, ASCE, 109(EM1), 192-214.

VITA

Ching-Jen Chang was born on September 2, 1972 in I-Lan, Taiwan. He received his Bachelor of the Science degree and Master of Science degree in Civil Engineering from National Chiao-Tung University in 1994 and 1996, respectively. He joined the Taiwan Army as a Second Lieutenant from 1996 to 1998. After military service, he participated in the construction of the Refuse Resource Recycle Incineration Plant in I-Lan County, Taiwan. At the same time, he offered the course “Computer Application in Structural Engineering” in National I-Lan University. He joined the School of Civil and Environmental Engineering at the Georgia Institute of Technology in the Fall Semester of year 2000 to pursue the degree of Ph.D.

He has developed the software system GT-SABRE for the analysis and simulation of curved I-girder bridge construction based on the FE++ framework. His current research interests include finite element technology, construction simulation of steel bridge structures and computer aided engineering.